HOKKAIDO UNIVERSITY

Title	Seismological Structure and Source Studies with Teleseismic Body-wave Analysis
Author(s)	垂水, 洸太郎
Degree Grantor	北海道大学
Degree Name	博士(理学)
Dissertation Number	甲第16259号
Issue Date	2025-03-25
DOI	https://doi.org/10.14943/doctoral.k16259
Doc URL	https://hdl.handle.net/2115/97676
Type	doctoral thesis
File Information	Kotaro_Tarumi.pdf

Hokkaido University Collection of Scholarly and Academic Papers : HUSCAP

Seismological Structure and Source Studies with Teleseismic Body-wave Analysis

(遠地実体波解析による地震学的構造および波源の研究)

Kotaro TARUMI

A thesis submitted for
the degree of Doctor of Philosophy

Department of Natural History Sciences
Graduate School of Science
Hokkaido University

March 2025

Abstract

We propose new approaches using teleseismic P-wave analyses to investigate seismic structures and source processes. The first half (Part I) of this thesis focuses on structural studies, with an emphasis on mapping the spatial distribution of seismic discontinuities in the upper mantle. The second half (Part II) aims to resolve the complex seismic wave sources using a source imaging method, P-wave back-projection. These broad topics are essential for advancing our understanding of Earth's internal structure and dynamics, including earthquake ruptures and volcanic eruptions.

A joint analysis method combining teleseismic receiver functions (RFs) and surface waves has recently been developed and applied to estimate seismic discontinuities in the upper mantle. This approach traditionally assumes a one-dimensional stratified structure beneath a seismic station, leading to the use of azimuthally averaged RF data, which represent wave-type conversions (from P to S, or vice versa) at seismic interfaces. However, lateral structural variations in the upper mantle generate significant azimuthal dependence in RFs, depending on the incoming directions of body waves. In this study, we utilize azimuth-dependent RFs to extend the conventional RF inversion method, enabling the detection of localized variations in seismic interfaces and their properties.

The new approach utilizing azimuth-dependent RFs is applied to the Australian continent. First, we construct a catalog of the orientations of horizontal sensors in seismometers installed across Australia, and compute P-wave RFs (P-RFs) with corrections for station orientations. The resultant datasets, even in the stable cratonic areas, exhibit significant dependence on the directions of seismic events. We incorporate the azimuth-dependent P-RFs into a joint inversion method with multimode surface wave dispersions (SWDs). This novel usage of P-RFs in joint inversions with multimode SWDs reveals localized variations in upper mantle discontinuities and associated elastic properties. By extensively applying the joint inversion method to a large number of permanent and temporary stations, we map the Australian upper

mantle discontinuities, including the Lithosphere-Asthenosphere Boundary (LAB), the Mid-Lithospheric Discontinuity (MLD), and X-discontinuity (X-D) beneath LAB.

The LAB is shallow (70–100 km) in Phanerozoic eastern Australia and deepens toward western cratonic regions (120–200 km). A thick lithosphere (170–200 km) with significant radial anisotropy but minimal S-velocity reductions is observed beneath central Australia. MLDs in cratonic regions are identified at three distinct depths (from 60 to 130 km), with either negative or positive S-velocity changes depending on the tectonic setting. X-Ds, characterized by velocity increases beneath the LAB, are detected at multiple depths (∼170 km, 220–280 km, and ∼310 km), often associated with a weakening of radial anisotropy below the X-Ds. The shallowest X-D (∼170 km) is predominantly found beneath eastern Australia and is likely influenced by thermal effects in the asthenosphere, while deeper X-Ds may correspond to the Lehmann discontinuity or phase transitions in pyroxene. These results demonstrate that our approach is effective for reconstructing upper mantle discontinuities and their elastic properties on both large and localized scales.

In the second half of this thesis, we explore the new applicability of back-projection (BP), a seismic source imaging method. The first application of the BP analysis is to teleseismic P-waves from a massive eruption at Hunga Tonga-Hunga Ha'apai in 2022. The BP results successfully detected the locations and timing of multiple explosions, even when P-waves from each eruption overlapped and were masked by other seismic signals and noises. The second application of the BP analysis involves multi-frequency teleseismic P-wave records generated by the 2024 Mw 7.5 Noto Peninsula Earthquake, which could be a doublet earthquake. The resultant BP images successfully depict the complex frequency-dependent seismic radiation process, suggesting contributions from crustal fluids and a complex fault system. These two applications demonstrate the potential of the BP method to track intermittent and continuous multiple sources and to resolve frequency-dependent radiation processes linked to complex source phenomena.

Observed teleseismic body waveforms contain abundant information about seismic structure and wave sources, making them invaluable for investigating seismic phenomena. Teleseismic data-oriented explorations through new approaches deepen our understanding of Earth's dynamics processes.

Acknowledgments

I would like to sincerely express my gratitude to everyone who supported me throughout my doctoral study.

First of all, I am deeply grateful to my supervisor, Professor Kazunori Yoshizawa, who provided me with invaluable guidance and advice from my master's course through to my doctoral research. He imparted scientifically insightful knowledge, ideas, skills, and techniques in seismology, academic writing, English communication, and conference presentations. He consistently encouraged me, even during my detours or prolonged explorations. Moreover, he dedicated substantial time and care to reviewing my research, papers, and thesis and offering constructive feedback. Without his support, I would not have been able to complete my Ph.D. thesis. Professor Yoshizawa is my role model in terms of research philosophy, and conducting doctoral research under his supervision is a great honor for me. Once again, I wish to express my deepest gratitude to him.

I would also like to deeply thank all the professors in the Solid Earth seminar. Professor Youichiro Takada provided invaluable advice on presentation techniques and the mindset of a researcher since my master's course, which was very helpful. Professor Makoto Naoi kindly fostered a friendly atmosphere and inspired new perspectives in seismology with machine learning. Conversations with Professor Kiyoshi Yomogida during office hours provided insightful comments and pleasant breaks. Professor Masato Furuya's lectures in the solid seminar were fascinating and were profoundly stimulating topics.

I also appreciate many researchers for constructive comments, advice, and encouragement regarding my research at academic conferences and workshops: Professors Takehi Isse, Kiwamu Nishida (ERI, the University of Tokyo), Professors Keiko Kuge,

and Mamoru Kato (Kyoto University). In particular, conversations with Prof. Isse and Prof. Kuge at AGU 2023 in San Francisco helped me consider my future career. Also, Prof. Kuge provided numerous constructive comments on my Ph.D. thesis.

I am thankful to Drs. Debasis Mohanty, Ayumu Mizutani, and Baigalimaa Ganbat, Messrs. Kouki Auchi, Tohma Tezuka, Taiyo Higa. Casual talks and research discussions with them in our student rooms warmly brightened and enriched my life. Conversations with Debasis and Baila-san helped me improve my English skills. I also thank geodesy laboratory members and all alumni of the solid seminar.

I acknowledge the broadband seismic waveform data provided by the IRIS Data Management Center. ObsPy (Beyreuther et al., 2010) is used for seismic waveform analysis and data acquisition. To generate all the figures in this thesis, I used matplotlib (Hunter, 2007), cartopy (Office, 2010), Generic Mapping Tools (Wessel et al., 2019), and PyGMT (Uieda et al., 2021). In this thesis, I employed earthquake catalogs by Global CMT (Dziewonski et al., 1981; Ekström et al., 2012) and JMA (JMA, 2024a), and the JSPJ fault model (MEXT, 2013). Most computations in Chapters 3 and 4 were done with Hokkaido University High-Performance Intercloud at the information initiative center, Hokkaido University, which enabled me to complete the research presented in Part I.

During my Ph.D. course, fellowships from Hokkaido University and JSPS have provided financial support to me (JST SPRING grant number JPMJSP2119 and JSPS KAKENHI grand number 24KJ0294). Also, the Bayesian inversion codes by Mr. Toru Taira, an alumnus of our seismology lab., were very helpful.

Chapter 2 is based on an original paper, "Station-orientation catalog for Australian broadband seismic stations" by K. Tarumi & K. Yoshizawa, submitted to *Pure and Applied Geophysics*. The work in Chapter 3 is based on an original paper, "Detecting rapid lateral changes of upper mantle discontinuities using azimuth-dependent P-wave receiver functions and multimode surface waves" by K. Tarumi & K. Yoshizawa, submitted to *Physics of the Earth and Planetary Interiors*. The work in Chapter 5 is based on an originally published paper, "Eruption sequence of the 2022 Hunga Tonga-Hunga Ha'apai explosion from back-projection of teleseismic P waves" by K. Tarumi & K. Yoshizawa, *Earth and Planetary Science Letter* (Tarumi & Yoshizawa, 2023), and

chapter 6 is based on another paper, "Frequency-dependent seismic radiation process of the 2024 Noto Peninsula earthquake from teleseismic P-wave back-projection" by K. Tarumi & K. Yoshizawa, submitted to *Earth and Planetary Science Letter*.

Finally, I extend my deepest gratitude to my parents, brother, and two sisters (*Ruru* and *Rin*) for their support and comfort.

Contents

Abstract i

Acknowledgments iii

1 Introduction **1**

1.1 Seismological studies using teleseismic body waves - two scopes of this thesis 1

1.2 Seismic structure in the continental upper mantle using teleseismic body waves 3

1.2.1 Detections of upper mantle discontinuities by teleseismic body waves 6

1.2.2 Continental upper mantle discontinuities 8

1.3 Source imaging using teleseismic body waves 11

1.4 Outlines of this thesis 14

I Seismic Structural Studies **17**

2 Station-orientation catalog for Australian broadband seismic stations **18**

2.1 Introduction 18

2.2 Data and Method 20

2.3 Results 22

2.3.1 Permanent Stations 22

2.3.2 Temporary Stations 28

2.4 Discussion and Conclusions 29

3 Detecting rapid lateral changes of upper mantle discontinuities using azimuth-dependent P-wave receiver functions and multimode surface waves 33

3.1 Introduction . . . 33
3.1.1 Recent receiver function inversions . . . 34
3.1.2 Australian tectonics and the scope of this chapter . . . 36
3.2 Data sets . . . 37
3.2.1 Multi-mode surface-wave dispersion . . . 37
3.2.2 Azimuth-dependent P-wave receiver functions for permanent stations . . . 38
3.3 Trans-dimensional Bayesian inversion . . . 44
3.3.1 Model parameterization . . . 44
3.3.2 The prior . . . 45
3.3.3 Likelihood function . . . 46
3.3.4 Reversible-jump sampling with Parallel Tempering . . . 47
3.4 Results of inversions for Australian stations . . . 48
3.4.1 Phanerozoic eastern Australia . . . 49
3.4.2 Cratonic central and western Australia . . . 53
3.5 Localized conversion point maps . . . 56
3.5.1 Phanerozoic eastern Australia . . . 57
3.5.2 Cratonic central and western Australia . . . 60
3.6 Discussion . . . 65
3.7 Conclusions . . . 69

4 Mapping upper mantle discontinuities beneath the Australian continent using multimode surface waves and receiver functions 71

4.1 Introduction . . . 71
4.1.1 Australian upper mantle discontinuities . . . 73
4.1.2 Scope of this chapter . . . 74
4.2 Data . . . 75
4.3 Methods for discontinuity detection and mapping . . . 79
4.3.1 Trans-dimensional Bayesian inversion and discontinuity detections 79

4.3.2 Regional-scale mapping process of seismic discontinuities 81
4.4 Seismic discontinuity maps beneath Australia 86
4.4.1 Moho discontinuity 86
4.4.2 Base of lithosphere 89
4.4.3 X-discontinuities 92
4.4.4 Mid-lithospheric discontinuities 95
4.5 Discussion 99
4.5.1 Comparison with previous MLD distribution 99
4.5.2 Interpretations of MLDs 101
4.5.3 Thick lithosphere in central Australia 105
4.5.4 Origins of X-Ds 107
4.6 Conclusions 110

II Seismic Source Studies 112

5 Eruption Sequence of the 2022 Hunga Tonga-Hunga Ha'apai explosion 113
5.1 Introduction 113
5.2 Data & Method 115
5.2.1 Dataset: teleseismic long-period P-waves 115
5.2.2 Back-projection analysis 117
5.2.3 Criteria for identifying the explosive eruptions 120
5.3 Eruption sequence inferred from back-projection with teleseismic P-waves 120
5.3.1 First sequence: Events A – N 121
5.3.2 Second sequence: Events O – S 124
5.4 Discussion 124
5.4.1 Multiple explosions detected by P-wave back-projection: Relation with surface wave trains 124
5.4.2 Eruption cycle and atmosphere-lithosphere coupled modes . . . 127
5.5 Conclusions 129

6 Frequency-dependent seismic radiation process of the 2024 Noto Peninsula earthquake from teleseismic P-wave back-projection 131
6.1 Introduction . . . 131
6.2 Data and Method . . . 134
6.2.1 Multi-frequency Teleseismic P-wave . . . 135
6.2.2 Back Projection with LQT coordinate system . . . 135
6.3 Results . . . 139
6.3.1 E1: Initial radiation around the hypocenter (0–18 s) . . . 140
6.3.2 E2: High-frequency radiation lacking low-frequency (18–28 s) . . 142
6.3.3 E3: Intense radiation in the inland of the Noto Peninsula (25–44 s) 142
6.3.4 E4: Intense radiation in the eastern offshore region (25–44 s) . . 142
6.4 Discussion . . . 144
6.4.1 E1′: Starting phase of this Earthquake . . . 146
6.4.2 E2′: Triggering the low-frequency radiation of E2, E3 and E4 . . 146
6.4.3 E4′: Stopping phase of E4 . . . 147
6.4.4 Frequency-dependent P-wave radiation and complex fault rupture process . . . 148
6.5 Conclusions . . . 150

7 Summary and prospects for future research 152
7.1 Summary of this thesis . . . 152
7.2 Future prospects . . . 154
7.2.1 Extending station-orientation catalog . . . 154
7.2.2 Additional constraints on the localized seismic discontinuity image 155
7.2.3 Azimuthal anisotropy . . . 155
7.2.4 Applications to other regions: Global perspectives on seismic discontinuities . . . 157
7.2.5 Capturing multiple earthquakes or non-earthquake sources . . . 157

A Supplementary information for Chapter 2 159
A.1 Station-orientation table . . . 159
A.2 Supplementary figures . . . 165

B Supplementary information for Chapter 3 **174**

B.1 Theoretical background of Receiver Functions 174

B.2 Supplementary figures for Chapter 3 177

C Supplementary information for Chapter 4 **186**

D Supplementary information for Chapter 5 **199**

D.1 Air-Earth coupled seismic normal mode: the 1991 Pinatubo and the 2022 Tonga 199

D.2 Event catalog detected by BP 202

D.3 Supplementary Figures 204

E Supplementary information for Chapter 6 **206**

Bibliography **212**

Chapter 1

Introduction

1.1 Seismological studies using teleseismic body waves - two scopes of this thesis

Teleseismic body waves, observed at distant receivers from their source locations, carry abundant information about both the seismic structure and the wave source. As the major part of the propagation paths of teleseismic body waves traverses the Earth's lower mantle - an area with relatively weak lateral heterogeneity - they have been extensively studied to infer the seismic structure of the upper mantle and source characteristics.

Figure 1.1 provides a schematic illustration of the relationship between seismic sources and receivers in studies of seismic structures and sources. When teleseismic body waves from multiple seismic sources are recorded at a single receiver, we can retrieve seismic structures directly beneath the seismic station (Figure 1.1 (a)), owing to their near-vertical incidence. Conversely, when teleseismic waves from a single seismic source are recorded at multiple receivers, we can resolve the physical properties of the seismic wave source (Figure 1.1 (b)).

Theoretically, an observed waveform $u(t)$ at a receiver can be expressed as:

$$u(t) = S(t) * G(t) * I(t) + N(t), \tag{1.1}$$

where $S(t)$, $G(t)$, $I(t)$, and $N(t)$ represent the seismic source term, the Green's function, the instrumental response, and the unknown noises, respectively. When the instrumental response is known, the remaining unknowns in (1.1) that can be determined from observations are the seismic source term and the Green's functions, which reflect the

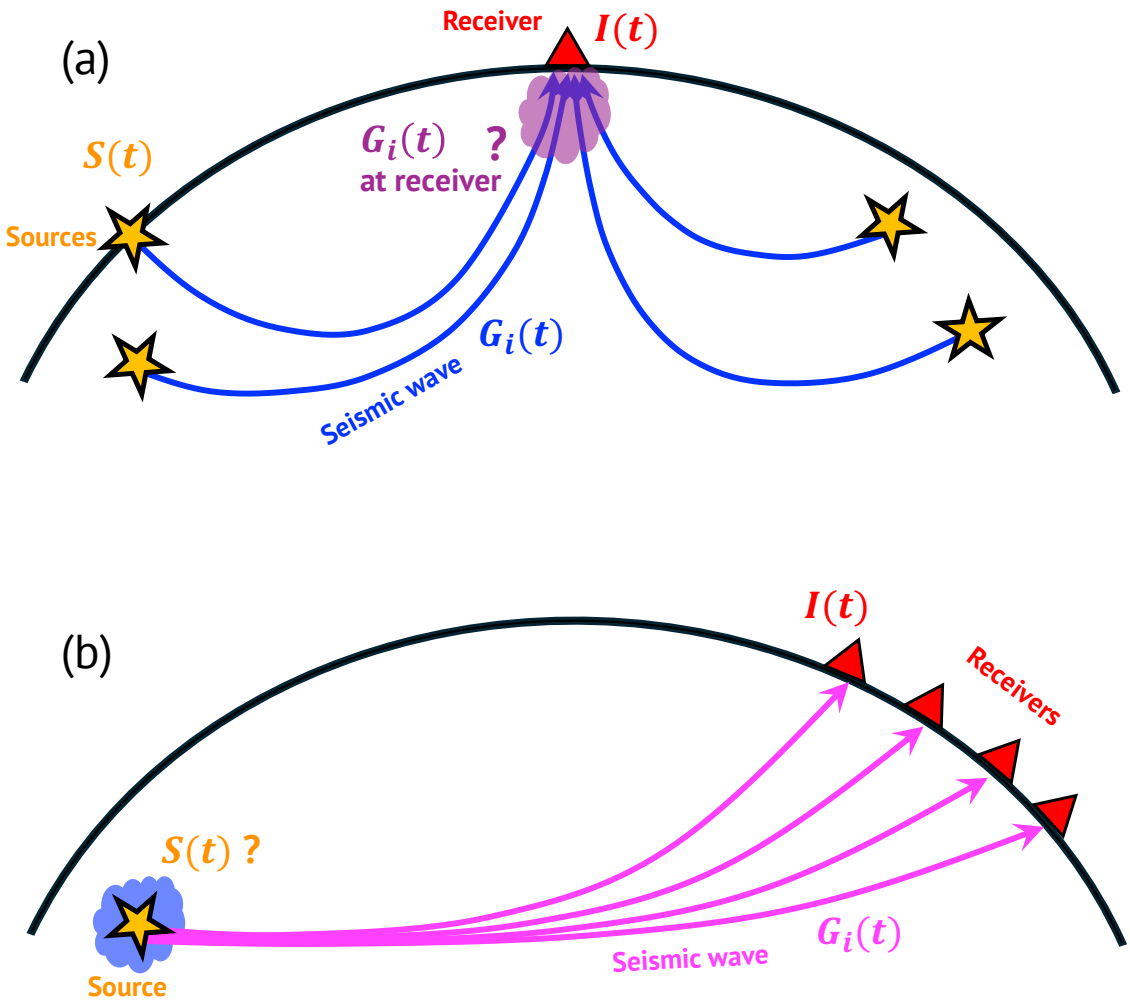

Figure 1.1: Schematic illustrations of seismic structural and source studies using teleseismic body waves. Red triangles and yellow stars indicate receivers and wave sources, respectively. The black line depicts the Earth's surface. The terms $S(t)$, $G_i(t)$, and $I(t)$ denote the seismic source term, the i-th component of Green's function, and the instrumental response, respectively. (a) An image of seismic structural study. Blue lines represent the ray path of seismic waves recorded at a receiver. Teleseismic body waves from multiple sources provide information about the seismic structure beneath the station, illustrated as a purple blurred region. (b) An image of seismic source study. Magenta lines indicate the ray path of seismic waves recorded at multiple receivers. Teleseismic body waves observed at multiple stations reflect properties of the seismic source, visualized by a blue blurred region.

structural effects along the propagating path. Since seismic structure and source characteristics are complementary, analyzing teleseismic body waves to resolve $S(t)$ and/or $G(t)$ provides valuable information on the Earth's internal structure and seismic source processes.

Based on these advantages for studying seismic structures and sources, this thesis proposes new approaches for teleseismic body wave analyses to estimate seismic structures in the continental upper mantle and to investigate seismic wave sources. The first objective is to develop a new approach for retrieving the detailed upper mantle structure and to apply this method to the Australian continent - one of the oldest but currently fastest-moving continents in the world (PART I: Chapters 2–4). The second objective is to explore new possibilities for seismic source imaging and to resolve seismic source phenomena using globally recorded teleseismic body waves for two recent disastrous events: the massive volcanic eruption in Tonga and the Noto earthquake in Japan (PART II: Chapters 5 and 6). In the following two sections, we summarize the current knowledge regarding the continental upper mantle structure and the methodologies for seismic source imaging.

1.2 Seismic structure in the continental upper mantle using teleseismic body waves

Probing the Earth's upper mantle structure is essential for understanding the Earth's tectonic history, past and present mantle dynamics, plate motion, and evolution, as well as earthquake and volcanic activities. In particular, continental plates, encompassing old and stable cratons formed in the Archean and Proterozoic eras, have remained buoyant and drifted across the Earth's surface over billions of years. The present-day structure of the continental upper mantle serves as a repository of complex, time-integrated tectonic records, including plate collision, subduction, and breakup. Thus, the detailed investigations of the seismic structure of continental lithosphere and asthenosphere offer invaluable insights into the Earth's geological processes and evolution.

The seismic structure of the continental upper mantle has been imaged through various approaches utilizing seismic surface waves and teleseismic body waves over several decades (e.g., Nakanishi & Anderson, 1983; Bostock & Rondenay, 1999; Masters et al.,

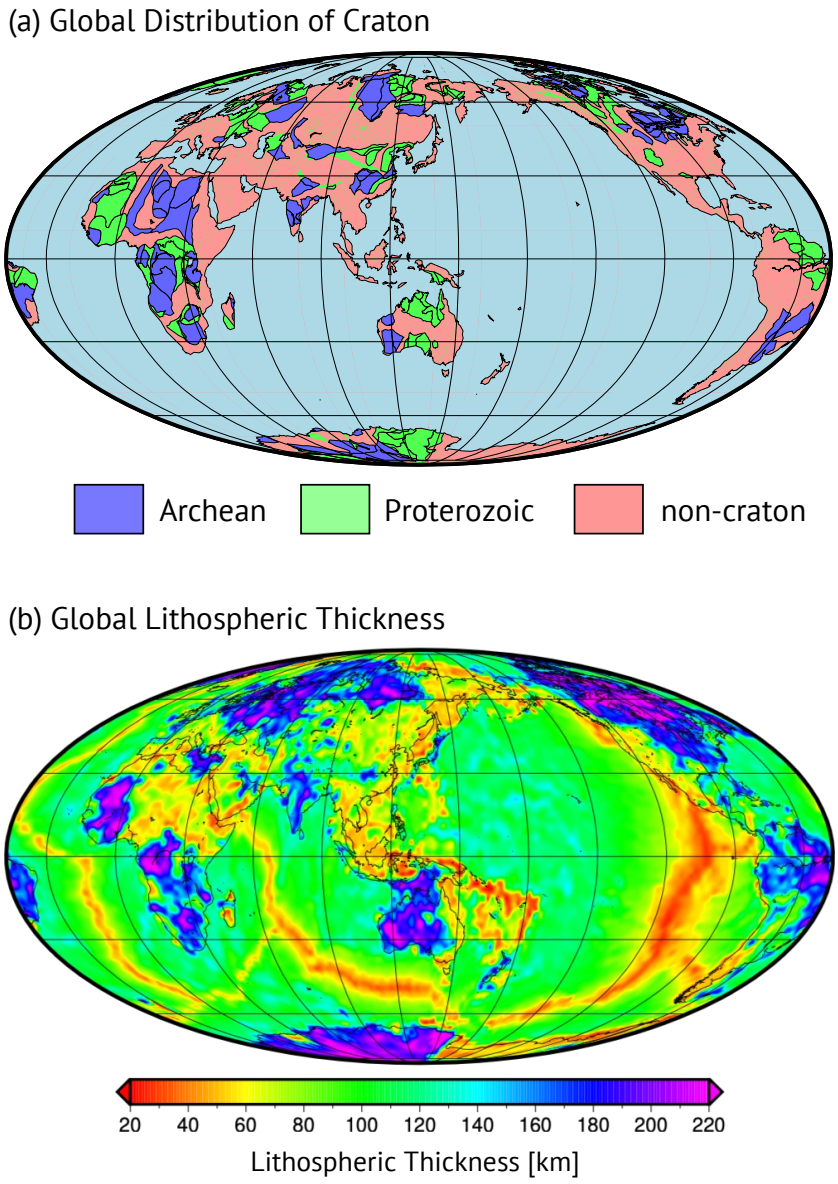

Figure 1.2: (a) Global cratonic distribution based on Hasterok et al. (2022). The blue and green shaded regions exhibit Archean and Proterozoic continental shields. The red-shaded areas indicate non-cratonic regions, such as orogenic belts and volcanic arcs. (b) A global lithospheric thickness model (Afonso et al., 2019), reconstructed using a compilation of various geophysical datasets, including gravity, geodetic, seismic, and petrological data.

1996; Yoshizawa & Kennett, 2004; Rychert & Shearer, 2009; Panning et al., 2010; Yuan et al., 2011; Yoshizawa, 2014; Isse et al., 2019; Liu et al., 2020; Pugh et al., 2021). These studies have provided significant insights, revealing a layered system within the upper mantle known as the lithosphere-asthenosphere system. The boundaries of these layers are characterized by sharp or gradual changes in elastic properties (e.g., seismic wave speeds), forming seismic discontinuities like the Lithosphere-Asthenosphere Boundary (LAB). The LAB has often been observed as a relatively sharp boundary under the oceanic lithosphere (e.g., Kawakatsu et al., 2009), while it generally becomes ambiguous and gradual under the stable continental lithosphere (e.g., Eaton et al., 2009). Beneath ancient continental regions, these discontinuities are believed to have been formed by past tectonic activity and plate evolution, serving as a *"record"* of the Earth's evolution processes.

Ancient continental cratons, such as western and central Australia, Siberia, eastern Antarctica, and northeastern North America, generally exhibit very thick lithosphere of about 200–300 km (Figure 1.2). The thickness of the cratonic lithosphere shaped in the Archean/Proterozoic eras cannot simply be explained by thermal cooling, like the typical oceanic lithosphere, and the formation process of such a thick lithosphere has been largely unknown. In contrast, a thinner lithosphere (20–100 km) has been observed in younger regions (Figure 1.2), such as continental margins and oceanic ridges, where the lithospheric layer is actively forming and evolving. In other words, the lithosphere-asthenosphere system of continental regions records the tectonic events it has experienced, telling us of its formation, growth, drift, deformation, and subsequent evolution. Investigating the seismic structures and interfaces beneath the continental region is therefore essential for understanding the Earth's tectonic history and evolution.

In this section, we summarize a key method for investigating seismic discontinuities beneath a seismic station, receiver functions, and our current knowledge of major continental seismic discontinuities, including the LAB.

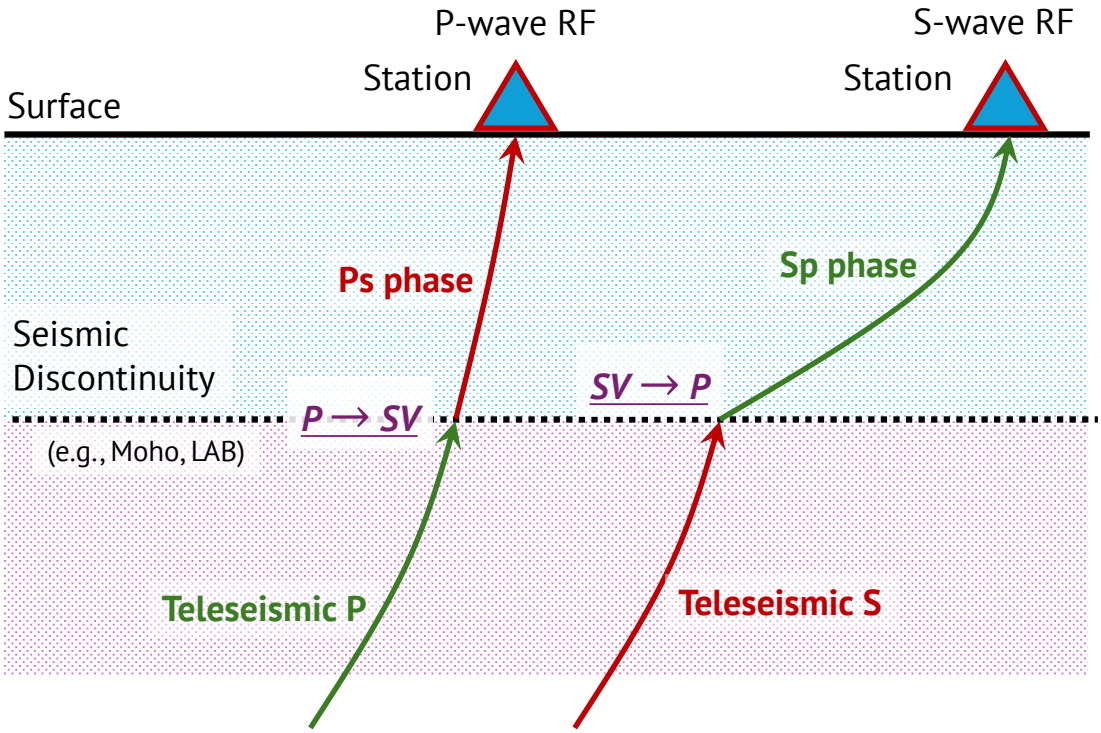

Figure 1.3: A schematic illustration of P-wave and S-wave receiver functions.

1.2.1 Detections of upper mantle discontinuities by teleseismic body waves

Seismic waves are a powerful tool for imaging the seismic structure of the Earth's upper mantle. Among them, seismic surface waves, which propagate along the Earth's surface, are characterized by their dispersive nature. The surface-wave dispersion arises from the vertical variations in seismic velocity structure (e.g., Takeuchi & Saito, 1972; Dziewonski & Hales, 1972), making surface waves particularly useful for reconstructing large-scale three-dimensional S-wave velocity models of the upper mantle (e.g., Nataf et al., 1986; Debayle et al., 2005; Yuan et al., 2011; Yoshizawa, 2014; Isse et al., 2019). However, due to their long-wavelengths, surface waves are less sensitive to sharp velocity changes across internal seismic discontinuities. This inherent limitation restricts their ability to resolve rapid structural variations.

On the contrary, seismic body waves are more sensitive to the internal structural boundaries. Teleseismic body waves, when encountering seismic interfaces, are converted into other wave types, such as, P-to-S converted waves (Ps) for incident P-wave and S-to-P converted waves (Sp) for incident S-wave, as schematically illustrated in

Figure 1.3. These converted waves are more sensitive to the sharpness of seismic velocity changes (or acoustic impedance) compared to surface waves and convey the information about seismic discontinuities.

Receiver functions (RFs), first introduced by Langston (1979), enable us to isolate converted phases from the primary incident phases. The amplitude of RFs corresponds to the direction and magnitude of seismic velocity gradients at depth. Positive peaks in RFs indicate an increase in velocity across an interface, while negative peaks indicate a decrease. For example, a converted phase at the Moho, characterized by a positive velocity jump, produces a positive amplitude in the RFs. Detailed descriptions of RFs can be found in Rondenay (2009), Kind & Yuan (2011), Kind et al. (2012) and Tarumi (2022).

RFs are sophisticated methods for imaging seismic discontinuities within the Earth (e.g., Bostock & Rondenay, 1999; Rychert & Shearer, 2009; Kind et al., 2012; Kim et al., 2021; Pugh et al., 2023) and have been applied extensively to studies of Mars (Knapmeyer-Endrun et al., 2021; Dai & Sun, 2023; Joshi et al., 2023; Shi et al., 2023). However, unlike surface waves, RFs cannot constrain absolute seismic velocities. To address this limitation, recent studies have increasingly adopted a joint approach that integrates surface wave data with teleseismic RFs to better estimate upper mantle discontinuities (e.g., Julià et al., 2000; Tkalčić et al., 2006; Bodin et al., 2012; Taira & Yoshizawa, 2020; Gama et al., 2021; Byrnes et al., 2023).

As imagined from the illustration in Figure 1.3, if a seismic discontinuity exhibits rapid lateral variations, the excitation of converted phases can strongly depend on the direction of the incoming waves. This azimuthal dependence provides valuable information on the shape and nature of seismic discontinuities. RFs have been particularly effective for imaging laterally varying seismic interfaces in subduction zones (e.g., Tonegawa et al., 2005; Gilbert et al., 2006; Shi et al., 2015; Cheng et al., 2017; Kim et al., 2021) and continental regions (e.g. Kind et al., 2012; Sippl, 2016; Kind et al., 2020). However, capturing these lateral variations often requires a dense network of seismic stations to obtain clear structural images, which is not always feasible in many continental regions.

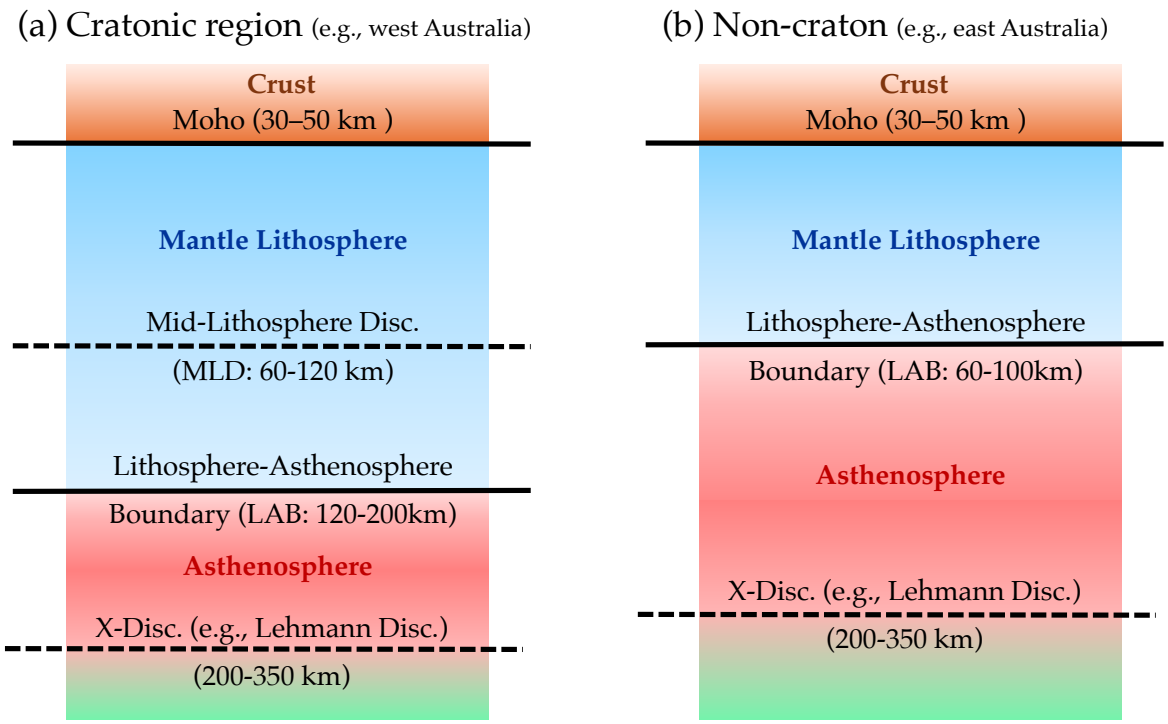

Figure 1.4: Schematic illustrations of layered upper mantle structures beneath continental regions. (a) Stable cratonic areas (e.g., central and western Australia, eastern US, etc.). (b) Recent orogenic belts (e.g., eastern Australia, western US, etc.).

1.2.2 Continental upper mantle discontinuities

The continental upper mantle comprises several layers, whose margins are characterized by elastic parameter contrast (e.g., seismic wave speeds). Figure 1.4 schematically illustrates two cases of a layered structure in the continental upper mantle, helping subsequent explanations about seismic discontinuities.

The lithosphere-asthenosphere boundary (LAB) is the most prominent discontinuity in the upper mantle, essential for understanding the interaction between the mantle lithosphere and the underlying asthenosphere. The continental lithosphere is considered as a rigid layer characterized by very high seismic velocities, while the asthenosphere is a ductile layer with lower seismic velocities, whose flow drives (or resists) plate motions (Ghosh et al., 2013). In young regions, such as the Phanerozoic orogeny (e.g., eastern Australia), the LAB exhibits a sharp negative velocity contrast at depth, which is clearly observed in RFs (e.g., Rychert & Shearer, 2009; Ford et al., 2010; Abt et al., 2010).

In contrast, the LAB beneath cratons has not been clearly resolved by either surface wave tomography or RFs (e.g., Eaton et al., 2009), due to the gradual decrease in seismic velocity from the lithosphere to the asthenosphere (e.g., Abt et al., 2010; Ford et al., 2010). This characteristic likely reflects the prolonged history of slow cooling in cratonic regions (e.g., Eaton et al., 2009; Fischer et al., 2010, 2020). A detailed topography map of the LAB is invaluable for uncovering the structure and dynamics of the upper mantle, which requires the integrated analysis of surface waves and body-wave RFs. However, the application of such comprehensive studies has been limited to the North American continent (Calò et al., 2016) and has yet to be extended to other regions.

Within the lithosphere above the LAB, additional seismic discontinuities also observed. Earlier studies have detected sharp positive velocity gradient at depths of approximately 75–120 km (e.g., Hales, 1969; Hales et al., 1980; Revenaugh & Jordan, 1991; Bodin et al., 2014; Calò et al., 2016; Chaudhury et al., 2021). More recently, S-wave RFs, which identify Sp converted phases, have revealed enigmatic seismic velocity drops within the cratonic lithosphere, referred to as the Mid-Lithospheric Discontinuity (MLD) (e.g., Sodoudi et al., 2009; Zheng & Romanowicz, 2012; Abt et al., 2010; Sodoudi et al., 2013; Wirth & Long, 2014; Krueger et al., 2021; Birkey et al., 2021). The presence of a velocity drop in the cold and stable cratonic lithosphere remains puzzling. In addition, the MLD often consists of multiple interfaces (e.g., Calò et al., 2016; Chen et al., 2018; Sun et al., 2018; Taira & Yoshizawa, 2020; Birkey et al., 2021; Liu et al., 2023).

These enigmatic MLDs likely reflect the complex evolutionary process of stable ancient cratons, which provides a key to understanding the origins of MLDs. Based on numerous earlier studies, including petrological investigations and laboratory experiments, the potential causes of MLDs have been proposed to include elastically accommodated grain-boundary sliding (e.g., Karato et al., 2015), rapid changes in Mg # (e.g., Yuan & Romanowicz, 2010; Sudholz et al., 2024), the presence of hydrous minerals (e.g., Selway et al., 2015; Fu et al., 2022), and seismic anisotropy (e.g., Selway et al., 2015; Yoshizawa & Kennett, 2015; Ford et al., 2016; Chen et al., 2021b). While these attempts for unified explanations provide general views, it is also valuable to in-

vestigate different features between cratons, as each craton reflects its unique tectonic history. Also, some fundamental questions remain unresolved, including whether the velocity change across the MLD is positive or negative and the lateral extent (or spatial distribution) of MLDs within the lithosphere.

In addition to the MLDs, other interfaces have been identified beneath the LAB in the deeper upper mantle at depths of around 200–350 km. One of the first reports of such a feature was by Inge Lehmann, who predicted a positive velocity contrast beneath the continental region at approximately 220 km depth (Lehmann, 1961). This feature was subsequently incorporated into the global 1-D reference Earth model, PREM (Dziewonski & Anderson, 1981). Since then, many studies have identified deeper positive seismic interfaces using various teleseismic body wave phases, such as Ps-converted phases and PP and SS precursors. These interfaces have been observed globally at depths around 150 km, 220 km, 260 km, and 300 km (Hales et al., 1980; Revenaugh & Jordan, 1991; Shearer, 1993; Deuss & Woodhouse, 2002; Schmerr & Garnero, 2006; Rychert et al., 2014; Pugh et al., 2021; Hua et al., 2023). However, significant uncertainties on these potential discontinuities remain regarding the spatial distribution, the number of discontinuities, and their elastic properties (velocity/impedance contrast and anisotropy).

These enigmatic interfaces below the LAB, referred to as X-Discontinuities (X-Ds), provide clues for understanding past tectonic history (e.g., Williams & Revenaugh, 2005; Srinu et al., 2021), present-day dynamics including upwelling material (e.g., Rein et al., 2020), and the layering system within the asthenosphere (Hua et al., 2023). The origins of X-Ds at depths of 200–350 km have been linked to mineral phase transitions, such as those of pyroxene or coesite (Akaogi et al., 1995; Williams & Revenaugh, 2005; Rein et al., 2020; Srinu et al., 2021; Pugh et al., 2021). These transitions may reflect present and past mantle dynamics. Among these, the X-Ds at around 220 km, often called the Lehmann discontinuity (e.g., Revenaugh & Jordan, 1991; Deuss & Woodhouse, 2004), has been attributed to a transition in the dominant mineral creep mechanism from dislocation to diffusion creep, as proposed by Karato (1992). This transition may mark the base of the anisotropic layer beneath the LAB, providing evidence of the lower boundary of the asthenosphere (Gaherty & Jordan, 1995; Calò

et al., 2016; Taira & Yoshizawa, 2020).

Mapping the detailed spatial distributions and elastic properties of these upper mantle discontinuities is crucial for advancing our understanding of Earth's dynamics. In particular, the investigations of the lithosphere-asthenosphere system beneath the continental regions, which serve as a rich archive of tectonic history, provide invaluable insights into past and present dynamic processes in the mantle.

1.3 Source imaging using teleseismic body waves

Investigating seismic sources is another important field in seismology. For several decades, many researchers have made significant efforts to image seismic source processes using teleseismic waveforms through various approaches (e.g., Bouchon, 1976; Kikuchi & Kanamori, 1982, 1991; Ishii et al., 2005; Yagi et al., 2012; Okuwaki et al., 2023).

One of the most effective techniques for resolving seismic source processes is waveform inversion (Hartzell & Heaton, 1983; Kikuchi & Kanamori, 1991; Yoshimoto & Yamanaka, 2014; Shi et al., 2018; Jia et al., 2022; Okuwaki et al., 2023). This method allows for reconstructing rupture history on fault surfaces with high resolution. Moreover, waveform inversion can integrate multiple datasets, including geodetic data, tsunami waveforms, and near-field strong motion data, enhancing the accuracy of estimated slip distributions (e.g., Yagi, 2004; Hartzell et al., 2013; Kobayashi et al., 2017; Metz et al., 2022; Ma et al., 2024). Despite its robustness, such waveform inversions have some difficulties in practical applications.

The first challenge is the requirement for a predefined fault plane model at seismic sources, whose errors in modeling may have a critical impact on the inversion results. To overcome this issue in fault modeling, Shimizu et al. (2019) and Yamashita et al. (2022) developed a sophisticated inversion method, the potency density tensor inversion, which simultaneously estimates fault geometry and slip history assuming only a model fault plane. However, it is still challenging to apply such advanced inversion methods to more complex cases involving multiple events, such as the 2021 South Sandwich Island Mw 8.2 Earthquake (Metz et al., 2022; Jia et al., 2022).

Another issue in source inversions is the limited frequency range that can be ana-

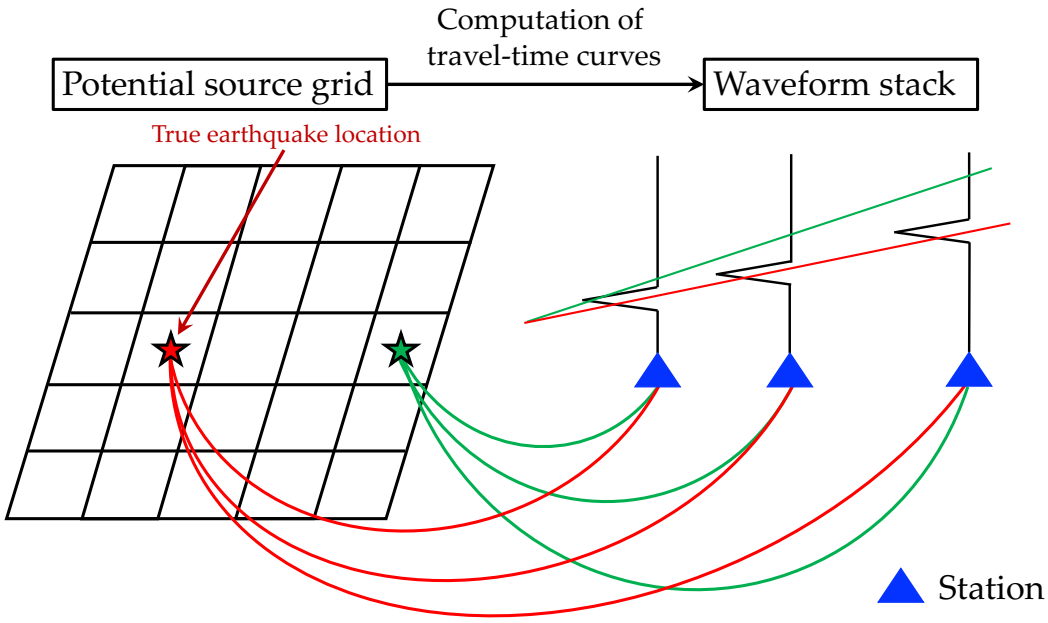

Figure 1.5: Schematic illustration of back-projection analysis.

lyzed; for example, high-frequency seismic signals (>1–2 Hz) are often excluded due to the high computation costs in computing Green's function and uncertainties caused by insufficient modeling of fine-scale seismic structures. However, high-frequency seismic waves radiated from the source play an important role in understanding the complexities of seismic source processes, including abrupt changes in slip and/or rupture velocities on the fault surface (e.g., Bernard & Madariaga, 1984; Spudich & Frazer, 1984; Beresnev, 2017), and the roughness of fault ruptures, such as the fault barriers and branching (e.g., Adda-Bedia & Madariaga, 2008; Uchide et al., 2013; Bruhat et al., 2016; Okuwaki & Yagi, 2017). Imaging the spatiotemporal distributions of high-frequency radiation sources is, therefore, essential for uncovering the complex seismic source processes.

Another highly effective approach for imaging seismic source processes is back-projection (BP) analysis (Ishii et al., 2005, 2007), which resolves some of the limitations in waveform inversions. The BP analysis time-reverses seismic signals back to their source region, identifying where seismic energy is radiated (Figure 1.5). This method does not require prior assumptions about the fault plane or impose restrictions on the frequency range, as it only involves computing travel times from potential source

locations to receivers and stacking seismic records.

Originally developed to estimate the rupture process of the 2004 Sumatra-Andaman earthquake using teleseismic P-waves recorded by the Hi-net array in Japan (Ishii et al., 2005, 2007), the BP method has since become a widely used method for investigating seismic radiation processes (e.g., Walker et al., 2005; Xu et al., 2009; Ishii, 2011; Palo et al., 2014; Kehoe et al., 2019; Shi & Wei, 2020; Kiser et al., 2021). In addition to teleseismic P-waves, the method has been extended to other seismic phases, including near-filed body waves and Rayleigh waves (e.g., Honda & Aoi, 2009; Roten et al., 2012; Honda et al., 2013; Oshima & Takenaka, 2020), and other teleseismic phases such as PP and PKP (e.g., Koper et al., 2012).

Although the theoretical foundations of the BP analysis remain a topic of debate (Fukahata et al., 2014; Okuwaki et al., 2018; Li et al., 2022), its widespread application has provided valuable insights into complex seismic radiation processes, including complex fault geometry (e.g., Uchide et al., 2013; Okuwaki & Yagi, 2017; Tan et al., 2019; Mai et al., 2023), deep-focus earthquakes not associated with fault slip (e.g., Ye et al., 2013, 2016; Kehoe et al., 2019; Kiser et al., 2021), abrupt changes in rupture or slip velocity (Okuwaki et al., 2014; Mai et al., 2023; Xu et al., 2024; Ma et al., 2024), and frequency-dependent radiation processes in subduction zone (e.g., Ishii, 2011; Koper et al., 2012; Wang & Mori, 2011; Yagi et al., 2012; Yin & Yao, 2016).

The frequency-dependent seismic radiation process is an essential aspect of understanding the multi-scale rupture dynamics of seismic sources. Low-frequency signals are particularly useful for imaging the macroscopic rupture process, as they are sensitive to regions of large slip. High-frequency seismic energy radiation, on the one hand, provides valuable insights into the complexities of the seismic source process (e.g., Okuwaki et al., 2018), such as abrupt changes in slip and/or rupture velocity on the fault surface (e.g., Bernard & Madariaga, 1984; Spudich & Frazer, 1984; Beresnev, 2017), the fault roughness features like barriers and branching (e.g., Adda-Bedia & Madariaga, 2008; Uchide et al., 2013; Bruhat et al., 2016; Okuwaki & Yagi, 2017).

In addition to analyzing fault rupture processes, the BP method has been used to detect aftershocks that are often obscured by overlapping seismic signals from large earthquakes and background noises (e.g., Kiser & Ishii, 2013a). Furthermore, by ap-

plying BP to anomalous events that intermittently generate seismic waves, it is possible to track the sequence of seismic energy excitation, offering new opportunities to study unusual seismic phenomena.

1.4 Outlines of this thesis

This thesis comprises two main parts, focusing on (I) seismic structural studies and (II) wave source studies, using teleseismic body waves:

- **Part I. Structural studies:** Spatial mapping of upper mantle discontinuities under the Australian continent using P-wave RFs and surface waves.
- **Part II. Source studies:** Applications of the back-projection method to a massive explosive eruption and an earthquake with a complex fault network.

Figure 1.6 summarizes the research contents and flow of this thesis.

In Part I, we propose a new strategy for mapping upper mantle discontinuities beneath continental regions by combining P-wave receiver functions (P-RFs) and surface wave analyses. This approach is applied to the Australian continent, which is a tectonically significant region characterized by the fast drifting speed and its composition encompassing both Precambrian cratonic areas and the younger eastern orogenic zone. The availability of many permanent and temporary stations with extensive seismicity surrounding the continent makes Australia an ideal target for our comprehensive study.

In Chapter 2, we first construct a station orientation catalog of horizontal sensors at all broadband seismic stations in Australia, which will be utilized in the subsequent chapters. Misalignment of horizontal sensors from the true geographic north and east directions may significantly affect waveform analyses. To prevent this issue, we measure the misorientation from the north using a large number of arrival-angle data of teleseismic P-waves and create a comprehensive catalog. This catalog is then utilized to improve the accuracy of teleseismic waveform analyses.

In Chapters 3 and 4, we use the refined teleseismic P-wave database, corrected for the sensor orientation, to investigate upper mantle discontinuities beneath Australia. Chapter 3 proposes our new approach to exploiting P-RFs to investigate continental upper mantle discontinuities. The azimuthal dependence of P-RFs, arising from the

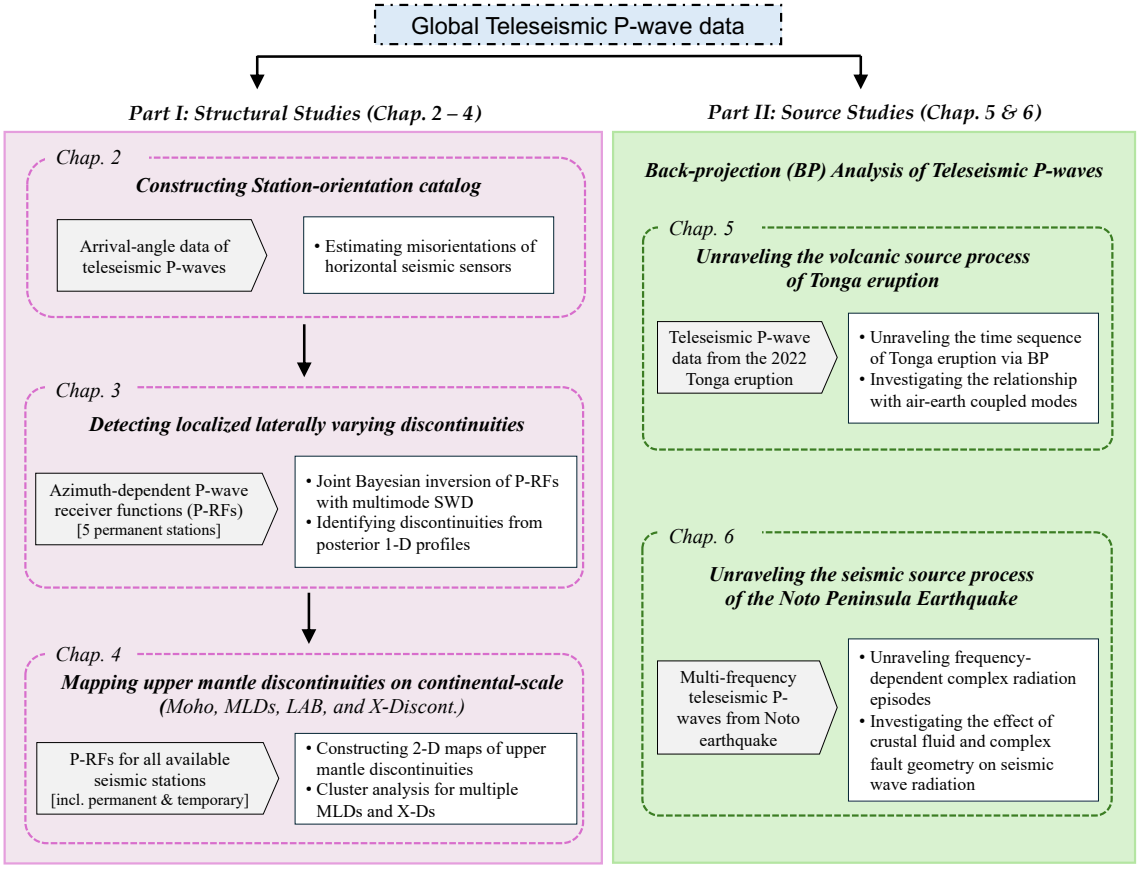

Figure 1.6: Contents and flow of this thesis. The left magenta area corresponds to Part I (Chapters 2–4), focusing on seismic structure studies, and the right green area represents Part II (Chapters 5 and 6), which explores source studies.

lateral variations of seismic structures near the station (as expected from the illustration in Figure 1.3), is useful for detecting rapid lateral variations of discontinuities beneath the station. We incorporate this concept into a joint inversion method that integrates azimuth-dependent P-RFs and multimode surface wave data, and apply it to five long-running permanent stations in Australia.

In Chapter 4, we expand this analysis to map the spatial distributions of upper mantle discontinuities across the Australian continent using the joint approach with P-RFs and surface wave data. This chapter provides new seismological insights into the spatial distribution and elastic properties of Australian MLDs and X-Ds, shedding light on the ancient and present-day tectonics that have shaped the current Australian continent.

In Part II, we present two new applications of back-projection (BP) analysis to estimate seismic wave sources. In Chapter 5, we apply BP to a non-earthquake event – the catastrophic eruption of the Hunga Tonga-Hunga Ha'apai volcano in 2022. This chapter explores the temporal evolution of the eruption sequence, which was so massive that the volcanic plume obscured satellite imagery and other observational data (NASA, 2022).

In Chapter 6, we introduce a new approach to effectively enhance target seismic signals during the stacking process in the BP analysis. This method is applied to multi-frequency teleseismic P-waves from the 2024 Mw 7.5 Noto Peninsula Earthquake, which was recorded as two distinctive events by the Japan Meteorological Agency. We investigate the remarkable frequency-dependent radiation process and discuss its relationship with the complex source environment, including intricate fault geometries and the presence of fluids in the source region.

Finally, Chapter 7 concludes this thesis, summarizing the key findings and proposing further directions for advancing the study of teleseismic body waves.

Part I

Seismic Structural Studies

Chapter 2

Station-orientation catalog for Australian broadband seismic stations

2.1 Introduction

A large number of broadband seismic stations deployed permanently or temporarily in the Australian continent have provided key information on seismic wave propagation (e.g., Kennett & Furumura, 2008), seismic sources (e.g., Hejrani & Tkalčić, 2020), and seismic structure (e.g., Kennett et al., 2013; Yoshizawa, 2014; Birkey & Ford, 2023; Eakin et al., 2023) in and around Australia. As an initial step for the three-component seismic waveform analysis, we generally rotate two horizontal components (e.g., NS / EW) to radial and transverse directions, supposing that the horizontal sensors are oriented in the north and east (or in reported) directions. However, as several earlier studies suggested, there is a possibility of nontrivial misorientation of horizontal components at some stations (e.g., Laske, 1995; Yoshizawa et al., 1999; Schulte-Pelkum et al., 2001). Also, temporal changes in the amplitude gain of seismometers may occur at some permanent stations over a long observation period (Ekström et al., 2006). Such errors or uncertainties in the reported catalog values, particularly the ambiguities in the horizontal-component orientation, would prevent us from performing precise waveform analyses that depend on the horizontal directions, such as shear-wave splitting measurements, Love-wave dispersion analysis, and the azimuthal dependency of receiver functions.

The horizontal orientation of seismic stations can be estimated by measuring the arrival angles of teleseismic P or Rayleigh waves at longer periods for a large number of seismic events (e.g., Laske & Masters, 1996; Yoshizawa et al., 1999; Schulte-Pelkum

et al., 2001; Larson & Ekström, 2002; Ekström & Busby, 2008). Rayleigh waves generally oscillate elliptically in the radial-vertical plane, but their particle motions become more complicated in heterogeneous and anisotropic media (Crampin, 1975). Moreover, due to the dispersive nature of surface waves, the arrival-angle anomalies (or deviations from the great-circle path) depend significantly on the frequency (Laske, 1995; Yoshizawa et al., 1999), which may increase uncertainties in the estimated station orientation. Furthermore, the overlaps by preceding Love waves in the transverse component make it difficult to perform arrival-angle analysis of Rayleigh waves at relatively shorter epicentral distances of less than 50° (Yoshizawa et al., 1999). On the contrary, the onset of teleseismic P-waves exhibits a relatively simple linear motion in the radial-vertical plane without frequency dependence. Teleseismic P-waves with the near-vertical incidence to the station mainly sample the lower mantle where lateral heterogeneities are weak. Thus, the ray-bending effects on P-waves due to strong lateral heterogeneity in the upper mantle can be milder than that on surface waves (Yoshizawa et al., 1999), in addition to the relatively smaller influence from anisotropy on P-waves compared to surface waves (Crampin et al., 1982).

Recently, major seismological data centers, such as IRIS (Incorporated Research Institutions for Seismology), have provided us with more precise information on the station orientation for their affiliated stations worldwide, including Australian stations. Given proper information from careful calibrations, many of the broadband horizontal channels in major stations in global networks (such as the Global Seismograph Network) have been named BH1 and BH2 (for the first and second components) rather than conventional BHN and BHE (North and East), when the true horizontal directions deviate from the geographic north and east (Ekström & Busby, 2008). Ekström (2008) has also provided practically useful tables on the station orientation for GSN stations until 2015. However, a number of seismic stations from local data providers and temporary seismic networks, including transportable seismic arrays (e.g., SKIPPY in Australia; van der Hilst et al., 1994), still lack precise information on horizontal orientations, which is crucial for researchers wishing to utilize these valuable waveform data sets.

In this chapter, we collect a large number of P-wave arrival angle data to estimate

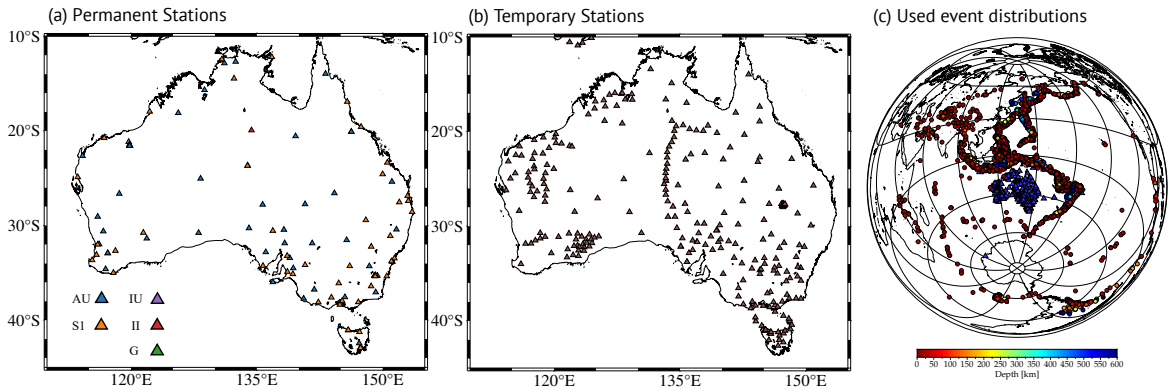

Figure 2.1: Broadband seismic stations and seismic events used in this study. (a) Permanent stations, with colors indicating different networks (AU, S1, IU, II, and G). (b) Temporary stations. (c) Seismic events used in this study, with colors representing source depths. Blue triangles are employed stations in (a) and (b).

the horizontal orientation of many broadband seismic stations in Australia, modeled on the method of polarization analysis by Vidale (1986) utilized in earlier study by Yoshizawa et al. (1999). Through the polarization analysis of teleseismic P-wave particle motions, we construct a complete catalog of the horizontal orientation of currently available broadband stations in Australia, which can be used for a variety of future applications of seismic data analyses with horizontal components.

2.2 Data and Method

We used the three-component teleseismic P-wave data downloaded from the IRIS Data Management Center (IRIS DMC) and Australian Passive Seismic Server (AusPass) for 4004 seismic events with moment magnitude Mw $\geq$ 5.5 from 1987 to 2019. Our dataset includes both permanent and temporary broadband stations shown in Figures 2.1 (a, b). Permanent seismic networks include IRIS/IDA (red triangles in Figure 2.1 (a); Network II), IRIS/USGS (purple triangles in Figure 2.1 (a); Network IU), GEOSCOPE (green triangles in Figure 2.1 (a); Network G), GeoScience Australia (blue triangles in Figure 2.1 (a); Network AU), and Australian Seismometers in Schools program (orange triangles in Figure 2.1 (a); Network S1). Temporary stations shown in Figure 2.1 (b) involve many temporary seismic arrays, SKIPPY (van der Hilst & Kennett, 1993), KIMBA (Kennett, 1997, 1998), QUOLL (Kennett et al., 1999), West Australia Cratons (Kennet, 2000), TRIGGER BB (Rawlinson & Kennett, 2001), TAS-

MAL (Kennett, 2003), CARPA - Linkage (Reading & Kennett, 2005), SOC - Southern Craton (Fontaine & Kennet, 2007), BILBY (Rawlinson & Kennet, 2008), Bass Strait (Reading & Rawlinson, 2011), Australia (Tkalčić et al., 2013b), Albany-Fraser Experiment (Tkalčić et al., 2013a), and Transitions in the Banda Arc-Australia continental collision (Miller, 2014).

We selected seismic events with Mw $\geq$ 5.5, distance ranges between 30 and 90 degrees, and normalized amplitude of P-wave radiation $>$ |0.3| estimated from the Global CMT catalog (Dziewonski et al., 1981; Ekström et al., 2012). We first corrected the instrument response, converted the waveform data into the displacement, and applied a bandpass filter between 0.03 and 0.1 Hz. Second, we rotated the two horizontal waveforms into the radial and transverse components based on the station catalog information of horizontal orientation provided by IRIS DMC and AusPass. To discard the low-quality data, we calculated signal-to-noise ratios (SNR) in the vertical and radial components and removed data with vertical SNR $<$ 5.0 or radial SNR $<$ 3.0. Then, for each seismic event and station, we performed a time-domain complex polarization analysis of Vidale (1986) to measure the horizontal arrival angles Θ of direct P-waves in a similar way to Yoshizawa et al. (1999), which is summarized in Figure 2.2. Since teleseismic P-wave is likely to linearly oscillate in the radial-vertical plane, we imposed the data selection criteria on the ellipticity parameter P_E smaller than 0.175. Third, we calculated the median of the time-dependent arrival angles for each event (an orange line in the third panel in Figure 2.2 (a)) in a selected time window. In this study, we set the time window as 7.5 s before and after the main P-wave pulse (Figure 2.2 (a)). Consequently, in the final step, we compiled a large number of arrival angle data from many seismic events to evaluate the misorientation of horizontal sensors. In this study, to reduce the influence of biased event distributions, we mainly adopted the median as a representative measure for arrival-angle anomalies (i.e., deviations from the great-circle direction) over the selected observation period (Figure 2.2 (b)), though we also reported the mean values in our full catalog (Tarumi & Yoshizawa, 2024). We conducted this final step for stations with more than 5 arrival-angle measurements, and discarded several stations with large uncertainties in the time-dependent polarization data via visual inspections. The resultant distribution of all employed events used in

this study is shown in Figure 2.1 (c).

Station metadata (or reported catalog information of horizontal orientation) for permanent stations is subject to change from time to time, reflecting irregular maintenance, calibrations, and replacement of instruments. For the permanent stations with a long observation period, we visually inspected the timing of sudden changes in the trend of estimated horizontal misorientation, allowing us to detect some temporal changes at unreported timings (e.g., AU.COEN in Figure 2.3 (f)). For the estimation of horizontal misorientation, we divide the period windows in which the median of measured arrival angles is computed, depending on each station, as shown in Figures 2.2 (b) and 2.3.

2.3 Results

Our arrival-angle measurements enabled us to detect probable misorientations from the geographic north for permanent and temporary stations (Figures 2.2, 2.3, 2.4, 2.5, and A.7). All results are summarized in Tables A.1, A.2 and A.3 in Appendix A. In this section, we explain our results on the permanent and temporary stations separately.

2.3.1 Permanent Stations

Figure 2.2 shows the summary of P-wave polarization measurements for IU.NWAO which has been a long-running station located in southeast Australia since 1992. According to the IRIS metadata catalog, the channel name of the horizontal components was changed from BHN/BHE to BH1/BH2 in September 2001. Our measured P-wave arrival angles show apparent temporal changes in the polarization trend at this time. The misorientation angle of horizontal sensors was estimated to be about 5.8° before September 2001, and it has decreased to 0.6° since then (by 2019, at least), indicating the improvement in the catalog information of this station.

Note that, for this station, Laske & Masters (1996), Yoshizawa et al. (1999), and Schulte-Pelkum et al. (2001), who employed the particle motion of either Rayleigh wave or teleseismic P-wave before 2000, have already reported the misalignment from the north by around 5°. In particular, our estimated misorientation angle (5.8°) before September 2001 in Figure 2.2 (b) is very close to the estimated value by Schulte-

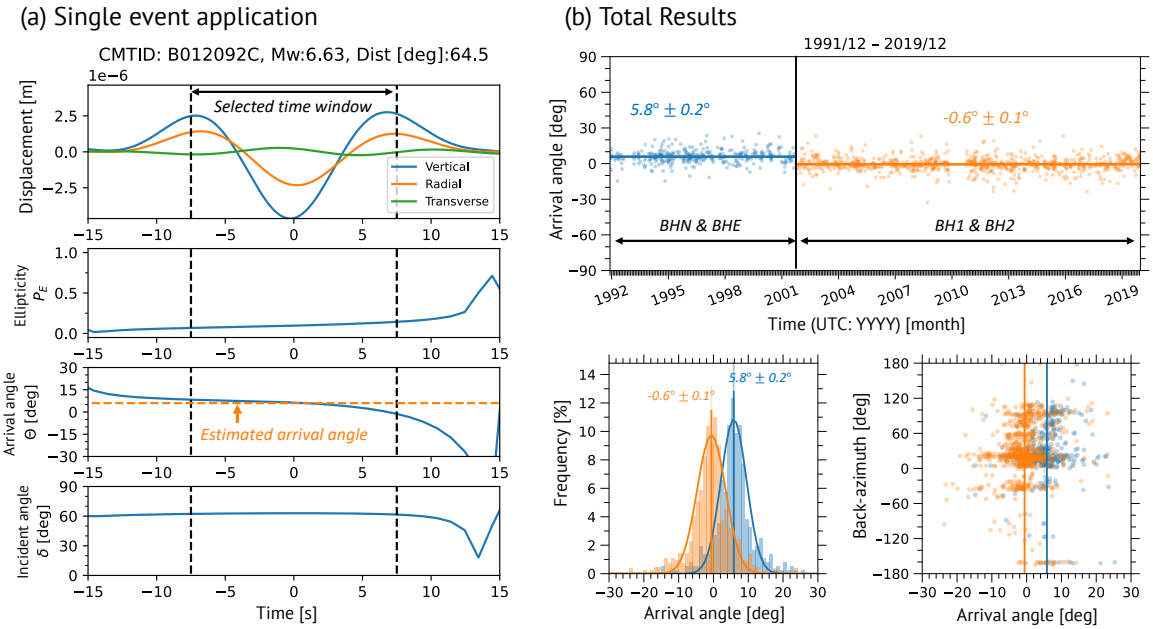

Figure 2.2: A visual summary of P-wave polarization analysis for IU.NWAO. (a) An example of teleseismic P-wave for an event at the epicentral distance of 64.5 degrees and the estimated polarization parameters. From top to bottom: three-component displacement waveforms rotated to the catalog values of IRIS metadata (blue: vertical; orange: radial; green: transverse), ellipticity P_E, arrival angle Θ on a horizontal plane, and incident angle δ for the P-wave particle motion. The arrival angle is measured clockwise from the radial (great-circle) direction so that a positive deviation indicates the arrival-angle anomaly to the east. In the third panel, a dashed orange line exhibits a median value in the selected time window encompassed by vertical dashed lines. (b) Compiled P-wave polarization data for all events used for the NWAO station. The top panel represents the time series of P-wave arrival angles. The colors for dots and lines represent the distinct period characterized by different trends of arrival angles. The timing of the arrival-angle trend change in September 2001 (indicated by a solid vertical line) matched well with the reported correction of horizontal components by IRIS. The bottom-left panel shows histograms and fitted Gaussian function for each period, and the bottom-right one indicates the back-azimuth dependence of the measured arrival angles for all employed events. In the top and bottom-left panels, the estimated station orientations and standard errors are labeled. The colors of the characters correspond to each distinct time period.

Pelkum et al. (2001), who employed the P wave data in the same period. Fontaine et al. (2009) also used similar P-wave datasets and identified a misalignment of 5°, which is consistent with our results. For the other GSN stations used in this study, our estimated orientations are generally in agreement with the previously published catalog (Ekström, 2008).

In addition to temporal changes, we can also see a back-azimuthal dependence in the arrival-angle data (Figure 2.2 (b, bottom-right panel)). Such azimuthal variations of arrival angles can also be observed at other stations, which may be worth further investigation in the future since they may reflect the lateral variations of heterogeneity and azimuthal anisotropy, including dipping interfaces, in the upper mantle beneath the seismic station (Schulte-Pelkum et al., 2001; Fontaine et al., 2009).

Figure 2.3 shows the summary of P-wave polarization data (arrival-angle anomalies from the great circle for each path) for six permanent and two temporary stations during their operation period until 2019. The horizontal-component channels of these stations have been reported as BHN/BHE since their installation. At G.CAN (Canberra by GEOSCOPE; Figure 2.3 (a)), the station orientation estimated in this study is nearly 0° (Table A.1 and Figure A.1), suggesting that this seismometer has been accurately oriented to the geographic north and east. AU.TOO (Figure 2.3 (b)) also shows no significant temporal changes, though our measurements suggest a slight misalignment (about -1.2°) from the north which can be almost negligible. At AU.BBOO and AU.KMBL stations (Figure 2.3 (c, d)), we can see clear temporal changes in the trends of polarization angles, which coincide well with the timing of reported maintenance and/or instrument replacement. On the other hand, at AU.STKA and AU.COEN (Figure 2.3 (e, f)), unknown temporal changes in polarization angles are detected at unreported timings. In particular, STKA exhibits a very large misalignment from the north by 30° since the early stage of its operation.

Compiled maps of the estimated horizontal misorientations for permanent stations are displayed in Figure 2.4, in which we show the misorientations in each period in Figures 2.4 (a-e), and those compiled for the entire period of our analysis in Figure 2.4 (f). For permanent stations including those in the S1 network, the station misorientations and their standard errors are summarized in time-dependent horizontal bar

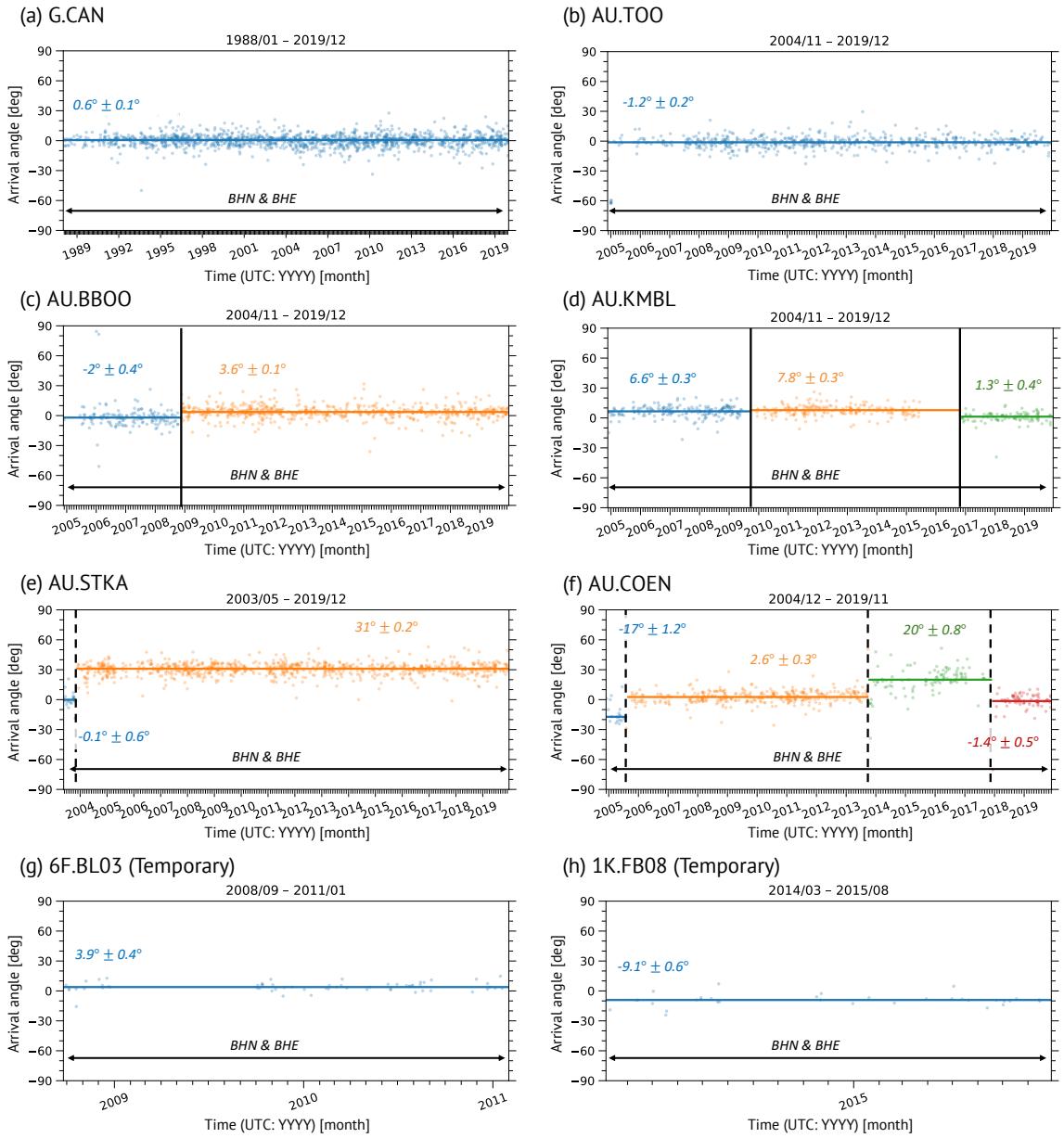

Figure 2.3: Time-dependent P-wave polarization data (arrival-angle deviation from the great circle) for selected stations, (a-f) permanent stations installed and maintained by GEOSCOPE (G) and Geoscience Australia (AU), and (g, h) temporary stations. Notations in these figures are the same as 2.2 (b, top panel). The vertical black lines represent the timing of significant trend changes in P-wave arrival angles. Solid vertical lines indicate the timing of the reported maintenance and/or replacement of instruments, and dashed vertical lines represent unknown temporal changes at unreported timings. As described in the main text, we did not identify temporal change for temporary stations.

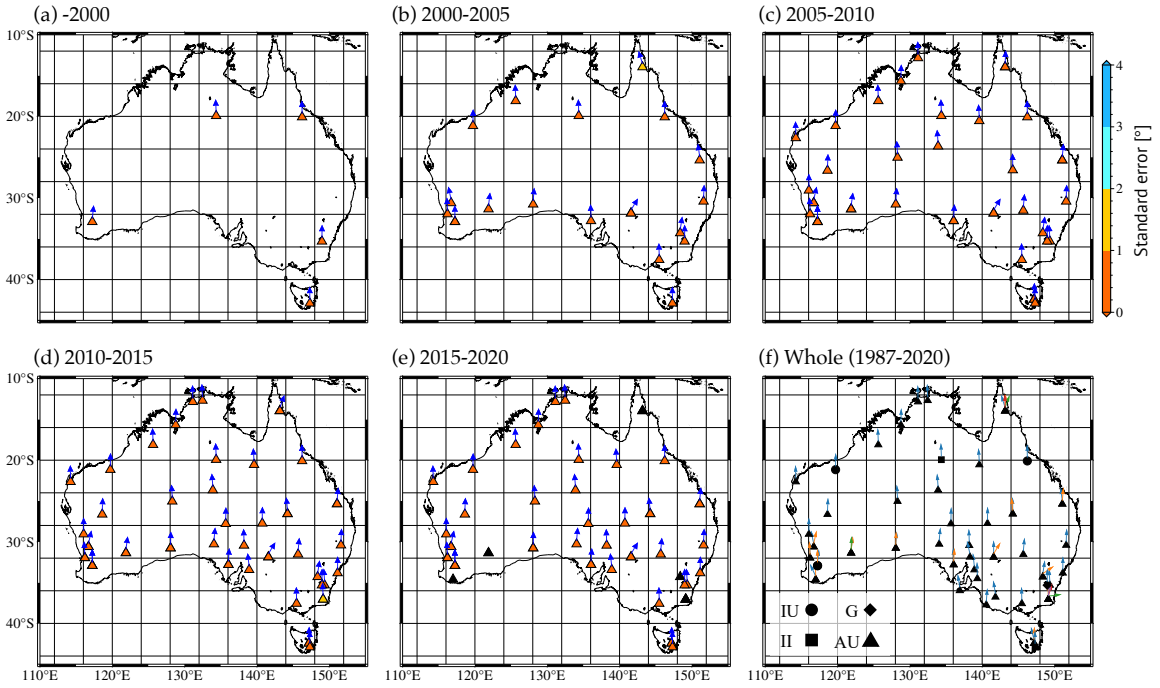

Figure 2.4: Map projections of horizontal misorientations from the geographic north for permanent seismic stations (II, IU, G, and AU) in Australia. (a-e) Arrows indicate the median directions of horizontal sensors over the designated period. Colors in the triangles indicate the estimated standard errors shown in the color bar on the right. Black triangles without arrows indicate stations with varying misorientations during the period. (f) A compiled map of estimated misorientations for the whole period of analysis. The colors of arrows indicate the horizontal sensor orientations in different periods. Black symbols indicate stations of different seismic networks.

graphs in Figures A.1, A.2, and A.5 and are separately tabulated in Tables A.1 and A.2 in Appendix A. In particular, we can identify significant time-dependent variations of misorientations for AU stations. These temporal changes mostly coincide with the reported timing of maintenance and/or replacement by the IRIS and AusPass. However, such temporal changes at several stations (e.g., AU.COEN) are found at unreported timings. The misorientation of some permanent stations from the geographic north is more than 10°, which may affect seismic waveform analysis, especially when using the horizontal components. Figure A.6 demonstrates the three-component seismograms observed at STKA to compare waveforms before and after correcting the station misorientations. In Figure A.6 (a), we can see the apparent energy leakage of the P-wave from the radial to transverse component. In Section 2.4, we will discuss the effects of the station correction on azimuth-dependent receiver function analyses.

Table 2.1: Comparison of recent misalignment measurements at AU stations by Eakin et al. (2023) and this study. Eakin et al. (2023) estimated these using PKS and/or SKS phases, as indicated. In the third column showing our results, the data period and the number of seismic events used are shown (e.g., 2011–2019; 100).

Station	Eakin et al. (2023) (PKS and/or SKS)	This study (Teleseismic P-wave)
AU.ARPS	-6° (SKS)	-9.4°±4.4° (2019; 6)
AU.FORT	0° (PKS), 3.5° (SKS)	4.4°±0.4° (2003–2011; 69) 1.4°±0.2° (2011–2019; 404)
AU.HTT	-4° (PKS), -3° (SKS)	-6.3°±0.2° (2010-2019; 399)
AU.KELC	-6° (SKS)	-9°±1.3° (2019; 19)
AU.MGBR	-10° (SKS)	4.4°±1.8° (2019; 30)
AU.MILA	6° (SKS)	1.7°±0.6° (2011–2014; 44) -2.5°±1.6° (2014–2016; 22) 83°±0.9° (2016–2018; 18) 17°±1.1° (2018–2019; 17) 6.5°±1.0° (2019; 12)
AU.MULG	6.6° (PKS & SKS)	5.0°±0.4° (2013–2019; 219)
AU.SDAN	2.5° (SKS)	-1.5°±0.7° (2018–2019; 48)
AU.STKA	31° (PKS & SKS)	-0.1°±0.6° (2003; 23) 31.0°±0.2° (2003–2019; 899)
AU.YAPP	-13.4° (PKS & SKS)	-13°±0.5° (2018–2019; 55)
AU.YNG	5° (PKS), 10° (SKS)	8.7°±0.3° (2004–2017; 429) 56°±1.2° (2017–2019; 42)

For AU stations, we compare our measurements with those from a recent study in Table 2.1; we present our estimated misalignments for selected AU stations, along with XKS-based measurements from Eakin et al. (2023). We focused on stations where Eakin et al. (2023) reported non-zero misalignments and extracted the most recent misorientation data from our catalog between 1987 and 2019 for comparison. Our measurements are generally in good agreement with those of Eakin et al. (2023). Note that large misalignments at AU.STKA are identical between both studies.

Figure A.7 shows the map of station orientations for the S1 network (broadband seismometers in schools; Balfour et al., 2014), which has been installed since 2011 (Salmon et al., 2011). Table A.2 lists the estimated station orientations and their standard errors. Note that the lower corner-frequency of seismometers (Güralp CMG-6TD) used for the S1 network (Balfour et al., 2014) is relatively high (0.03Hz) compared to other permanent networks. Although we could obtain many high-quality arrival-angle data when analyzing waveforms in the higher-frequency range (e.g., 0.1–1.0 Hz), we could not gather sufficient arrival-angle measurements to evaluate the station orientation for half of the S1 network since our current analysis focuses on longer-period datasets (0.03–0.1 Hz). As a result, our S1 network catalog (Table A.2) includes only 13 stations (Figures A.5 and A.7).

2.3.2 Temporary Stations

The seismic records of temporary stations are generally less than two years long, and we could not find any significant temporal changes in the horizontal orientation. Figures 2.3 (g) and (h) show examples of a time-dependent polarization measurement for selected temporary stations. As expected from the limited data acquisition period, we could not observe any significant temporal changes in the time-series data of these stations. In Figure 2.5, we compiled the station orientation for all temporary stations that met the criteria described in Section 2.2. Also, we summarized the station orientations and their standard errors in Figures A.3 and A.4 and Table A.3. While some stations exhibit relatively large misalignments, the horizontal sensors at almost all temporary stations generally align with the geographic north and east directions (Figures 2.5 and A.3), suggesting proper installation. We also compare XKS-based measurements from

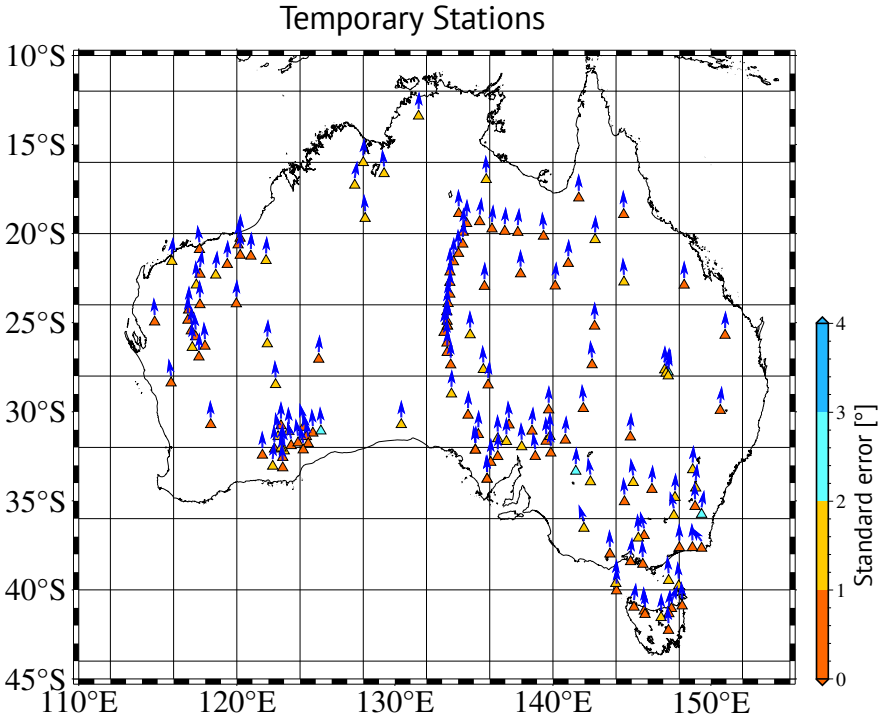

Figure 2.5: Station misorientations from the geographic north in a horizontal sensor for temporary seismic stations.

Eakin et al. (2023) and teleseismic P-wave measurements from this study in Table 2.2, similar to the previous subsection. Overall, for most temporary stations, our results are generally consistent with those of Eakin et al. (2023). The discrepancies at some stations may be attributed to the utilized recording periods, the measurement quality for different seismic phases, and the number of employed events.

2.4 Discussion and Conclusions

In this section, we briefly examine the effect of the station correction on P-wave receiver function (P-RF) analysis. We computed the P-RFs at AU.STKA, where a large misorientation of over 30° was observed, and analyzed the differences between uncorrected and corrected P-RF data for both radial and transverse components. In these calculations, we considered the azimuthal dependence of P-RFs, which arises from the varying incoming directions (or back-azimuths) of teleseismic P-wave. The azimuth-dependent radial P-RFs reflect lateral variations in seismic discontinuities around the station (e.g., Tonegawa et al., 2005; Kawakatsu et al., 2009; Kumar & Kawakatsu, 2011). In addition,

Table 2.2: Same as Table 2.1, but for selected temporary stations.

Station	Eakin et al. (2023) (PKS and/or SKS)	This study (Teleseismic P-wave)
1E.SQA01	5° (SKS)	3.0°±2.4° (2013–2014; 7)
1E.SQA09	10° (SKS)	16.0°±1.4° (2013–2014; 7)
1E.SQA11	10° (SKS)	9.2°±1.3° (2013–2014; 7)
1P.BA12	-25° (SKS)	-36.0°±0.9° (2011-2013; 9)
1P.BA13	0° (SKS)	-1.8°±0.8° (2011–2013; 26)
1P.BA19	9° (SKS)	-2.7°±0.8° (2011–2013; 16)
7H.TB03	5° (SKS)	-3.0°±1.0° (2011-2013)
7I.GA06	-5° (PKS), 0° (SKS)	-6.3°±0.9° (2004; 7)
7I.GA08	-5° (SKS)	-3.4°±0.9° (2004–2005; 10)
7I.TL10	-7° (PKS & SKS)	-6.1°±0.8° (2003–2005; 19)
7I.TL14	0° (PKS), 8° (SKS)	-4.4°±0.7° (2003–2005; 38)
7I.TL17	5° (SKS)	-1.4°±0.4° (2003–2005; 30)
7K.SOC03	0° (PKS), 5° (SKS)	2.7°±1.26° (2007–2008; 6)

incorporating transverse P-RFs enables us to infer seismic anisotropy in the crust and upper mantle (e.g., Park & Levin, 2016; Shiomi, 2017; Birkey & Ford, 2023). Significant uncertainties in the horizontal component orientations could lead to misinterpretations in the results of P-RF analysis.

Figure A.6 shows an example of teleseismic P-wave records observed at AU.STKA before and after the correction for station orientation, clearly indicating the energy leakage of P-wave from radial to transverse in the uncorrected horizontal traces. Using these two sets of teleseismic P-wave data, we computed radial and transverse P-RFs for two incoming directions within narrow distance ranges (10°) (Figure 2.6 (a, c)). After calculating individual P-RFs, we selected P-RF traces using the cross-correlation coefficient (CC)-based selection method (Tkalčić et al., 2011), stacking all traces with CC > 0.7. The resulting stacked P-RF traces are shown in Figure 2.6 (b, d), and the stacking process is visually summarized in Figures A.8 and A.9. The radial P-RFs are generally consistent regardless of the correction of misorientation. Still, the relative amplitude of converted phases for the direct P-wave can be modulated, potentially affecting analyses that rely on RF amplitude. For the transverse RFs, clear differences emerge between the uncorrected and corrected P-RF traces. In the uncorrected transverse P-RFs, we can see clear signals of direct P-wave, Moho-converted phases, and their multiple reflections, contaminating the P-to-SH converted phases. This con-

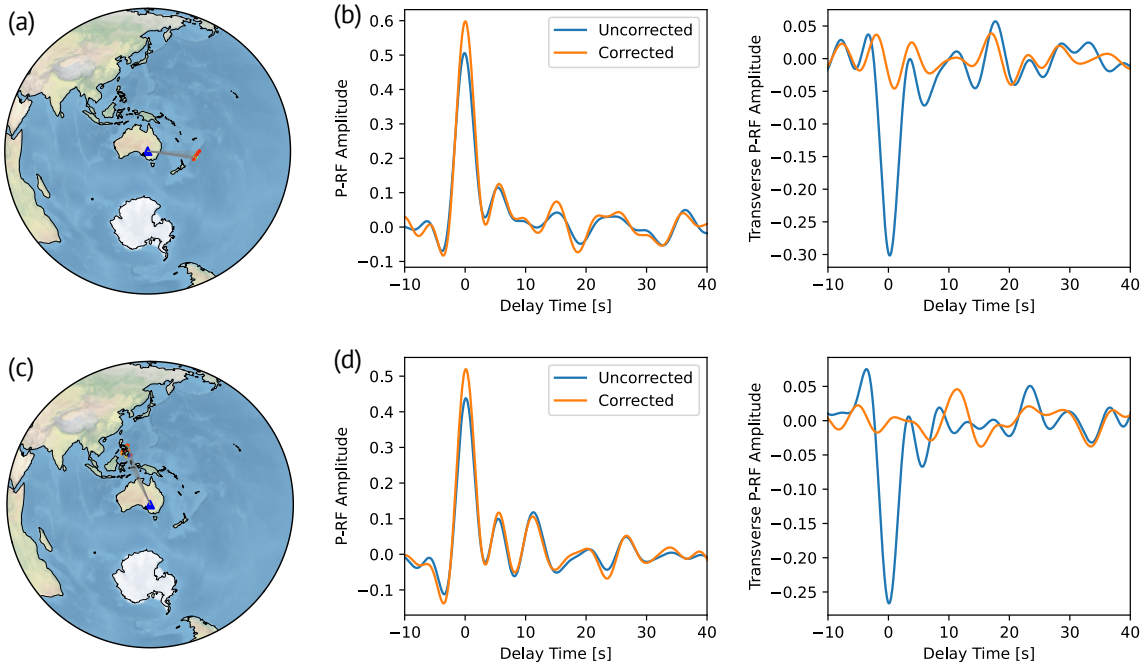

Figure 2.6: Comparison of P-wave receiver functions (P-RFs) for AU.STKA. (a, c) Maps showing event groups used for the P-RF analysis. (b) Stacked radial and transverse P-RFs for the eastern events shown in (a). Blue and orange lines represent P-RFs from uncorrected and corrected teleseismic P-wave data, respectively. (d) Same as (b), but for the northwestern events shown in (c).

tamination prevents us from properly interpreting P-to-SH conversions, which can be generated by anisotropic properties or oblique interfaces. Therefore, proper corrections of station azimuths during the waveform processing are essential for the accurate interpretation of both radial and transverse P-RF amplitudes.

In this study, we constructed a comprehensive station orientation catalog for Australian broadband seismic stations by analyzing long-period teleseismic P-wave particle motion data. The catalog includes temporal variations in station misorientations. While the timing of these changes is generally consistent with the published IRIS catalog, some stations exhibit changes at unexpected times. Finally, we assessed the utility of our catalog in receiver function analysis, demonstrating that correcting for station misorientation can significantly affect the amplitude analysis of RFs, particularly in the transverse component.

Chapter 3

Detecting rapid lateral changes of upper mantle discontinuities using azimuth-dependent P-wave receiver functions and multimode surface waves

3.1 Introduction

Upper mantle discontinuities are key to understanding the evolutionary processes of the continental lithosphere and underlying asthenosphere. Seismic interfaces within the continental upper mantle are essential for clarifying the tectonic processes that long-lived continents have undergone. Although these seismic discontinuities have been extensively investigated in various seismological studies, their spatial distributions and elastic properties remain controversial, even in continental regions with extensive seismic networks (e.g., Fischer et al., 2020).

Many earlier tomography models based on surface wave data have provided valuable insights into the seismic structure of the continental upper mantle (e.g., Debayle & Kennett, 2000; Yoshizawa & Kennett, 2004; Yuan et al., 2011), revealing the thick lithosphere in continental cratons and the thinner lithosphere in younger, tectonically active regions (Fischer et al., 2020). However, surface wave approaches have intrinsic limitations in constraining upper mantle interfaces, as the long wavelengths of surface waves are insensitive to sharp velocity gradients. In contrast, teleseismic receiver functions (RFs) have been widely used to image the upper mantle discontinuities, owing to their good sensitivities to impedance contrasts and their capability to identify conversions of P-to-S (Ps) or S-to-P (Sp) phases across interfaces (e.g., Rychert et al., 2005,

2007; Abt et al., 2010; Ford et al., 2010; Liu et al., 2020; Rein et al., 2020).

Recent RF studies analyzing Sp conversions have reported enigmatic interfaces beneath continental cratons, associated with sharp S-wave speed reductions above the Lithosphere-Asthenosphere Boundary (LAB), known as the Mid-Lithospheric Discontinuity (MLD) (Fischer et al., 2010, 2020). Like the LAB, the MLD is key to unraveling ancient tectonic history preserved within the cratonic lithosphere. Moreover, other seismological studies have suggested the existence of an enigmatic X-discontinuity (or considered as the Lehmann discontinuity) beneath the LAB (Rein et al., 2020; Srinu et al., 2021; Pugh et al., 2021). However, unlike surface waves, RFs cannot directly constrain 3-D seismic velocity structures, leaving the spatial distribution and elastic properties of upper mantle discontinuities a subject of ongoing debate.

3.1.1 Recent receiver function inversions

Over the past few decades, numerous studies have combined surface wave dispersion (SWD) data with teleseismic RFs to overcome the inherent limitations of surface-wave and body-wave analyses (Julià et al., 2000; Vinnik et al., 2005; Bodin et al., 2012; Tkalčić et al., 2011; Bodin et al., 2014; Calò et al., 2016; Kim et al., 2016; Taira & Yoshizawa, 2020; Ai et al., 2023). Recent joint inversion studies have utilized the hierarchical trans-dimensional Bayesian inference to estimate seismic wave speed structures, including the depths of upper mantle discontinuities (e.g., Bodin et al., 2012, 2014; Kim et al., 2016; Taira & Yoshizawa, 2020; Ai et al., 2023; Akuhara et al., 2023). However, this widely used joint inversion approach encounters challenges in imaging deep upper mantle discontinuities (e.g., LAB, X-D) due to the limited sensitivity of fundamental-mode SWD data and the reliance on stacked RFs.

Although SWDs enable us to constrain the absolute seismic shear velocity, the exclusive use of the fundamental modes limits the imaging of deeper structures below 200 km. The sensitivity of the fundamental mode SWDs diminishes significantly at greater depths, especially for Love wave (Figure B.3 in Appendix B). In contrast, surface wave overtones become sensitive to deeper structures, enabling better resolution throughout the entire upper mantle (e.g., Yoshizawa & Kennett, 2004; Yoshizawa & Ekström, 2010; Xu & Beghein, 2019). However, since multimode phase speed measurements are

not straightforward, several earlier studies employed only fundamental-mode SWDs (e.g., Calò et al., 2016). To enhance vertical resolution, Taira & Yoshizawa (2020) incorporated multimode SWDs into joint inversions with the P-wave RFs (P-RFs).

While RF inversions typically rely on stacked RFs derived from numerous individual RFs from many events, this approach presents two major difficulties due to intrinsic issues in the stacking process: the dependence of RF data on the range of epicentral distances and the back-azimuth of seismic events. The first issue is related to the moveout effect arisen from dependence on the distance range. This effect results in relative travel time differences between a parent phase (P-wave for P-RFs; S-wave for S-RFs) and the daughter phases (S for P-RFs; P for S-RFs), which vary with epicentral distance (or the slowness) (e.g., Kind & Yuan, 2011). To address this issue, conventional RF inversion studies have often limited the range of epicentral distances (e.g., Bodin et al., 2014; Calò et al., 2016; Taira & Yoshizawa, 2020). The second issue is the azimuthal dependence of RFs on the incoming direction of teleseismic parent waves, which results from lateral variations in seismic structure and the presence of layered anisotropic media with a horizontal symmetry axis (i.e., the azimuthal anisotropy) (Levin & Park, 1997; Frederiksen & Bostock, 2000; Frederiksen et al., 2003; Tonegawa et al., 2005; Nagaya et al., 2008; Kumar et al., 2011; Park & Levin, 2016).

These issues are generally neglected in many RF studies that employ either time-to-depth migration or inversions for velocity profiles (e.g., Rychert et al., 2005; Abt et al., 2010; Ford et al., 2010; Bodin et al., 2014; Taira & Yoshizawa, 2020; Birkey et al., 2021). However, such azimuth-dependent RFs have proven useful for imaging laterally heterogeneous structures through common conversion point (CCP) stacking, both in subduction zones (e.g., Tonegawa et al., 2005; Gilbert et al., 2006; Shi et al., 2015; Cheng et al., 2017; Kim et al., 2021) and continental regions (e.g. Kind et al., 2012; Sippl, 2016; Kennett & Sippl, 2018; Kind et al., 2020). Although CCP stacking can yield clear structural images, it requires a dense station distribution, which is not always available in target research areas. Azimuth-dependent RFs have also been used to map crustal and mantle azimuthal anisotropy (Shiomi & Park, 2008; Nagaya et al., 2008; Bianchi et al., 2010; Nagaya et al., 2011; Ford et al., 2016; Chen et al., 2021b). Bodin et al. (2016) pioneered the use of azimuth-dependent P-RFs in the trans-

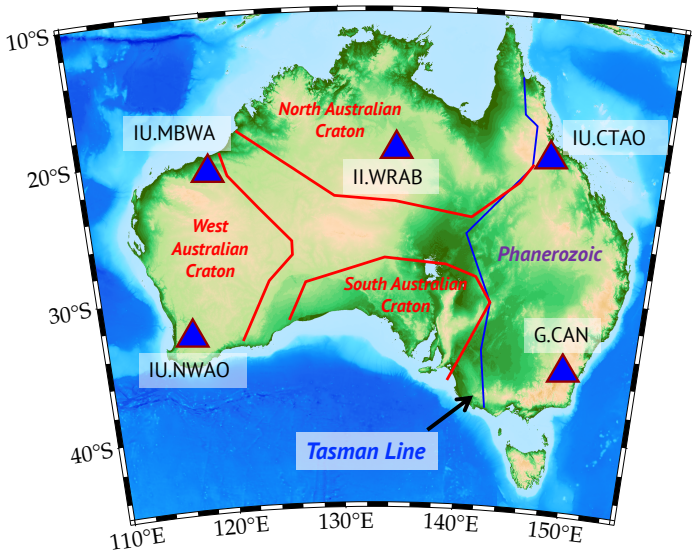

Figure 3.1: Map of the study region showing the locations of employed permanent stations (triangles). Red lines represent the cratonic margins of the North Australian Craton (NAC), South Australian Craton (SAC), and West Australian Craton (WAC). The blue line delineates the Tasman Line, the surface geological boundary separating cratonic regions in central and western Australia from the Phanerozoic basement in eastern Australia.

dimensional inversion to estimate azimuthal anisotropy beneath a station. However, no studies have yet attempted to image lateral variations in seismic interfaces through inversion.

Calò et al. (2016) employed the azimuth-dependent dataset of P-RFs to examine differences in inversion results. Although they observed variations in the inverted shear wave profiles and discontinuity depths, they did not account for these azimuthal effects. If rapid changes in discontinuity depth exist beneath a station, performing multiple inversions with RF datasets from different azimuth groups could capture such localized variations, potentially offering deeper insights into seismic interfaces, even from a single station.

3.1.2 Australian tectonics and the scope of this chapter

The Australian continent is the fastest-moving continental plate, drifting at about 6–7 cm/year (Argus et al., 2011), which was formed through ancient collisions of three major cratons - the West Australian Craton (WAC), the North Australian Craton

(NAC), and the South Australian Cratons (SAC) - during the Proterozoic era (1.3–1.0 Ga) (e.g., Myers et al., 1996; Yoshida & Yoshizawa, 2020). The present-day continent comprises cratonic regions in central and western Australia and the eastern province formed by the Phanerozoic orogeny (Figure 3.1). Previous three-dimensional shear wave speed models from surface-wave tomography (e.g., Fishwick et al., 2008; Kennett et al., 2013; Yoshizawa, 2014; Magrini et al., 2023) have revealed the large-scale lithosphere-asthenosphere system beneath the Australian continent. The Australian LAB is relatively flat across the cratonic zones but rapidly deepens westward in Phanerozoic eastern Australia (e.g., Kennett et al., 2013; Yoshizawa, 2014; Davies et al., 2015; Magrini et al., 2023). Based on multimode surface-wave tomography, Fishwick et al. (2008) proposed a stepwise lithospheric change from east (100 km) to west (100–150 km), potentially inducing strong azimuthal dependencies in P-RFs.

In this study, we aim to estimate localized variations in the depths of upper mantle discontinuities using azimuth-dependent P-RFs. We incorporated azimuth-dependent P-RFs into the joint Bayesian inversion with multimode SWDs (Taira & Yoshizawa, 2020) and applied this approach to five long-standing permanent stations in the Australian continent (Figure 3.1). We then compiled multiple inversion results to map Ps conversion depths around each station, revealing new insights into Australian upper mantle discontinuities. Our key findings on the MLDs and X-Ds provide valuable clues to understanding the spatial distribution and physical properties of these interfaces.

3.2 Data sets

Here, we summarize our data sets of multimode phase speeds of Rayleigh and Love waves (surface save dispersions: SWDs) and P-to-S receiver functions (P-RFs), which are used in the joint inversion analyses described in the following section.

3.2.1 Multi-mode surface-wave dispersion

Our SWD dataset is based on the phase speed maps constructed by Yoshizawa (2014), as used by Taira & Yoshizawa (2020). This dataset from Yoshizawa (2014) comprises regional-scale multi-mode phase speed maps that cover Australia and surrounding regions.

Yoshizawa (2014) initially performed non-linear waveform fitting to measure path-averaged multimode phase speeds ray path. This method, originating with Yoshizawa & Kennett (2002b), was further refined with empirical criteria to automatically extract the multi-mode dispersion data (Yoshizawa & Ekström, 2010). Although overtone phase speed measurements are challenging due to the overlap of multiple modes, the fully nonlinear waveform fitting approach effectively extracts phase speed information for multimode surface waves (Yoshizawa & Kennett, 2002b; Yoshizawa & Ekström, 2010; Xu & Beghein, 2019). This method has also been applied to seismic records from Mars (Xu et al., 2021) and ambient noise tomography (Takagi & Nishida, 2022). In the second step, Yoshizawa (2014) performed 2-D mapping of the measured multimode phase speeds, incorporating the finite-frequency effects on seismic surface waves using the influence zone concept from Yoshizawa & Kennett (2002a). Including finite-frequency effects accounts for lateral heterogeneities around the great-circle path between a source and a receiver, resulting in a high-quality multimode SWD database.

From these multimode phase velocity maps, we extract localized dispersion curves at each station. Extracted phase speed dispersion diagrams are shown in Figure B.4. Surface wave overtones are sensitive to structures below 200 km depth (Figure B.3), while the fundamental mode sensitivity is limited to shallower depths ($<$ 200km), particularly with the rapid decay of the sensitivity kernel for the fundamental Love wave. This limited sensitivity results in reduced resolution of SH wave speed or radial anisotropy structures. Taira & Yoshizawa (2020) demonstrated that higher-mode dispersion curves enhanced the vertical resolution of radially anisotropic structures. Following previous research, we use phase speed dispersion data from the fundamental up to the 4th higher mode. The period ranges for each mode of Rayleigh and Love waves used in this study are summarized in Table 3.1.

3.2.2 Azimuth-dependent P-wave receiver functions for permanent stations

We used three-component broadband seismograms, rotating the two horizontal components into radial and transverse components. P-RFs were estimated by deconvolving the vertical component from the radial component (Langston, 1979). While our waveform processing generally follows Taira & Yoshizawa (2020), we made minor updates

Mode	Rayleigh	Love
Fundamental	30 – 200 s	30 – 200 s
1st	35 – 170 s	33 – 170 s
2nd	55 – 150 s	60 – 125 s
3rd	45 – 90 s	50 – 95 s
4th	35 – 65 s	45 – 70 s

Table 3.1: Period ranges of surface wave dispersion data. Ordinal numbers indicate overtones.

to the deconvolution method and treatment of azimuthal dependencies in P-RFs. To accurately handle azimuth-dependent P-RFs, we made collections of horizontal misorientations of each station using our station orientation catalog available through the Zenodo repository (Tarumi & Yoshizawa, 2024).

For waveform processing, we selected events with moment magnitudes between 5.5 and 7.5, normalized P-wave radiation above |0.5| (from the Global CMT catalog (Dziewonski et al., 1981; Ekström et al., 2012)), epicentral distances between 30 and 90 degrees, and event depths less than 300 km. Figure 3.4 (e) shows the distribution of all selected events, and Figure B.5 displays employed event distributions for each station. Seismograms were bandpass-filtered in two frequency ranges (0.03–0.2 Hz and 0.03-0.5 Hz). We discarded low-quality waveforms with S/N ratios below 5 on the vertical component and below 3 on the radial component. We then deconvolved the vertical component from the radial component based on the multi-taper receiver function technique (Shibutani et al., 2008), applying a water-level of 0.1% for the maximum amplitude in the frequency domain to stabilize spectral division in the frequency domain, instead of a Gaussian high-cut filter as introduced in the original method of Shibutani et al. (2008).

Conventional RF inversion studies, particularly in continental regions, generally stack large amounts of P-RF data while restricting events in a limited range of epicentral distance and/or back-azimuth (e.g., Julià et al., 2000; Bodin et al., 2012; Vinnik et al., 2014; Kim et al., 2016; Calò et al., 2016; Taira & Yoshizawa, 2020). The stacked RF is often treated as an averaged P-RF, representing a 1-D stratified structure around the station and neglecting azimuthal variations due to the incoming direction of P-waves. However, P-RFs are sensitive to the back-azimuth of events, as they reflect lat-

eral structural changes or anisotropic layering around the station (e.g., Tonegawa et al., 2005; Kumar et al., 2011; Park & Levin, 2016). Teleseismic P-waves are converted to S-waves when transversing structural boundaries, so rapid lateral variations in seismic structure beneath a station induce significant back-azimuthal dependencies in P-RFs on the incoming P-wave direction (e.g., Figure 3.3 (b)). These azimuthal dependencies in RFs, which have been neglected in earlier studies (e.g., Taira & Yoshizawa, 2020), can be potentially useful for mapping localized lateral changes in P-to-S conversion points.

To utilize the azimuthal dependencies in P-RFs that reflect the lateral changes in interface depths, we adopt a binned-stack approach with 10-degree ranges and intervals for both epicentral distance and back-azimuth to estimate the azimuth-dependent P-RFs. To maintain a high-quality dataset in this stacking process, we employ the cross-correlation-based selection method (Tkalčić et al., 2011), as in Taira & Yoshizawa (2020). This method selects P-RF traces for stacking based on normalized cross-correlation coefficients (NCC) between all P-RF pairs. In this study, we grouped P-RF traces with NCC >0.8 for the 0.03–0.2 Hz range and NCC >0.7 for the 0.03–0.5 Hz range, discarding groups with fewer than 10 traces.

Figure 3.2 shows examples of azimuth-dependent P-RF dataset for CTAO, located in northwestern Australia. Figure 3.2 (a) presents a map of events used to compute the RFs visualized in Figures 3.2 (b) and (c). While both P-RFs reflect the seismic structure beneath CTAO, the expected conversion points differ laterally by 100–150 km at 200 km depths. In Figures 3.2 (b) and (c), distinct differences in the shapes of back-azimuth-ordered and stacked RFs are visible (e.g., at 5, 8, and 20 s). Around 5 s, the stacked P-RF from western events (green line in Figure 3.2 (c)) clearly exhibits a positive signal, which is unclear in the stacked P-RF from eastern events (green line in Figure 3.2 (b)). Around 8 s in the eastern P-RFs (Figure 3.2 (b)) and 20 s in the western P-RFs (Figure 3.2 (c)), strong negative phases are evident. Besides, these differences in azimuth-dependent P-RFs seem to be coherent within each back-azimuth range (left panels in Figure 3.2 (b, c)), implying structural variations beneath the station along the ray-paths.

Figure 3.3 (a) displays a compilation of stacked P-RFs at CTAO as a function

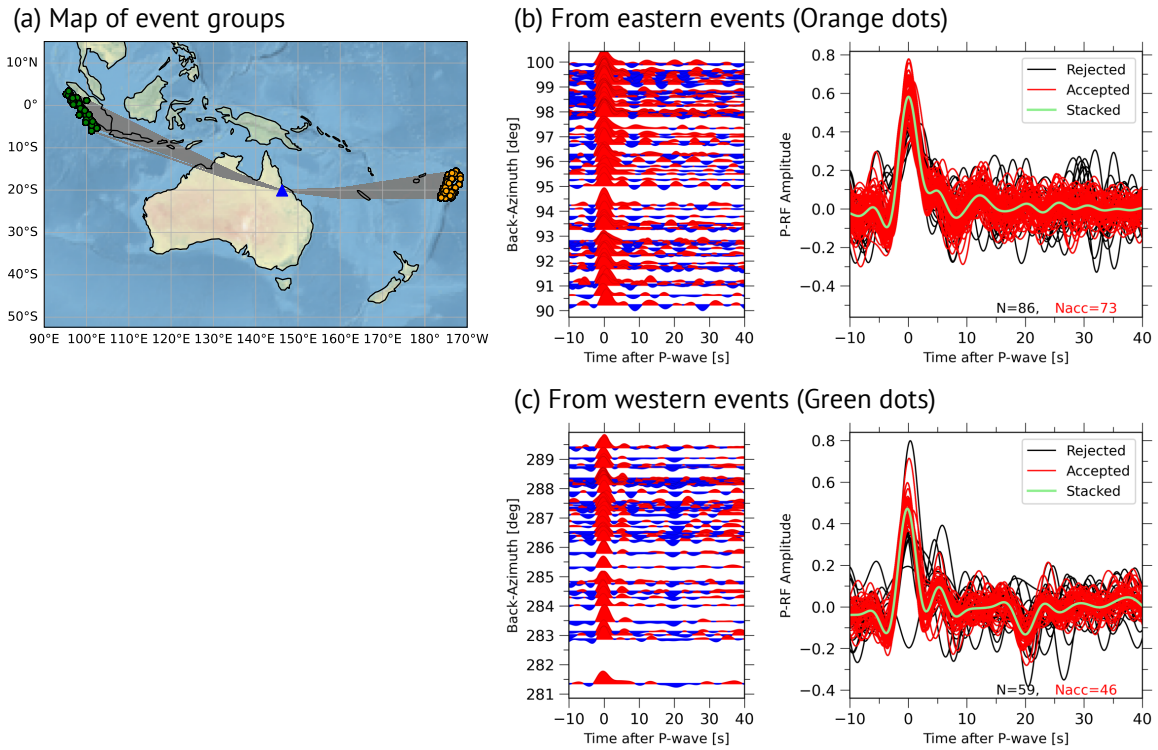

Figure 3.2: Example of the binned-stacking process for P-RFs at CTAO. (a) Map of seismic events for two groups, with orange and green dots representing eastern and western events, respectively. Gray lines indicate ray paths from each event location to the station. (b) P-RF stacking process for the eastern event group (orange dots in (a)) with a back-azimuth range between 90° and 100°. The left panel shows individual P-RF traces that meet all selection criteria outlined in the main text, with positive and negative phases filled in red and blue. The right panel shows the stacking process, where green, red, and black lines represent stacked, accepted, and rejected traces based on cross-correlation selection. N and N_{acc} denote the total number of traces and the number of accepted traces, respectively. (c) Same as (b) but for the western event group (green dots in (a)).

of back-azimuth, along with a schematic illustration of the plausible origin of these azimuthal dependencies. Figure B.6 shows the frequency dependence of azimuth-dependent P-RFs at CTAO, covering four frequency ranges (i.e., 0.03–0.125 Hz; 0.03–0.2 Hz; 0.03–0.5 Hz; 0.04-1.0 Hz). In Figure 3.3 (a), as described, P-to-S conversions appear as isolated phases at around 5 s in the western and northern directions, whereas in the east, these conversions become less distinct due to overlap with the direct P-wave. In higher frequency ranges (Figure B.6 (c, d)), the positive phases at 5 s are more prominent than in lower frequency P-RFs (Figure 3.3 (a)). Additionally, at higher fre-

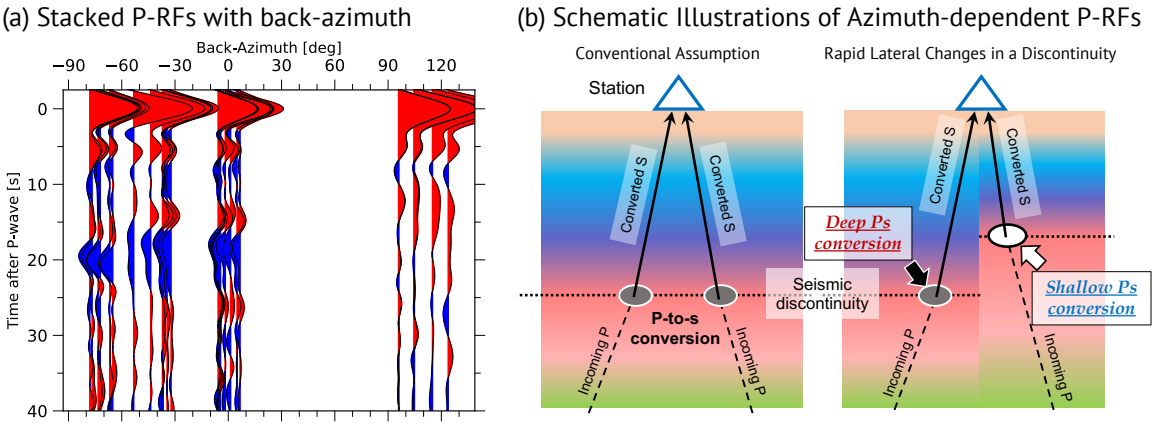

Figure 3.3: Azimuth-dependent P-RF dataset for CTAO and schematic illustrations of azimuthal dependence in P-RFs. (a) Compilation of stacked P-RF traces at CTAO with respect to back-azimuth, measured clockwise from the north. The color scheme for filled phases is the same as the right panels in Figures 3.2 (b and c). (b) Schematic illustrations of potential origins of azimuthal dependence in P-RFs. The left panel shows the P-to-S conversion assuming a 1-D stratified model, where conversion locations are independent of the incoming P-wave directions. In contrast, the right panel illustrates a scenario with rapid lateral structural changes around the seismic station, where conversion points vary with the event's azimuth.

quencies, remarkable differences also emerge before the Moho conversions, potentially indicating lateral variations in crustal structure, although this is beyond our current scope. In the later phases (after 5 s), significant negative phases around 20 s appear in the west and north directions, but these negative phases are absent in the eastern P-RFs. These trends remain consistent in higher frequency P-RFs (Figure B.6) and are robust, though they become slightly less clear due to contamination from multiple reflections from the Moho, shallower interfaces, and other scattered phases.

The significant negative phases at 20 s likely originate from a rapid velocity reduction in the upper mantle. Around CTAO, previous tomographic models have suggested that the upper mantle structure undergoes rapid lateral changes, possibly reflecting the transition between the eastern Phanerozoic and western cratonic regions (e.g., Fishwick et al., 2008; Yoshizawa, 2014; de Laat et al., 2023). Figure 3.3 (b) provides a schematic illustration of Ps conversion points with and without such structural changes. Conventional RF studies in continental regions have implicitly assumed a 1-D stratified layered model beneath the station (left panel in Figure 3.3 (b)). However, in the sce-

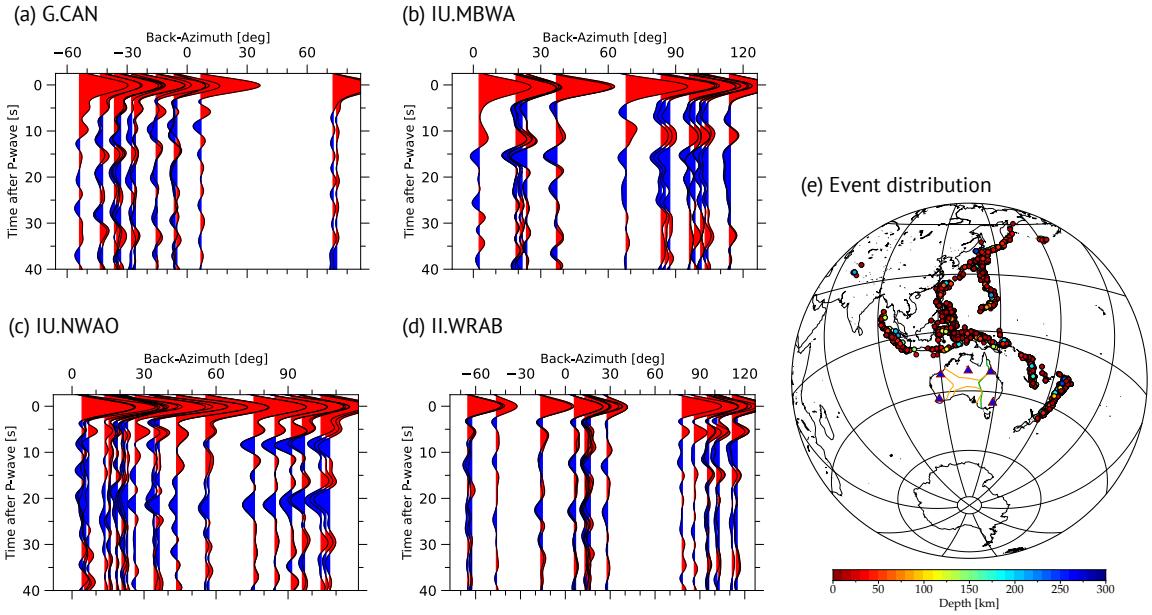

Figure 3.4: (a–d) Azimuth-dependent P-RF datasets (0.03–0.2 Hz) of the four stations used in this study: (a) G.CAN, (b) IU.MBWA, (c) IU.NWAO, and (d) II.WRAB. Figure notations are the same as Figure 3.3 (a). (e) Map of all events used in this study, with blue triangles indicating station locations and colored circles representing individual seismic events. Yellow and green lines delineate the major cratonic boundaries and the Tasman Line.

nario depicted in the right panel of Figure 3.3 (b), the conversion points from P to S vary with the incoming direction of teleseismic P-waves, which serve as the parent phase for the converted S-waves. The azimuth-dependent P-RFs observed at CTAO likely result from lateral localized variations in the upper mantle interface.

Figure 3.4 shows azimuth-dependent P-RF datasets (0.03–0.2 Hz) at four stations, excluding CTAO: (a) G.CAN (b) IU.MBWA, (c) IU.NWAO, and (d) II.WRAB. Figure B.7 presents the shorter-period datasets (0.03–0.5 Hz) for these stations. Except for MBWA (Figure 3.4 (b)), clear positive conversion phases are observed at 5–6 s in Figures 3.4 (a), (c), and (d), suggesting the thick crust or the deep Moho (Kennett et al., 2023). On the contrary, the lack of positive phases at 5 s in MBWA may indicate the thinner crust, around 30 km in thickness (e.g., Taira & Yoshizawa, 2020; Kennett et al., 2023), which is also shown in Figure B.7 (b). As shown in MBWA (Figure 3.4 (b)), long-period P-RFs may not adequately constrain the Moho depth and crustal structure in regions with thinner crust. Thus, we used higher-frequency data (0.03–0.5

Hz) from 10 s after the main P-phase in the inversion process described in the next section. For four stations (Figure 3.4 (a-d)), the later phases after 5–6 s indicate the azimuthal dependence, though this tendency is weaker compared to CTAO (Figure 3.3 (a)), implying that lateral variations in seismic structure beneath these stations may be milder.

3.3 Trans-dimensional Bayesian inversion

We apply hierarchical trans-dimensional Bayesian inference (Bodin et al., 2012) to invert azimuth-dependent P-RFs and multimode SWDs (phase speeds of Rayleigh and Love waves). This probabilistic approach allows for flexible sampling of model parameters and requests fewer a priori constraints than traditional linearized inversion methods. The trans-dimensional algorithm treats both the number of parameters (e.g., the number of layers) and data uncertainties as unknowns, allowing for exploration across the entire model parameter space. We consider the Bayesian theorem extended into a hierarchical trans-dimensional formulation as follows,

$$p(\mathbf{m}(k), k, \sigma \| \mathbf{d}) \propto p(\mathbf{d} \| \mathbf{m}(k), k, \sigma) p(\mathbf{m}(k)) p(k) p(\sigma), \tag{3.1}$$

where $p(A\|B)$ is the conditional probability density function (p.d.f.) of the occurrence of A given B. $p(\mathbf{m}(k), k, \sigma\|\mathbf{d})$, $p(\mathbf{d}\|\mathbf{m}(k), k, \sigma)$, $p(\mathbf{m}(k))$, $p(k)$, and $p(\sigma)$ represent the posterior, likelihood, model prior, hyperpriors for the number of model parameters and the data noise, respectively. To estimate the posterior probability, we employ the reversible-jump Markov chain Monte Carlo (RJMCMC) method (Green, 1995), which efficiently samples model parameters to fit the observed data.

3.3.1 Model parameterization

In this study, we assume a one-dimensional stratified structure beneath each station. The stratified model parameters follow Taira & Yoshizawa (2020), comprising interface depths z and perturbations in SV and SH wave velocities from the reference model, δV_{SV} and δV_{SH}. Using the hierarchical trans-dimensional scheme, we also include data noises σ for two frequency ranges of P-RFs and each mode of multimode SWDs σ, as well as the number of layers k as parameters to be recovered. Thus, the model parameter vector $\mathbf{m}$ is defined as $[\sigma, k, \mathbf{z}, \delta\mathbf{V_{SV}}, \delta\mathbf{V_{SH}}]$.

The spherical radially anisotropic S-wave model is perturbed to the 400 km depth, combined with the PREM (Dziewonski & Anderson, 1981) below 400 km. Other elastic parameters are scaled based on the shear-velocity structure and replaced by the 1-D reference model. For P-waves, we maintain the fixed ratio between V_P and V_S to the AK135 model (Kennett et al., 1995) and calculate V_P from V_S. The density structure ρ is scaled with compressional wave speeds through the empirical relationship $\rho = 2.35 + 0.036(V_P - 3)^2$ (e.g., Tkalčić et al., 2006; Bodin et al., 2012, 2014; Taira & Yoshizawa, 2020). The radial anisotropy parameter η and anelastic attenuation values of Q_κ and Q_μ are fixed to a modified PREM where the 220 km discontinuity is smoothed.

3.3.2 The prior

Prior probabilities for model parameters are defined using uniform or normal distributions. For the number of parameters k and data uncertainties σ, we assume uniform distributions over the ranges [5, 61] and [0.01, 0.2], respectively. The prior for the depth is uniformly distributed from 0 to 400 km.

For S-wave perturbations, we use a zero-mean Gaussian prior with a standard deviation of $\sigma = 0.3$ km/s, following Akuhara et al. (2021) and Ai et al. (2023). Local reference models for each station are derived from the three-dimensional radially anisotropic S-wave speed model by Yoshizawa (2014), which has been optimized for multimode SWDs through linearized inversions, providing good resolution in the deep upper mantle. The crustal model, however, is approximated using the 3SMAC model (Nataf & Ricard, 1996) since phase velocities from seismic surface waves at periods longer than 30 s have limited sensitivity to shallow structures. To represent the Australian crustal structure accurately, we replace the crustal SV velocity model of Yoshizawa (2014) with the AuSREM crustal S-wave speed model and local Moho depth (Kennett et al., 2011; Salmon et al., 2013; Kennett et al., 2023). Radial anisotropy is fixed to the Yoshizawa (2014) model. As a result, our local reference model reflects both the crustal and upper mantle structure of Australia. Figure B.8 displays the reference structural model used for each station.

3.3.3 Likelihood function

The likelihood functions measure the consistency between synthetic and observed data. Since we incorporate both surface-wave dispersion curves and P-RFs, our likelihood term is defined by the joint probability:

$$p(\mathbf{d}\|\mathbf{m}(k),\sigma) = \; p(\mathbf{d_{SWD}}\|\mathbf{m}(k),\sigma_{\mathbf{SWD}})\; p(\mathbf{d_{PRF}}\|\mathbf{m}(k),\sigma_{\mathbf{PRF}}), \tag{3.2}$$

where the first and second terms in the right-hand of (eq. 3.2) correspond to the likelihood probability density functions for SWD and P-RF, respectively. These are formulated based on the Gaussian distributions following Taira & Yoshizawa (2020):

$$p(\mathbf{d_{SWD}}\|\mathbf{m}(k),\sigma_{\mathbf{SWD}}) = \prod_{i=0}^{4} \frac{1}{\sigma_i^{\mathrm{R}}\sqrt{(2\pi)^{N_{\mathrm{R}_i}}}} \exp\left(-\frac{\|\mathbf{d}_i^{\mathrm{R}} - \mathbf{g}_i^{\mathrm{R}}(\mathbf{m}(k))\|^2}{2\sigma_i^{\mathrm{R},2}}\right) \tag{3.3}$$

$$\times \prod_{i=0}^{4} \frac{1}{\sigma_i^{\mathrm{L}}\sqrt{(2\pi)^{N_{\mathrm{L}_i}}}} \exp\left(-\frac{\|\mathbf{d}_i^{\mathrm{L}} - \mathbf{g}_i^{\mathrm{L}}(\mathbf{m}(k))\|^2}{2\sigma_i^{\mathrm{L},2}}\right), \tag{3.4}$$

and

$$p(\mathbf{d_{PRF}}\|\mathbf{m}(k),\sigma_{\mathbf{PRF}}) = \prod_{i=1}^{2} \frac{1}{\sigma_i^{\mathrm{PRF}}\sqrt{(2\pi)^{N_{\mathrm{PRF}_i}}}} \exp\left(-\frac{\|\mathbf{d}_i^{\mathrm{PRF}} - \mathbf{g}_i^{\mathrm{PRF}}(\mathbf{m}(k))\|^2}{2\sigma_i^{\mathrm{PRF},2}}\right), \tag{3.5}$$

where $\mathbf{d}^{\mathrm{R}}$, $\mathbf{d}^{\mathrm{L}}$, and $\mathbf{d}^{\mathrm{PRF}}$ represent the observed data for Rayleigh and Love wave dispersion curves and P-RFs, respectively, and $\mathbf{g}^{\mathrm{R}}$, $\mathbf{g}^{\mathrm{L}}$, and $\mathbf{g}^{\mathrm{PRF}}$ denote the forward-modeled data for each dataset. For synthetic data calculations, we use the normal mode theory (DISPER80; Takeuchi & Saito, 1972; Saito, 1988) for SWD computations and the Thomson-Haskell method (Thomson, 1950; Haskell, 1962) for P-RF modeling, which is widely used in Monte-Carlo inversion studies (e.g., Bodin et al., 2012, 2016; Calò et al., 2016; Taira & Yoshizawa, 2020). Since these approaches are based on a 1-D stratified flat Earth model, we apply an Earth-flattening correction to account for the spherical Earth model.

To investigate the lateral variations of discontinuity depths, we performed inversions using local SWDs from the surface-wave tomography model as well as P-RFs for each azimuth-distance bin. Note that the local multimode SWDs were fixed for each station (Figure B.4) because they reflect the local seismic structure around a seismic station as seen by long-wavelength surface waves.

3.3.4 Reversible-jump sampling with Parallel Tempering

To estimate ensemble solutions, we use the reversible-jump Markov chain Monte Carlo (RJMCMC) scheme (Green, 1995). RJMCMC aims to infer the posterior density of model parameters by iteratively exploring model parameter spaces of varying dimensions. In each iteration, a new model parameter vector is proposed by randomly selecting one of several perturbation patterns: (1) create a new layer, (2) remove a layer, (3) perturb a data error, (4) adjust a transition depth, (5) perturb the SV wave speed in a layer, or (6) perturb the SH wave speed in a layer. We then compute the synthetic data and likelihood function based on the proposed model. The model acceptance is determined using the Metropolis-Hastings (MH) algorithm (Metropolis et al., 1953; Hastings, 1970). To enhance convergence speed and improve acceptance rates, we apply the Parallel Tempering (PT) method to the MH algorithm (Sambridge, 2014), as implemented in Taira & Yoshizawa (2020) and Akuhara et al. (2021). PT enables broader exploration of the model parameter space by running multiple Markov chains in parallel, each with a different temperature. Consequently, our MH acceptance criterion, based on the likelihood probability, is expressed as:

$$\alpha_{MH} = \min\left\{1, \left[\frac{p(\mathbf{d}\|\mathbf{m}_j, k_j, \sigma_j)}{p(\mathbf{d}\|\mathbf{m}_i, k_i, \sigma_i)}\right]^{1/T_j} \times \left[\frac{p(\mathbf{d}\|\mathbf{m}_i, k_i, \sigma_i)}{p(\mathbf{d}\|\mathbf{m}_j, k_j, \sigma_j)}\right]^{1/T_i}\right\}, \tag{3.6}$$

where α_{MH} is the acceptance probability in the PT framework, subscripts i and j denote the i-th and j-th MCMC chains, and T_n is the temperature of the n-th chain. In PT, each chain runs in parallel at a different temperature. In this study, we run 40 chains in parallel, 10 of which are set as unit temperature, while the remaining 30 chains have higher temperatures following $T_i = 200^{i/30}$, resulting in a maximum temperature of 200 °C.

For RJMCMC sampling, we set the maximum iteration number of 150,000, discarding the initial 50,000 models as the burn-in period. To avoid autocorrelated samples, we store the models at intervals of 100 iterations, resulting in posterior distributions constructed from 10,000 models.

3.4 Results of inversions for Australian stations

The trans-dimensional Bayesian inversion estimates the probability density functions of model parameters. From these probabilistic models, we identify seismic discontinuities (i.e., Moho, LAB, MLDs, and X-Ds) based on S-wave velocity changes through a combination of automated and visual inspections. Hereafter, we focus on the isotropic S-wave speed derived by the voigt average, $V_{S_{iso}} = \sqrt{\frac{2V_{SV}^2+V_{SH}^2}{3}}$, and the radial anisotropy, $\xi = (\frac{V_{SH}}{V_{SV}})^2$.

Using our posterior distributions, the Moho can be identified as the depth of the maximum positive $V_{S_{iso}}$ jump, mostly consistent with the AusMoho depth (Kennett et al., 2023) constructed by compiling multiple geophysical datasets (e.g., reflection profiles and refraction explorations). S-wave speeds in the asthenosphere are generally slower than the lithosphere, and the LAB is often characterized by the significant S-wave speed reduction in the upper mantle (e.g., Kennett et al., 2013). Thus, we first imposed an isotropic S-wave speed of less than 4.7 km/s as an LAB criterion, then determined the LAB as a $V_{S_{iso}}$ or V_{SV} drop of over 0.04 km/s around the Lithosphere-Asthenosphere Transition (LAT) identified by Yoshizawa (2014) from vertical gradients in shear wave speed profiles. However, at WRAB in the southern North Australian Craton (NAC), the high isotropic S-wave speed extends to 200–300 km depth, and no significant velocity reduction is observed within the LAT range. In such cases, we determined the depth of the lithospheric base by identifying a positive jump in radial anisotropy, ξ, following Plomerová et al. (2002).

With the mantle lithosphere thickness defined, we identified MLDs within the mantle lithosphere and X-Ds underlying the LAB or lithospheric base. MLDs are marked by a $V_{S_{iso}}$ or V_{SV} change of at least 0.02 km/s above the LAT upper bound or selected LAB depths and are detected primarily at stations in cratonic areas (MBWA, NWAO, and WRAB). For X-Ds, we identified S-wave speed jumps of over 0.04 km/s beneath the selected LAB. Both MLDs and X-Ds may occur at multiple depths. To examine the relationship between MLDs/X-Ds and the radial anisotropy without bias, we did not adopt any criteria related to radial anisotropy when identifying MLDs and X-Ds.

This section discusses our results separately for the Phanerozoic and cratonic provinces

of Australia. For the Phanerozoic province, we present inversion results for CTAO and CAN (Figures 3.5 and 3.6). For cratonic regions, Figure 3.7 shows joint inversion results at two stations, MBWA and NWAO, in the WAC, and Figure 3.8 presents the results at WRAB in the NAC. Employed event distributions are also displayed in Figures 3.5, 3.6, 3.7, and 3.8. Previously estimated discontinuity depths from earlier studies (Yoshizawa, 2014; Birkey et al., 2021; Kennett et al., 2023) are superimposed on the resultant 1-D profiles, including AusMoho depth, the first and second negative peaks in S-RF profiles from Birkey et al. (2021), and LAT upper and lower bounds from Yoshizawa (2014), as indicated in each figure and caption.

3.4.1 Phanerozoic eastern Australia

3.4.1.1 CTAO station

Selected inversion results at the CTAO station for the eastern, western, and northern event groups are shown in Figure 3.5. Posterior distributions for hyperparameters (i.e., the number of layers and data noises) and data misfit distributions are summarized in Figures B.9, B.10, and B.11. In the inversion results at CTAO, distinct azimuthal dependencies are observed in both isotropic S-wave and radial anisotropy profiles (Figure 3.5 (b–d)). The data misfits are sufficiently low, with each P-RF well reproduced (Figures B.9, B.10, and B.11), indicating that the velocity structures are reliably resolved. Identified upper mantle discontinuities vary with the incident directions of teleseismic P-waves corresponding to each event group.

In all inversion results (Figure 3.5 (b–d)), we can see shear wave speed jumps at around 40 km, corresponding to the Moho, consistent with the AusMoho model (Kennett et al., 2023) and Taira & Yoshizawa (2020). Some variations in crustal structures are present in the results for different event directions but are not discussed here, as our focus is on the upper mantle discontinuities. Note that our long-period SWD dataset has limited sensitivity to constrain the absolute shear velocity in the crust.

The LAB depths, marked by shear velocity reductions, vary by event group, suggesting lateral changes in lithospheric thickness. In the eastern results (Figure 3.5 (b)), an S-wave velocity drop appears at around 60 km within the LAT, which may be

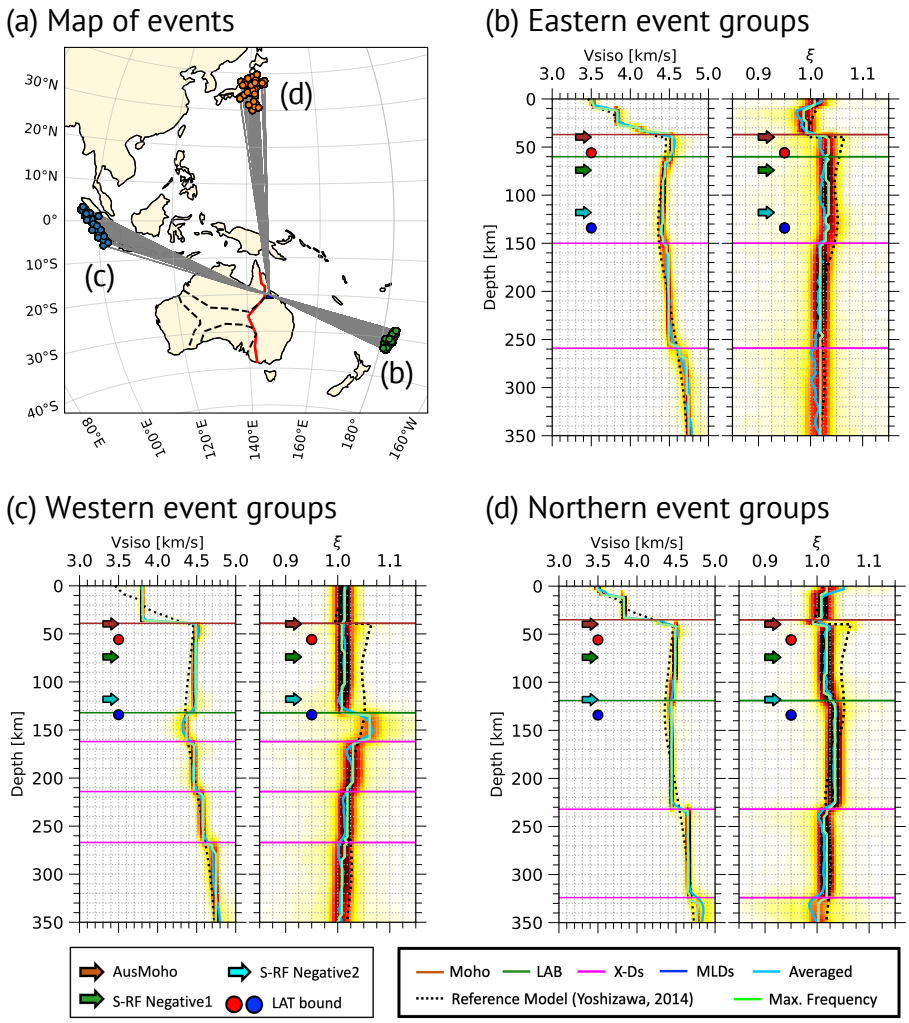

Figure 3.5: Examples of joint inversion results for CTAO. (a) Event distribution, with colored dots representing seismic events grouped by direction and a blue triangle indicating the target station. Black dotted and red lines are the major cratonic boundaries and the Tasman Line, respectively. (b) Posterior distributions of isotropic S-wave speed $V_{S_{iso}}$ and radial anisotropy ξ retrieved from the eastern event group, with sky blue, purple, and light green lines indicating the mean and mode (maximum frequency) models, respectively. Black dotted lines show the reference model for the inversion. Colored horizontal lines are identified discontinuities (brown: Moho, blue: MLDs, green: LAB or Lithospheric base, magenta: X-Ds). Brown arrows indicate the AusMoho depth Kennett et al. (2023), while green and light blue arrows represent the depths of the first and second maximum negative peaks in S-RF profiles (Birkey et al., 2021). Red and blue dots exhibit the upper and lower depths of the Lithosphere-Asthenosphere Transition (LAT) derived from Yoshizawa (2014). All notations are shown at the bottom of the figure. (c, d) Same as (b), but for the western and northern event groups.

comparable to the S-RF's negative phase at 74 km (Birkey et al., 2021). Western and northern results show a deeper velocity drop at 120–130 km, above the lower bound of LAT (Figure 3.5 (c, d)), consistent with the second negative peak of S-RF at 118 km. Increasing radial anisotropy ξ across these interfaces (Figure 3.5 (b–d)) is consistent with the expected horizontal shear flow in the asthenosphere.

These findings suggest rapid lateral LAB depth variations around CTAO, from 60–70 km in the east to 120-130 km in the west and north, supporting a step-wise lithospheric model by Fishwick et al. (2008) and the azimuth-dependent variations seen in the P-RF profiles (Figure 3.3).

Below the LAB at CTAO, we identify multiple S-velocity jumps at around 170, 220, 270, and 330 km, consistent with Revenaugh & Jordan (1991), who proposed similar multiple discontinuities based on path-averaged ScS reverberations. They interpreted shallower interfaces around 170 and 220 km as the Lehmann discontinuity and the deeper interfaces as the X-Ds. Although we cannot decisively identify the Lehmann discontinuity, these multiple discontinuities, associated with positive S-velocity jumps, coincide with regions of weakened anisotropy, as noted in Taira & Yoshizawa (2020).

3.4.1.2 CAN station

For the CAN station, inverted S-velocity profiles for different event groups are consistent (Figure 3.6), unlike the result for CTAO in Figure 3.5. Clear S-wave velocity jumps at 40 km depth indicate the Moho, which is slightly shallower than AusMoho. While the Australian Moho map (e.g., Kennett et al., 2023) suggests a locally thicker crust in southeastern Australia, its northern area indicates a thinner crust, which may be reflected in our results. The LAB is identified by a sharp velocity reduction at around 80 km depth within the LAT, similar to the S-RF negative peaks reported by Birkey et al. (2021). Like CTAO, the LAB coincides with increased radial anisotropy, suggesting the effects of horizontal mantle flow beneath it. Our data suggest an interface with a shear velocity drop at 65km depth, consistent with another negative S-RF phase at 50–60 km in Birkey et al. (2021). Below the LAB, we detect multiple discontinuities with positive velocity gradients and similar anisotropy characteristics to CTAO, showing decreased ξ. The detected depths are close to those at CTAO: 140-150

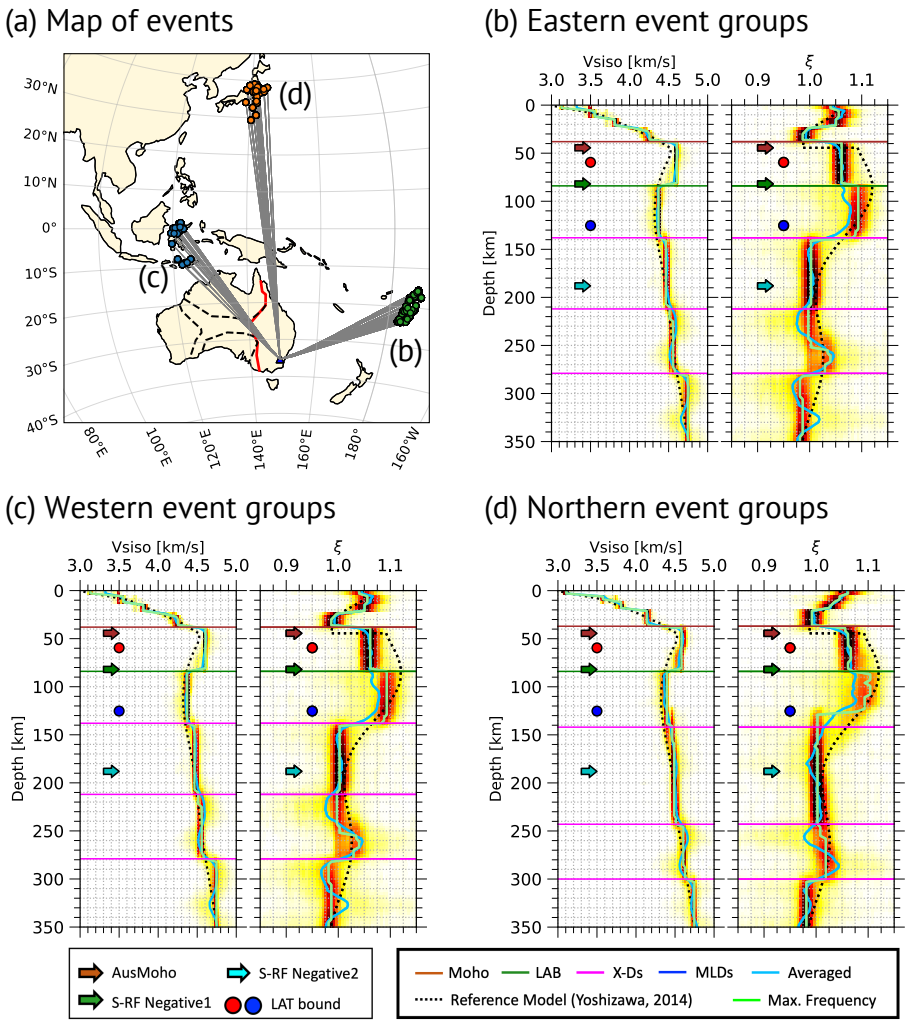

Figure 3.6: Same as 3.5, but for G.CAN.

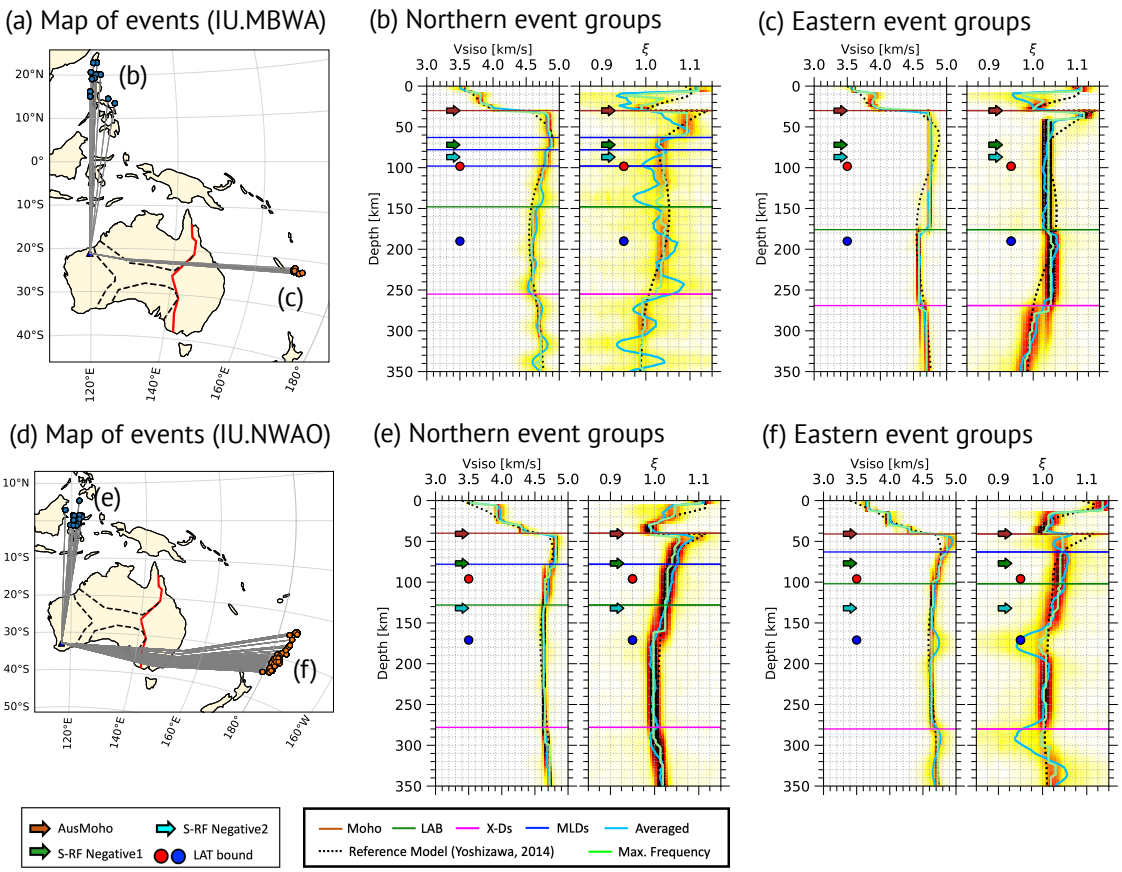

Figure 3.7: Same as Figure 3.5, but for IU.MBWA and IU.NWAO.

km, 220–260 km, and around 300 km.

3.4.2 Cratonic central and western Australia

3.4.2.1 MBWA and NWAO stations in western Australia

Figure 3.7 shows inversion results using multiple event groups for both the MBWA and NWAO stations located in the Archean cratons. At MBWA located near the northeastern margin of the Pilbara craton, facing the suture zone between WAC and NAC, azimuthal dependency is evident, likely due to the structural differences along the northern and eastern paths (Figure 3.7 (b, c)). In contrast, NWAO located in the southwestern area of the Yilgarn craton, where eastern and northern ray-paths propagate through the stable cratonic region, exhibits weaker azimuthal dependency (Figure 3.7 (e, f)). Our results from the northern event groups are generally consistent with the S-RF studies (Birkey et al., 2021).

At MBWA in Figure 3.7 (a-c), azimuth-independent Moho depths are observed around 30 km, consistent with AusMoho (Kennett et al., 2023). The LAB, characterized by a shear velocity drop (> 0.04 km/s), is estimated at 150 km in the north and 170–180 km in the east, with a weaker increase in radial anisotropy than eastern Australia. Multiple MLDs are identified at the lithospheric depths, consistent with previous studies (Taira & Yoshizawa, 2020; Sun et al., 2018), showing decreasing radial anisotropy across the MLDs as suggested by Yoshizawa & Kennett (2015) and Kennett et al. (2017). The second and third MLDs (Figure 3.7 (b)) exhibit negative velocity changes, supporting the earlier S-RF study by Birkey et al. (2021). A single X-D is observed at around 270 km, accompanying the weakening of radial anisotropy.

At NWAO in Figure 3.7 (d-f), azimuth-independent Moho depths are identified at 40 km. MLDs are found at a depth of 60 km in the eastern path and 80 km in the northern path, similar to the results from S-RF (Birkey et al., 2021). LAB signatures are detected at 130 km depth in the northern path, which is consistent with the second negative peak in S-RF by Birkey et al. (2021), and at 100 km in the eastern path. The X-Ds under the LAB are seen in the range from 250 to 300 km, consistent with the depths identified by Taira & Yoshizawa (2020) at 270 km and the Lehmann discontinuity by Revenaugh & Jordan (1991) at around 255–280 km.

3.4.2.2 WRAB station in central Australia

Figure 3.8 shows the inversion resultants at WRAB, located in the NAC, for three event groups. Despite being located in the stable craton, WRAB, three inversion results at WRAB display clear azimuthal dependence of radially anisotropic S-wave profiles (Figure 3.8 (b-d)). No significant S-wave speed drops are observed, and the signature of the asthenosphere or low-velocity zone is unclear beneath WRAB. A high-velocity structure (4.7–4.8 km/s) extends from just below the Moho (around 50 km) to the deep upper mantle, with a clear increase in radial anisotropy around the LAT.

For WRAB, the lithosphere base is defined by increased radial anisotropy, consistent with previous tomographic studies that indicate a thick high-speed region in the southern NAC (e.g., Yoshizawa, 2014; Magrini et al., 2023; de Laat et al., 2023). Despite the absence of a clear low-velocity zone in the AusREM model (Kennett et al.,

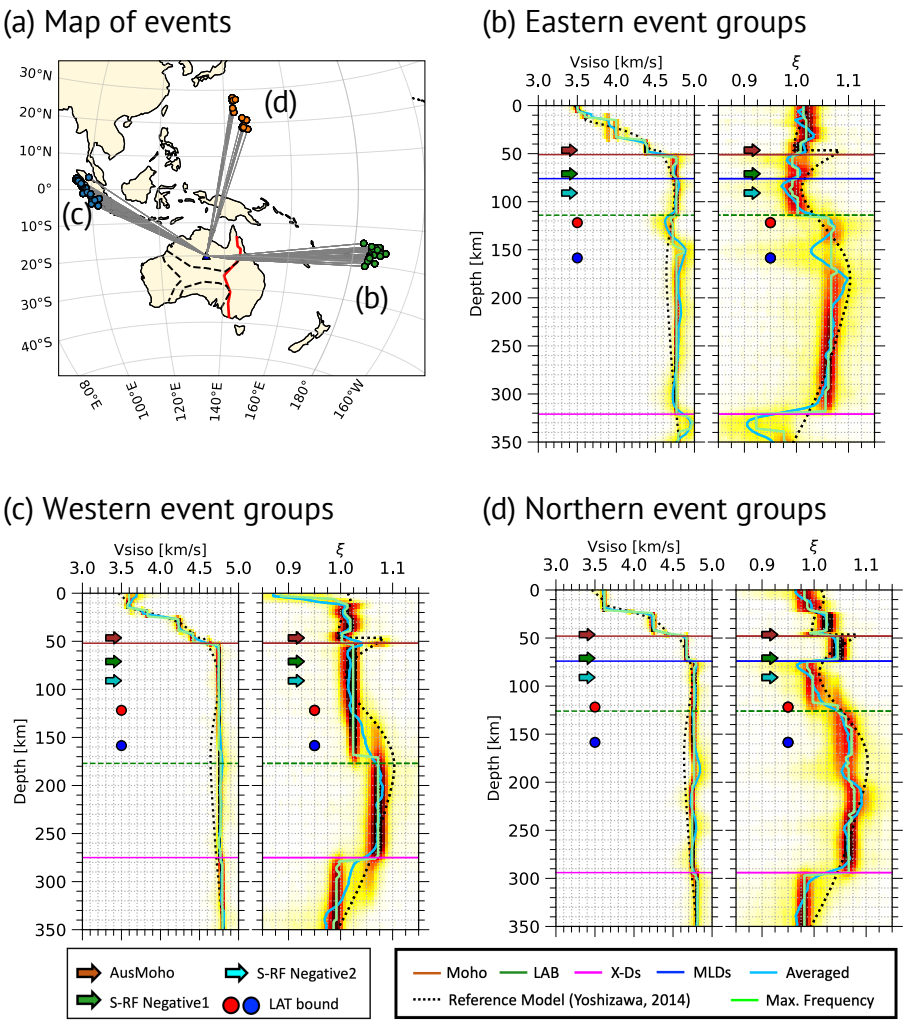

Figure 3.8: Same as Figure 3.5, but for II.WRAB. The horizontal green dashed lines represent the estimated base of the lithosphere (relevant to LAB but identified based on radial anisotropy).

2013), anomalous radial anisotropy with $V_{SH} > V_{SV}$ (Yoshizawa, 2014; Yoshizawa & Kennett, 2015) and the alignment of azimuthal anisotropy with plate motion direction (e.g., Simons et al., 2002; Fishwick et al., 2008; de Laat et al., 2023) suggest that the horizontal shear flow in the ductile asthenosphere drives the fast motion of the Australian plate. Thus, defining the lithosphere base via radial anisotropy can be a reasonable criterion.

The estimated lithosphere base from the increased radial anisotropy for WRAB varies with the incoming P-wave directions: the western path indicates a thicker lithosphere of about 180 km, while the northern and eastern paths show a thinner lithosphere of about 120–130 km. X-Ds are detected at around 300 km, at which radial anisotropy is weakened and approaches isotropy (SH $\approx$ SV). In the lithospheric depth, we can identify minor S-wave velocity changes at 70-80 km depth in the northern and eastern paths, equivalent to MLD depths inferred from S-RFs (Birkey et al., 2021). However, our models show a positive velocity jump with decreasing anisotropy, contrasting with earlier MLD observations from S-RFs (Ford et al., 2010; Birkey et al., 2021).

3.5 Localized conversion point maps

After gathering Ps conversion depths for each discontinuity in the 1-D profiles, we created conversion point (CP) maps to visualize lateral variations of Ps-conversion depths around each station, representing the spatial distribution of seismic discontinuity. This approach is similar to Ford et al. (2010) with S-RFs, in which S-to-P conversion points tend to be distant from the station ($\approx$ 250–350 km at 200 km depth). Our P-RF datasets provide the P-to-S conversion points within 100–150 km around the station, enabling more localized mapping of each discontinuity.

To estimate CP maps, at first, we constructed a local reference 1-D shear velocity model for each station from the average of the mode (maximum frequency) models for azimuth-dependent 1-D S-wave profiles (e.g., green lines in Figures 3.5, 3.6, 3.7 and 3.8). The P-wave structure is derived from the scaling of the S-wave based on AK135 (Kennett et al., 1995) as in the inversion. Then, the local 1-D reference model is used to compute ray paths to estimate the lateral locations of the Ps conversion points for

the azimuth-dependent boundary depths explained in the previous section. To quantify the uncertainties of our depth estimations, we employed interquartile ranges (IQR) for each discontinuity depth from the ensemble solutions, as the resultant probabilistic densities do not always follow the Gaussian distribution.

Resultant CP maps and their depth uncertainties are shown in Figure 3.9 and 3.10 for two Phanerozoic stations and Figures 3.11 and 3.12 for three cratonic stations, including Moho, MLDs, LAB, and X-Ds. In this section, we investigate the spatial distribution of seismic discontinuities around each station based on these CP maps.

3.5.1 Phanerozoic eastern Australia

Figure 3.9 and 3.10 show CP maps and uncertainties (derived from IQR) for the Moho, LAB, and X-Ds around CTAO and CAN stations. Due to the limitations of event distributions, southern areas for both stations are unsampled, so we focus on the northwestern, northern, and eastern CPs. The IQR for the Moho are small ($\approx$ 3 km), while those for deeper interfaces are relatively large ($\approx$ 10 km).

3.5.1.1 Moho, LAB, and X-Ds in eastern Australia

For the Moho, CP depths (left panels in Figure 3.9) exhibit almost no significant azimuthal dependence at both stations, suggesting a nearly consistent crustal thickness. Around CAN, our results reflect somewhat shallower northern Moho depths, aligning with Kennett et al. (2023). Similarly, CTAO shows a nearly constant Moho depth at around 40 km.

In contrast, the CP maps of the LAB (middle panels in Figure 3.9) reveal distinct images for each station, consistent with inversion results (Figures 3.5 and 3.6). At CTAO, LAB depths increase from east to west, with the depth ranging from 70 km to 120–130 km, supporting a stepwise lithospheric thickening at the eastern continental margin (Fishwick et al., 2008) and the rapid deepening of the LAT upper bound to the northwest of CTAO (Yoshizawa, 2014). At CAN, however, the LAB depth remains consistent at 65–80 km, suggesting stable lithospheric thickness to the north, as seen in previous models (Fishwick et al., 2008). Also, S-wave reductions are more pronounced at CAN, as observed in the tomography model by Yoshizawa (2014).

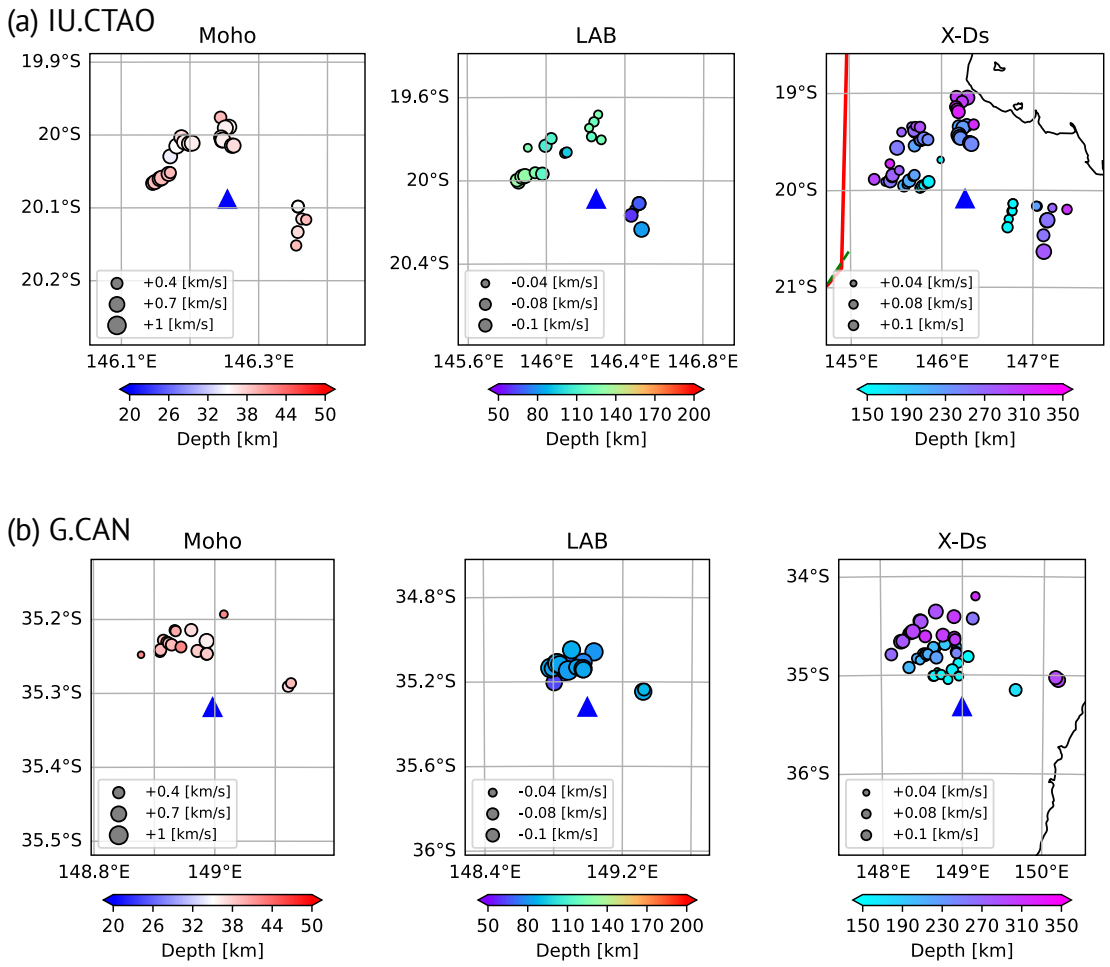

Figure 3.9: Conversion points (CPs) maps for Moho, LAB, and X-Ds at two stations in eastern Australia: (a) IU.CTAO and (b) G.CAN. For each station, the CP maps for Moho, LAB, and X-Ds are shown from left to right. A red line in the rightmost panel of (a) indicates the Tasman line. Blue triangles on all maps represent the station locations. Circles indicate the inferred Ps conversion locations, with color and size representing the depth and magnitude of the shear wave velocity across the interface.

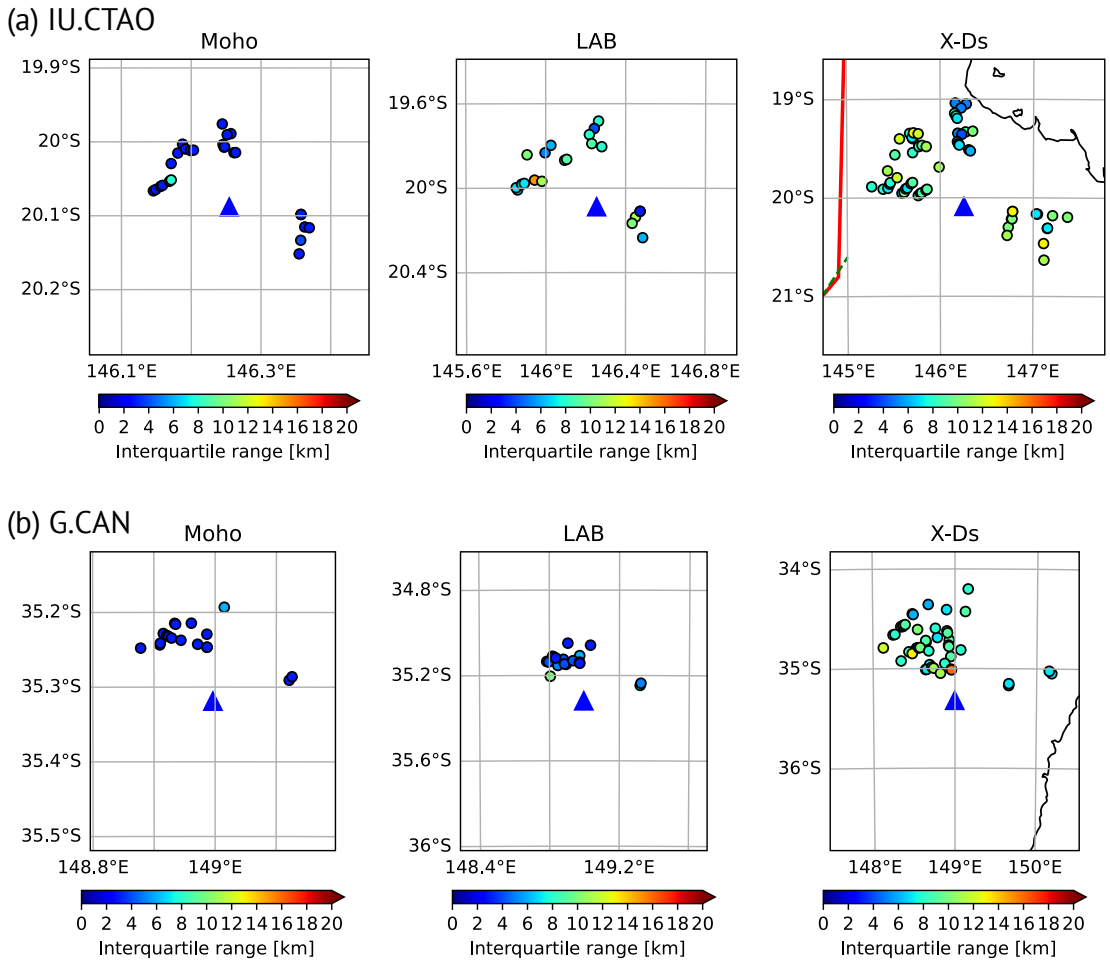

Figure 3.10: Uncertainties of conversion depths for Moho, LAB, and X-Ds: (a) IU.CTAO and (b) G.CAN. Circles are the location of conversion points, with colors indicating the interquartile ranges (IQR).

The CP maps of X-Ds (right panels in Figure 3.9) indicate multiple interfaces with positive shear wave speed jumps clustered around 170 km, 250 km, and 310 km. The shear wave speed changes across these interfaces are smaller than those across the LAB, likely undetectable by long-wavelength surface waves only. In the similar depth ranges, Taira & Yoshizawa (2020) identified two interfaces at 230–240 km and 300–310 km, and Revenaugh & Jordan (1991) also detected two interfaces at 180–220 km (the Lehmann discontinuity) and around 330 km (X-D), although our CP maps for X-Ds suggest three or four distinct interfaces beneath the LAB.

3.5.2 Cratonic central and western Australia

Figure 3.11 displays CPs from the Moho, MLDs, LAB (or lithospheric base), and X-Ds at MBWA, NWAO, and WRAB stations, and Figure 3.12 shows the uncertainties of discontinuity depths based on IQR. Note that, unlike Figure 3.9 for stations in eastern Australia, where MLD is generally unclear, we add the MLD's CP map in Figure 3.11 in the mid-left panels, with circles and crosses indicating negative and positive S-wave speed changes, respectively. For WRAB, the mid-right panel represents the lithospheric thickness estimated from radial anisotropy as described in Section 3.4.2.2.

Except for the lithospheric base beneath WRAB, Figure 3.12 indicates that the IQRs for the upper mantle discontinuities (MLD, LAB, and X-Ds) are generally around 10–15 km, which are greater than those in the eastern Phanerozoic area (Figure 3.10). Larger uncertainties in the LAB depth possibly reflect the smooth transition from the lithosphere to the asthenosphere under the cratonic areas (e.g., Yoshizawa, 2014). Besides, the lithospheric base under WRAB shows larger IQRs than the other two cratonic stations, MBWA and NWAO (Figure 3.12). These results are expected from the somewhat ambiguous definition of the lithospheric base using radial anisotropy since the horizontally polarized S velocity (V_{SH}) cannot be constrained by the receiver functions used in this study.

3.5.2.1 Moho, LAB, and X-Ds in cratonic regions

For the Moho, CP maps at MBWA and NWAO are almost azimuth-independent, but WRAB shows varying depths of about 10 km between the north and east (leftmost

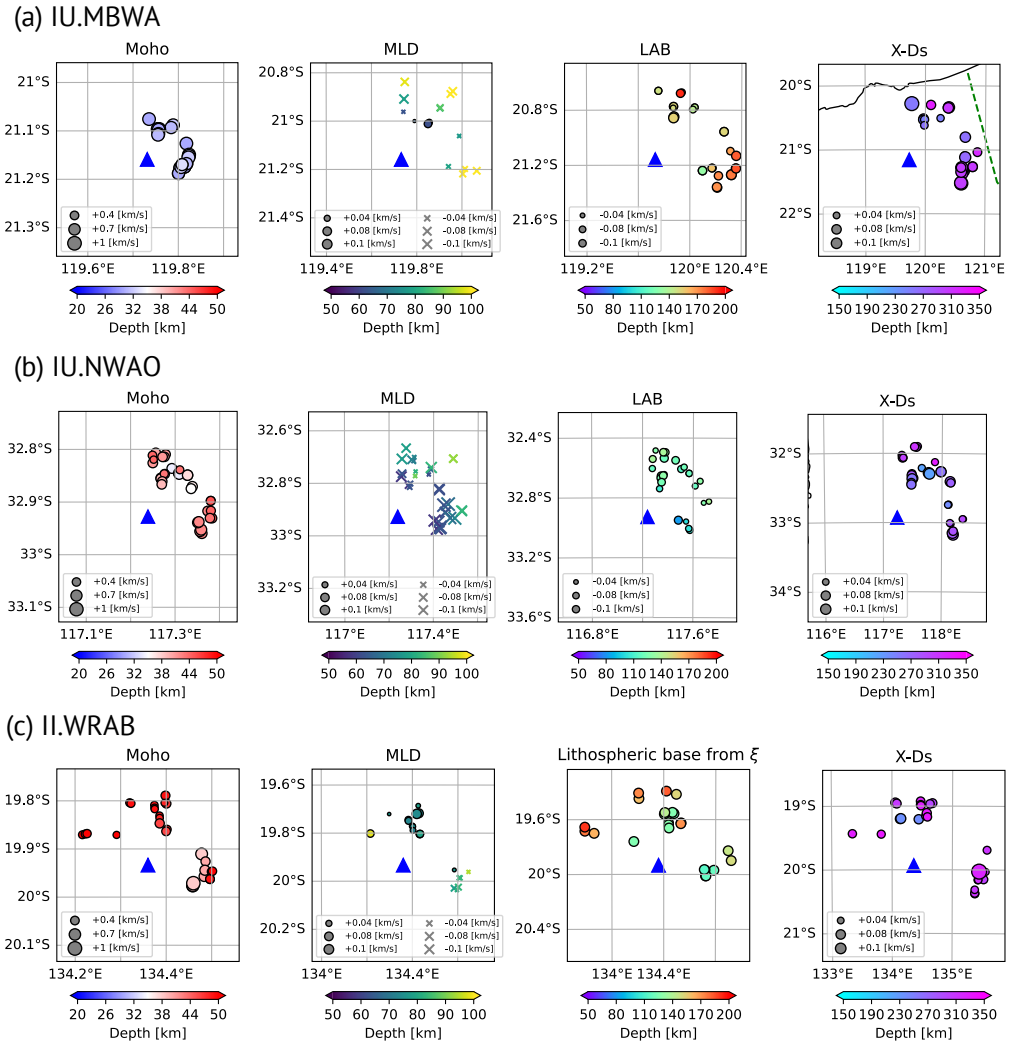

Figure 3.11: Same as Figure 3.9, but for three cratonic stations where MLDs have been observed: (a) IU.MBWA, (b) IU.NWAO, and (c) II.WRAB. CP maps for MLDs are added to the mid-left panel in all stations. Note that the mid-right panel for (c) II.WRAB represents the lithospheric base derived from an increase of radial anisotropy ξ, for which the circle sizes are constant, unlike other panels. The mid-left panel displays the CPs for MLDs, with circles and crosses indicating negative and positive changes in shear velocity, respectively.

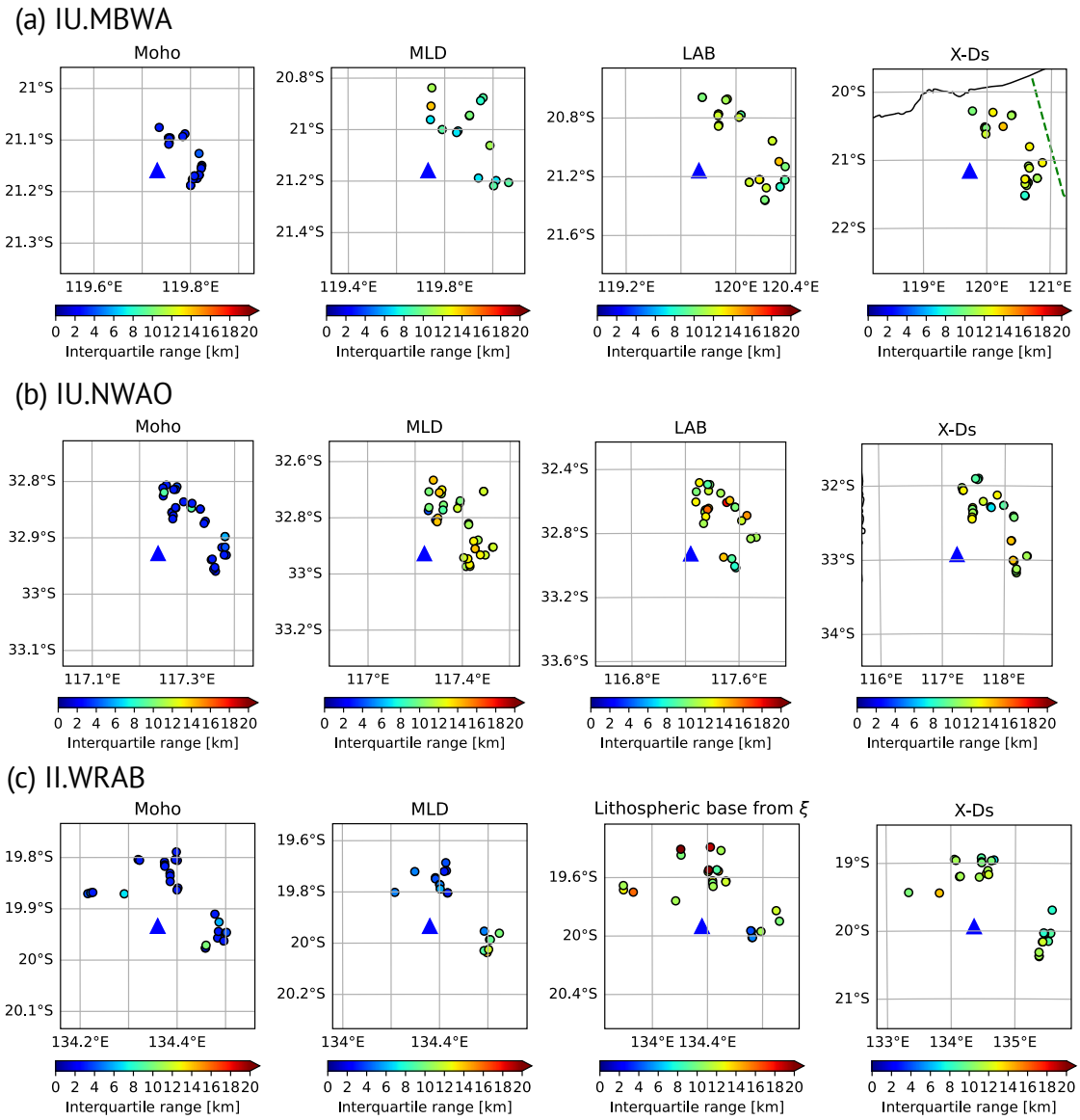

Figure 3.12: Same as Figure 3.10 (depth uncertainties from IQR), but for (a) IU.MBWA, (b) IU.NWAO, and (c) II.WRAB stations.

panels in Figure 3.11 (a-c)). This variation, also seen in array-based P-RF studies (Sippl, 2016) and in our P-RF data (Figures 3.3 and B.7), suggests changes in Moho geometry around WRAB.

The LAB/lithosphere base shows clear azimuthal trends, especially at MBWA and WRAB. At MBWA, the LAB deepens westward from 140–150 km to 170 km depth, possibly reflecting the structural transition near the tectonic margin between the Pilbara craton and the suture zone. At NWAO, the LAB appears to deepen slightly from the south (100–110 km) to the north (130 km), consistent with previous models (Kennett et al., 2013; Yoshizawa, 2014; Magrini et al., 2023). Comparing the two stations in the WAC, the velocity change at MBWA is likely more pronounced than at NWAO (Figure 3.11 (a, b)). For WRAB, where lithospheric base depths are inferred from radial anisotropy, the lithospheric thickness varies from 120-140 km in the southeast to about 180 km in the northwest (Figure 3.11 (c)), consistent with the LAB model from fundamental-mode surface waves (Magrini et al., 2023). The upper limit of the LAT derived from the multimode surface waves (Yoshizawa, 2014) indicate that WRAB is located at the transition between the shallow and deep LAT regions. Our results may reflect such lateral heterogeneity in the upper mantle structure.

The CP maps for X-Ds, associated with positive velocity changes and weaker radial anisotropy, show less azimuthal dependence than the LAB or the lithospheric base at all three stations (right panels in Figure 3.11). While we did not detect localized X-D variations, CP depths indicate two distinct depths for each station: 260 km and 300–310 km for MBWA, 220 km and 270–290 km for NWAO, and 240 km and 320 km for WRAB. The shallower depth at MBWA is equivalent to the Lehmann discontinuity identified by Taira & Yoshizawa (2020), though we did not observe an interface at 200 km as reported by Drummond et al. (1982). Besides, the deeper interface at 300 km has not been reported previously. At NWAO, the deeper depth matches observations in Revenaugh & Jordan (1991), while the shallower one has not been reported. For WRAB, our CP map for X-Ds cluster below 300 km depths, with a previously unreported discontinuity around 230–240 km (Figure 3.11 (c)). Earlier studies using P-wave amplitudes and travel times (Hales et al., 1980; Leven, 1985) also suggested discontinuities around 200 km and 325 km beneath the NAC. Some of our X-Ds are consistent with these

earlier findings, suggesting multiple interfaces are present. Extended spatial mapping with more stations will be essential for further investigating the X-Ds (or Lehmann discontinuity).

3.5.2.2 MLDs in cratonic regions

The CPs of MLDs beneath MBWA and NWAO show shear wave speed reductions at multiple depths within the lithosphere (Figure 3.11), consistent with earlier studies (Ford et al., 2010; Sun et al., 2018; Taira & Yoshizawa, 2020; Birkey et al., 2021). At MBWA, smaller samples show the shear wave speed jumps at 60 km, possibly related to shallower positive S-RF phases indicated by Birkey et al. (2021).

On the contrary, MLDs at WRAB exhibit unique characteristics (mid-left panel in Figure 3.11 (c)). In the east, shear wave speed reductions at 80–90 km are consistent with negative MLDs detected in S-RF and joint inversion studies (Ford et al., 2010; Birkey et al., 2021; Taira & Yoshizawa, 2020). The earlier inversion study by Taira & Yoshizawa (2020) mainly used events from the Tonga-Kermadec Trench, detecting the negative MLDs at 80 km, which matches our results in the east of WRAB. In the north, however, we observe increased S-wave speeds at 70–80 km, aligning with classical studies that detected a positive velocity step at around 75 km in the NAC using the events from the Banda Sea, equivalent to the Hales discontinuity (Hales et al., 1980). This contrasts with negative MLDs found in S-RFs for the northern piercing points (Ford et al., 2010), possibly due to the intrinsic differences between P-RFs and S-RFs, such as conversion points, incident angles, and wavelength.

An alternative explanation may involve vertical variations in azimuthal anisotropy. Selway et al. (2015) suggested MLDs in RFs could result from azimuthal anisotropic layering through simple forward modeling of RFs. Similarly, Chen et al. (2021b) and Birkey & Ford (2023) discussed the link between the depths of MLDs and vertical changes in azimuthal anisotropy, using azimuth-dependent radial and transverse P-RFs in Australian cratons. Around WRAB, layered azimuthal anisotropy has been imaged by surface wave tomography (Simons et al., 2002; Debayle et al., 2005; de Laat et al., 2023). Incorporating azimuthal anisotropy in our joint inversion methods of P-RFs and SWDs will provide additional constraints on the nature of MLDs, though

it is beyond the scope of the current study.

Although our dataset does not involve azimuthal anisotropy, it includes multimode Love and Rayleigh wave dispersions in addition to P-RFs, allowing us to analyze radial anisotropy across MLDs. Yoshizawa & Kennett (2015) compared their radially anisotropic S-wave model derived from the multimode SWDs and S-RFs by Ford et al. (2010), suggesting that the MLDs may be linked to the vertical changes (weakening) of radial anisotropy. Subsequent studies proposed that MLDs may involve multiple interfaces (Sun et al., 2018; Taira & Yoshizawa, 2020; Chen et al., 2021b; Birkey et al., 2021), though the relationship between MLDs and radial anisotropy ξ remains unclear.

To investigate this point, we examined the vertical gradient signs of ξ across MLDs in Figure 3.13, excluding CPs with change smaller than 1 %. The resultant CP maps in (Figure 3.13) reveal distinct patterns by station. At MBWA, shallower MLDs show a decrease in ξ, while deeper interfaces indicate increasing anisotropy (Figure 3.13 (a)). At NWAO, shallow eastern MLDs ($\approx$ 60 km) show increasing ξ, while deeper MLDs (70–80 km) show a decrease (Figure 3.13 (b)). At WRAB, azimuthal dependency aligns with S-wave speed changes (Figure 3.13 (c)): positive speed changes coincide with weakened radial anisotropy and vice versa. Although the localized CPs do not fully clarify the nature of multiple MLDs, these new findings may contribute to understanding the origins of MLDs.

3.6 Discussion

To validate our approach of estimating localized conversion depths using azimuth-dependent radial P-RFs, we plot the estimated conversion points at CTAO, CAN, and WRAB on the E-W cross sections of the tomography model from Yoshizawa (2014) in Figure 3.14. Since the employed events are mostly distributed in a limited range from the northwest to the east of Australia, we lack CP samples in the south of all stations. We selected three stations (CTAO, CAN, and WRAB), for which nearly 180° in back-azimuth is covered, excluding MBWA and NWAO to avoid biases due to very limited azimuthal coverage (about 90°).

Figure 3.14 compares our estimated CPs for MLDs, LAB, and X-Ds with the surface-wave tomography models (Yoshizawa, 2014) with depth uncertainties estimated

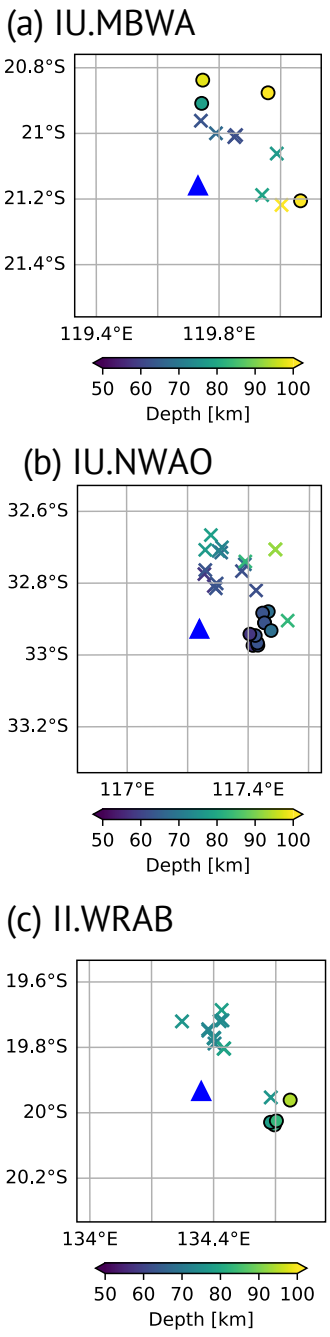

Figure 3.13: The vertical change in radial anisotropy (> 1%) across the MLDs at (a) IU.MBWA, (b) IU.NWAO, and (c) II.WRAB. Blue triangles represent station locations. Colored symbols denote the conversion points, with color indicating depth. Circles and crosses denote positive and negative changes in radial anisotropy ξ with depth, respectively.

from the IQRs for each discontinuity. Projected conversion points (CPs) are located within 70 km of each station. The background contours display isotropic S-wave speed in the top panels and radial anisotropy in the bottom.

The LAB (or the lithospheric base) CPs are located at the transition to a relatively lower-velocity zone, particularly evident at CTAO and CAN (Figure 3.14). Beneath CTAO, our estimates closely match the lateral change in the low-velocity zone. For WRAB, the lithospheric base is situated within a low-velocity zone relative to the surrounding area, supporting our definition based on radial anisotropy can be reasonable in the southern NAC. These LAB CP depths generally align with the regions of intense radial anisotropy, reflecting the asthenospheric shear flow. Thus, our local CP maps effectively capture the lateral variations of lithospheric thickness.

The X-D CPs, associated with S-wave velocity increases, coincide with weakened radial anisotropy, which is consistent with characteristics of the Lehmann discontinuity (L-D) as previously described (e.g., Gaherty & Jordan, 1995; Thybo, 2006; Calò et al., 2016; Taira & Yoshizawa, 2020), suggesting a transition from dislocation to diffusion creep across the L-D (Karato, 1992). Although our CPs for X-Ds are observed at multiple depths with varied agreement to previous studies, they likely correspond to the L-D as the base of the anisotropic layer (Gaherty & Jordan, 1995; Karato, 1992). Furthermore, our detected X-D depths form some clusters at specific depths, consistent with earlier studies (Hales et al., 1980; Leven, 1985; Revenaugh & Jordan, 1991; Taira & Yoshizawa, 2020), suggesting multiple interfaces below the LAB. These CPs contribute to understanding large-scale X-D distributions, which could further illuminate the origins of these interfaces when combined with other geophysical insights, such as the phase transitions of constituent minerals.

In Figure 3.14 (c) at WRAB, MLDs are observed at multiple depths from 60–90 km, where the S-wave velocity is notably high ($\approx$ 4.75 km/s), with weak velocity changes in the uppermost mantle beneath the station. The tomographic S-wave model in Figure 3.14 (c) shows a positive velocity gradient in these depths, matching the MLDs north of WRAB (around 70 km depth), characterized by positive velocity jumps in our observation (Figure 3.11 (c)). In contrast, the MLDs east of WRAB (around 80 km depth) appear near a relatively lower-velocity zone extending to the LAT, likely

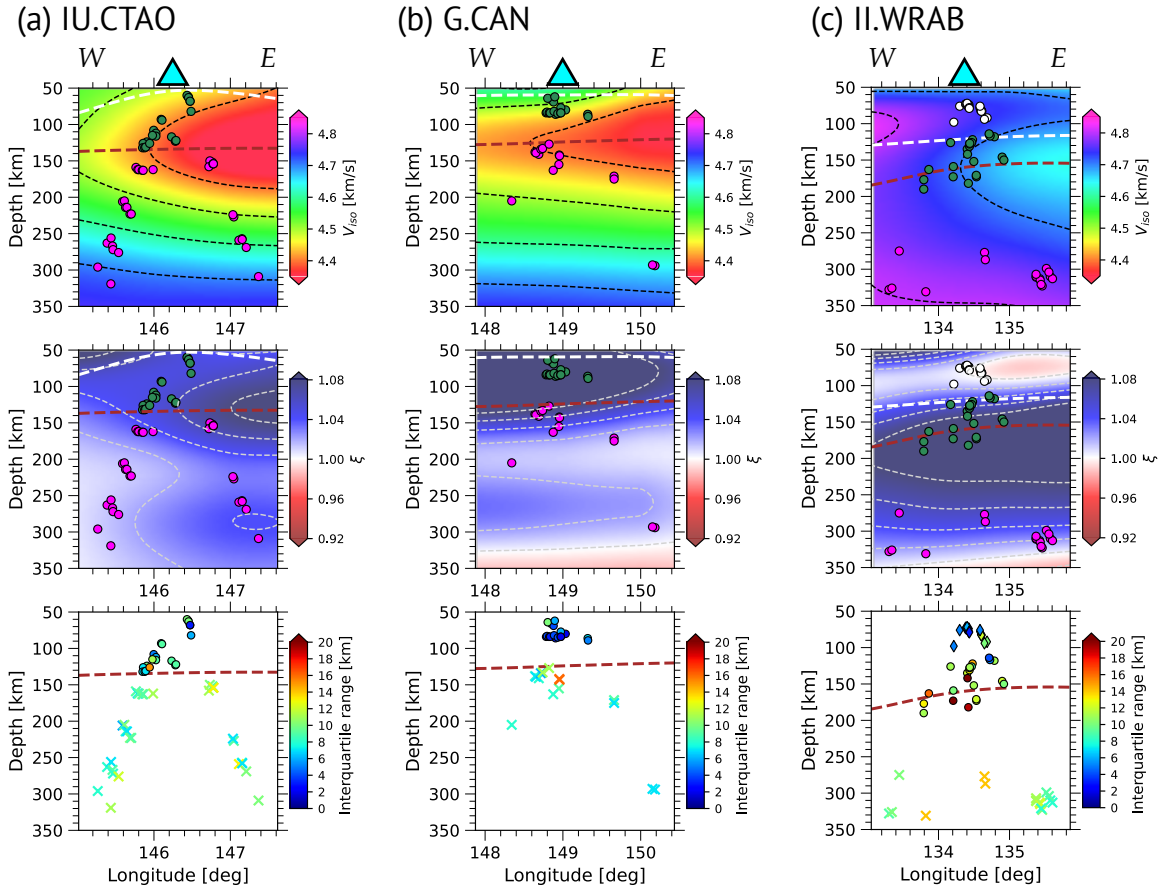

Figure 3.14: Comparison of conversion points from this study with E-W cross-section of the isotropic S-wave speed (top panels) and radial anisotropy (middle panels) models by Yoshizawa (2014), and interquartile ranges (bottom panels): (a) IU.CTAO, (b) G.CAN, and (c) II.WRAB. Cyan triangles show station locations. White and red thick dashed lines indicate the upper and lower bounds of the LAT (Yoshizawa, 2014). Black and white thin dashed lines represent shear wave speed contours of 0.1 km/s and the radial anisotropy of 0.04. White, green, and magenta dots denote conversion points for the MLDs, lithospheric base, and X-Ds, respectively. Circles, crosses, and diamonds in the bottom panels represent IQR-based uncertainties for the LAB (or lithospheric base), X-Ds, and MLDs, respectively.

corresponding to negative S-RF peaks.

Some earlier S-RF studies have suggested negative peaks at MLD depths (Birkey et al., 2021), suggesting shear velocity reduction, where positive velocity jumps are detected in the north of WARB in our study. One possible explanation is the influence of azimuthal anisotropy, which our current study did not consider but can be a topic of future work. In addition, MLDs identified in both S-RF studies and our model may be related to reductions in radial anisotropy within the lithosphere (Figures 3.13 and 3.14; Yoshizawa & Kennett, 2015; Taira & Yoshizawa, 2020). Recent azimuthal anisotropy model also indicates rapid fast-axis changes at the MLD depths (de Laat et al., 2023), suggesting that some MLDs may reflect changes in anisotropic properties, which can also be evident from the azimuth-dependent transverse P-RFs (Birkey & Ford, 2023).

Moreover, the MLD characteristics appear to vary by tectonic province, likely due to distinct ancient tectonic events in each craton. Applying our joint inversion approach to more stations across Australia will allow us to better map MLD distribution and elastic properties, providing further insights into these regional differences.

3.7 Conclusions

In this study, we introduced a new approach using azimuth-dependent P-wave receiver functions (P-RFs) in the framework of joint Bayesian inversions with multimode surface wave data. Azimuthal variations in P-RFs generally indicate lateral changes in seismic interfaces or anisotropic layering beneath a station. Based on the posterior of local 1-D profiles, we estimated the major seismic interfaces in the upper mantle, which led to the construction of conversion point maps for each discontinuity.

Through analysis of five permanent stations, we identified some notable characteristics of upper mantle discontinuities beneath Australia, which can be summarized as follows:

1. Beneath CTAO in northeastern Australia, the lithosphere-asthenosphere boundary (LAB) deepens sharply from ∼70 km in the east to 120-130 km toward the west and north. In contrast, the LAB under CAN is nearly flat at ∼80 km.

2. In the stable craton of western Australia, the LAB depth varies laterally, though

more gradually than in the eastern Phanerozoic region.

3. Australian X-discontinuities (X-Ds) beneath the LAB appear at three to four distinct depths, indicating multiple interfaces with weakened radial anisotropy.

4. MLDs consist of multiple interfaces at varying lithospheric depths, with different elastic properties by location. In particular, MLDs beneath WRAB include shallower positive discontinuities previously unreported in Australian S-RF studies.

Due to the limitations of our data set to five permanent stations, the spatial distributions of upper mantle discontinuities remain unconstrained. In the next chapter, we incorporate all the available permanent and temporary stations across Australia to construct a comprehensive map of the lithosphere, MLDs, and X-discontinuities beneath the LAB using our approach proposed in this study. This mapping will clarify continental-wide distributions and the seismological nature of each discontinuity, deepening our understanding of Australia's ancient and present tectonics.

Chapter 4

Mapping upper mantle discontinuities beneath the Australian continent using multi-mode surface waves and receiver functions

4.1 Introduction

Continental upper mantle discontinuities provide keys to unravel Earth's tectonic history and present-day mantle dynamics. Surface-wave tomography has been a particularly powerful tool for reconstructing large-scale seismic images of the upper mantle, enhancing our understanding of the lithosphere and asthenosphere systems in both continental and oceanic regions, which are closely linked to the forces driving plate motions (e.g., Yoshizawa, 2014; Isse et al., 2019; Yoshida & Yoshizawa, 2020). In addition, the receiver function method, which is effective in detecting seismic discontinuities beneath seismic stations, has recently revealed the enigmatic mid-lithospheric discontinuity (MLD) beneath the cratonic lithosphere, along with the lithosphere-asthenosphere boundary (LAB) (e.g., Rychert & Shearer, 2009; Liu et al., 2020; Kind et al., 2020). The MLD may reflect the ancient evolutionary process of stable cratonic regions, while the LAB may be affected by the present-day plate motion and mantle flow. Therefore, it is essential to simultaneously capture the distributions and characteristics of both the MLD and LAB.

The upper mantle discontinuities beneath Australia provide critical insights into the formation and deformation of the continental lithosphere over Earth's history. The Australian continent was assembled during the mid-Proterozoic (1300–1000 Ma) through the amalgamation of three cratonic blocks: the West, North, and South Australian Cratons (Figure 4.1). A suture zone exists between the three cratonic blocks, which

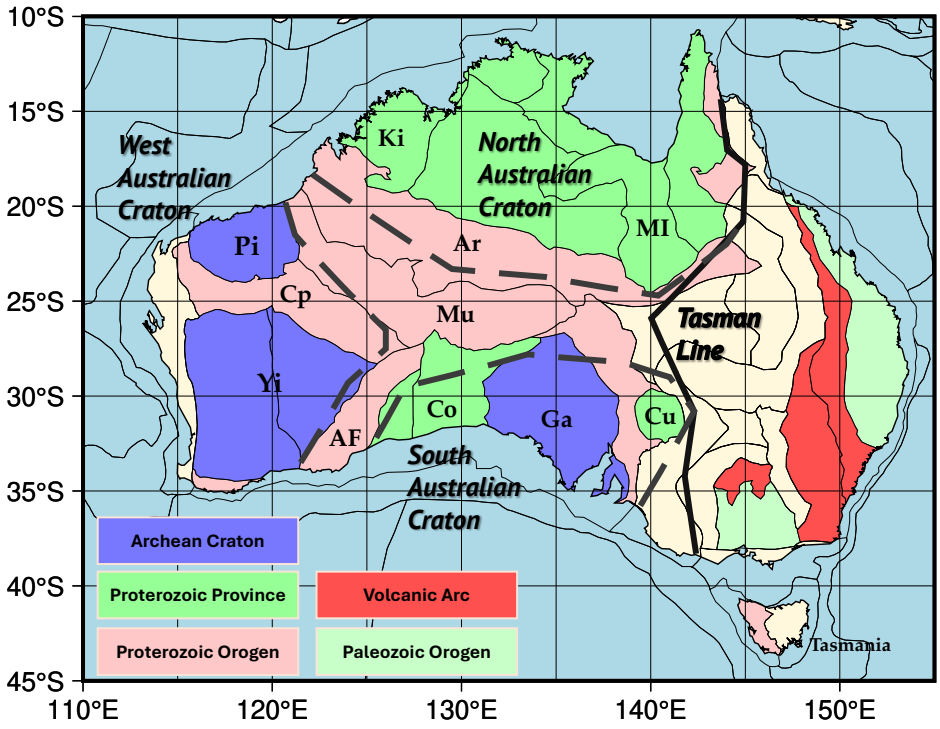

Figure 4.1: A tectonic map of the Australian Continent. Black solid and dashed lines delineate the boundaries of the major cratonic blocks (West, North, and South Australian Cratons) and the Tasman line. The boundaries of tectonic provinces are adapted from Hasterok et al. (2022) to reflect the local geological setting. The map highlights major tectonic provinces, including AF (Albany-Fraser belt), Ar (Arunta block), Co (Coompuna Province), Cp (Capricorn Orogeny), Cu (Curunamoa Craton), Ga (Gawler Craton), Ki (Kimberley Block), MI (Mount Isa Block), Mu (Musgrave Block), Pi (Pilbara Craton), and Yi (Yilgarn Craton).

underwent multiple orogenic events, culminating in the Alice-Springs Orogeny ($\sim$ 400 Ma). The present Australian continent is characterized by western and central cratonic areas juxtaposed with the eastern Phanerozoic orogenic zone (Figure 4.1). Investigating the upper mantle discontinuities across Australia offers valuable insights into the evolutionary process shaping the continent.

4.1.1 Australian upper mantle discontinuities

The upper mantle discontinuities beneath Australia, including the Lithosphere-Asthenosphere Boundary (LAB), have been extensively investigated through various seismological and petrological approaches over the past several decades (e.g., Hales et al., 1980; Revenaugh & Jordan, 1991; Fishwick et al., 2008; Ford et al., 2010; Chen et al., 2021b; Sudholz et al., 2024). Owing to the continuous efforts in expanding broadband seismic networks across the continent, including permanent and temporary stations (e.g., Rawlinson & Kennet, 2008; van der Hilst & Kennett, 1993), a number of 3-D shear velocity models have been proposed primarily based on surface wave tomography, providing clues of the Australian lithosphere-asthenosphere system (e.g., Fishwick et al., 2008; Kennett et al., 2013; Yoshizawa, 2014; Magrini et al., 2023). These studies reveal that the Australian LAB rapidly deepens from the eastern orogenic zone (50–100 km depth) to the cratonic areas in central and western Australia (around 120–200 km depth). However, surface waves are inherently less sensitive to sharp structural changes due to their long wavelengths, resulting in limited vertical resolution. In contrast, receiver functions (RFs) are highly sensitive to the impedance contrast across seismic discontinuities, and have been used to investigate the Australian upper mantle discontinuities (Ford et al., 2010; Birkey et al., 2021; Chen et al., 2021b). Despite these efforts, the sparse distribution of permanent broadband stations (Figure 4.2 (a)) has hindered constraining the spatial distribution of seismic discontinuities beneath the Australian upper mantle.

Within the lithospheric depth, potentially sharp negative velocity jumps at multiple depths in cratonic areas have been observed in recent studies using S-wave receiver functions (S-RFs) (e.g., Ford et al., 2010; Birkey et al., 2021), although such depths are generally characterized by high-velocity anomaly in surface wave tomography. These

enigmatic mid-lithospheric discontinuities (MLDs) in the Australian lithosphere have also been detected at multiple depths through other seismological approaches (Sun et al., 2018; Kennett & Sippl, 2018; Taira & Yoshizawa, 2020; Chen et al., 2021b), suggesting that S-wave velocity changes across these MLDs do not always appear as negative shifts (e.g., Hales et al., 1980; Taira & Yoshizawa, 2020), which was also discussed in Chapter 3. Moreover, the characteristic properties of radial and/or azimuthal anisotropy may be varying across the MLDs (Yoshizawa & Kennett, 2015; Kennett et al., 2017; Taira & Yoshizawa, 2020; Chen et al., 2021b; Birkey & Ford, 2023). Although the elastic properties of MLDs are essential to understanding their physical nature, there remain many questions, such as the numbers, the spatial distributions, and the style of velocity changes (positive/negative) across the MLDs, and their cause.

In addition to lithospheric interfaces, earlier studies (Hales et al., 1980; Drummond et al., 1982; Leven, 1985) identified deeper interfaces characterized by positive velocity jumps, detected in seismic waveforms recorded in northern and western Australia at depths around 200 and/or 325 km. Revenaugh & Jordan (1991) also suggested that the Australian upper mantle may host multiple discontinuities beneath the LAB. More recent work (Taira & Yoshizawa, 2020) combining P-RFs and surface wave dispersion data detected similar positive interfaces beneath five GSN stations in Australia, suggesting that one of these interfaces may correspond to the Lehmann discontinuity (Lehmann, 1961) and indicate the base of anisotropic layer (i.e., asthenosphere) (Gaherty & Jordan, 1995; Taira & Yoshizawa, 2020). However, the nature and distributions of these enigmatic X-discontinuities beneath LAB remain understood via localized analyses (Gaherty & Jordan, 1995; Taira & Yoshizawa, 2020).

4.1.2 Scope of this chapter

In this chapter, we investigate the spatial distributions of seismic discontinuities in the Australian upper mantle through joint inversions using multimode surface-wave dispersions (SWDs) and P-wave RFs (P-RFs). At first, we estimate a large-scale topography map of the lithospheric base beneath Australia. Conventional LAB models (e.g., Kennett et al., 2013; Birkey et al., 2021) have been retrieved sorely based on

the information derived from either surface waves or receiver functions. Although Taira & Yoshizawa (2020) combined multimode SWDs with P-RFs to tackle the joint inversion analysis through Bayesian inference, their analysis was limited to localized applications. Here, we apply trans-dimensional joint Bayesian inversions to large data sets of broadband permanent and temporary stations across Australia, proposing an updated map of lithospheric thickness.

Additionally, we investigate the distribution and elastic properties of enigmatic MLDs and X-discontinuities (X-Ds). Previous MLD findings (e.g., Hales et al., 1980; Sun et al., 2018; Taira & Yoshizawa, 2020; Birkey et al., 2021) have been challenging to make a unified interpretation of these discontinuities due to inconsistencies in the nature of shear velocity changes and the presence of multiple interfaces. These discontinuities may offer potential insights into the past tectonic processes and present-day mantle dynamics (e.g., Srinu et al., 2021; Hua et al., 2023; Boyce et al., 2024). This study compiles the joint inversion results from numerous broadband stations in Australia to present new seismological evidence for the MLDs and X-Ds along with a revised lithospheric base model, providing a comprehensive discussion of their characteristics and plausible origins.

4.2 Data

This study employs multimode surface wave dispersions (SWDs) of Rayleigh and Love waves, derived from phase speed maps by Yoshizawa (2014), along with P-to-S receiver functions (P-RFs), following the methodology outlined in Chapter 3.

Our objective is to detect and image seismic discontinuities throughout the upper mantle above the mantle transition zone (< 400 km). Taira & Yoshizawa (2020) demonstrated that the multimode SWDs significantly enhance the resolution of deep upper mantle SH-wave structure (i.e., radially anisotropic S-wave structures) since Love wave overtones are particularly sensitive below 200 km (e.g., Yoshizawa & Ekström, 2010). Thus, the use of multimode SWDs is essential for this analysis. Using high-resolution phase speed maps (Yoshizawa, 2014) enables us to explore the relationship between radial anisotropy and upper mantle discontinuities. Examples of multimode phase speed maps of Rayleigh and Love waves are shown in Figure C.1 in Appendix C.

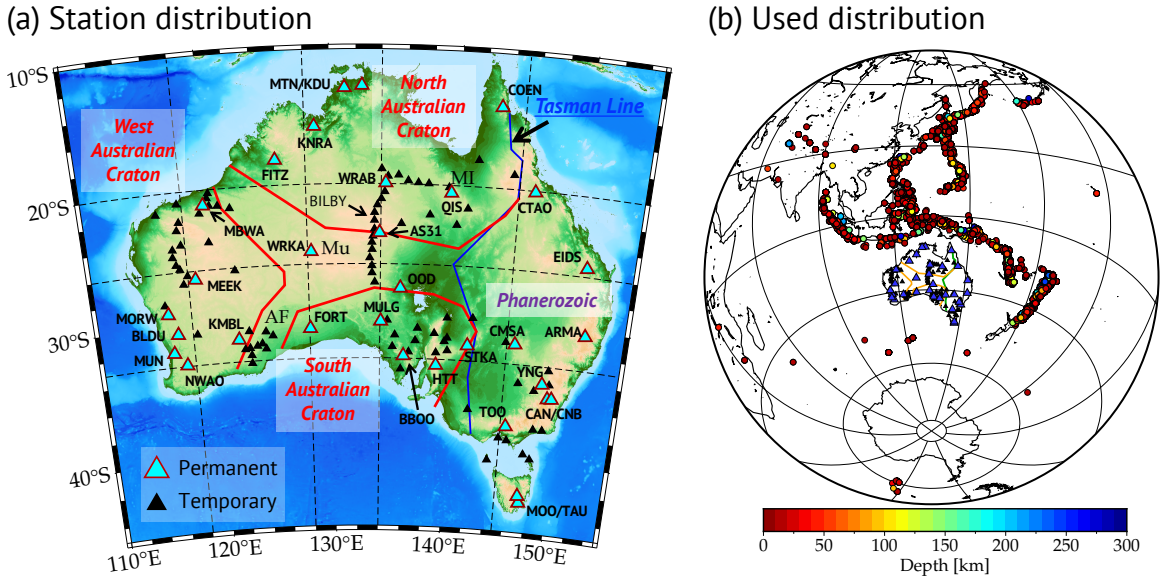

Figure 4.2: (a) Map of the study area showing employed stations. Cyan and black triangles indicate permanent and temporary stations, respectively, with permanent station names labeled. All station names are shown in Figure C.2. Red lines represent the cratonic margins of the North Australian Craton (NAC), the South Australian Craton (SAC), and the West Australian Craton (WAC). The blue line denotes the Tasman Line, the geological boundary between the cratonic and eastern Phanerozoic regions. The Musgrave Province, the Mt. Isa Block, and the Albany-Fraser Belt are labeled as Mu, MI, and AF, respectively. Dashed lines represent cross-section paths shown in Figures 4.5, 4.6, 4.7, C.6, and C.7, along S20°, S26°, S33°, E118°, E128°, E134°, and E145°. (b) Map of event distributions used in receiver function analyses. Blue and black triangles present permanent and temporary stations. Colored circles indicate seismic events, while yellow and green lines are the major tectonic boundaries, the same as (a).

For receiver function analysis, we utilized 32 permanent stations and 86 temporary stations across the Australian continent (Figure 4.2 (a)). For permanent stations, we applied azimuth-dependent P-RFs using the signal-processing approach described in Chapter 3. Although the azimuthal dependence of RFs has been generally neglected in earlier studies of RF inversions (e.g., Calò et al., 2016; Taira & Yoshizawa, 2020), it needs to be treated carefully taking account of lateral variations of the discontinuity depths under the seismic station, as indicated in Chapter 3. Due to the shorter observation periods of temporary stations, we adjusted the data selection criteria accordingly. The employed events are shown in Figure 4.2 (b).

Examples of resultant P-RFs are shown in Figure 4.3, displaying clear azimuthal

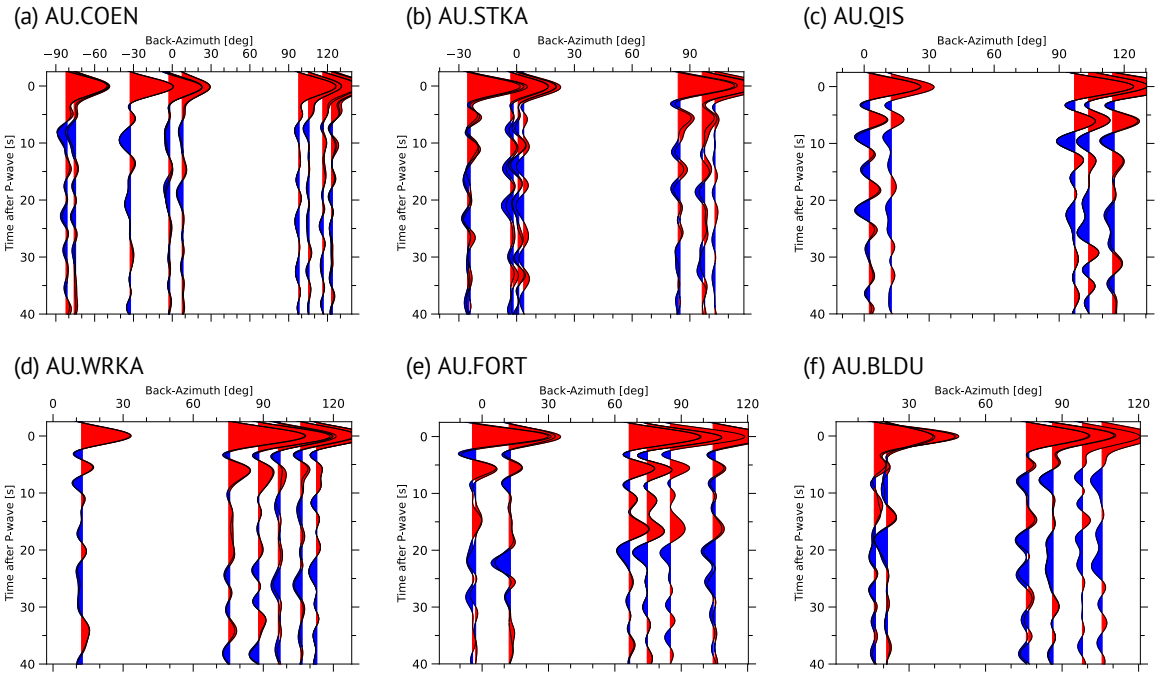

Figure 4.3: Examples of azimuth-dependent P-RFs for six permanent stations: (a) AU.COEN, (b) AU.STKA, (c) AU.QIS, (d) AU.WRKA, (e) AU.FORT, and (f) AU.BLDU. Positive and negative phases in P-RFs are shaded in red and blue, respectively.

dependencies at all stations, especially at COEN (Figure 4.3 (a)), located at the north-eastern tip of the continent (Figure 4.2). Figure C.4 shows shorter-period receiver functions for the same stations as in Figure 4.3, representing the robustness of main signals even in shorter-period ranges despite contamination from multiple reverberations and scattered phases. At FORT (Figure 4.3 (e)), remarkable differences between low- and high-frequency datasets are observed, aligning with previous RF study (Ford et al., 2010). The P-wave reflectivity profile at AU.FORT reveals intense reflection phases from shallower structure (i.e., crust or sediment layer) (Kennett, 2015), with multiples that are weaker in the lower frequency profiles, consistent with our P-RF dataset (Figure 4.3).

In addition to permanent stations, we incorporated temporary stations deployed since 1993, including Skippy (van der Hilst & Kennett, 1993), QUOLL (Kennett et al., 1999), WA Cratons (Kennet, 2000), TASMAL (Kennett, 2003), CARPA-Linkage (Reading & Kennett, 2005), SOC-Southern Craton (Fontaine & Kennet, 2007), BILBY (Rawlinson & Kennet, 2008), Bass Strait (Reading & Rawlinson, 2011), and Albany-

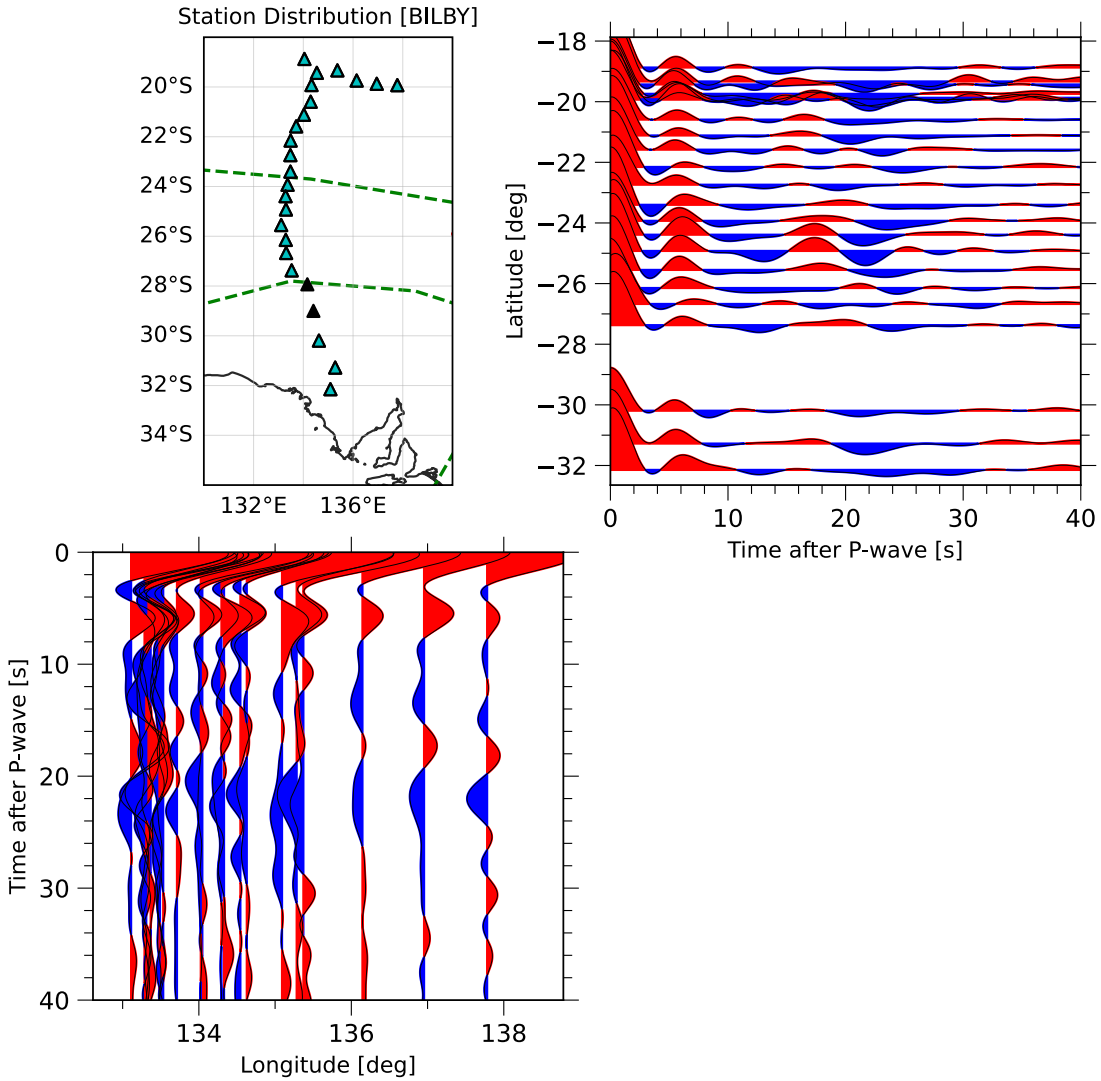

Figure 4.4: Stacked P-RFs observed at the BILBY array (Rawlinson & Kennet, 2008). The top left panel displays a map of the BILBY stations (triangles), with major tectonic boundaries (green dashed lines) of the NAC and SAC. Colored triangles indicate stations that meet the data selection criteria, as described in the main text. The top-right panel represents the Ps receiver functions sorted by latitude, and the bottom panel by longitude.

Fraser Experiment (Tkalčić et al., 2013a). Data processing for temporary stations was nearly identical to that for permanent stations. However, due to the shorter operation periods (1-2 years), we relaxed the criteria on epicentral distance and back-azimuth ranges of seismic events to better detect discontinuity depths. Thresholds for the cross-correlation selection (Tkalčić et al., 2006, 2011) were reduced to 0.7 for 0.03–0.2 Hz and 0.6 for 0.03–0.5 Hz to retain more traces in the stacking process, as visualized in Figure C.5. For continental-scale discontinuity mapping, we applied lower weighting factors to temporary stations than permanent stations.

Figure 4.4 presents the stacked Ps receiver functions obtained from BILBY (Rawlinson & Kennet, 2008). The general P-RF characteristics are similar to Sippl (2016), especially the Moho-converted phases, which appear as positive signals at around 5–6 seconds. Later phases exhibit continuous changes across longitude and latitude, likely reflecting upper mantle heterogeneity. Although local azimuth-dependent variations around individual stations cannot be extracted in temporary stations due to the limitation of the observation period, the temporary stations provide valuable complementary data (locally averaged S-wave model) to supplement the sparse distribution of permanent stations (Figure 4.2).

4.3 Methods for discontinuity detection and mapping

4.3.1 Trans-dimensional Bayesian inversion and discontinuity detections

To jointly invert multimode SWDs and P-RFs, we employed the hierarchical trans-dimensional Bayesian inversion scheme (Bodin et al., 2012; Calò et al., 2016; Taira & Yoshizawa, 2020), following Taira & Yoshizawa (2020) as described in Chapter 3. The Bayesian inference enables us to represent the model parameters as the probability density functions, allowing us to treat the number of parameters and the data uncertainties as unknown parameters in the optimization process, which have generally been predefined as a priori parameters in conventional linearized inversions. This advanced inversion technique has recently been widely used in joint inversions involving multiple datasets (e.g., Kim et al., 2016; Calò et al., 2016; Akuhara et al., 2023). While such trans-dimensional inversion is computationally demanding, we employed the parallel tempering method (Sambridge, 2014) to expedite the convergence of parameter search,

as in Taira & Yoshizawa (2020). Detailed formulations and workflows are described in Bodin et al. (2012), Taira & Yoshizawa (2020), and Chapter 3.

As outlined in Chapter 3, we retrieved radially anisotropic S-wave speed models, including discontinuity depths, using the multimode SWDs and P-RFs. After inversions, we computed isotropic S-wave speed using the Voigt average of the inverted SV and SH velocities, $V_{S_{iso}} = \sqrt{\frac{2V_{SV}^2+V_{SH}^2}{3}}$, and radial anisotropy, $\xi = (\frac{V_{SH}}{V_{SV}})^2$, following Yoshizawa (2014).

Using the radially anisotropic models, at first, we determined the Moho and LAB based on vertical changes in shear wave speed. When a low-velocity zone and/or a shear velocity drop were absent or unclear, we defined the lithospheric base using radial anisotropy (ξ) following Plomerová et al. (2002). In estimating the lithospheric base, we incorporated the Lithosphere-Asthenosphere Transition (LAT) defined by Yoshizawa (2014). The LAT is characterized by the vertical gradient of S-wave velocity from the multimode surface-wave tomography model, with the upper and lower bounds derived from the negative peak of the S-wave gradient and the depth of minimum velocity, respectively, indicating potential lithospheric thickness with a gradual transition from the lithosphere to asthenosphere.

After defining the crust and mantle lithosphere, we identified Mid-Lithospheric Discontinuities (MLDs) within the mantle lithosphere and X-discontinuities (X-Ds) beneath the LAB. The following criteria were used to define these discontinuities:

- Moho: The location of maximum S-wave speed increase around the reference Australian Moho depth (Kennett et al., 2023).

- Lithospheric base: If the S-wave speed is below 4.7 km/s near the LAT, the LAB is marked by a 0.04 km/s S-velocity drop. When the low-velocity zone is unclear (e.g., southern NAC and the suture zone), we used a depth with a rapid increase in radial anisotropy to define the lithospheric base (Plomerová et al., 2002).

- MLDs: Depths with an S-velocity change of over ± 0.02 km/s above the LAB or the upper bound of LAT.

- X-Ds: Positive S-velocity jumps of more than 0.04 km/s below the lithospheric base.

As in Chapter 3, we did not impose any criteria on radial anisotropy when identifying MLD and X-Ds to allow an unbiased analysis of radial anisotropy variations across these discontinuities. After detecting interfaces, we computed azimuth-dependent conversion point depths to map at permanent stations to map lateral changes in the seismic discontinuities around the station.

4.3.2 Regional-scale mapping process of seismic discontinuities

Our azimuth-dependent P-RF analysis for the permanent stations, as described in Chapter 3, allows us to estimate the local lateral variations in seismic discontinuities around each station. However, as our current scope is to map upper mantle discontinuities at a continental scale, we calculate a representative interface depth for each station.

For each permanent station, we computed a weighted average of conversion points based on isotropic S-wave reductions across the LAB, to represent the local LAB depth. If the lithospheric base is defined by radial anisotropy, we take the mean of the selected depths. Similarly, we determined representative Moho depths by weighting based on S-velocity jumps. For temporary stations, discontinuity depths are estimated using the same criteria as described in the previous subsection. For MLDs and X-Ds, we conduct an additional clustering analysis, which will be explained in detail in the next section.

We then compare these estimated conversion point depths with the surface-wave tomography model (Yoshizawa, 2014) in Figure 4.5 and examine azimuthally-averaged posterior distributions and discontinuity depths for permanent stations in Figure 4.6. This approach enables us to effectively capture both the large-scale features of the Australian upper mantle interface and their lateral variations.

4.3.2.1 Conversion points vs. tomography model

Figure 4.5 shows the distribution of conversion points (CPs) overlaid on cross-sectional tomographic models of isotropic S-wave speed and radial anisotropy (Yoshizawa, 2014), with the upper and lower bounds of the LAT (Yoshizawa, 2014) superimposed.

LAB-related CPs are generally distributed in the low-velocity zone and within the LAT, with green and white dots situated between the white and red dashed lines (Figure

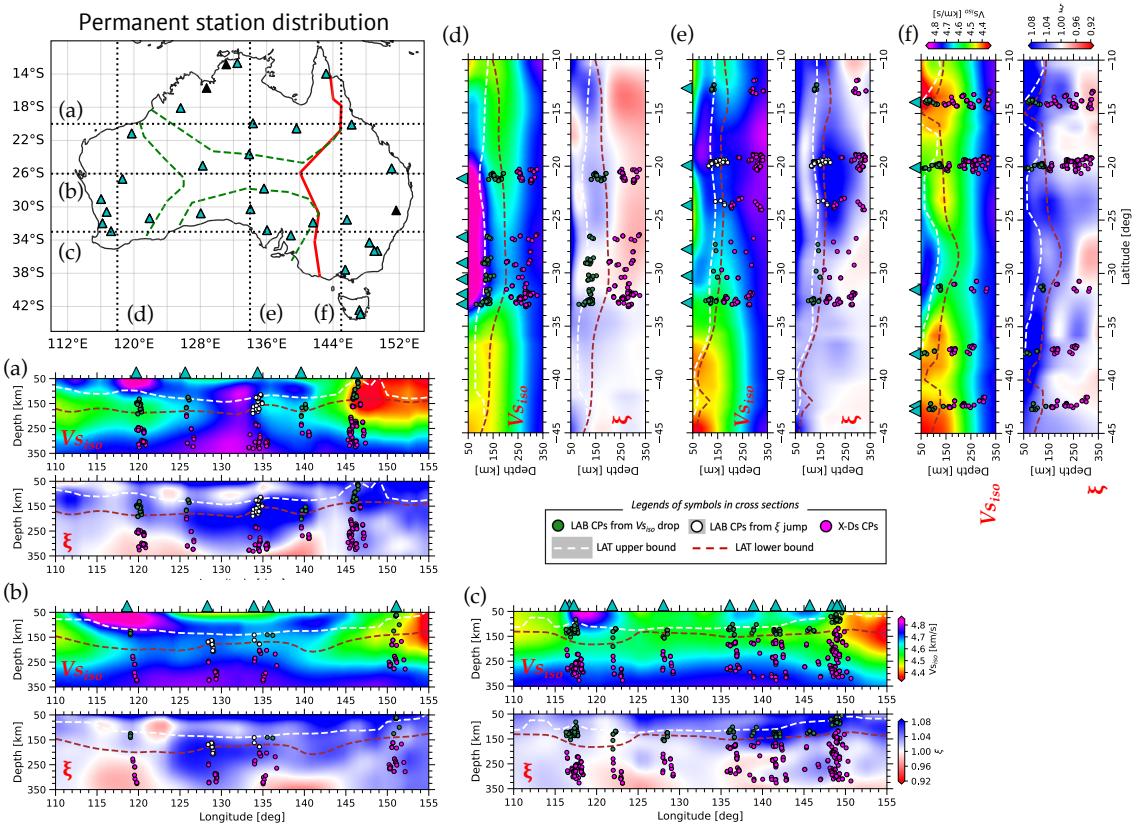

Figure 4.5: Cross-sectional view of conversion points for the LAB and X-Ds. The top-left panel shows the distribution of employed permanent stations (cyan triangles), with major tectonic boundaries and the Tasman Line drawn by green dashed and red solid lines, respectively. (a–c) E-W cross-sections of isotropic S-wave speed and radial anisotropy models reconstructed from multimode surface-wave tomography (Yoshizawa, 2014), with the upper and lower bounds of the LAT indicated by white and red dashed lines. Green and white dots represent LAB (or lithospheric base) conversion depths from individual inversion results, while magenta dots indicate X-Ds conversion points. (d–f) Same as (a–c), but for N-S cross-sections.

4.5). In Phanerozoic eastern Australia and the West Australia Craton (WAC), the LAB CPs correspond to the transition depths between high-speed to the low-velocity zones (Figure 4.5 (a, b, c, d, f)). At these depths, radial anisotropy (ξ) increases gradually, especially in southeastern and northeastern Australia (Figure 4.5 (a, c, f)).

In the southern part of North Australian Craton (NAC) and the suture zone (Figure 4.5 (a, b, e)), although the LAB signature in shear velocity changes are unclear, CPs at the lithospheric base (white dots) align with the depth of relatively lower-velocity anomaly in the tomographic model (Yoshizawa, 2014). Radial anisotropy sharply in-

creases across these CPs, indicating that our definition of the lithospheric base can be a reasonable choice in the lithosphere-asthenosphere system beneath cratonic areas with weak S-velocity drop.

X-D CPs (magenta dots) are scattered at various depths where S-wave velocity increases with depth, forming clusters based on tectonic provinces. Along S33° (Figure 4.5 (c)), from E135° to E150°, three X-D clusters appear at around 140–170 km, 240–260 km, and 280–325 km. At the shallowest depth, radial anisotropy notably decreases, particularly in eastern Australia and the SAC (Figure 4.5 (c)), as also shown in radially anisotropic S-wave velocity profiles (Figure 4.6). Although shallow X-D clusters are absent in some regions, the relationship between X-D CPs and radial anisotropy is observed across other cross-sections, with depth variations depending on the tectonic province.

4.3.2.2 Azimuthally-averaged 1-D radially anisotropic S-wave models

Figures 4.6 and C.6 present azimuthally-averaged posterior densities and estimated Moho and LAB depths for permanent stations within 2° along S33° , S20°, and S26°. Figures 4.7 and C.7 provide similar information for N-S cross-sectional stations along E118°, E128°, E134°, E145°, and E155°. Each radially anisotropic 1-D profile includes boundary estimates from AusMoho (Kennett et al., 2023), LAT (Yoshizawa, 2014), and negative S-RF phases (Birkey et al., 2021). Brown and green horizontal lines indicate the estimated azimuthally-averaged Moho and LAB (or lithospheric base), while the colored bars on the right vertical-axis of each panel exhibit individual discontinuity depths derived from azimuth-dependent 1-D profiles. In this study, we consider the azimuth-averaged 1-D radially anisotropic S-wave speed models and the Australian lithospheric base.

Along the E-W cross-sectional profiles (Figures 4.6 and C.6), lithospheric thickness (light-blue shaded area) gradually varies in the cratonic province (120–150 km), but thins rapidly toward eastern Australia (70–100 km). While azimuth-dependent LAB depths (leftmost green bars) mostly align with azimuthally averaged LAB depth (green horizontal lines), stations like MBWA and CTAO exhibit wide-spread distributions (Figure C.6), indicating localized lateral variations in the LAB (as shown in Chapter

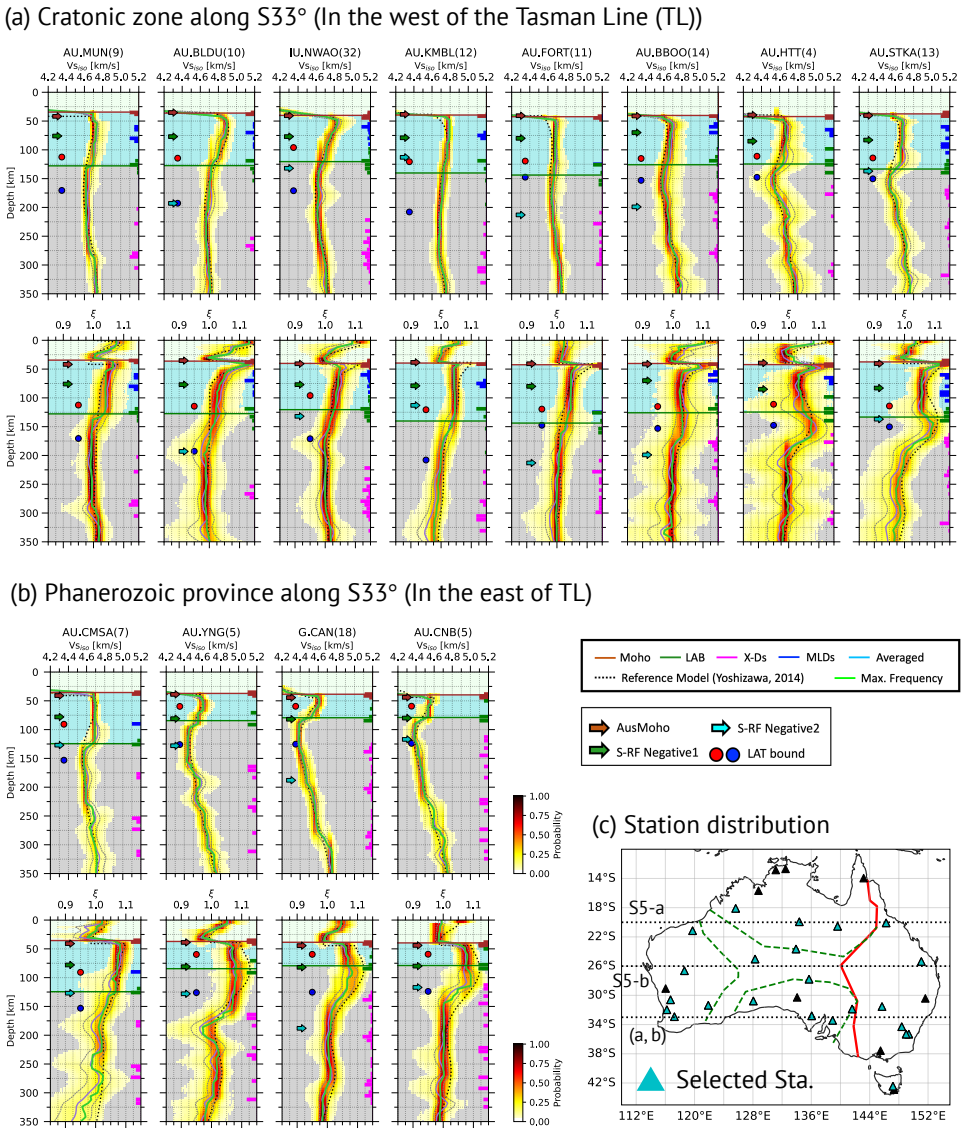

Figure 4.6: Azimuthally-averaged 1-D posterior densities of radially anisotropic S-wave models for permanent stations along S33°. (a) Probabilistic models for stations in the cratonic area, with station names and the number of inverted 1-D profiles (i.e., azimuth-dependent 1-D models) indicated at the top, aligned from west to east. The upper and lower panels show vertical profiles of isotropic S-wave speed and radial anisotropy, with brown and green horizontal lines representing the weighted-average Moho and LAB depths, respectively. Light-green and light-blue shaded regions indicate the crustal and lithospheric zones. The rightmost colored bars display normalized histograms for the identified discontinuity depths. Boundary estimates and 1-D profiles from earlier studies are superimposed as colored arrows, circles, and black dotted curves, as displayed above (c). (b) Same as (a), but for stations in the Phanerozoic region (east of the Tasman Line). (c) Map showing the distribution of permanent stations, with cyan for selected stations and black for others. Black dotted lines represent locations at S20° , S26°, and S33° shown in Figure C.6 (a, b).

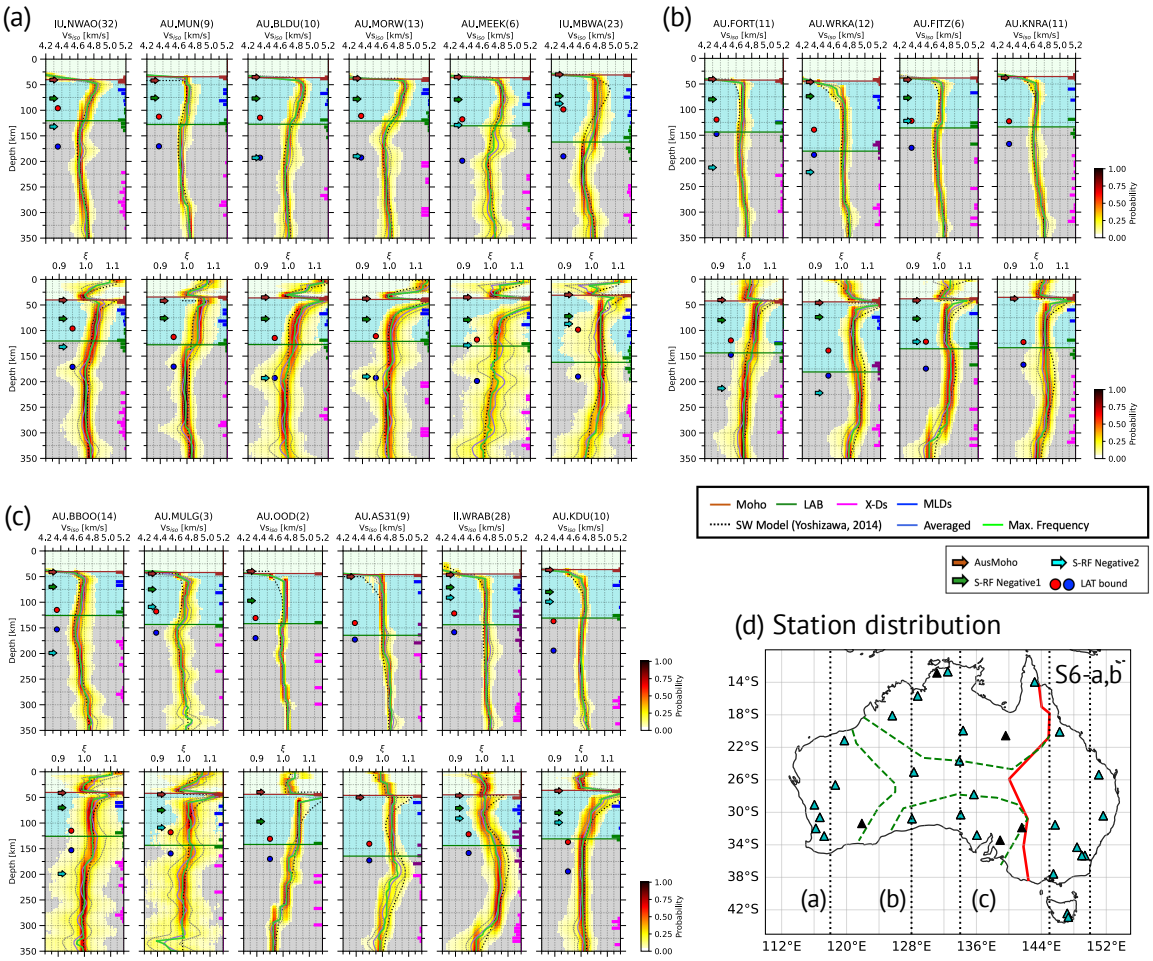

Figure 4.7: Same as Figure 4.6, but for the N-S cross-sectional views of 1-D profiles along E118° (a), E128° (b), and E134° (c), aligned from south to north. Additional figures showing the same views along E145° and E155° are shown in Figure C.7.

3). In the suture zone, WRKA and AS31 stations reveal anomalously thick lithosphere, extending to 170–200 km depths (Figure 4.7 (b, c)).

The sharpness of the S-wave velocity drop varies by tectonic provinces. In eastern Australia and the eastern SAC (Gawler craton), significant shear wave reductions are observed at the azimuthally-averaged LAB (green horizontal lines), accompanied by a sharp increase in radial anisotropy (Figure 4.6), suggesting strong shear flow in the asthenosphere. To the contrary, the WAC shows moderate S-wave reductions and weak anisotropy (Figures 4.6 (a) and 4.7 (a)).

Profiles for WRKA, AS31, and WRAB, characterized by very thick lithosphere, exhibit a high-velocity zone (4.7–4.8 km/s) extending to the 350 km depth from the average Moho (brown lines). Although no S-wave speed decrease is observed, radial anisotropy strengthens significantly ($\sim$ 10 %) below the lithospheric base. These features, corroborated by dense temporary stations from the southern NAC to the SAC (BILBY (Rawlinson & Kennet, 2008) in Figures 4.2 and 4.4) and the Albany-Fraser belt (ALFREX: Tkalčić et al. (2013a)), likely reflect structural characteristics of the Australian cratonic suture zone and adjacent region, such as the southern NAC.

4.4 Seismic discontinuity maps beneath Australia

In this section, we compile the conversion depths for each station to estimate the spatial distribution of each discontinuity. Spatial interpolation provides insights into the large-scale structure of upper mantle discontinuities, while the station-based conversion depth maps reveal localized variations that enhance our interpretation.

For the Moho and the lithospheric base, the mapping strategy follows the straightforward approach described in Section 4.3.2. For X-Ds and MLDs, however, we performed clustering analyses before mapping to group the conversion points into three or four categories. The following subsections provide details of methodologies and the results of these clustering analyses.

4.4.1 Moho discontinuity

Regional-scale Australian Moho models have been developed in several studies (e.g., Kennett & Saygin, 2015; Birkey et al., 2021; Kennett et al., 2023; Magrini et al., 2023).

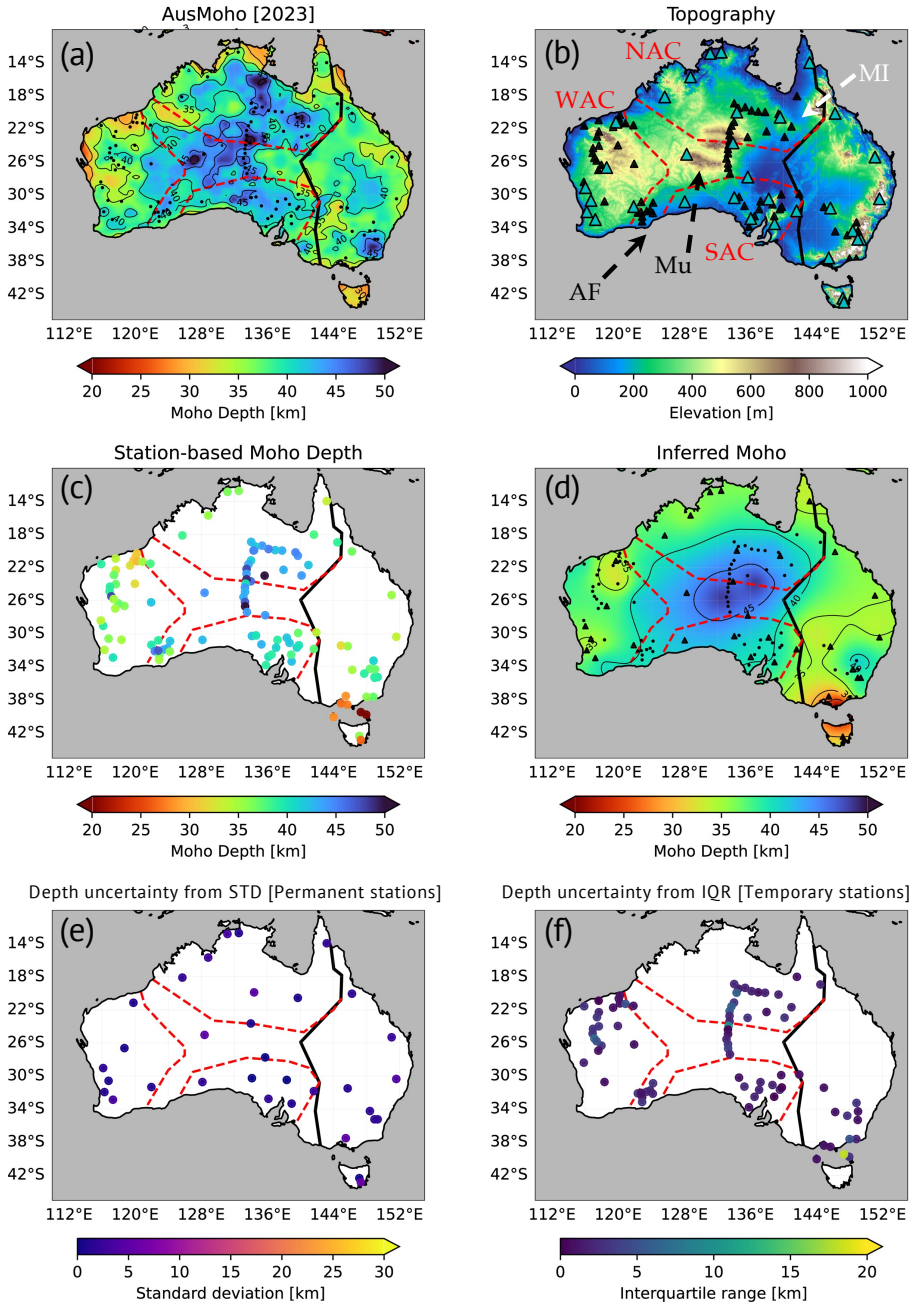

Figure 4.8: Map of the Moho discontinuity. Tectonic boundaries of WAC, SAC, NAC, and Tasman Line are drawn by red dashed lines and black solid lines in all panels. (a) The AusMoho model (Kennett et al., 2023), with black dots indicating station locations used in this study. (b) Surface topography and station distributions. WAC: West Australian Craton, NAC: North Australian Craton, SAC: South Australian Craton, AF: Albany-Fraser orogenic belt, MI: Mout Isa Block, Mu: Musgrave Province. (c) Station-based Moho depths. (d) Spatially interpolated Moho map from (c), with black triangles and circles representing permanent and temporary stations, respectively. The black contours indicate depth intervals of 5 km. (e) The standard deviation of the Moho depth for the permanent stations derived from the azimuth-dependent conversion points. (f) Uncertainties of the Moho depth for the temporary stations estimated from IQR.

In particular, Kennett et al. (2023) provided a comprehensive Australian Moho model (Figure 4.8 (a)) by integrating various geophysical observations, including reflection and refraction surveys and receiver function analyses.

Our resulting Moho map is shown in Figure 4.8 (c, d), with station-based Moho depths in (c) and their spatial interpolation in (d). Overall, our Moho model reveals deepening toward the central region from the continental margin (Figure 4.8 (c, d)).

In the Phanerozoic province, our model estimates the crustal thickness around 35 km, with locally deep Moho in southeastern Australia ($\sim$ 40–50 km near Canberra) and shallow Moho near Tasmania ($\sim$30 km) (Figure 4.8 (c, d)). Along the Tasman Line, marking the transition between cratonic and the Phanerozoic basement, the crust-mantle boundary shows rapid changes: the southern transition zone has a thinner crust (30–35 km), while the northern zone has a thicker crust (40 km).

In the cratonic regions, the Moho varies by tectonic province (Figure 4.8 (c, d)). The crust-mantle boundary is relatively flat at $\sim$ 45 km across the southern and central NAC, while the WAC shows greater variation. The Pilbara craton has a thinner crust ($\sim$ 30 km), whereas the Yilgarn craton has a thicker crust (35-40 km). In the cratonic suture zone, the Moho deepens to $\sim$ 50 km, with localized deepening extending beyond 50 km in the Alice-Springs Orogeny and the Musgrave Province.

Our model agrees with recent Moho models (Kennett et al., 2023; Magrini et al., 2023), showing overall features and localized crustal variations. Some discrepancies, such as in northern NAC, are likely due to station coverage. In central Australia and the Albany-Fraser belt (AF in Figure 4.8 (b)), localized deepening patterns also matched with the AusMoho model (Figure 4.8 (a); Kennett et al. (2023)) and receiver function studies (Sippl, 2016; Kennett & Sippl, 2018; Sippl et al., 2017).

Figure 4.8 (e, f) indicates compiled uncertainties of the estimated Moho depths. For the permanent stations, we show the standard deviations of the depth of azimuth-dependent conversion points at the Moho derived from the azimuth-dependent P-RFs (Figure 4.8 (e)). This deviation can be statistically regarded as not only an uncertainty of estimated depths but also the azimuth-dependent variation of the Moho depths around a permanent station. For the temporary stations, we employ the interquartile range (IQR) of the Moho depth from the inverted posterior distribution, which repre-

sents the estimated errors. The Moho depth uncertainties of this study are estimated to be about a few kilometers (Figure 4.8 (e, f)).

4.4.2 Base of lithosphere

The thickness of the Australian lithosphere has been explored through various approaches (e.g., surface-wave tomography; receiver functions; travel-time tomography), yielding consistent large-scale models that show lithospheric thickening from the eastern Phanerozoic provinces to the western cratonic areas (e.g., Fishwick et al., 2008; Kennett et al., 2013; Yoshizawa, 2014; Davies et al., 2015; Magrini et al., 2023; de Laat et al., 2023). In this study, we combined multimode SWD with P-RFs, sensitive to seismic interfaces, to propose an updated model of lithospheric thickness. Figure 4.9 presents the resulting lithospheric base model, displaying station-based conversion depths and their spatial distribution across Australia in (a) and (b).

In the younger orogenic zone of eastern Australia, the LAB is shallow (60–100 km), thickening rapidly westward toward the Precambrian cratonic areas ($\sim$ 120 km). The northeastern lithosphere, estimated at $\sim$ 100 km thick, shows a sharp lateral change from east to west (Figure 4.9), as also evidenced by azimuth-dependent inversion results for the CTAO station in Chapter 3. In southeastern Australia, including Tasmania (S45°–S22°), the LAB depth is around 80 km, thickening toward the SAC margin (Figure 4.9).

Beneath southeastern Australia (around S33°/E144°), a somewhat thicker lithosphere (100–120 km) is observed, which is similar to the cratonic lithosphere (Figure 4.9). In addition, the S-wave speed in this layer exceeds 4.6 km/s, equivalent to that observed in the SAC (Figure 4.6), suggesting that this area may represent a cratonic-style lithosphere rather than typical Phanerozoic lithosphere (Simons et al., 2002; Fishwick et al., 2008; de Laat et al., 2023). This observation implies that the surface geological trace of the Tasman Line may not necessarily represent its subsurface extension in the mantle. Still, a nearby temporary station (7I.TL16) indicates a shallower LAB (about 100 km) in this area (Figure 4.9 (a)), consistent with the trend in the Moho model (Figure 4.8 (a, c)), suggesting complex crustal and lithospheric structures in the transition area between Phanerozoic and cratonic provinces.

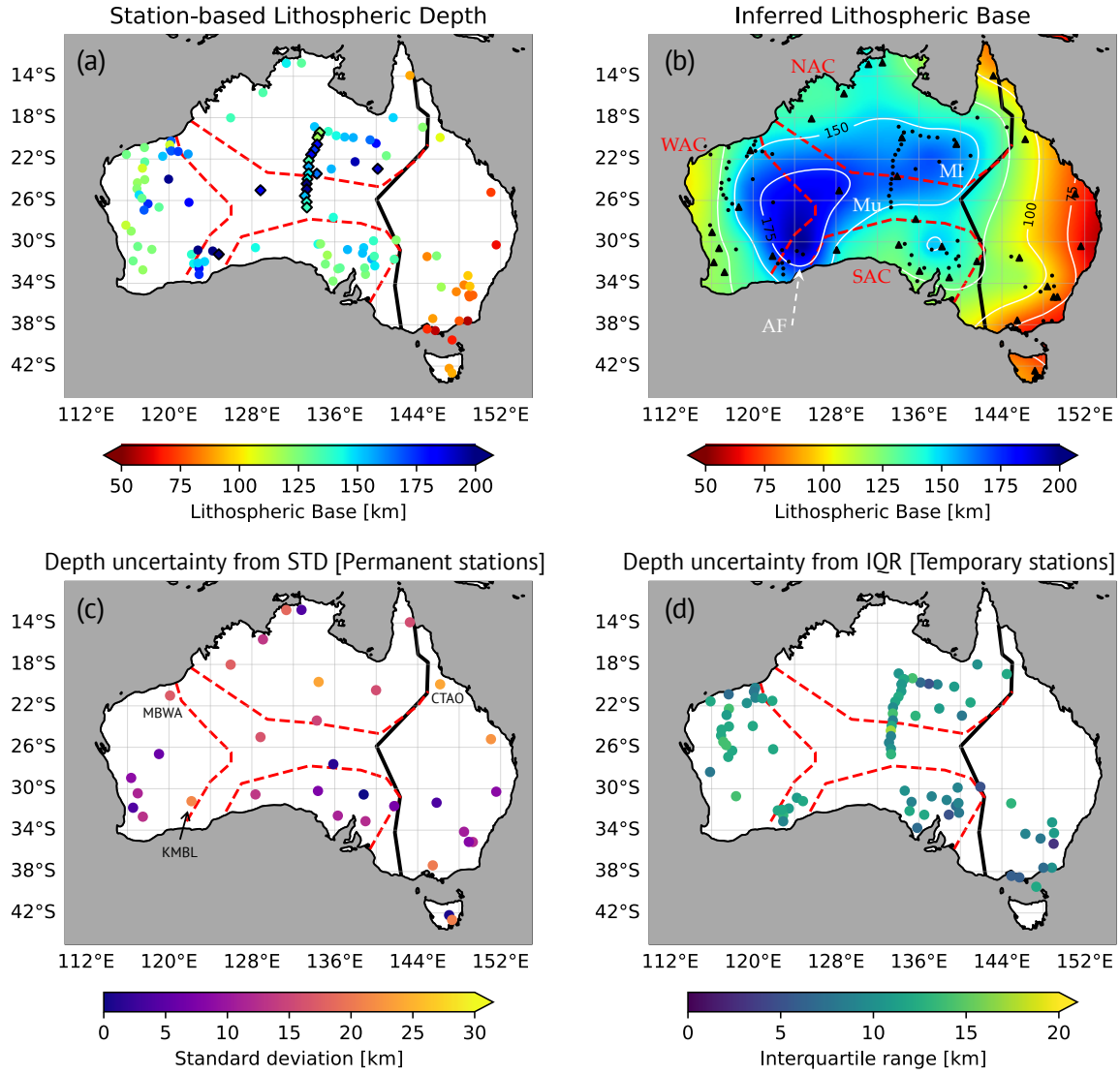

Figure 4.9: Map of lithospheric base. (a) Same as Figure 4.8 (c), but showing the lithospheric base. Diamonds indicate the lithospheric base derived from radial anisotropy where S-wave reductions are unclear. (b) Same as Figure 4.8 (d), but for lithospheric thickness. Thin white contours represent depth intervals of 25 km. (c, d) Same as Figure 4.8 (e, f), but for the lithospheric base. WAC: West Australian Craton, NAC: North Australian Craton, SAC: South Australian Craton, AF: Albany-Fraser orogenic belt, MI: Mount Isa Block, Mu: Musgrave Province.

In contrast, the lithosphere within major cratonic blocks is relatively flat at 120–150 km and deepens to ∼200 km in central Australia (Figure 4.9). The LAB in the SAC is notably flat at ∼130 km, with a slight deepening (∼150km) just north of the Gawler craton (Figure 4.9). Meanwhile, the lithospheric thickness in the WAC and NAC varies laterally toward the cratonic suture zone.

In the western WAC, a flat LAB at ∼120 km deepens gradually toward the cratonic suture zone. Lithosphere thickening is observed at the edge of the Archean Yilgarn and Pilbara cratons (Figure 4.9 (a)), reaching 170–200 km depths. The southern NAC features a thicker lithosphere than the WAC and SAC, estimated at 150–170 km depths (Figure 4.9). Based on station-based LAB depths (Figure 4.9 (a)), localized deepening of the lithospheric base (180–200 km) is evident in the southern NAC and the Mount Isa Block (MI in Figure 4.1).

In the suture zone, particularly the Musgrave province, we observe evidence of anomalously thick lithosphere reaching 170–200 km (Figure 4.9 (a)). Another area of thickened lithosphere appears at the boundary between the WAC and SAC, within the mid-Proterozoic orogenic zone (AF: the Albany-Fraser orogenic belt), also showing localized variations in lithospheric thickness.

The overall pattern in Figure 4.9 suggests a deepening of LAB from eastern Australia to cratonic central/western Australia, consistent with previous lithosphere models based on surface-wave tomography (Fishwick et al., 2008; Kennett et al., 2013; Yoshizawa, 2014; Magrini et al., 2023). Although lateral resolution is still limited in northern NAC due to station coverage, our LAB model (Figure 4.9 (a)) involves some localized features derived from joint analysis using multimode SWDs and P-RFs, such as locally thickened lithosphere in the suture zone.

Figure 4.9 (c, d) corresponds to the depth uncertainties for the lithospheric base as in Figure 4.8 (e, f) for the Moho. Individual uncertainties for the temporary stations are generally smaller than 15 km (Figure 4.9 (d)), which is also seen in the individual inversion results for most permanent stations. However, we can see relatively greater standard deviations (computed from the azimuth-dependent conversion depths) for some permanent stations near the major tectonic boundaries, e.g., CTAO, MBWA, KMBL, reflecting the significant lateral structural variations under these stations.

4.4.3 X-discontinuities

Before mapping, we conducted a clustering analysis. As explained in Section 4.3.2, the X-Ds form clusters at various depths, depending on tectonic provinces (Figure 4.5). We applied k-means clustering to group the estimated X-Ds based on five parameters: horizontal location (longitude and latitude), depth, radial anisotropy value, and vertical change in radial anisotropy. For the k-means cluster analysis, the number of clusters, N_c, must be predefined. We set N_c to 3 or 4 based on the depth distribution of identified X-Ds (Figure 4.5), pre-clustering histograms, and the silhouette scores. To preserve physical meaning, we did not standardize model parameters, although this is commonly done in statistical analysis. Here, we mainly discuss the case of $N_c = 3$ for simplicity, with results for $N_c = 4$ shown in Figures C.9 and C.10.

Figure 4.10 shows the results of clustering analysis. The primary factors in this analysis are the location and depths of the conversion points, as data standardization was not applied. Other model parameters, however, also correlate with depths, supporting the validity of our analysis. From Figure 4.10 (a), we identify three distinctive interfaces: 170km-D, 260km-D, and 310km-D.

For permanent stations, which include azimuth-dependent X-D estimates, we applied the same procedures as for the Moho and lithospheric base, described in Section 4.3.2. Specifically, after clustering, we computed a representative depth for each cluster at permanent stations by averaging conversion points within the same group, weighted by shear wave speed changes.

To determine the existence of an X-D quantitatively, we treated the conversion points in each cluster as a point cloud to calculate the normalized Gaussian kernel density, representing the probability of a Ps conversion from an X-D. Regions where this probability is less than 0.1 are defined as uncertain areas for an X-D.

The resultant maps for the three discontinuities underlying the LAB are displayed in Figure 4.11: (a, c, e) show the station-based map for each discontinuity, and (b, d, f) show spatially interpolated results, with masked regions indicating uncertain areas for X-Ds. The depth uncertainties of these X-Ds are shown in Figure C.8. Figures C.10 and C.11 present similar maps as Figures 4.11 and C.8, but with four clusters ($N_c = 4$).

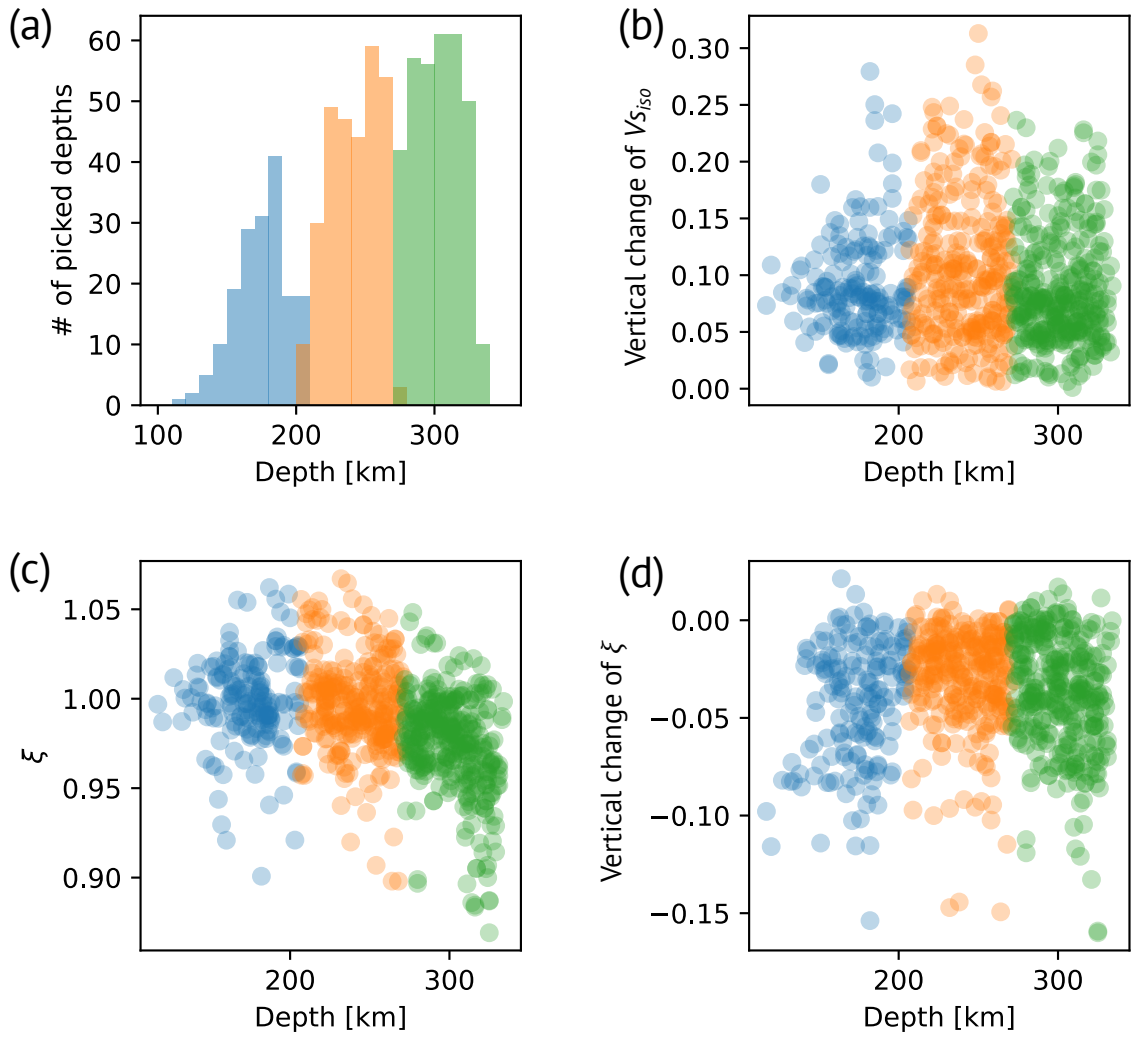

Figure 4.10: Results of the clustering analysis for the conversion points of X-Ds, with clusters numbered from 1 to 3 represented by blue, orange, and green. (a) Histograms of X-D depths for each cluster. (b, c, d) Relationship between shear wave velocity change, radial anisotropy, and vertical change in radial anisotropy.

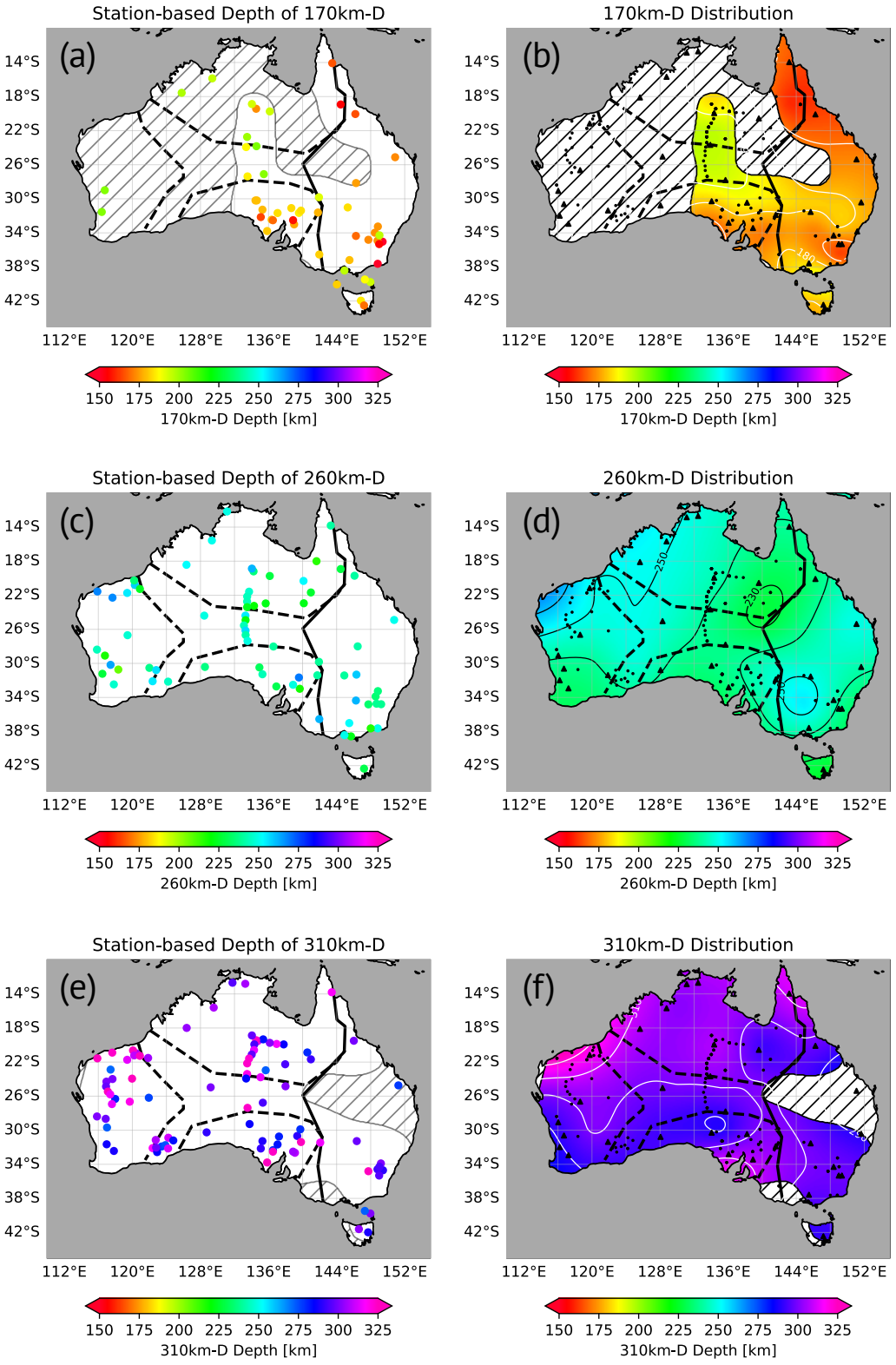

Figure 4.11: Maps of X-Discontinuities. (a, c, e) Same as Figures 4.8 (c) and 4.9 (a), but for the 170km-D, 260km-D, and 310km-D. Black solid and dashed lines represent the Tasman Line and cratonic boundaries, respectively. (b, d, f) Same as Figure 4.8 (d) and 4.9 (b), but for the 170km-D, 260km-D, and 310km-D. Thin black or white contours indicate 10 km depth interval. In (a, b, e, f), shaded area represents regions with unclear presence of discontinuity, as inferred from normalized Gaussian kernel density explained in the text.

The 170-km discontinuity (170km-D), the shallowest X-D, is mainly observed in the eastern Phanerozoic province and the eastern SAC, with limited detection in the WAC and NAC (Figures 4.5 and 4.11 (a, b)). In northeastern and southeastern Australia, 170km-D lies at 150–170 km depth, gradually deepening to 170-190 km in the SAC, although this trend is less clear in its southern part. In the suture zone and NAC, it shows a rapid deepening to 210 km. Dividing the CPs of X-Ds into four clusters ($N_c = 4$) reassingns this deepening to another cluster (Figure C.10), suggesting a potentially different interface at around 220 km.

The 260-km discontinuity (260km-D) spans the entire continent, with depth ranging from 225 km to 270 km with gradual lateral variations (Figure 4.11 (c, d)). In the Yilgarn and Gawler cratons and Mount Isa province (MI in Figure 4.1), it is relatively shallow (225–240 km), while it reaches ∼270 km at the northwestern WAC margin and southeastern Australia. The 310km discontinuity (310km-D) is the deepest X-D, covering all over Australia but less clear in central eastern Australia (Figure 4.11 (e, f)).

The depths of these X-Ds are consistent with previously detected interfaces. A recent S-wave receiver function study detected a positive S-wave speed jump around 150 km (Hua et al., 2023). In continental region, the positive velocity gradient at 150 km (PVG-150) would concentrated primarily in the Phanerozoic and younger orogenic zones, possibly consistent with our 170km-D. In addition, they noted a globally sporadic positive velocity gradient at 260 km (PVG-260), consistent with our 260km-D. Classical seismic studies also reported multiple upper mantle discontinuities with positive velocity jumps from 200 to 350 km under the LAB (Hales et al., 1980; Drummond et al., 1982; Leven, 1985; Revenaugh & Jordan, 1991), which generally corroborate our results.

4.4.4 Mid-lithospheric discontinuities

Our results indicate the presence of multiple MLDs (Figures 4.6, 4.7, and C.6). Similar to the X-Ds, we applied the clustering analysis to the CPs of MLDs prior to mapping. In identifying MLDs, we considered S-velocity changes without distinguishing between positive and negative shifts. For clustering analysis, we included vertical changes in

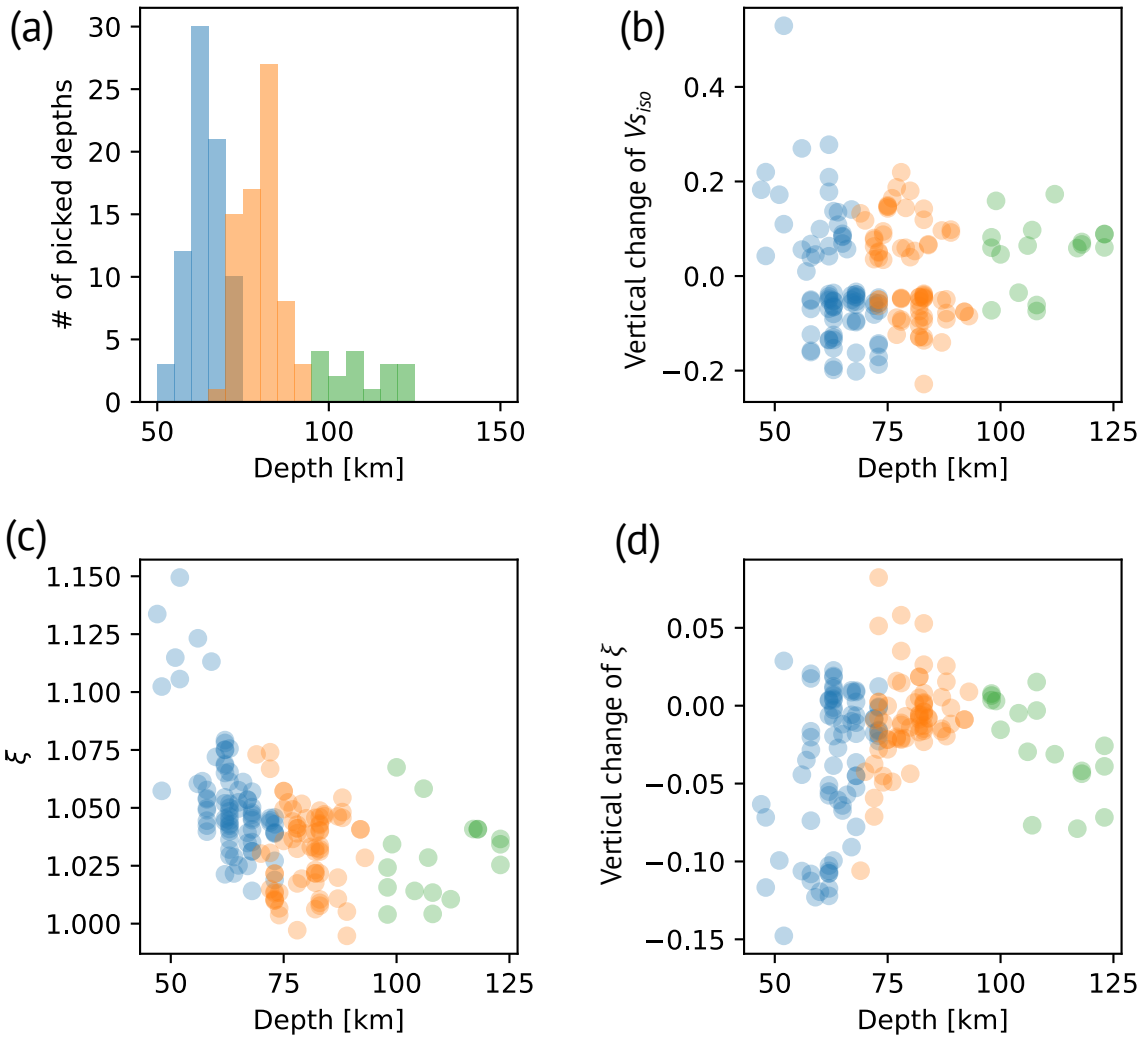

Figure 4.12: Same as Figure 4.10, but for MLDs.

S-wave speed among the five parameters used to classify the groups of X-Ds. Here, we set the number of clusters for MLDs to 3, as the $N_c = 4$ case lowered the silhouette score.

Figure 4.12 shows the results of clustering analysis for the CPs of MLDs. Depth is the primary parameter in this clustering, as with the X-Ds. We designate clusters 1 to 3 as MLD1, MLD2, and MLD3, respectively. Figure 4.13 provides three types of maps for each MLD: depth distribution (leftmost panels), the signs of vertical changes in S-wave speed, and radial anisotropy (second and third panels). Unlike other interfaces, we did not create interpolate maps of MLDs, as each MLD class contains both positive and negative velocity changes. Figure C.12 shows the uncertainty based on the IQR

for each MLD.

Our results reveal that MLDs comprise multiple interfaces at three depths: MLD1 at 60–70 km, MLD2 at 75–90 km, and MLD3 around 100 km (Figures 4.12 (a) and 4.13 (a-1, b-1, c-1)). Distinct MLDs are evident in the three cratonic blocks (WAC, SAC, NAC). MLD1 and MLD2 are present beneath all three cratonic blocks, whereas MLD3 is sparse in the WAC and SAC. In the suture zone, MLDs are mapped only in the Musgrave province and the Albany-Fraser belt (Figures 4.13 (a-1, b-1)). The depth distributions of MLD1 and MLD2 are consistent with previous S-RF observations (Ford et al., 2010; Birkey et al., 2021), which identified MLDs characterized by negative S-velocity changes. In this study, however, we observe both positive and negative S-velocity changes across MLDs (Figures 4.12 (b) and 4.13 (b-1, b-2, c-1, c-2)). Additionally, the vertical variation in shear wave velocity (δV_S) and radial anisotropy ($\delta\xi$) across MLDs shows dependence on the tectonic province (two right panels in Figure 4.13 (a, b, c)). We will subsequently provide separate discussions for MLD1/MLD2 and MLD3.

In the WAC, excluding the Albany-Fraser belt (AF), we mainly observe two MLDs (MLD1 and MLD2). For MLD1, negative δV_S is concentrated along the continental margin, while positive δV_S is only found within the Archean (Pilbara and Yilgarn) cratons (Figure 4.13 (a-2, b-2)). In contrast, $\delta\xi$ in the WAC is generally negative, regardless of location and depth. Around AF, δV_S is negative, as in the WAC, but this region shows positive $\delta\xi$ (Figure 4.13 (a-2, b-2)). In the SAC, δV_S is primarily negative, while $\delta\xi$ varies with depth: negative at MLD1 and positive at MLD2 (Figure 4.13 (a-2, b-2)). In most areas of the NAC, δV_S across MLD1 and MLD2 are generally positive, contrasting to earlier results from S-RFs studies (Ford et al., 2010; Birkey et al., 2021).

MLD3 (Figure 4.13 (c)) is largely absent in most cratonic regions except for the NAC, associated with positive δV_S at around 100 km. Outside the NAC, MLD3 appears only beneath the Pilbara craton (Archean) and the Coompuna province (Proterozoic) (Pi and Co in Figure 4.1), with negative $\delta\xi$ in the NAC and SAC, and positive in the Pilbara craton of the WAC.

MLD1 and MLD2 in the WAC and SAC generally show S-wave velocity reductions,

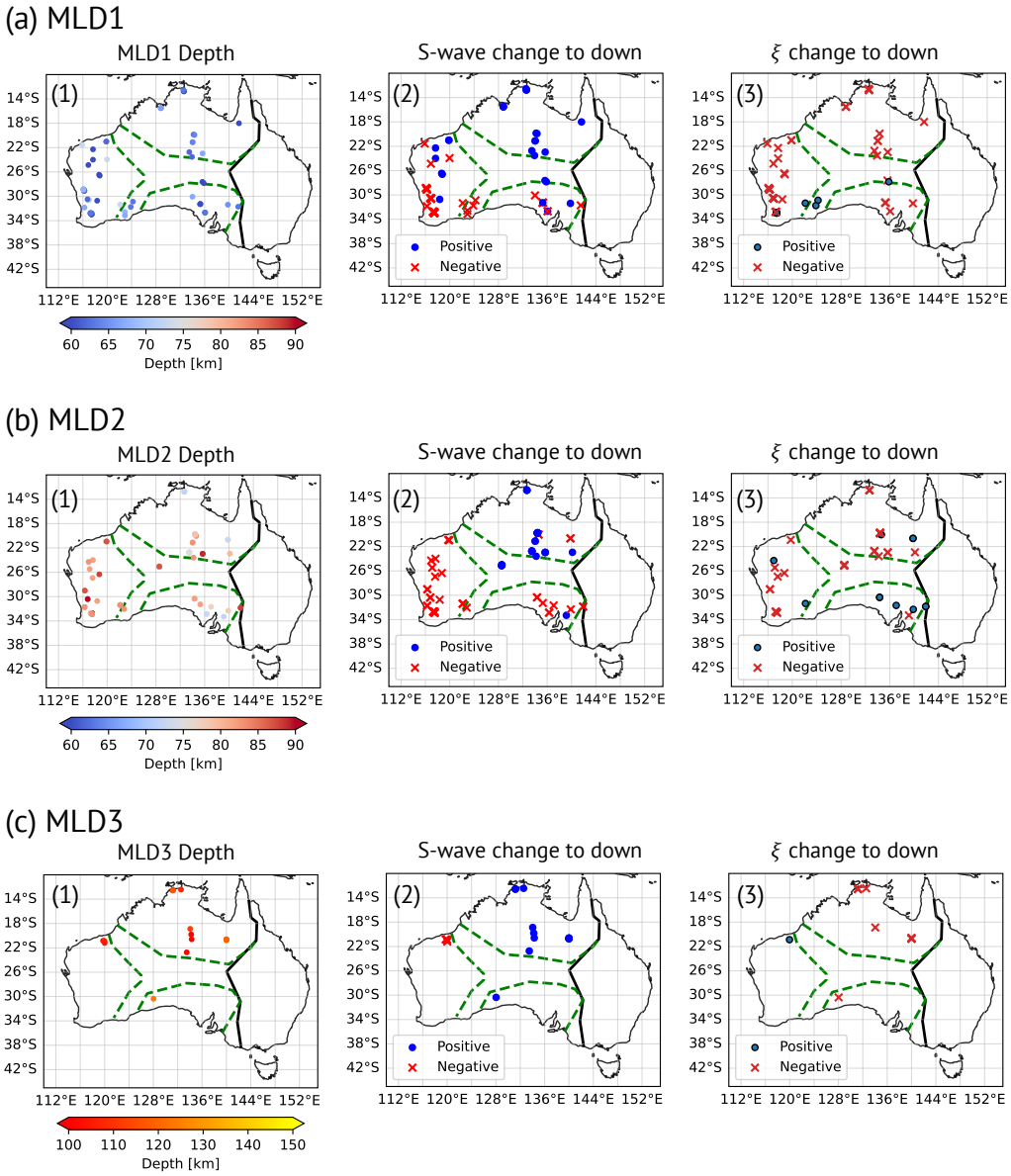

Figure 4.13: Spatial distribution of each MLD group: (a) MLD1 (blue in Figure 4.12), (b) MLD2 (orange in Figure 4.12), and (c) MLD3 (green in Figure 4.12). The left panels, (1), show the depth of MLD conversion points. The second and third panels, (2) and (3), display the vertical changes in isotropic S-wave speed and radial anisotropy, with circles and crosses indicating positive and negative changes, respectively. MLD CPs with smaller change in ξ (< 1 %) are excluded, so symbol locations may differ between the second and third panels. Black solid and green dashed lines denote the Tasman Line and major tectonic boundaries of the WAC, NAC, and SAC, respectively.

consistent with earlier S-RF studies involving other continental regions (e.g, Abt et al., 2010; Kumar et al., 2012; Liu et al., 2020; Birkey et al., 2021). However, in the NAC, we find multiple MLDs characterized by distinct positive velocity jumps, agreeing with early observations of a positive step-like velocity jump in mid-lithospheric depths (∼75 km) (Hales et al., 1980; Leven, 1985). Similar observations of positive MLD velocity jumps have also been made in North America (Calò et al., 2016), including that MLDs are not exclusively associated with S-wave velocity reductions. Across MLDs, vertical changes in radial anisotropy are primarily negative (Figure 4.12), though some positive changes appear in MLD2 beneath the SAC (Figure 4.13 (b)). This continental-scale observation may provide new insights into the nature of seismological MLDs.

4.5 Discussion

4.5.1 Comparison with previous MLD distribution

We can find Ps conversion points at multiple depths in the cratonic lithosphere, which are characterized by not only $\delta V_S < 0$ but also $\delta V_S > 0$ in Figures 4.12 and 4.13. As explained in the previous section, the MLD beneath the NAC comprises multiple interfaces accompanied by $\delta V_S > 0$, contrasting to recent S-RF observations (Ford et al., 2010; Birkey et al., 2021). We will discuss the causes of positive interfaces and the discrepancies between S-RF observations in the next subsection. The MLDs characterized by $\delta V_S < 0$ from the earlier S-RF analysis (Ford et al., 2010; Birkey et al., 2021) are also detected in this study and widely distributed in the WAC and SAC (i.e., except for the NAC) below 75 km-depth (Figure 4.13). However, some MLD CPs in the WAC and SAC accompany the positive velocity gradient, mainly in the shallow depth above 70 km (Figure 4.13), which has not been reported in earlier S-RF studies in Australia (Ford et al., 2010; Birkey et al., 2021).

Figure 4.14 illustrates the cross-sectional conversion points (CPs) of three MLDs classified in this study, representing the vertical distributions of CPs for multiple MLDs. While the MLDs associated with $\delta V_S > 0$ (positive MLD) exist at multiple depths in the NAC, they distributed mainly in the shallower MLD1 group in the WAC and SAC (Figure 4.14), especially beneath the Archean cratons of Pilbara, Yilgarn, and Gawler. In particular, the shallow positive MLD in the WAC cannot be observed

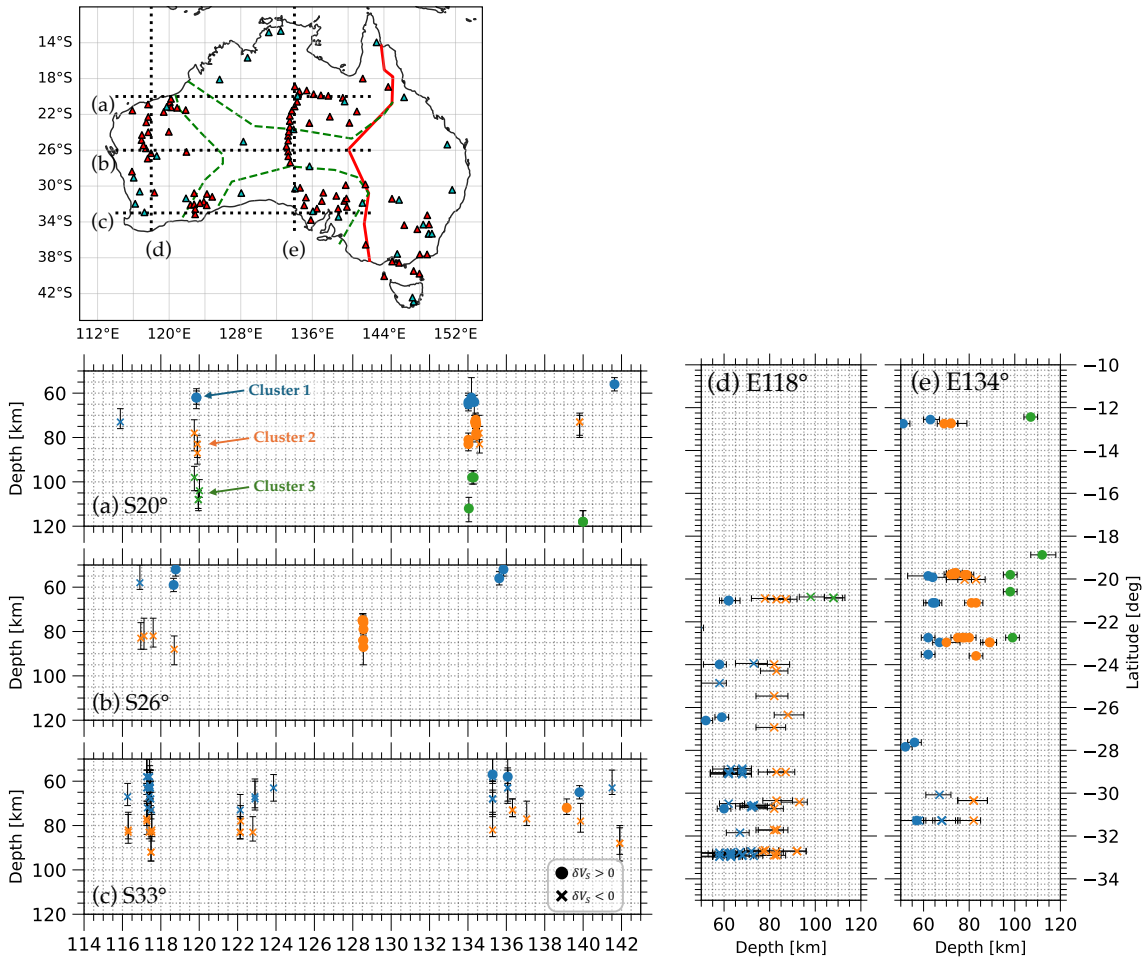

Figure 4.14: Cross-sectional view of clustered MLD conversion points. The top-left panel shows the station distribution used in this study (cyan: permanent stations, red: temporary stations), where the dashed lines labeled with (a–e) indicate the cross-sectional lines. (a–c) E-W cross-sectional plots of the MLD CPs. The selection criteria for CPs are the same as in Figure 3.14, but the background tomography models are excluded. The colored dots and crosses (blue: MLD1, orange: MLD2, green: MLD3) denote the MLD CPs corresponding to positive and negative δV_s, respectively. Error bars represent the IQR-based uncertainties which are estimated from the inverted posterior distributions. (d, e) Same as (a–c), but for the N-S cross-sections.

at the continental margin and appears only within the Archean Yilgan and Pilbara cratons (Figure 4.13).

Birkey et al. (2021) employed S-RFs and detected negative MLDs in the cratonic region, though just a single MLD was found in the southern WAC. On the other hand, Sun et al. (2018) and Chen et al. (2021b) estimated multiple lithospheric discontinuities through P-wave reflectivities and harmonic decompositions of azimuth-dependent P-RFs, respectively. Our maps of MLDs shown in Figures 4.13 and 4.14 support the latter studies based on the teleseismic P-waves. Such differences in P and S-wave analysis results may be due to the intrinsic differences in the wavelength and conversion (or piercing) points of the incident P or S waves. The sensitive region of the S-to-p (Sp) converted phases of the S-RF tends to be much broader than that of P-to-s (Ps) phases; e.g., the conversion points are approximately 40–60 km away from the station for Ps and 100–150 km for Sp (for CPs at around 100 km depth). The P-wave-based analysis reflects the structure near the seismic station, which may better constrain multiple discontinuities under the station than S-RFs.

4.5.2 Interpretations of MLDs

The mid-lithospheric discontinuities (MLDs) beneath Archean and Proterozoic cratonic regions, which can comprise multiple interfaces (e.g., Sun et al., 2018), likely record ancient tectonic processes such as formation, deformation, and thermal events. Numerous studies have attempted to explain the origins of MLDs, often characterized by negative velocity contrasts at lithospheric depths. These explanations, derived from seismological and petrological observations, laboratory experiments, and geodynamic modeling in the mantle, remain debated (e.g., Karato et al., 2015; Selway et al., 2015; Yoshizawa & Kennett, 2015; Chen et al., 2021b; Krueger et al., 2021; Fu et al., 2022; Birkey & Ford, 2023; Sudholz et al., 2024). Proposed causes of MLDs include thermal effects (e.g., Thybo & Perchuć, 1997; Karato et al., 2015), chemical compositional changes (e.g., Selway et al., 2015; Sudholz et al., 2024), and the layered anisotropy (e.g., Yoshizawa & Kennett, 2015; Ford et al., 2016; Birkey & Ford, 2023). While this study focuses on thermal and anisotropic properties, chemical layering may also contribute to MLD formation, reflecting the complexity of cratonic evolution, though unconstrained

by our seismological data.

Figure 4.15 illustrates radial anisotropy ξ around each MLD. Considering $\delta\xi$ (Figure 4.13 (a-3, b-3, c-3)), as well as Figure 4.12 (c), radial anisotropy generally decreases with depth, approaching isotropy. This trend, previously reported by Yoshizawa & Kennett (2015) and Kennett et al. (2017), is particularly evident in the WAC and NAC. Next, we discuss the causes of MLDs by investigating the sign of δV_S, incorporating information on radial anisotropy and our lithospheric thickness model (Figure 4.9).

4.5.2.1 MLDs accompanying S-velocity reduction ($\delta V_S < 0$)

The MLDs characterized by S-velocity reduction ($\delta V_S < 0$) are observed at the edges of the Archean cratons in the WAC (Figure 4.13 (a-2, b-2)), where the shear wave velocity in the uppermost lithosphere is significantly high, reaching 4.8–5.0 km/s. At these depths, radial anisotropy is strong ($\approx$ 7–8 %) with $\delta\xi < 0$ (Figures 4.13 (a-3, b-3) and 4.15), suggesting the presence of a highly rigid and cold craton preserving the effects of past tectonic processes. These MLDs are unlikely to result from thermal effects, which would make the lithospheric layer deformable, as supported by temperature models (Tesauro et al., 2020). Recent seismological studies (Chen et al., 2021b,a; Birkey & Ford, 2023) suggested the topography of the lithosphere base at the western WAC margin may relate to MLDs via azimuth-dependent P-RFs and/or SKS splitting analyses. Specifically, Birkey & Ford (2023) implied the lithosphere thinning to the west under western WAC margin may possibly contribute to the edge-driven mantle convection, which is consistent with our LAB map (Figure 4.9).

The Albany-Fraser orogeny belt (AF), adjacent to the Yilgarn craton, also shows MLDs with negative δV_S, and increased radial anisotropy ($\delta\xi > 0$) across the MLD (Figures 4.13 (a-2, 3 and b-2, 3) and 4.14 (c)). Strong radial anisotropy ($\approx$ 5–6 %) at lithospheric depths (Figure 4.15 and Yoshizawa (2014)) likely records the effects of mid-Proterozoic orogenic events at 1300 Ma and 1160 Ma (Clark et al., 2000; Spaggiari et al., 2015). Rapid cooling following these events, particularly in the western AF (Scibiorski et al., 2015, 2016), likely contributed to localized lithosphere thickening (Figure 4.9).

In the eastern SAC, we observe multiple MLDs with $\delta V_S < 0$, but with varying

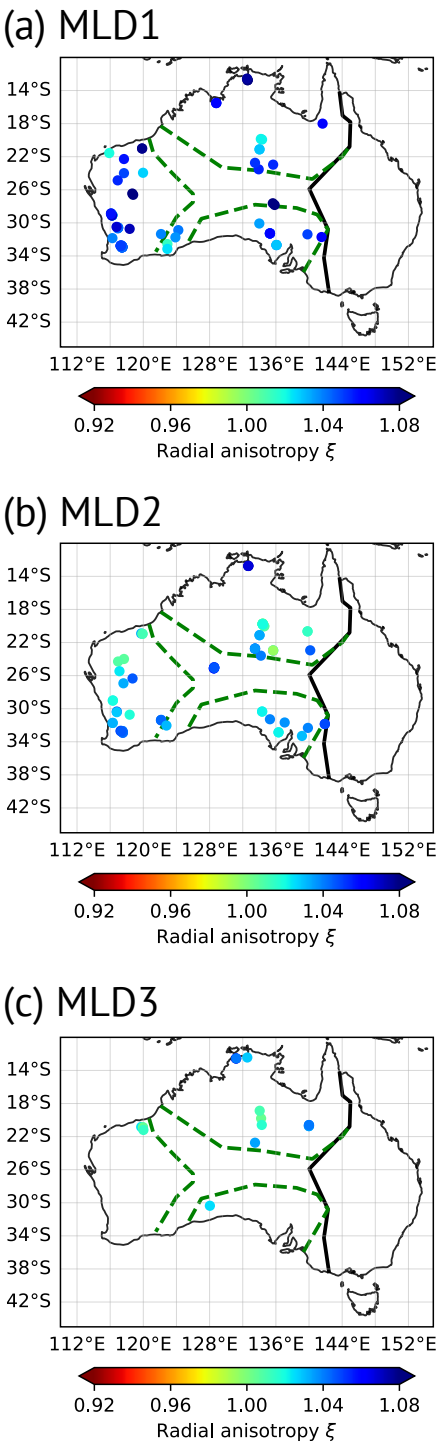

Figure 4.15: Radial anisotropy around each MLD: (a) MLD1, (b) MLD2, and (c) MLD3. Black solid lines indicate the Tasman Line, and green dashed lines the major tectonic boundaries of the WAC, NAC, and SAC.

$\delta\xi$ across MLD1 and MLD2. The shallower MLD resembles those in the WAC, with $\delta V_S < 0$ and $\delta\xi < 0$, while the deeper MLD exhibits $\delta\xi > 0$, suggesting a more deformable nature. Yoshizawa (2014) attributed the thinner lithosphere beneath the Gawler craton to the basal erosion during the breakup from the Antarctic continent since 180 Ma (Williams et al., 2019). The presence of MLD2 may reflect remnants of this erosion, potentially influenced by the upwelling of hot asthenospheric material, as evidenced by high-temperature zones beneath the SAC (McLaren et al., 2003; Goes et al., 2005; Tesauro et al., 2020).

4.5.2.2 MLDs accompanying S-velocity increase $\delta V_S > 0$

MLDs in the NAC and shallow depths of Archean cratons in the WAC are identified by positive velocity gradients ($\delta V_S > 0$; middle panels in Figure 4.13 and Figure 4.14). Unlike MLDs with $\delta V_S < 0$, these can be simply attributed to step-like S-wave jumps caused by slow cooling processes during the formulation of the stable continental cratons. Our observations, which contrast with S-RF studies (Ford et al., 2010; Birkey et al., 2021), agree with earlier studies using regional P-wave analyses (Hales et al., 1980; Leven, 1985).

A plausible explanation for these discrepancies is the influence of complex anisotropic layering, apart from the intrinsic differences between P- and S-RFs. Selway et al. (2015) demonstrated that both azimuthal and radial anisotropic layering could produce negative phases in S-RFs. Rapid vertical and lateral variations in lithospheric depths, observed seismologically beneath northern and central Australia (Birkey & Ford, 2023; Yoshizawa, 2014; Yoshizawa & Kennett, 2015; de Laat et al., 2023), further complicate interpretations. To reconcile S-RF studies and our inversion results, it is essential to account for anisotropic structural effects on receiver functions (e.g. Park & Levin, 2016). Besides, fine-scale heterogeneity can create apparent radial anisotropy and seismic discontinuities (e.g., Fichtner et al., 2013; Kennett et al., 2017), potentially influencing RF observations.

4.5.3 Thick lithosphere in central Australia

Anomalously thick lithosphere, reaching depths of about 200 km, is evident in the eastern Yilgarn craton, southern NAC, and the cratonic suture zone, as revealed by our joint inversion of receiver functions and multimode surface waves (Figure 4.9). In central Australia, significant radial anisotropy with weak S-wave velocity reduction is observed (Figures 4.7 (b, c) and C.6). Figure 4.16 shows the posterior distributions of the isotropic shear wave speed and radial anisotropy for permanent and temporary stations deployed in central Australia. These NS-cross-sectional profiles also highlight the picked depths of lithospheric base located at the positive jump of radial anisotropy with little S-wave speed drops, except for BL06 (northernmost station in BILBY (Rawlinson & Kennet, 2008)). This distinctive feature in the mid-Proterozoic province may reflect the ancient amalgamation processes during the mid-Proterozoic era (1300–1000 Ma) (Myers et al., 1996).

The Musgrave orogeny, located in the suture zone, experienced ultra-high temperatures around 1220-1120 Ma due to upwelling asthenospheric materials (Smithies et al., 2011, 2015), likely associated with the amalgamation of cratons. Such extreme thermal conditions could have weakened the lithospheric structure, enabling the suture zone to act as a buffer zone during the collision of the NAC, SAC, and WAC (e.g., Yoshida, 2012; Yoshida & Yoshizawa, 2020). Following this extensive tectonic-thermal event, central Australia, including the southern NAC, underwent repeated deformation by compression and extension cycles until the Alice-Springs Orogeny (∼400 Ma) (Kennett & Iaffaldano, 2013; Thiel et al., 2020). These tectonic processes likely influenced both the lithosphere-asthenosphere system and crustal structure beneath the region. The present-day observations of anomalous radial anisotropy beneath the lithospheric base (Figure 4.7 (c) and Yoshizawa & Kennett (2015)) could signify the frozen-anisotropy, preserved through multiple tectonic deformations and potentially enhanced by ongoing plate motion.

The minimal S-wave speed drop provides insights into the unique lithospheric structure of central Australia. There are few records of the tectonic activity after the Alice-springs orogeny (∼400 Ma) which was the last major tectonic event in central Australia (e.g., Aitken & Betts, 2009; Aitken et al., 2009), despite some localized fault movement

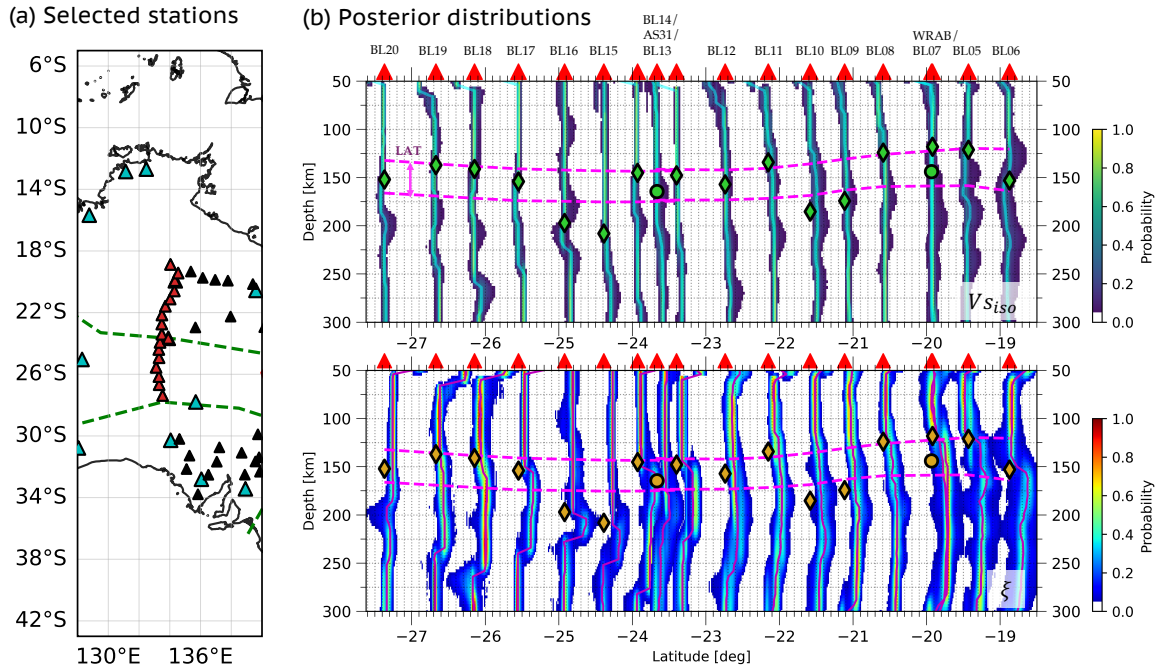

Figure 4.16: Posterior distributions of isotropic shear wave velocity and radial anisotropy at permanent and temporary stations deployed in central Australia. (a) Map of seismic stations. The red triangles represent the selected stations used in (b), while cyan and black ones correspond to other permanent and temporary stations. (b) Probabilistic profiles of isotropic S-wave (top panel) and radial anisotropy (bottom panel). In the top panel, the vertical profiles are plotted by adjusting the uppermost mantle S-velocity (or radial anisotropy) to be located at the latitude of stations. Colored dots and diamonds (green in the top panel and orange in the bottom panel) indicate the depths of the estimated lithospheric base for permanent stations (WRAB and AS31) and selected temporary stations (Rawlinson & Kennet, 2008), where the values for two permanent stations correspond to the azimuthally-averaged depths that are the same as in Figure 4.7. Colored lines (cyan in the top and magenta in the bottom) delineate the maximum frequency model derived from the emsemble solutions. Two pink curves exhibit the upper and lower bounds of the LAT from Yoshizawa (2014).

and/or thermal erosion (e.g., Sandiford et al., 2001). Thus, this region might have relatively remained tectonically quiescent, with no significant deformation or thermal events. The stability likely facilitated a long-term cooling process, preventing chemical or thermal erosion. Furthermore, if the suture zone acted as a buffer during craton amalgamation (Yoshida, 2012), the southern NAC may have moved coherently with the present plate motion directed northward (Argus et al., 2011). This scenario could have contributed to the development of the tectosphere (Jordan, 1975, 1978, 1988), explaining the thick lithosphere with minimal S-wave speed reductions. The observed MLD characteristics in the southern NAC ($\delta V_S > 0$ and $\delta\xi < 0$), potentially reflecting a highly rigid and non-deformable nature, support this hypothesis. These features reflect the tectonic quiescence and stable evolution of the continental lithosphere in this region.

4.5.4 Origins of X-Ds

The resultant X-D maps indicate the existence of multiple X-Ds below the lithospheric base, estimated at around 170 km, 220–270 km, and around 310 km (Figures 4.10 (a), 4.11, C.9, and C.10). These X-Ds are characterized not only by S-wave speed jumps but also by a weakening of anisotropy across the discontinuities (Figures 4.5, 4.6, 4.7, C.6, C.7, and 4.10), providing key insights into their enigmatic nature. In this subsection, we discuss potential geophysical causes of these X-Ds and their relationship with the Lehmann discontinuity.

4.5.4.1 170km-discontinuity

The distribution of 170km-D, except for the NAC and suture zone, appears robust in both the three- and four-cluster scenarios (Figures 4.11 and C.10). The 170km-D is mainly observed in regions with relatively thinner lithosphere, such as the Phanerozoic provinces and eastern SAC, which correlate with high-temperature zones (Goes et al., 2005; Tesauro et al., 2020). This suggests that the thermal structure may play a key role in forming the 170km-D.

A global S-RF study by Hua et al. (2023) identified an interface with a positive velocity gradient at ∼150–180 km in young, active regions (e.g., eastern Australia), in-

terpreted as the bottom of the low-velocity zone in the high-temperature asthenosphere. Our 1-D posterior density results for the eastern SAC and Phanerozoic Australia support this finding (Figures 4.6, 4.7, C.6, and C.7), as a pronounced low-velocity zone is evident above the 170km-D. Thus, the 170km-D may correspond to the base of a particularly low-velocity layer in the asthenospheric mantle.

Hua et al. (2023) proposed that the PVG-150 represents the base of a partially molten layer, based on synthetic S-RF simulations. However, our inversion results do not show clear evidence of partial melting above 170km-D. Even in easternmost Australia (e.g., G.CAN; AU.CNB; AU.YNG), the minimum isotropic S-wave velocity remains at ∼4.4 km/s, which is higher than the expected value for a partially molten layer ($V_{S_{iso}}$ <4.4 km/s, e.g., Hua et al. (2023)). Besides, previous tomography models (Fishwick et al., 2008; Yoshizawa, 2014; Magrini et al., 2023) have not imaged such a low-velocity zone in cratonic regions including the SAC. Therefore, for the Australian continent, it is unlikely that the 170km-D corresponds to the base of a partially molten layer. Instead, both the 170km-D and the PVG-150 by Hua et al. (2023) likely indicate the base of the lowest velocity zone in the asthenosphere, shaped by thermal structure rather than partial melting. To explore the effect of the partial melt on the 170km-D, further investigations are required to estimate the anelastic attenuation in the upper mantle (e.g. Dalton et al., 2008).

The 170km-D also exhibits a notable weakening of radial anisotropy, with a slightly stronger rate of decrease compared to other X-Ds (Figures 4.6, C.6, C.7, and 4.10 (c)). That trend is particularly clear in southeastern Phanerozoic areas (Figures 4.6 and C.7), where anomalous radial anisotropy reflects intense asthenospheric flow. Recent mantle flow modeling by Eakin et al. (2023) suggests strong mantle flow at depths of 120-150 km, weakening down to 200 km. Thus, the rapid decrease in radial anisotropy associated with mantle flow is likely a significant factor in the seismologically detected 170km-D.

4.5.4.2 Deeper X-discontinuities

Both the 260km-D and 310km-D are less distinct compared to the 170km-D. If $N_c = 4$ is chosen, part of the 170km-D in the NAC and suture zone is assigned to cluster 2,

which extends at around 220 km (Figures 4.11 and C.10). While this interface at ∼220 km in the NAC aligns with earlier discussion by Hales et al. (1980) and Leven (1985), its identification remains uncertain, and the qualitative characteristics of 260km-D become less consistent. Given the significant lateral heterogeneity in both thermal and seismic structures across the Australian continent (Tesauro et al., 2020), the depths of phase transitions may vary regionally, preventing us from robust conclusions about the deeper X-Ds compared to the 170km-D.

As a hypothesis, deeper X-Ds could be attributed to mineral phase transitions. Previous studies on X-Ds below 200 km (e.g., Revenaugh & Jordan, 1991; Williams & Revenaugh, 2005; Kemp et al., 2019; Srinu et al., 2021; Pugh et al., 2023) suggest that the 220-270 km X-Ds may correspond to the phase transition from the orthopyroxene to high-pressure clinopyroxene (Opx-HPCpx) (Akashi et al., 2009; Jacobsen et al., 2010), while the ∼300km X-Ds may result from the coesite to stishovite (Co-St) transition (e.g., Akaogi et al., 1995; Ono et al., 2017), both of which exhibit positive Clapeyron slopes ($dP/dT > 0$).

In cold cratonic regions, the Opx-HPCpx transition depth appears relatively shallower (220–240 km), whereas, in warmer regions like eastern Australia and the northwestern WAC, it deepens slightly to 250–265 km. Eastern Australia's hotspot track, associated with low-velocity anomalies (e.g., Davies et al., 2015; Rawlinson et al., 2016), may contribute to the deeper phase transition. Also, the Co-St phase transition could explain the ∼300 km X-Ds (Rein et al., 2020; Srinu et al., 2021; Pugh et al., 2023), though this mechanism may not fully account for the depths observed beneath the cratonic regions.

4.5.4.3 Relationship with the Lehmann discontinuity

One or more of the detected X-Ds may correspond to the Lehmann discontinuity (L-D), first identified in continental regions by Lehmann (1961). Previous studies (Revenaugh & Jordan, 1991; Taira & Yoshizawa, 2020) inferred the presence of the L-D at depths of 180-280 km beneath the Australian continent, with its depths varying based on whether it is located within a cratonic province. While our findings on X-Ds do not directly complement those studies, the detected depth range of X-Ds aligns with the

potential depth of the L-D (Figures 4.5 and 4.10).

Laboratory experiments suggest that the L-D may be attributed to a transition in mineral creep behavior from dislocation to diffusion (Karato, 1992), which seismologically manifests as a transition from anisotropic to isotropic properties, potentially representing the base of the asthenosphere. Gaherty & Jordan (1995) and Taira & Yoshizawa (2020) further suggested that the L-D may be associated with a weakening of radial anisotropy. These previous interpretations are in good agreement with our observations of X-Ds, which also exhibit decreasing anisotropy (Figures 4.5 and 4.10). Thus, it is plausible that one or more of the X-Ds detected in this study may correspond to the L-Ds, providing localized seismological evidence for this enigmatic discontinuity.

4.6 Conclusions

In this study, we conducted a comprehensive spatial mapping of the Australian upper mantle discontinuities using station-based 1-D S-velocity profiles derived from the joint Bayesian inversions of multimode surface waves and P-wave receiver functions. The results provide new seismological insights into the lithospheric and asthenospheric structure, advancing our understanding of the tectonic evolution of the continent. The key findings for each upper mantle interface are summarized as follows:

1. *Mid-Lithospheric Discontinuities (MLD):* Australian MLDs are found at multiple depths ranging from 60 to 120 km. Their elastic properties (S-velocity change, radial anisotropy) vary with tectonic provinces and depths, offering insights into their origins and relationships with ancient tectonic processes. The S-velocity changes across the MLDs depend on locations, with the velocity increase beneath the North Australian craton (NAC) and the velocity reductions in the West and South Australian Cratons (WAC and SAC).

2. *Lithospheric Thickness:* The lithospheric thickness varies regionally: 70–100 km in eastern Australia, 120–150 km in the cratonic blocks, 170–200 km in the suture zone, and the southern NAC. Anomalously thick lithosphere underlies significant radial anisotropy ($\approx$ 10 %) without S-wave speed reductions, likely originating

from the cratonic amalgamation process during the mid-Proterozoic era.

3. *X-discontinuities (X-Ds):* The X-Ds include multiple interfaces at depths around 170 km, 220–270 km, and around 310 km, forming three or four distinct groups. The 170km-D is observed primarily in the eastern young orogenic zone and the eastern SAC, which can be related to the thermal structure. A common feature of X-Ds is the weakening of radial anisotropy across these interfaces.

Part II

Seismic Source Studies

Chapter 5

Eruption Sequence of the 2022 Hunga Tonga-Hunga Ha'apai explosion

5.1 Introduction

The explosive eruption occurred at the Hunga Tonga-Hunga Ha'apai volcano on January 15, 2022, which was a climactic eruption in a series of volcanic processes that started in December 2021 (Zhao et al., 2022). The volcanic explosivity index (VEI) of this eruption has been estimated to be 5–6 (e.g., Zhao et al., 2022; Poli & Shapiro, 2022). This event might be one of the most energetic eruptions in history (Global Volcanism Program, 2013). USGS's earthquake catalog reported this eruption as an event with Ms 5.8 that occurred at 04:14:45 UTC (USGS, 2022). It generated atmospheric waves (e.g., Lamb waves), tsunamis, and seismic waves recorded worldwide (e.g., Kubota et al., 2022; Matoza et al., 2022). The ash plume reaching the mesosphere was captured clearly by satellite images (NASA, 2022). In a huge volcanic eruption, it is well known that the Earth's free oscillations at specific frequencies (e.g., 3.7 mHz; 4.4 mHz) can be coupled with atmospheric modes, generating atmospheric resonant oscillations with the Earth (Kanamori & Mori, 1992; Watada & Kanamori, 2010). Like the 1991 Pinatubo eruption, the spectral peak of the Earth's normal mode at 3.7 mHz has been observed in the seismic records of this eruption (Matoza et al., 2022). In addition, we identify a series of longer-period surface waves from multiple sources at distinct origin times for shorter-period surface waves (Figure 5.1), indicating the influence of the atmosphere-lithosphere coupling.

This explosive eruption has been investigated using a variety of geophysical observations. Poli & Shapiro (2022) performed a back-projection style analysis using long-

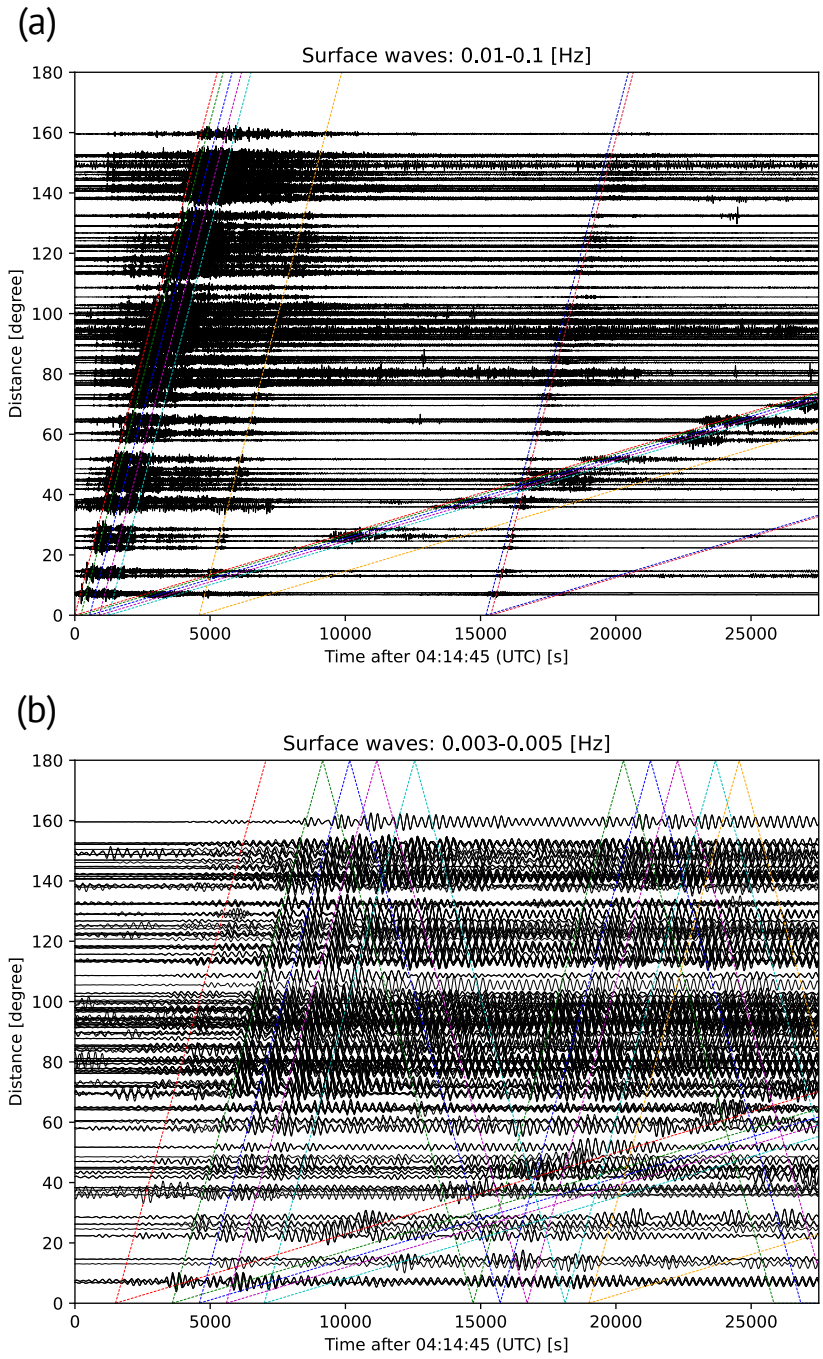

Figure 5.1: Seismic traces in the vertical components for (a) 0.01–0.1 Hz and (b) 0.003–0.005 Hz. In all figures, dashed lines exhibit the travel-time curves of surface waves (a: 3.8 km/s; b: 3.6 km/s) and ground motions induced by infrasound waves (0.3 km/s). Line colors indicate the origin times detected by visual inspections of surface waves (a: 0 s, 220 s, 550 s, 900 s, 1250 s, 4600 s, 15200 s, 15380 s; c: 1500 s, 3600 s, 4600 s, 5600 s, 7000 s, 19000 s).

period surface waves (e.g., Ekström, 2006) and estimated the origin time of the volcanic eruption at 04:16:07 UTC and its volcanic explosivity index (VEI) as 6. Astafyeva et al. (2022) used the ionospheric TEC data to detect multiple volcanic explosions and suggested that the initial eruption and a major explosion occurred at around 04:05:54 UTC and 04:18:10, respectively. Vergoz et al. (2022) analyzed infrasound, hydroacoustic, and seismic waves, identified the initial event at about 04:00 UTC and the major eruption at 04:15 UTC, and roughly discussed an eruption episode on January 15, 2022. Also, they suggested that the last eruption in a series of these eruptions occurred at 08:31 UTC from global geophysical observations. Matoza et al. (2022) compiled multiple geophysical data (seismometers, GNSS receivers, GNSS R0 sounding, Microbarometer, Hydrophone, DART buoy). They found that the eruptions consisted of at least two discrete events (around 04:15 and 08:30), each with a long duration.

Most geophysical studies on this large explosive eruption in Tonga have primarily focused on the observations of lower-frequency signals, which can help unravel the overall picture of the eruption. Nevertheless, the detailed eruption sequence can be better constrained by seismic body waves at relatively higher frequencies than dispersive surface waves at lower frequencies. In this study, we focus on teleseismic P-waves and clarify the series of explosive eruptions in detail based on the back-projection (BP) analysis of global seismic records. We discuss probable synchronization between the eruption cycle estimated from the BP analysis and the eigenfrequency of the atmosphere-lithosphere coupled mode.

5.2 Data & Method

5.2.1 Dataset: teleseismic long-period P-waves

In this study, we employed teleseismic P-waves with epicentral distances from 30° to 98° (Figure 5.2). We used vertical-component broadband seismograms provided by IRIS DMC (Incorporated Research Institutions for Seismology, Data Management Center). All seismograms were corrected for the instrument response and band-pass filtered between 0.03 and 0.08 Hz.

Before the back-projection analysis described in the next section, we conducted a careful data-selection process for teleseismic P-waves data. The procedure is similar

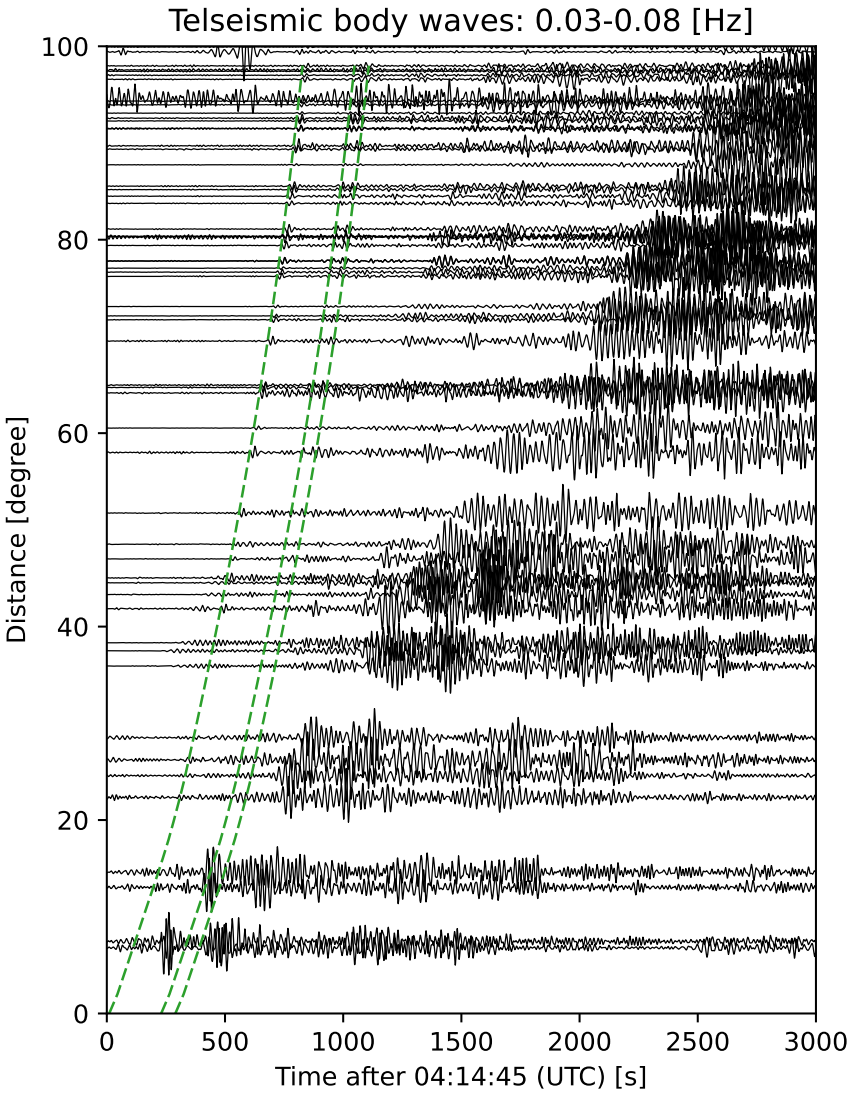

Figure 5.2: Teleseismic body-wave traces. The origin time is 04:14:45 (UTC). Green dashed lines show the travel-time curves of direct P-waves due to three major eruptions for the reference Earth model, AK135.

to a cross-correlation-based selection method by Tkalčić et al. (2011), originally developed for extracting coherent receiver functions from noisy data sets. Here, we utilized this method for P-waves for a reference event that occurred at 04:14:45 UTC, which is used as a reference time in the subsequent analysis of this study. First, we computed normalized cross-correlation coefficients (NCC) and lag times between all trace pairs from 100 s before and 100 s after the theoretical arrival time of the direct P-wave computed for a reference spherical Earth model, AK135 (Kennett et al., 1995). Second, we constructed a group for each seismic trace, including other traces with NCC > 0.7. Then, we selected only one group of traces with the largest number of waveforms and corrected their travel times with the lag times derived in the cross-correlation step. Finally, we removed the traces with waveform anomalies beyond 3σ from the averaged waveform. Through this data-selection process, we selected 223 highly coherent waveforms in the epicentral distance range from 47° to 95° (Figure 5.3 (a, b)).

Note that, although we focus only on the direct P-waves in this study, other teleseismic phases (e.g., Pdiff; PKIKP; PP; PS) generated by the reference event have also been observed in vertical and radial components. Figure 5.4 shows the teleseismic traces with theoretical travel times of these phases in the same time window as Figure 5.2.

5.2.2 Back-projection analysis

The back-projection (BP) analysis reverses seismic signals back to a potential source region where seismic waves are radiated, which has been developed and applied for imaging the source process of large earthquakes (e.g., Ishii et al., 2005, 2007). A schematic illustration of the BP method is shown in Figure 1.5. In this study, we used the BP method combined with the N-th root stack technique to enhance coherent signals effectively (Rost & Thomas, 2002; Honda & Aoi, 2009; Xu et al., 2009; Honda et al., 2013). This BP process with the N-th root stack can be expressed as,

$$s_j(t) = \frac{1}{M} \sum_{i=1}^{M} \mid u_i(t + \tau_{ij}) \mid^{\frac{1}{N}} \cdot \mathrm{sgn}(u_i(t + \tau_{ij})) \tag{5.1}$$

$$S_j(t) = \mid s_j(t) \mid^{N} \cdot \mathrm{sgn}(s_j(t)) \tag{5.2}$$

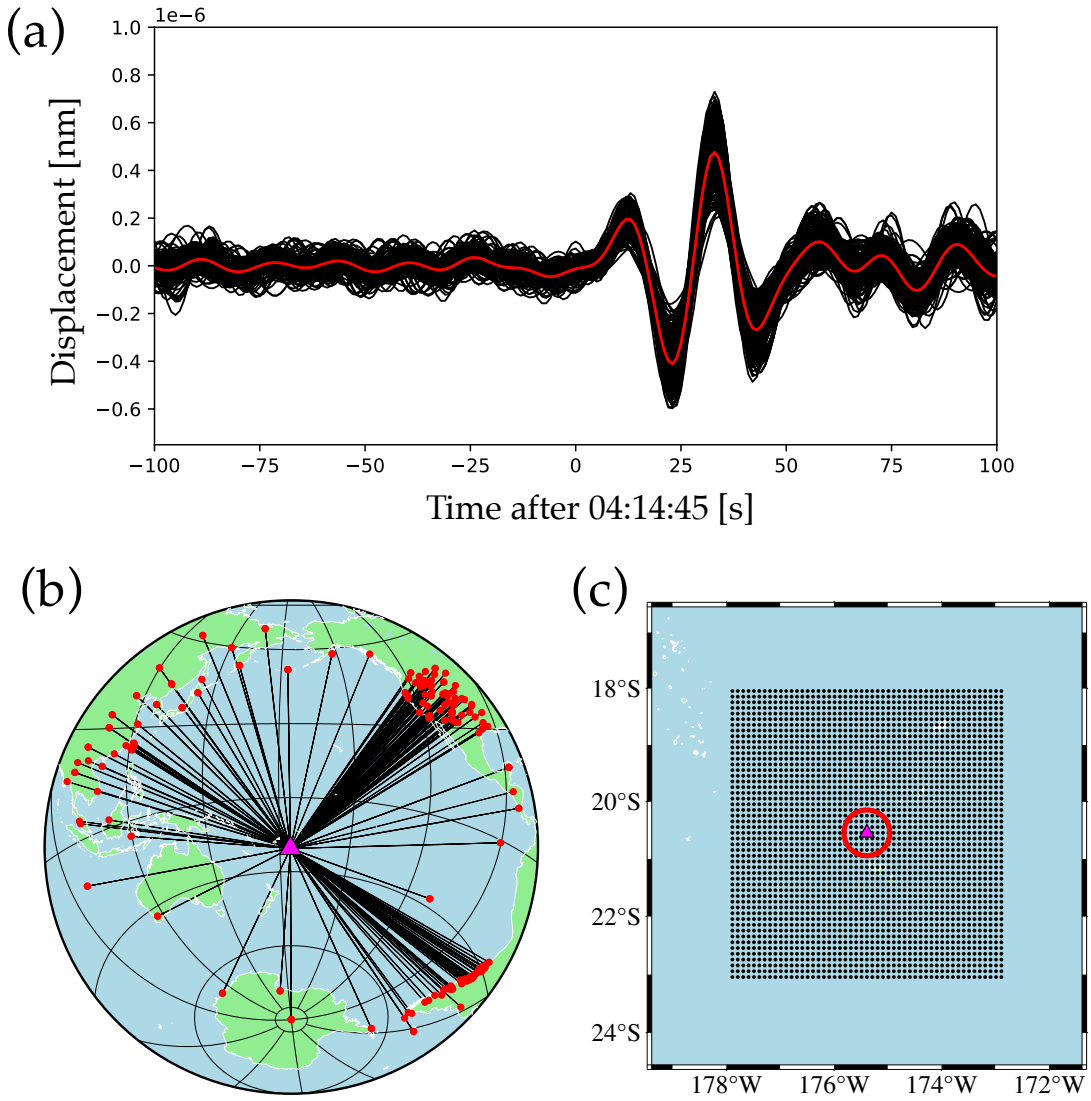

Figure 5.3: (a) Teleseismic P-waves used in the back projection. Black lines indicate individual waveforms that survived the data-selection criteria, and a red line the stacked waveform. (b) Station distributions for selected waveforms. Red dots and a magenta triangle show stations used in the back-projection and the Hunga Tonga-Hunga Ha'apai volcano. (c) An enlarged map of the back-projected area around the volcano. A magenta triangle and black dots exhibit the volcano and possible source grids, respectively. A red circle shows a region used to judge whether a back-projected event is associated with the volcanic eruption or not.

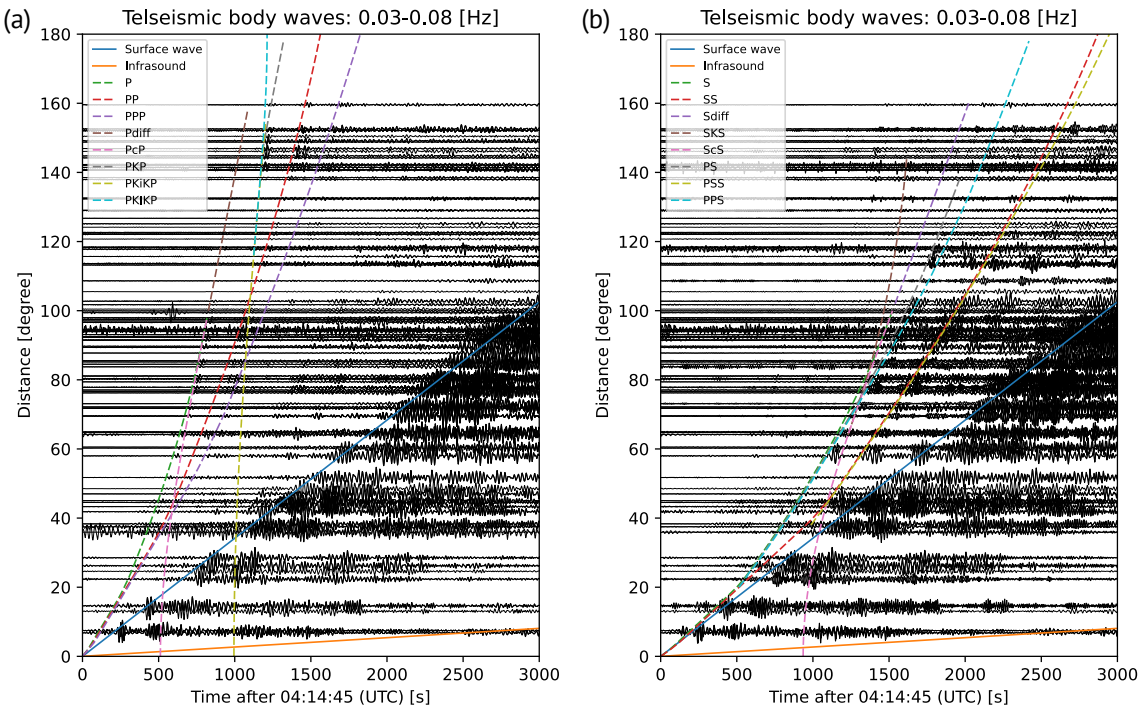

Figure 5.4: Seismic traces of teleseismic body waves in the vertical component (a) and the radial component (b). Theoretical travel-time curves are computed for the AK135 model.

where M is the number of stations, τ_{ij} the travel time between the i-th station and j-th source grid, u_i a seismogram at the i-th station, and $S_j(t)$ the stack of waveforms at j-th source grid associated with the radiation power of seismic waves. Here, we set $N = 4$. Because BP is based on the slant-stacking with travel-time corrections, a reference phase (e.g., direct P) and the phases with the same slowness should be enhanced through the stacking process, while other seismic phases with different slowness and incoherent noises can be canceled out. Thus, BP enables us to estimate the source locations from which target seismic waves (with a selected slowness) are radiated, including other minor events that may be masked by larger signals from major events (e.g., Kiser & Ishii, 2013a).

For computing travel times of the direct P-waves, we used the reference 1-D Earth model, AK135 (Kennett et al., 1995). Potential source grids were set in a $\pm 2.5°$ by $\pm 2.5°$ region around the Hunga Tonga-Hunga Ha'apai volcano with a $0.1°$ grid interval (Figure 5.3 (c)). We back-projected seismic traces from 1200 s before and about 6 hours after the arrival time of P-waves from the reference event at 04:14:45 UTC since

we cannot find clear signals corresponding to this eruption beyond 6 hours (Matoza et al., 2022).

5.2.3 Criteria for identifying the explosive eruptions

In this study, we estimated the back-projected P-wave amplitude over time by integrating $S_j(t)$ every 10 s and normalized by the maximum amplitude. This process can be represented as follows,

$$BP_j(t) = \frac{1}{\max(BP_j(t))} \int_{t-\delta t}^{t+d\delta t} S_j(t^{'})dt^{'} \tag{5.3}$$

where $BP_j(t)$ is the BP amplitude at j-th source grid. δt is the half-length of a time window for the integration, where $\delta t = 5$ s in this study. A time series of the BP amplitude is then constructed from the maximum amplitude in the back-projected source area (Figure 5.3). The resultant BP images represent the source locations that radiated P-waves.

Based on the location and strength of back-projected amplitude, we employ the following criteria to evaluate whether a detected event is associated with an explosive eruption or not:

- Location of radiation source: 0.4° around the Hunga Tonga-Hunga Ha'apai volcano
- Peak BP amplitude > 0.005.

5.3 Eruption sequence inferred from back-projection with teleseismic P-waves

Figures 5.5 and 5.6 show snapshots of BP results and time-series BP amplitude made by the peak amplitude within the back-projected region, respectively. Tables D.1 and D.2 in Appendix D.2 summarize the details of all detected events. Our BP analysis detected at least 19 events associated with explosive eruptions (A – S in Figure 5.5), implying that the eruption sequence can be divided into the first and second sequences. Note that the time series of peak BP amplitudes (Figure 5.6) includes several peaks that are not classified as volcanic eruptions based on the criteria described in the previous section. Such events can be interpreted as earthquakes nearby the volcano (Figure

D.2 in Appendix D), although their identification is beyond the scope of this study. We also performed additional BP analyses with different parameter settings (including various N-th root stacks, frequency ranges, and reference models) summarized in the Appendix D (Figures D.3 and D.4). These experiments confirm that our major results in Figures 5.5 and 5.6 are robust and are not severely affected by the subjective parameter selections. In this section, we discuss the eruption sequence and several major eruptions by comparing their origin times with other studies.

5.3.1 First sequence: Events A – N

In the first sequence, we recognize at least 14 explosive eruptions and 16 unknown events, including earthquakes, that excited P waves. This sequence begins at 04:02 UTC and continues for about 30 minutes at least. Figures 5.5 and 5.6 show that, after 04:14:55 UTC, the volcanic eruptions radiated significant P waves, as seen in the first remarkable spike in the time series of BP amplitude. In this study, we further divided the first sequence into two stages: the preliminary and explosive stages (Figure 5.6). The satellite images from GOES-18 (NOAA: National Oceanic and Atmospheric Administration) and Himawari-8 (JMA: Japan Meteorological Agency) captured the ash plume at 04:10 UTC (NASA, 2022), implying that the volcanic eruption started before this time. Vergoz et al. (2022) analyzed the infrasound waves and suggested the starting time was about 04:00 UTC. From the TEC perturbations, Astafyeva et al. (2022) identified the origin time of the initial event as 04:05:54.164 s UTC. Our estimate of 04:02 UTC from the BP results (Figures 5.5 and 5.6) agrees with those previous studies based on other geophysical observations. After the initial eruption in the preliminary stage of the first sequence, several explosive eruptions occurred sporadically, which eventually escalated to a large eruption at 04:14:55 UTC.

The preliminary stage continued for about 12 minutes. Then, the explosive stage, comprised of a series of significant radiation of P-waves, started at about 04:14:55 UTC (event F), corresponding to the reference event of this study taken from the USGS catalog (Section 5.2). Poli & Shapiro (2022) and Matoza et al. (2022) indicated that the eruption was not only characterized by long duration but also composed of multiple explosions. Our results show the intermittent radiation of P-waves from the volcano.

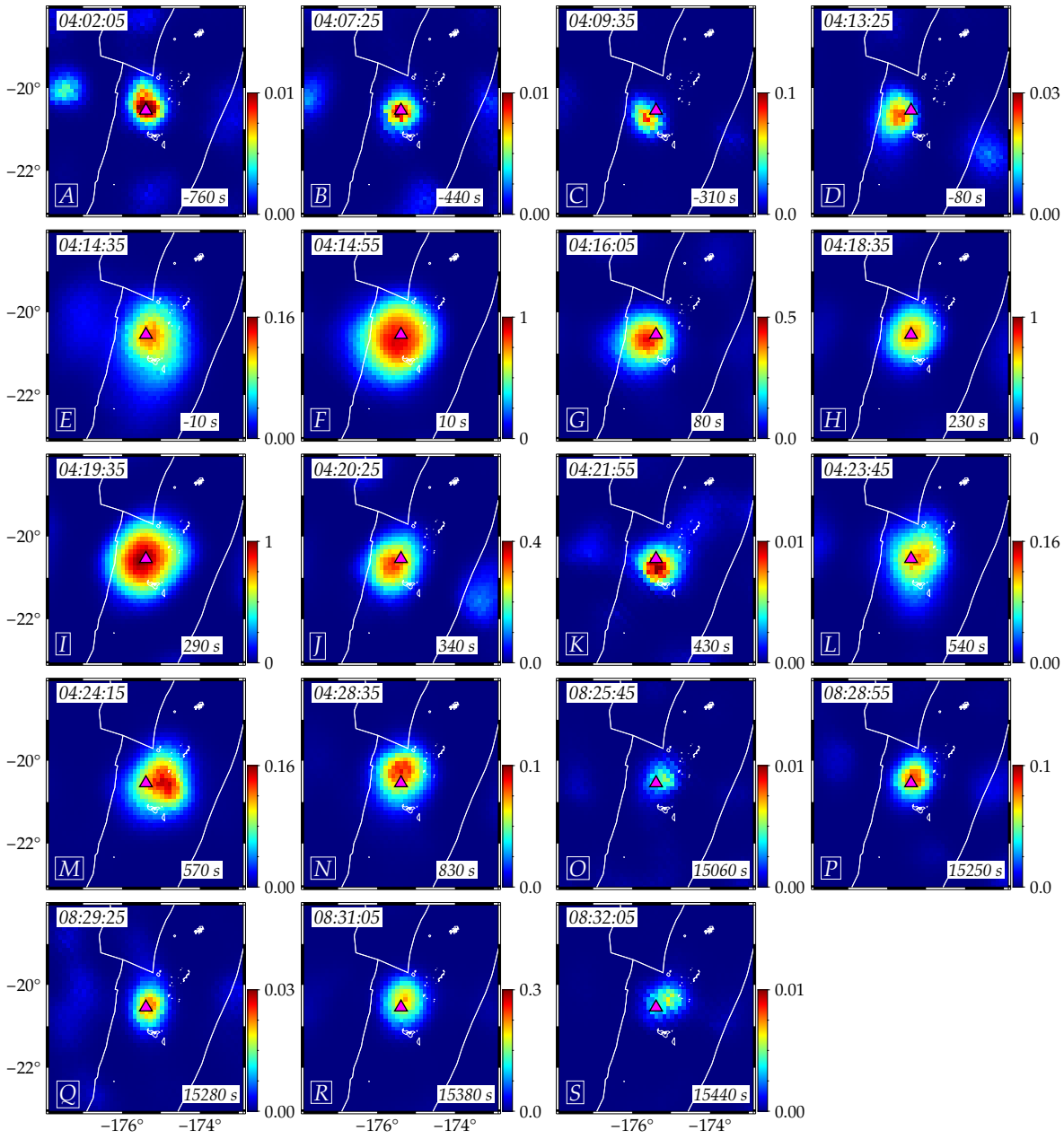

Figure 5.5: Snapshots of BP results. UTC and elapsed times relative to the reference time at 04:14:45 (UTC) are shown in each snapshot. A magenta triangle shows the location of the Hunga Tonga-Hunga Ha'apai volcano. White lines indicate the plate boundaries (Bird, 2003). The scales of color bars indicating the relative power of P-wave radiation are adjusted for each snapshot.

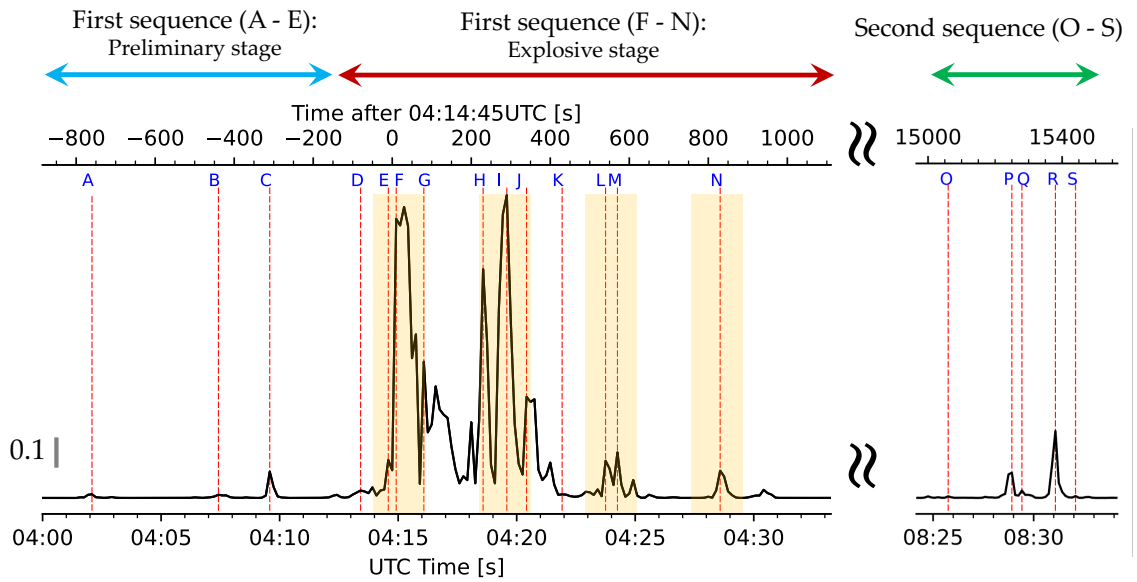

Figure 5.6: Time series of peak back-projected amplitude within the source region. Red dashed lines indicate the timing of identified explosive eruptions. Yellow regions display event groups at about 270 s intervals.

We detected at least 14 explosive eruptions and 16 other events, including earthquakes, in the first 1250 s (by 04:35 UTC) after the reference event. Poli & Shapiro (2022) back-projected Rayleigh waves (0.01 – 0.04 Hz) and estimated the origin time of surface wave radiation at 04:16:00 UTC. The 60 s time shift from our result can be mainly due to the dispersive nature of long-period surface waves, which would represent a centroid time rather than the time of initiation. Vergoz et al. (2022) examined the correlation between infrasound, hydroacoustic, and seismic data and also estimated 04:15 UTC as the beginning time of the most powerful eruption.

Our BP results indicate two significant eruptions (H and I in Figures 5.5 and 5.6) after the reference event F. The BP amplitude of event I is slightly greater than the reference event F. Astafyeva et al. (2022) identified the origin time of the most powerful explosion at 04:18:10.110 s UTC, which is closer to the two later eruptions (H and I) found in this study. These facts imply that those later events may represent the largest explosive events during the eruption sequence. Moreover, Vergoz et al. (2022) discussed that explosions around 04:20–04:30 UTC might contribute to the emission of atmospheric Lamb waves by investigating the envelopes of infrasound waves recorded globally. These two later eruptions can be a key to understanding a fuller picture of

the Hunga Tonga eruption, including the generation of atmospheric Lamb and coupled waves with the solid Earth (e.g., Watada & Kanamori, 2010; Matoza et al., 2022).

After these massive eruptions, the first sequence of volcanic eruptions might end at around 04:35 UTC. Such intermittent explosions for more than half an hour may generate seismic surface waves and infrasound waves with long duration, as observed in the lower-frequency signals (Figures 5.1). Previous research suggested that volcanic activity may have continued even after this time (Matoza et al., 2022; Astafyeva et al., 2022). However, our BP analysis has intrinsic limitations in detecting events after 04:35 UTC because energetic Rayleigh waves from the earlier explosions dominate the vertical-component seismograms in a wide range of epicentral distances (Figure 5.2). Thus, relatively weak teleseismic P-waves are buried, which makes it difficult to detect the meaningful signals of explosive eruptions with the BP analysis.

5.3.2 Second sequence: Events O – S

The second part of the eruptions started about 4 hours after the end of the first sequence and continued for 6–7 minutes. The strongest eruption in this sequence is identified at 08:31 UTC in this study, which agrees with the previous estimate; e.g., Matoza et al. (2022) and Vergoz et al. (2022) reported the eruption at around 08:31 from infrasound and hydroacoustic data. Our BP analysis identifies 5 plausible eruptions (events O – S) starting at about 8:26 UTC. The second sequence gradually escalates into the primary eruption at 08:31 UTC (event R in Figures 5.5 and 5.6).

5.4 Discussion

5.4.1 Multiple explosions detected by P-wave back-projection: Relation with surface wave trains

Based on the time series of explosive eruptions detected by the P-wave back-projection in the previous section, theoretical arrival times of surface waves for each explosion are compared with observed surface wave records in this section. Figure 5.7 (a, b) shows vertical-component seismograms in the frequency range from 0.01 to 0.08 Hz, with theoretical arrival times computed from the origin time of each explosion. For simplicity, we select seismic stations near the volcano with an epicentral distance (Figure 5.7 (c)).

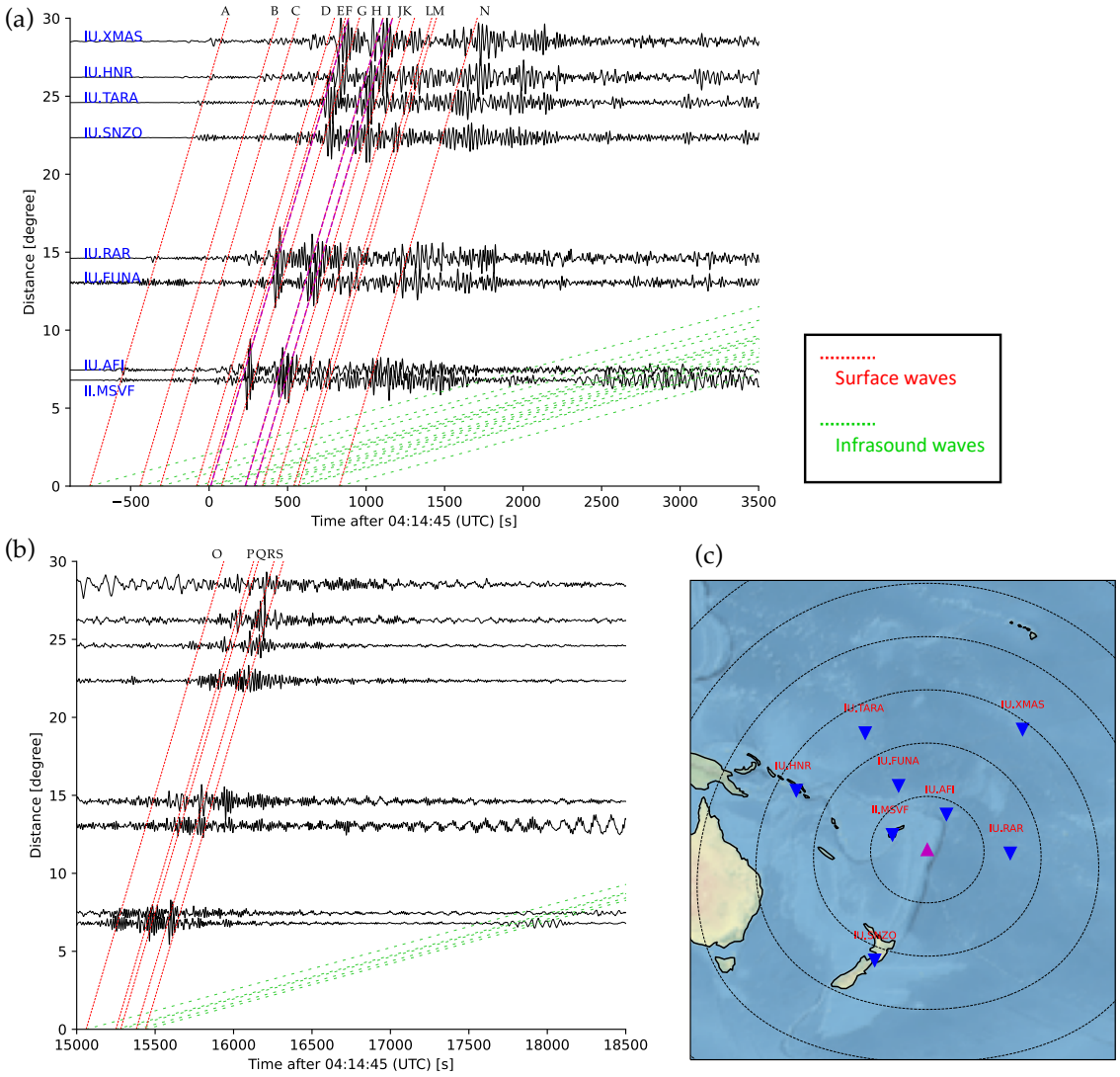

Figure 5.7: (a) Surface wave traces for the first sequence recorded at stations with blue inverse triangles in (c). Red dotted lines indicate the theoretical arrival times of surface waves from each explosive event detected in this study. Green dashed lines are the theoretical arrival times of infrasound waves induced by the explosions. Magenta lines show the three major explosions (events F, H, and I). (b) Same as (a), but for the second sequence. (c) A map of stations at epicentral distances less than 30°, where distance contour lines are plotted every 10°.

In the first and second sequences, the observed Rayleigh wave trains closely match the expected arrival times from the detected explosions. As shown in the BP results in Figures 5.5 and 5.6, the initial eruption in the first sequence was identified at about 04:02 UTC (i.e., about 12 minutes before the reference event). In the preliminary stage of the first sequence (Figure 5.6 and Table D.1), we can see weak surface-wave arrivals from these events. Note that the arrival-time fluctuations of surface waves in the relatively higher frequency range (0.01–0.08 Hz) reflect the strong lateral heterogeneity in the oceanic upper mantle.

In the explosive stage of the first sequence (after the reference event), we can see a series of surface wave trains with large amplitude generated by multiple explosive events, which are also consistent with the computed arrival times for the detected events. Ground motions induced by infrasound waves from these explosions are also observed as later arrivals. In addition, for major explosive events F, H, and I, we can visually identify the arrivals of teleseismic P-waves, surface waves, and infrasound waves in observed waveforms. Even after the last-detected explosive eruption (event N) in the first sequence, we can still see surface wave packets, which may come from an event other than the eruption (such as an earthquake) within the time window of the first sequence (Table D.1). Note that our BP analysis with teleseismic P-waves has inherent difficulties in detecting events after the arrival of surface wave packets from the massive explosions (i.e., events F, H, and I) at the epicentral distance over (corresponding to about 1300 s after the reference time) since relatively weak P waves tend to be entirely masked by the energetic surface waves.

In the second sequence (Figure 5.6 and Table D.2) for the events O – S, we can observe Rayleigh-wave arrivals consistent with theoretical travel times computed from the origin times of these events. The corresponding infrasound waves are clear, as in the case of the first sequence, even though the P-wave radiation from explosions in the second sequence is relatively weak (Figure 5.5).

Although surface waves can be used to investigate the large-scale picture of the eruption process (e.g., Poli & Shapiro, 2022), long-period surface-wave constraints on eruption details are weak. In contrast, teleseismic P waveforms at higher frequencies have a greater resolution for the source processes, which can be represented by a

downward single force for volcanic eruptions (e.g., Kanamori & Given, 1982; Kanamori et al., 1984). Thus, even if multiple explosions occur in relatively short time differences, the observed time series of P-waves is likely to reflect both the impulsive source time function and the number of events, which enables us to unravel the eruption sequence. For example, the event groups around 200–300 s after the reference event (Figure 5.6) are likely to be identified as one large eruption from surface wave analysis (Figure 5.7) and P-waves at a lower frequency range (e.g., 0.01–0.04 Hz, Figure D.3-(b)). On the contrary, the BP analysis with P-waves at a higher frequency range (0.03–0.08 Hz) used in this study allows us to shed light on each eruption episode.

5.4.2 Eruption cycle and atmosphere-lithosphere coupled modes

Figure 5.8 displays the amplitude spectra of the 12-hour vertical-component seismograms for the Tonga explosion compared with the 1991 eruption of Mt. Pinatubo in the Philippines. Many earlier studies have reported the observations of acoustic resonant oscillations between the atmosphere and solid Earth during large volcanic eruptions, such as the 1991 Pinatubo (Kanamori & Mori, 1992; Watada & Kanamori, 2010) and the 2014 eruption of Mt. Kelud in Indonesia (Nakashima et al., 2016). In particular, Earth's spheroidal modes at 3.7 and 4.4 mHz tend to be coupled strongly with the fundamental and higher modes of atmospheric normal modes (Watada & Kanamori, 2010). Compared with the other two eruptions in Pinatubo and Kelud, the amplitude spectra for the Tonga eruption are characterized by the remarkable peak at 3.7 mHz, while the other two eruptions exhibit more prominent peaks at 4.4 mHz or higher frequencies (Watada & Kanamori, 2010; Nakashima et al., 2016). Matoza et al. (2022) has reported the marked spectral peak at 3.7 mHz for the Hunga-Tonga eruption, which was globally observed in seismic ground motions.

The time intervals of explosions in the first sequence (Figure 5.6) from our BP analysis suggest that the explosive eruptions of Hunga Tonga intermittently occurred at nearly 270–280 s intervals, corresponding to the eigenfrequencies of the atmosphere-lithosphere coupled spheroidal mode at 3.7 mHz. Such a quasi-periodic eruption sequence has not been observed clearly in earlier studies based on lower-frequency information. This is an unexpected outcome from the BP analysis using teleseismic

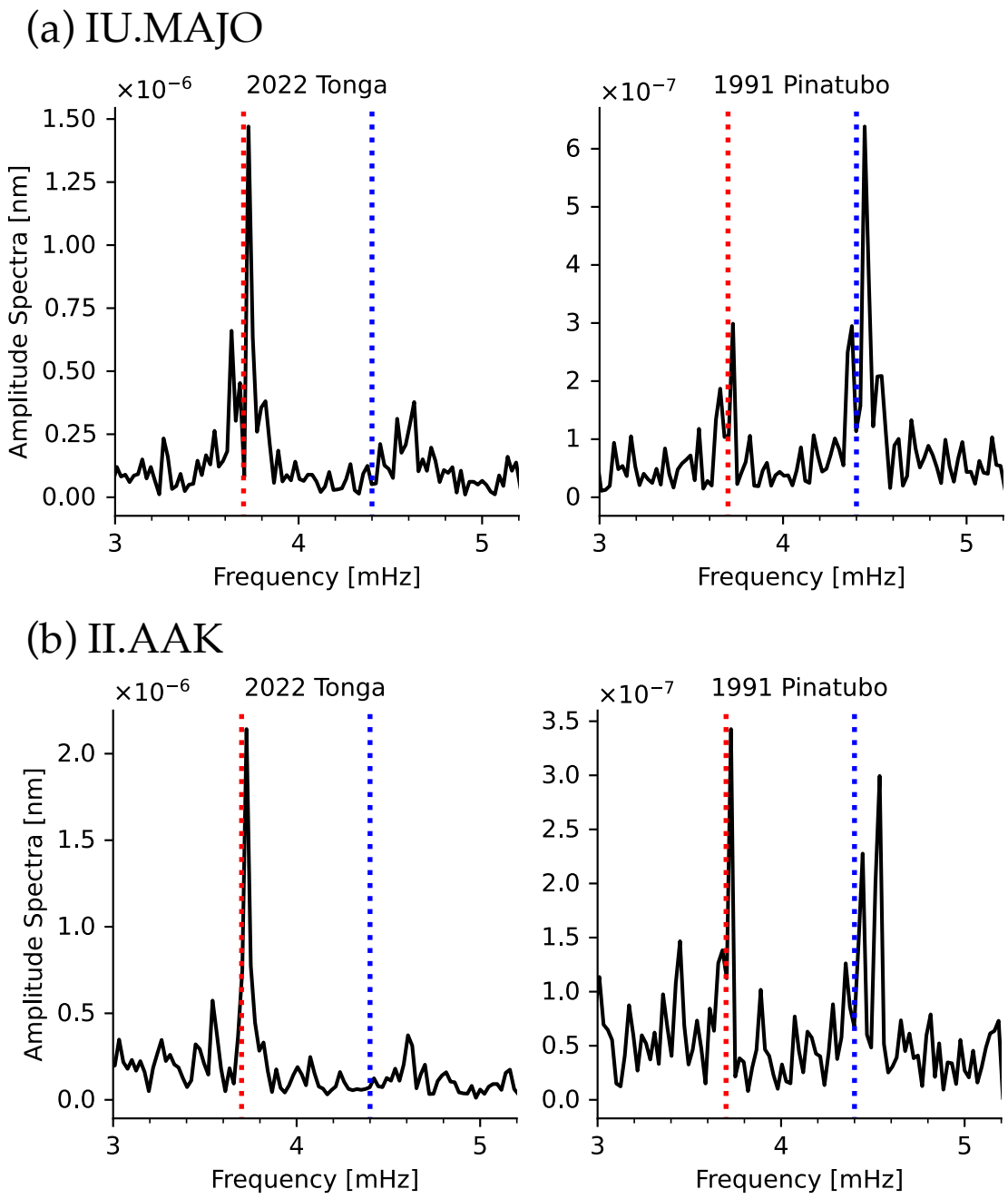

Figure 5.8: Amplitude spectra of vertical-component seismograms for two stations, (a) MAJO and (b) AAK. Left and right panels in (a) and (b) show the amplitude spectra for the 2022 Tonga and 1991 Pinatubo eruptions, respectively. Red and blue dashed lines indicate 3.7 mHz and 4.4 mHz.

P-waves. Owing to the greater resolution of P-waves at a higher frequency, we could resolve the detailed time series of explosive events.

The coincidence of the prominent spectral peak at 3.7 mHz and the eruption cycles with the interval of about 270–280 s indicate that the timing of subsequent eruptions after the first massive explosion at Hunga Tonga may be synchronized with the eigenperiod of the atmosphere-lithosphere coupled normal mode. As a plausible mechanism of such resonance, we may envisage that the pressure change caused by the atmospheric free oscillations from the first large explosion (event F), which coupled with the Earth's spheroidal mode, may have induced the subsequent explosions (i.e., events I, L, and N). Alternatively, there may be a possibility that the timing of volcanic processes of the submarine volcano, including phreatomagmatic explosions, matched coincidentally with the eigenperiod of the atmosphere-lithosphere coupled mode. The detailed mechanisms of such a quasi-periodic eruption cycle may be worth further investigation.

5.5 Conclusions

In this study, we performed the back-projection analysis using the teleseismic P-waves to clarify the detailed eruption processes of the Hunga Tonga-Hunga Ha'apai volcano on January 15, 2022. Our findings in this study can be summarized as follows.

1. The Tonga eruption comprises two distinctive sequences.

2. The first sequence started at 04:02 UTC and continued for about 30 minutes at least. The most intensive eruption occurred at 04:15 UTC and 200–300 seconds afterward. The Hunga Tonga-Hunga Ha'apai eruption comprised at least 3 major explosions (evens F, H, and I in Figures 3 and 4) and a number of moderate explosive events.

3. The second sequence started about 4 hours after the end of the first sequence and continued for about 6–7 minutes, which comprised 5 moderate explosive eruptions.

4. The origin times of explosive events determined in this study are well matched with the surface wave trains at a relatively higher frequency (0.01–0.08 Hz).

5. The intermittent eruption cycles of about 270–280 s in the first sequence may have been synchronized with the eigenfrequency of atmospheric resonant oscillations with the Earth at 3.7 mHz.

Chapter 6

Frequency-dependent seismic radiation process of the 2024 Noto Peninsula earthquake from teleseismic P-wave back-projection

6.1 Introduction

On January 1st, 2024, a large and devastating earthquake with a moment magnitude (Mw) of 7.5 (Dziewonski et al., 1981; Ekström et al., 2012) occurred in the Noto Peninsula in Japan, causing widespread destruction and collapse of numerous buildings, with over 400 casualties reported by the Fire and Disaster Management Agency (FDMA; FDMA (2024)) of Japan. Several locations recorded the maximum seismic intensity of 7, the highest on the Japan Meteorological Agency (JMA) scale, with the Noto Peninsula experiencing strong ground motion and coastal uplift. This earthquake also generated a tsunami with a maximum height of 5 meters, which was observed not only around the peninsula but also in Korea, North Korea, and Russia (Fujii & Satake, 2024; Mizutani et al., 2024).

This destructive earthquake has been identified as a thrust fault based on local JMA (2024a) and global seismic waveform analyses (e.g., global CMT; Dziewonski et al., 1981; Ekström et al., 2012) (Figure 6.1). The aftershock distribution provided by JMA indicates that the source fault length extends to about 150 km (JMA, 2024a) (blue dots in Figure 6.1), which is more extensive than other inland earthquakes of similar magnitude in Japan. In addition, the fault geometry appears complex; the inland region mainly dips toward the southeast, while the offshore region may involve northwest-dipping faults. Several studies have analyzed the seismic source process using the seismic records from near-field and teleseismic stations, geodetic data (e.g.,

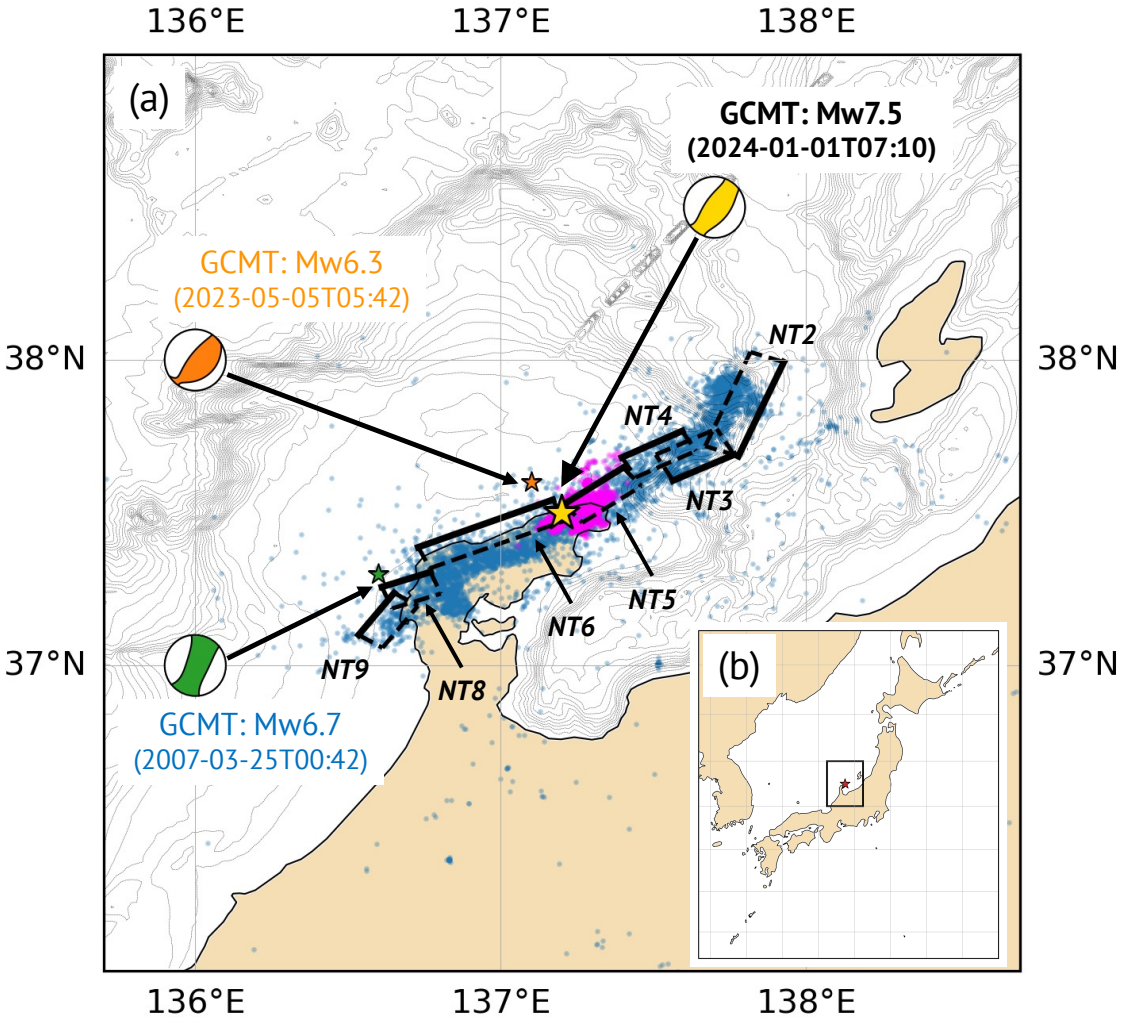

Figure 6.1: (a) The locations of the Mw 7.5 2024 Noto Peninsula Earthquake on January 1st, 2024, and its aftershocks as well as recent large earthquakes in our study area. All origin times are in UTC. The yellow star and focal mechanism represent the epicenter of the Mw 7.5 event on January 1st, 2024, and its focal mechanism from Global CMT (Dziewonski et al., 1981; Ekström et al., 2012). Blue dots indicate the distribution of aftershocks until January 14th, 2024 (JMA, 2024a). The other two stars and corresponding focal mechanisms denote past large events in 2007 and 2023. Magenta dots represent the preceding seismic events (since November 2020) leading to the Mw 7.5 mainshock, as reported by Yoshida et al. (2023b). Seven black rectangles exhibit the fault models from the Japan Sea earthquake and tsunami project (JSPJ) (MEXT, 2013), NT2, NT3, NT4, NT5, NT6, NT8, and NT9, in which solid black lines indicate the top of each fault. Inset (b) displays a broader-scale map indicating the location of the study area. The black rectangle encompasses the area shown in (a), where the red star marks the epicenter of the Mw 7.5 main event reported by USGS (USGS, 2024).

GNSS), and local tsunami waveforms (e.g., Fujii & Satake, 2024; Okuwaki et al., 2024; Mizutani et al., 2024; Kutschera et al., 2024; Ma et al., 2024; Xu et al., 2024). Many of these studies have identified two large-slip areas in the western inland and eastern offshore regions of the Noto Peninsula, resulting from bilateral rupture propagation from the hypocentral region toward these slip areas.

Seismic swarms have occurred near the hypocenter of the Mw 7.5 event since November 2020 (e.g., Amezawa et al., 2023; Nishimura et al., 2023; Yoshida et al., 2023a), likely driven by the upward migration of fluid (Nishimura et al., 2023). The presence of high pore pressure may be related to the complex fault rupture processes, such as super-shear rupture (Pampillón et al., 2023). Additionally, fluids can effectively weaken the fault cohesion, possibly causing the fault to slip more easily (Gabriel et al., 2012; Madden et al., 2022). Earlier works employing seismic data (Okuwaki et al., 2024; Kutschera et al., 2024; Ma et al., 2024; Xu et al., 2024) suggest that the complex source process within the intricate fault network may be controlled by upward-migrating crustal fluids. Interestingly, Kutschera et al. (2024) argued that the fault rupture may have been renucleated in the hypocentral region 20 s after the origin time (2024-01-01T07:10:10 UTC), which may result from the fault weakening by the high pore pressure. Meanwhile, Yoshida et al. (2024) relocated the aftershock distribution and discussed the relationships among the local seismicity, the Mw 7.5 earthquake, hidden faults, and the upward migrating fluid. Investigations into this devastating Mw 7.5 earthquake are crucial for understanding the influence of the crustal fluids on fault behavior.

The frequency dependence of the rupture process remains a controversial topic in seismic source studies (Koper et al., 2011; Ishii, 2011; Koper et al., 2012; Yagi et al., 2012). Low-frequency signals are particularly useful for imaging the macroscopic rupture process, as they are sensitive to regions of large slip. High-frequency seismic energy radiation, on the one hand, is essential for understanding the complexities of the seismic source process (e.g., Okuwaki et al., 2018). Previous studies including theoretical analysis, laboratory experiment, and seismic waveform analysis have shown that high-frequency P-waves can reflect abrupt changes in slip and/or rupture velocity on the fault surface (e.g., Bernard & Madariaga, 1984; Spudich & Frazer, 1984; Beresnev,

2017), as well as the fault roughness, such as the fault barriers and branching (e.g., Adda-Bedia & Madariaga, 2008; Uchide et al., 2013; Bruhat et al., 2016; Okuwaki & Yagi, 2017). Furthermore, many classical studies suggest that high-frequency radiation coincides with the termination of fault rupture or slip, a phenomenon known as the stopping phase (e.g., Savage, 1965; Bernard & Madariaga, 1984). Thus, incorporating both high- and low-frequency teleseismic signals enables a comprehensive understanding of earthquake rupture process across a broad range of frequencies.

For the Noto peninsula earthquake, Okuwaki et al. (2024) and Kutschera et al. (2024) highlighted the complexities of the fault geometry through sophisticated teleseismic waveform inversion, which may have contributed to the generation of high-frequency seismic waves. In the Mw 7.9 Türkey-Kahramanmaras earthquake, Mai et al. (2023) used teleseismic P-wave back-projection in two frequency bands (0.1–0.5 Hz; 0.5–1.0 Hz) to detect the stopping phase, which has proven useful for investigating the mechanisms of small earthquakes (e.g., Imanishi & Takeo, 1998, 2002), resulting from abrupt rupture termination. High-frequency seismic waves are crucial for understanding complex seismic source processes, making frequency-dependent radiation analysis valuable in elucidating the mechanisms of this devastating earthquake.

In this study, we investigate frequency-dependent seismic-wave radiation processes using the back-projection (BP) of teleseismic P-waves across multiple frequency ranges (0.03–0.3 Hz; 0.05–0.5 Hz; 0.1–1.0 Hz; 0.3–2.0 Hz). By analyzing the time series of BP images for different frequency ranges, we explore the relationship between high-frequency seismic wave radiation and the large-scale rupture process characterized by lower-frequency P-wave radiation.

6.2 Data and Method

This earthquake is listed as two separate events in the earthquake catalog of the Japan Meteorological Agency (JMA, 2024a); M_{jma} 5.9 and M_{jma} 7.6. However, for the purpose of our analysis, we treat these two earthquakes as a single Mw 7.5 event.

6.2.1 Multi-frequency Teleseismic P-wave

We used three-component seismograms at global seismic stations downloaded from the IRIS Data Management Center. Prior to waveform processing, we removed the instrument response from the raw data, converted them to displacement waveforms, and resampled them at 0.1 s intervals.

Our data selection method generally follows Tarumi & Yoshizawa (2023). First, we selected seismic stations located between 30° and 95° from the epicenter, as our target phase is the teleseismic P-wave. Second, we grouped displacement waveforms based on a cross-correlation coefficient (CC) greater than 0.7 and corrected the travel time using the lag time to account for 3-D structural effects. In this process, the time window was set to 15 s before and 15 s after the theoretical P-wave arrival times based on the AK135 model (Kennett et al., 1995). Finally, we retained the group containing the largest number of waveforms for the back-projection analysis.

To estimate the frequency-dependent seismic radiation, we applied multiple band-pass filters to three-component seismograms with multiple frequency ranges: 0.03-0.3 Hz, 0.05-0.5 Hz, 0.1-1.0 Hz, and 0.3-2.0 Hz. The prescribed waveform-selection steps were conducted in each frequency range. Figure 6.2 shows an example of our teleseismic dataset for the lowest-frequency range, 0.03-0.3 Hz, while Figures E.1, E.2, and E.3 in Appendix E display the datasets for the other frequency bands. For all frequency bands used in this study, our teleseismic datasets exhibit good azimuthal coverage (e.g., Figure 6.2), ensuring high resolution in the back-projection analysis (e.g., Okuwaki et al., 2014; Kiser & Ishii, 2017).

6.2.2 Back Projection with LQT coordinate system

Seismic back-projection (BP) analysis time-reverses observed seismograms to the source time and locations from which the target seismic phase is radiated. BP was originally developed to image the rupture evolution (Ishii et al., 2005, 2007) and has been widely used in seismic source studies involving the detection of aftershocks hidden in large earthquakes (e.g., Kiser & Ishii, 2013a), the estimation of tsunami-generating regions (Mizutani & Yomogida, 2022), and tracking the eruption sequence on the 2022 Tonga eruption (Tarumi & Yoshizawa, 2023).

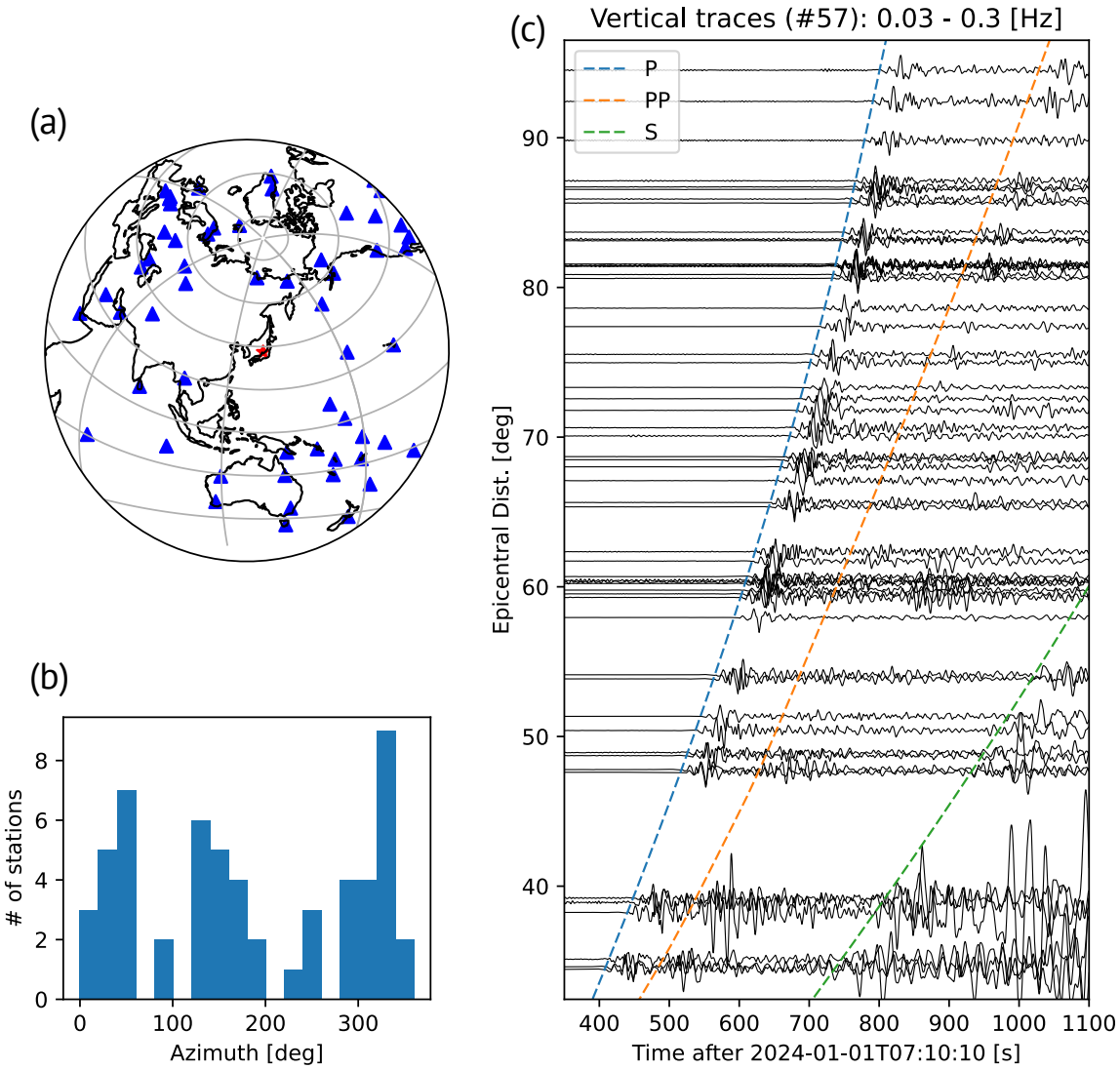

Figure 6.2: Teleseismic waveform dataset used for the BP analysis with a frequency range of 0.03-0.3 Hz. (a) Map of the stations used. The red and blue triangles indicate the hypocenter and seismic stations, respectively. (b) Histogram of the azimuths from the source to the stations. (c) Vertical-component seismograms, scaled by the maximum amplitude of direct P phase. The blue, orange, and green lines represent the travel-time curves for P, PP, and S waves, respectively.

BP analysis has generally been performed using the vertical-component seismograms (e.g., Ishii et al., 2007; Kiser & Ishii, 2013b; Xu et al., 2009; Okuwaki et al., 2014; Kehoe et al., 2019; Tarumi & Yoshizawa, 2023), as teleseismic P-waves are primarily recorded in the vertical component. However, the particle motion of teleseismic P-waves is inclined, involving some amount of signals in the horizontal (radial) component, even at epicentral distances of around 90°. This inclination increases at stations closer to the source. Thus, to consider the total amplitude of P-waves, it is preferable to incorporate the two horizontal components in addition to the vertical component. In this study, we employ the LQT coordinate system (also known as the ray-coordinate system) (Vinnik, 1977) to implement the BP analysis (hereafter referred to as the LQT-BP method). Figure 6.3 illustrates the ray-coordinate system. This new coordinate system, commonly used in receiver function studies (e.g., Kind & Yuan, 2011), is derived by rotating the three-component seismograms into the direction of the P-wave incidence (L), the perpendicular direction to the L-component (Q), and the transverse direction (T) (Vinnik, 1977) (Figure 6.3). The use of the LQT system enhances the direct P-wave signal, potentially leading to more refined BP images.

In our BP analyses, we utilized the N-th root stacking method (Rost & Thomas, 2002), which effectively enhances coherent signals. This robust stacking approach has been applied in many previous BP studies (Xu et al., 2009; Honda et al., 2011, 2013; Mizutani & Yomogida, 2022; Tarumi & Yoshizawa, 2023), enabling us to suppress noises and to enhance the BP images for target signals, such as P-waves.

Our LQT-BP analysis can be formulated as follows,

$$L'_j(t, \mathbf{x}_j) = \frac{1}{M} \sum_{i=1}^{M} \mid l_i(t + \tau_{ij}) \mid^{\frac{1}{N}} \cdot \mathrm{sgn}(l_i(t + \tau_{ij})) \tag{6.1}$$

$$L_j(t, \mathbf{x}_j) = \mid L'_j(t) \mid^{N} \cdot \mathrm{sgn}(L'_j(t, \mathbf{x}_j)) \tag{6.2}$$

where M is the number of stations, τ_{ij} the predicted arrival time between the i-th station and the j-th source grid, l_i an L-component seismogram at the i-th station, $\mathbf{x}_j$ the coordinate point of j-th source grid, and $L_j(t)$ the stack of L-component waveforms at the j-th source grid associated with the total radiation power of seismic waves. In this study, we adopted $N = 4$ for all frequency ranges. Finally, to extract the

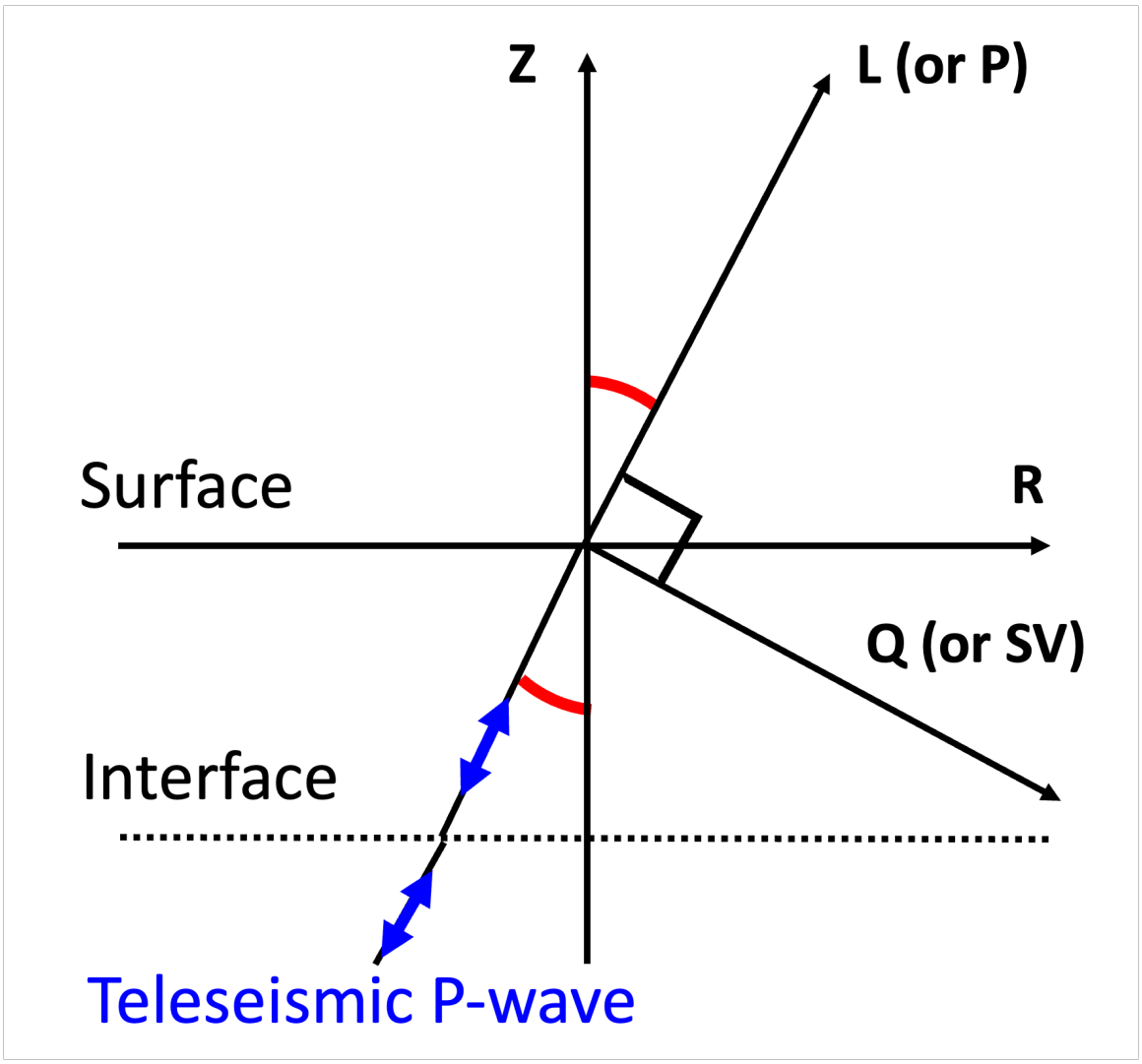

Figure 6.3: Schematic illustration of the LQT coordinate system at a seismic station.

spatiotemporal radiation intensity $BP(t, \mathbf{x}_j)$, we integrate $L_j(t, \mathbf{x}_j)$ as follows,

$$BP(t, \mathbf{x}_j) = \frac{1}{\delta t} \int_{t-\delta t}^{t+\delta t} L_j(t^{'}, \mathbf{x}_j) dt^{'}, \tag{6.3}$$

where δt represents an integration interval. In this study, the interval is adaptively defined as half of the averaged period $T^{'}$ for each frequency range, with a minimum δt of 1 second.

The LQT-BP method employed in this study requires both the travel time and the incident angle of the P-wave before stacking (eqs. (6.1) and (6.2)). To calculate the theoretical arrival times and incident angles of P-waves, we used a 1-D spherical structure model AK135 (Kennett et al., 1995). Potential source grids are distributed between $-1.5°$ and $+1.5°$ around the epicenter (E137.2, N37.5) at a depth of 10 km, sufficiently covering the potential source region (Figure 6.1). The source grid interval is set to 0.05°, except for the highest frequency range (0.3–2.0 Hz), where it is reduced to 0.015° to take account of the shorter wavelength.

6.3 Results

Our BP analysis successfully estimated the frequency-dependent P-wave radiation process. The results are displayed in Figures 6.4 and 6.5. Figure 6.4 presents the multi-frequency BP snapshots at 5-second intervals, with the fault models from the Japan Sea earthquake and tsunami project (JSPJ; MEXT (2013)) superimposed. Figure 6.5 shows a temporal radiation power of P-waves for each frequency band. Figure 6.6 shows the time evolution of P-wave radiation, projected along the N60°E line, with the projected points indicated in Figure E.4.

Across all frequency ranges, the radiation areas cover the JSPJ fault model (black dotted squares in Figures 6.4). The P-wave radiation extended from the epicenter toward the western inland and eastern offshore regions (Figure 6.4) and persisted for approximately 44 s, with peak radiations occurring 30-40 s after the origin time (07:10:10 UTC) (Figure 6.5). The radiation sequence can be divided into four main episodes (Figures 6.6): [E1] initial radiation near the hypocenter (0–18 s), [E2] intense high-frequency radiation between the initial stage and the subsequent main radiation phases (18–28 s), [E3] strong radiation in the inland region of the Noto Peninsula (25-44 s),

and [E4] significant radiation in the eastern offshore region (25-44s). Hereafter, in each episode, relatively higher-frequency P-wave radiations are denoted with a superscript prime (e.g., E1′ for higher frequency signals corresponding to the first episode, E1).

The rupture episodes characterized by low-frequency radiation are consistent with previous studies using teleseismic P-waves (Okuwaki et al., 2024; Kutschera et al., 2024; Ma et al., 2024; Xu et al., 2024), which identified a bilateral rupture propagating toward the southwest inland and eastern offshore regions from the hypocenter over approximately 40 s. However, prior to this main bilateral migration, during [E2], high-frequency P-waves (0.1–1.0 Hz and 0.3–2.0 Hz, E2′) were radiated intensely from the hypocentral area between 18–25 s, despite the absence of low-frequency energy (Figures 6.4, 6.5, and 6.6), a distinct feature of this Mw 7.5 earthquake.

Figure E.5 displays the BP results derived from conventional BP imaging using only the vertical component of P-waves. The LQT-BP results (Figures 6.4 and 6.5) resemble those from the traditional BP (Figure E.5), but the LQT-BP method slightly enhances the P-wave sources, suggesting that the ray-coordinate system allows us to extract P-wave amplitudes effectively. Still, for the discussion of the source rupture process, the choice of a coordinate system for stacking seismograms seems not to be critical.

6.3.1 E1: Initial radiation around the hypocenter (0–18 s)

This episode corresponds to the initial rupture stage of the Mw 7.5 earthquake in the hypocentral area. At this initial stage, relatively high-frequency P-wave radiation (0.3–2.0 Hz, E1′) is observed preceding the low-frequency component near the hypocenter during the first 0–10 s (Figures 6.4 (d) and 6.6 (d)). Between 10 and 15 s, the main seismic radiation shifts to the lower-frequency range (0.05-0.5 Hz), which becomes the dominant seismic energy source in this stage. The seismic radiation then fades (Figures 6.4 (b) and 6.6 (b)). The early stage of this episode (0–10 s) may be comparable to the initial quiet slip and slow rupture process described by Okuwaki et al. (2024), Ma et al. (2024), and Xu et al. (2024).

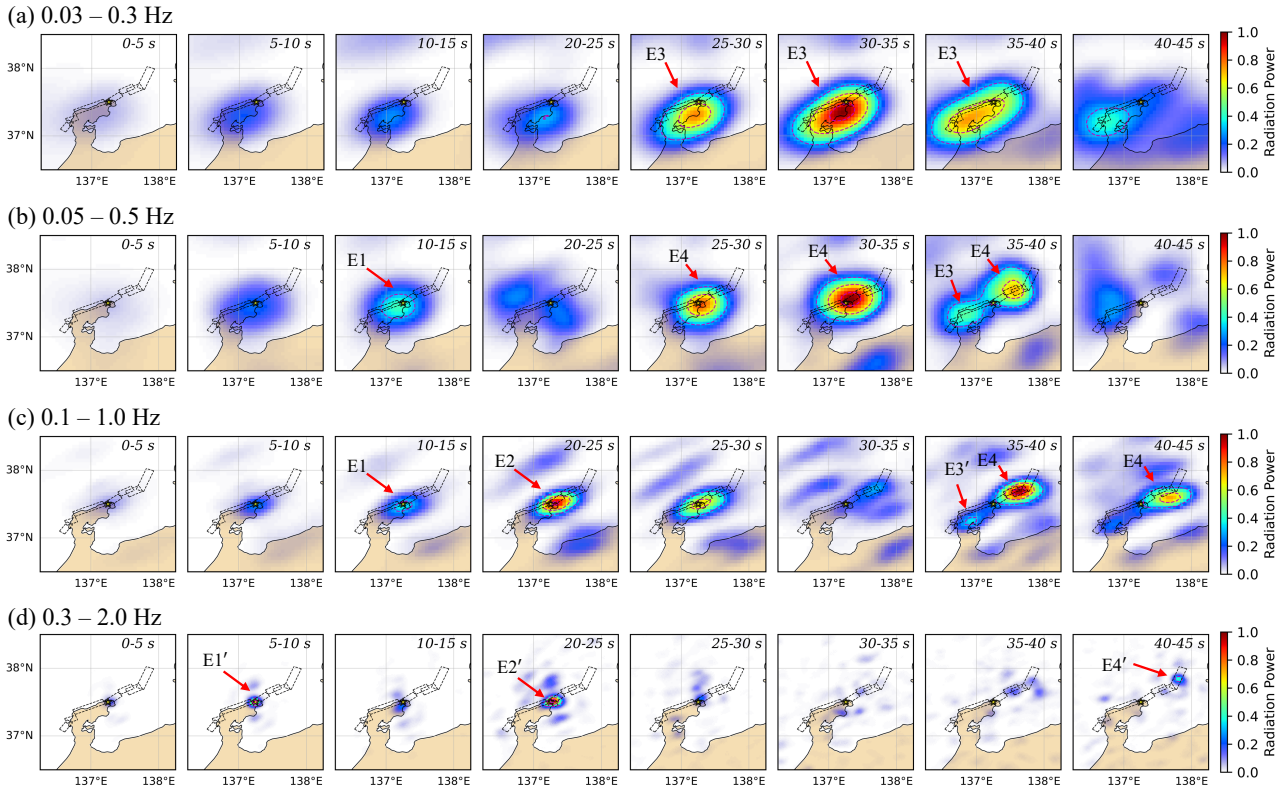

Figure 6.4: BP snapshots with 5-second intervals for multiple frequency bands: (a) 0.03–0.3 Hz, (b) 0.05–0.5 Hz, (c) 0.1–1.0 Hz, and (d) 0.3–2.0 Hz. Rectangles with black dotted lines represent the fault models from the JSPJ (MEXT, 2013), NT2, NT3, NT4, NT5, NT6, NT8, and NT9, marked in Figure 6.1. Yellow stars indicate the epicenter of the Mw 7.5 event (USGS, 2024), which occurred at 07:10:10 (UTC). Magenta thin contour lines show radiation intensities at 30 %, 60 %, and 90 %. Radiation power is normalized to the maximum value for each frequency band. The red arrows highlight the locations of notable higher-frequency (HF) radiation (E1′, E2′, E3′, and E4′) and the corresponding lower-frequency radiation (E1, E2, E3, and E4).

6.3.2 E2: High-frequency radiation lacking low-frequency (18–28 s)

Between 18 and 28 s, intense high-frequency P-waves radiation (0.1–2.0 Hz, E2′) emerges from the hypocentral region, while low-frequency P-waves (0.03–0.5 Hz) are notably absent. This frequency-dependent behavior is reflected in the time-dependent radiation power (Figure 6.5). The highest-frequency P-wave radiation is concentrated around the hypocenter between 18 and 25 s (E2′), during which low-frequency radiation temporarily ceases (Figures 6.4, 6.5, and 6.6), creating a hole in the low-frequency radiation. During this gap, the high-frequency component (0.1–2.0 Hz) dominates the total radiation power (Figure 6.5). This distinct high-frequency radiation may be essential to understanding the rupture process of this Mw 7.5 earthquake, possibly serving as a bridge between the initial stage (E1) and the main rupture stages (E3 and E4).

6.3.3 E3: Intense radiation in the inland of the Noto Peninsula (25–44 s)

This episode represents one of the most significant stages of seismic radiation, extending across the entire peninsula (Figure 6.4 (a)). The dominant frequency content of this episode is in the lowest frequency range (0.03-0.3 Hz) of our analysis. The substantial low-frequency radiation propagates toward the southwestern inland areas of the Noto Peninsula from 25 to 44 s (Figure 6.4 (a)). From 28 s to 40 s, the low-frequency P-wave radiation reaches its peak intensity, representing the most powerful phase of this Mw 7.5 earthquake (Figures 6.4 and 6.6). This intense low-frequency radiation may have contributed to the destructive damage in the inland areas of the peninsula. The migration speed of the fault rupture area between 28 and 35 s is estimated to be approximately 3.0 km/s (Figure 6.6). This stage notably lacks high-frequency signals, but after 40 s, the low-frequency radiation gradually diminishes, accompanied by a weak emission of higher-frequency signals (0.1–1.0 Hz, E3′) near the southwestern tip of the peninsula (Figures 6.4 and 6.6).

6.3.4 E4: Intense radiation in the eastern offshore region (25–44 s)

E4 corresponds to intense radiation in the eastern offshore region, primarily within the frequency ranges of 0.05-0.5 Hz and 0.1–1.0 Hz (Figures 6.4 and 6.6). During this stage, the P-wave radiation source propagates from the vicinity of the hypocenter toward the

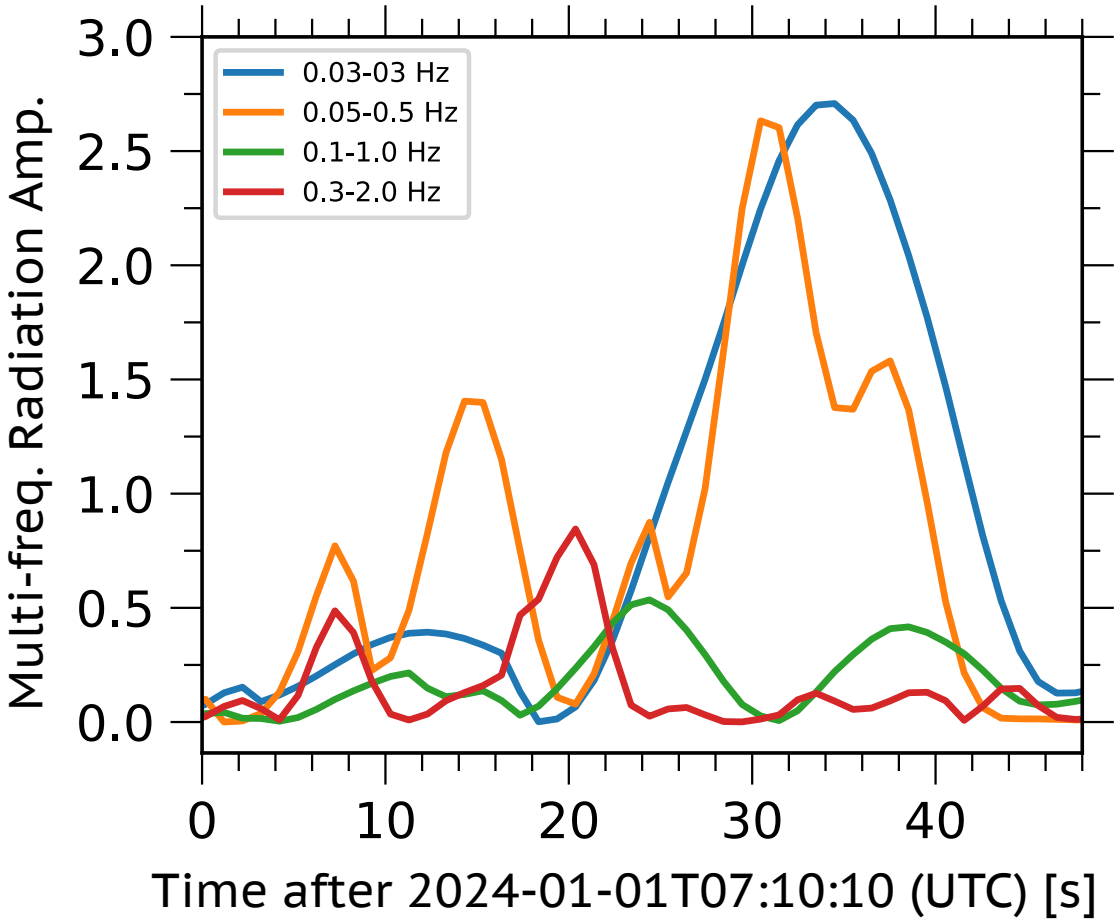

Figure 6.5: P-wave radiation power as a function of time across multiple frequency bands, with colored lines indicating different frequency ranges: blue (0.03–0.3 Hz), orange (0.05–0.5 Hz), green (0.1–1.0 Hz), and red (0.3–2.0 Hz).

eastern offshore region, lasting from 20 to 25 s. The radiation peaks at 30–35 s in the offshore regions, similar to the inland radiation in E3 (Figures 6.4, 6.5, and 6.6), potentially contributing to tsunami generation. The migration speed of the rupture front during this stage is somewhat slower than that in E3, with an estimated speed of less than 3.0 km/s (Figure 6.6). Around 38 s, this stage abruptly ceases seismic radiation, accompanied by a notable increase in higher-frequency P-wave emissions (E4′ in Figures 6.4, 6.5, and 6.6). The location of this frequency transition coincides with the eastern offshore fault (N2) (Figure 6.4 (c,d)).

6.4 Discussion

The resultant BP images reveal a notable frequency dependence, indicating significant complexity in the seismic radiation processes of this Mw 7.5 earthquake. These complex processes may be attributed to crustal fluids that have driven long-term seismic swarms in this region since November 2020 (Amezawa et al., 2023). Nishimura et al. (2023) proposed that the upward migration of fluids weakened fault strength, generating the preceding seismic swarms in the Noto Peninsula. Yoshida et al. (2024) suggested that the crustal fluid may have triggered the main rupture process associated with E3 and E4 in this study. Additionally, Nakajima (2022) identified a high Vp/Vs ratio in the lower crust beneath the hypocentral area, indicating fluid-rich material. The source region for this destructive event comprises a complex fault system (MEXT, 2013). While the southwestern faults dip toward the southeast, the northeastern offshore region has an opposite dipping direction toward northwest (Figures 6.1 and 6.4, and MEXT (2013)), as evidenced by the aftershock distribution (JMA, 2024a). Relocated seismic events also revealed a fault system with multiple hidden faults (Yoshida et al., 2024), suggesting that the hypocentral area likely comprises at least three intersecting faults.

In this section, we first reveal the sources of the prominent highest frequency P-waves (0.3–2.0 Hz), E1′, E2′, and E4′. Such high-frequency P-waves generally reflect complex and smaller-scale fault processes rather than the macroscopic rupture process. Typically, high-frequency seismic signals are generated by rapid changes in rupture and/or slip speed, complex fault branching, and interactions with fault barriers and

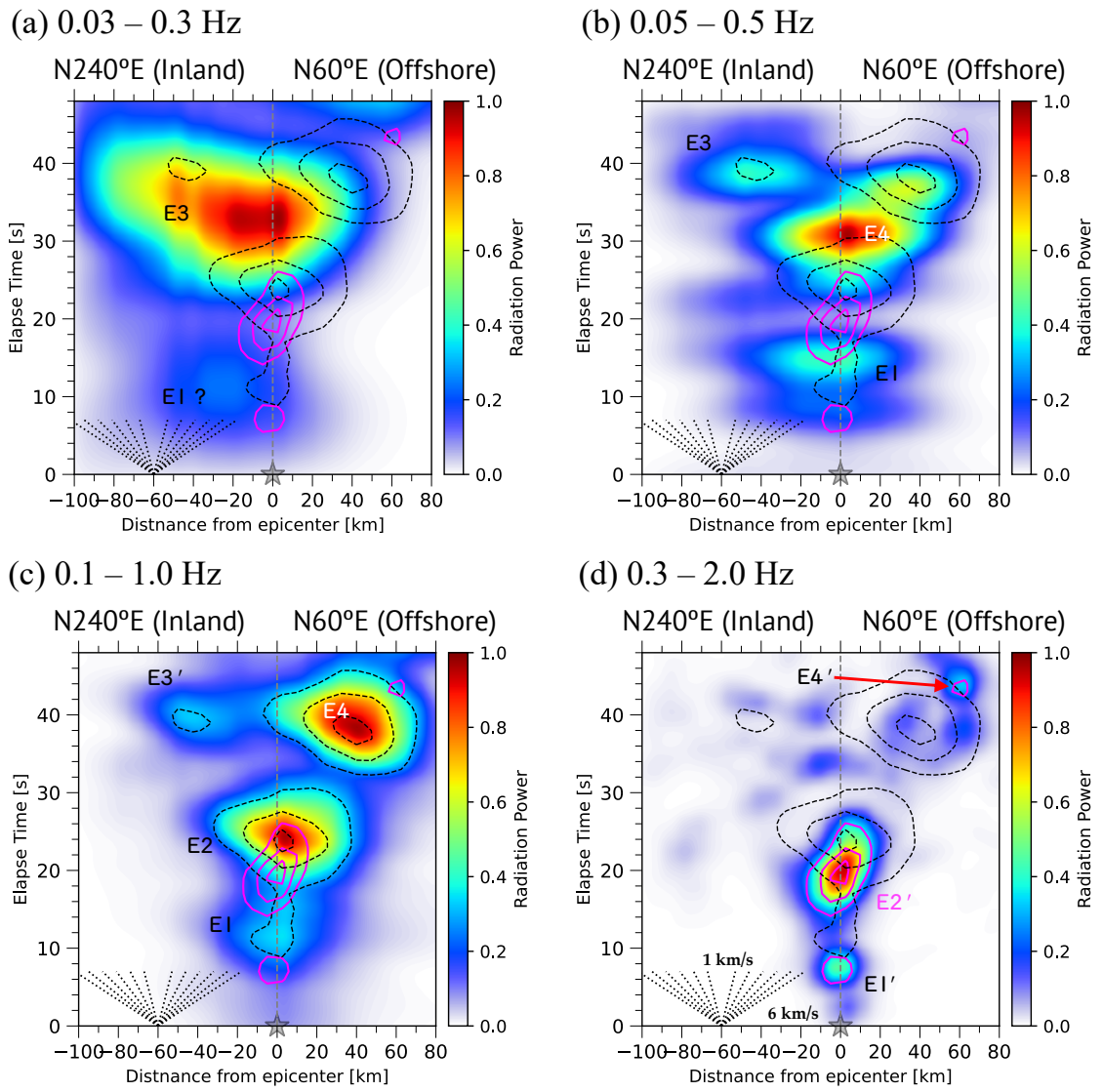

Figure 6.6: Time evolution of P-wave radiation projected along the N60°E line for multiple frequency bands: (a) 0.03–0.3 Hz, (b) 0.05–0.5 Hz, (c) 0.1–1.0 Hz, (d) 0.3–2.0 Hz. Gray stars represent the epicenter. Vertical dashed lines divide the positive and negative sides in the horizontal axis, corresponding to the northeast offshore and southwest inland parts of the Noto Peninsula, respectively. Dashed lines in the lower left indicate rupture velocities, ranging from 1.0 to 6.0 km/s. E1, E2, E3, and E4 represent the radiation episodes identified in this study. In all panels, black and magenta contour lines indicate 30 %, 60 %, and 90 % of the highest-frequency radiation (black dashed: 0.1–1.0 Hz, magenta solid: 0.3–2.0 Hz).

asperities (e.g., Savage, 1965; Madariaga, 1977; Spudich & Frazer, 1984; Bernard & Madariaga, 1984; Madariaga, 2003; Adda-Bedia & Madariaga, 2008; Beresnev, 2017; Marty et al., 2019), all of which are essential for unraveling this complex earthquake. Following the clarification of these smaller-scale complexities in seismic radiation, we further discuss the broader frequency-dependent characteristics of the radiation processes derived from our BP analysis.

6.4.1 E1′: Starting phase of this Earthquake

The first instance of high-frequency radiation, E1′ (Figure 6.6), likely represents the initiation of the fault rupture process or the starting phase (Madariaga, 1977). At the onset of rupture, substantial energy is required to accelerate the rupture rapidly as strain energy is released (Madariaga, 1983). E1′ follows the lower-frequency energy (0.05–1.0 Hz) concentrated near the hypocentral region (Figure 6.6), suggesting that it may be the initial triggering event of this Mw 7.5 earthquake.

Following this initiation phase, the region radiating P-waves does not spread significantly at this stage (Figure 6.4), which could result from a slower rupture speed (Okuwaki et al., 2024; Ma et al., 2024; Xu et al., 2024). Due to the presence of crustal fluid near the hypocentral region (Nakajima, 2022), the rupture front may not accelerate effectively. This observation supports the discussion of fluid-induced slow rupture initiation, accompanied by high-frequency seismic radiation, as proposed by Ma et al. (2024).

6.4.2 E2′: Triggering the low-frequency radiation of E2, E3 and E4

The second event of high-frequency seismic emission (E2′ in Figure 6.6 (d)) likely reflects a secondary initiation within a doublet event sequence. According to the JMA earthquake catalog (JMA, 2024a), this Mw 7.5 earthquake involves two distinct events of M_{jma} 5.9 (at 16:10:9.54) and M_{jma} 7.6 (at 16:10:22.57), where M_{jma} is JMA's magnitude scale based on observed displacement and/or velocity waveform amplitude (JMA, 2024b). The larger event occurred about 10–15 s after the smaller M_{jma} 5.9 foreshock. The timing of E2′ inferred from this study is roughly consistent with the origin time of the larger M_{jma} 7.6 event. Yoshida et al. (2024) relocated the doublets and nearby

earthquakes, suggesting that both the M_{jma} 5.9 foreshock and the M_{jma} 7.6 mainshock occurred on the same fault plane. Thus, E2 in our BP results from teleseismic records likely corresponds to the initiation of the larger mainshock in this doublet earthquakes.

Crustal fluids, identified by an anomalously high Vp/Vs ratio near the E2 location (Figure 6.4 (c, d)) (Nakajima, 2022), likely influence the source of E2. Yoshida et al. (2024) suggested that the foreshock triggered the mainshock through the upward migration of fluids, while Ma et al. (2024) suggested that this earthquake sequence began with a slow rupture in a fluid-rich zone, followed by a faster rupture in a drier region. This sequence may be represented in our BP images: i.e., E1 associated with the initial slow rupture, transitioning to the more rapid rupture propagation of E3 and E4, directed to the west and east, respectively (Figures 6.4 and 6.6). The high-frequency event E2 appears to mark the transition from E1 to the subsequent rapid propagation in E3 and E4 (Figures 6.4, 6.5, and 6.6), acting as a bridge for the abrupt change in rupture speed. While such a transition may occur without elevated pore pressure conditions (e.g., Bruhat et al., 2016), crustal fluids may facilitate the effective acceleration of the rupture front (Pampillón et al., 2023). Consequently, the higher-frequency radiation of E2 may result from a combination of abrupt rupture speed changes due to upward-migrating fluids and the initiation of the secondary event in the doublet earthquakes.

Although the complexity of fault geometry may also play a role (MEXT, 2013; Yoshida et al., 2024; Okuwaki et al., 2024), the lack of high-frequency P-wave radiation during E3 and E4 (except for a minor emission at the end of E4) may indicate limited influence from the complex fault network or heterogeneities such as fault barriers.

6.4.3 E4′: Stopping phase of E4

The fourth high-frequency emission event (E4′ in Figures 6.4 (d) and 6.6 (d)) likely represents the stopping phase of fault rupture in the northeastern offshore area of the Noto Peninsula, coinciding with the location of the offshore fault N2 (MEXT, 2013) shown in Figure 6.1. Classical studies have shown that abrupt rupture termination can effectively generate high-frequency seismic energy (Savage, 1965; Madariaga, 1977). Fault slip models by Fujii & Satake (2024) and Mizutani et al. (2024), based on geodetic

and tsunami waveform data, suggested that the northeastern offshore fault N2 did not slip. Besides, seismic waveform inversions including the near-field data (Ma et al., 2024; Xu et al., 2024) found minimal slip on the northeastern offshore fault patch. These observations agree well with our results, which indicate a stopping phase at the northeastern end of the source region near the N2 fault.

6.4.4 Frequency-dependent P-wave radiation and complex fault rupture process

The low-frequency BP image (0.03-0.5 Hz) reveals the large-scale rupture process, which is consistent with other results of seismic waveform inversions (Okuwaki et al., 2024; Kutschera et al., 2024; Ma et al., 2024; Xu et al., 2024), indicating the bilateral rupture from the hypocentral location. Unlike these previous studies, our multi-frequency BP approach uncovers complex frequency-dependent characteristics in P-wave radiation from the complicated rupture process of multiple fault segments. The most prominent P-wave radiation observed in this study occurs in the lowest-frequency range (0.03–0.3 Hz) in the inland regions of this peninsula (E3), and another notable low- to intermediate-frequency (0.05–0.5 Hz) radiation mainly originates from the northeastern offshore region (E4) (Figure 6.4-(a, b)). Note that intense high-frequency components (0.1–2.0 Hz) precede these dominant lower-frequency radiations. In this subsection, we discuss the relationship between these lower- and higher-frequency radiation processes in more detail.

A distinct transition in the frequency components of radiated P-waves from high (0.1–2.0 Hz) to low (0.03–0.5 Hz) frequencies after 18 seconds is clearly shown in Figures 6.4 and 6.6. E3 appears to be triggered by the high-frequency emission event E2, transitioning smoothly into an intense low-frequency emission (0.03–0.3 Hz) (Figures 6.4 and 6.6). Notably, after this frequency transition, E3 radiates almost no higher-frequency radiation and gradually fades after 40 s (Figures 6.4 and 6.6) . This behavior can be attributed to near-surface shallow large slip as inferred from the previous waveform inversions (Okuwaki et al., 2024; Ma et al., 2024; Xu et al., 2024). Fault slips at shallower depths often exhibit longer rise times, as seen in the previous inversion studies of other inland earthquakes (e.g., Ji et al., 2015; Hao et al., 2017). Although the exact depth of the P-wave source remains undetermined due to the lack of depth

resolution, the lowest-frequency P-wave radiation in the southwestern inland region persists somewhat longer than in any other areas (Figure 6.4 and 6.6). Consequently, E3 may not release intense high-frequency energy due to the relatively low slip rate at shallow depths, while the crustal fluid may contribute to further suppressing the higher-frequency signals.

At the end of E3, relatively higher-frequency energy (0.05–0.5 Hz and 0.1–1.0 Hz) are emitted from the southwestern tip of the peninsula (E3′ in Figures 6.4 and 6.6), which can be interpreted as the stopping phase of E3. However, this termination does not involve the highest-frequency P-wave, which instead appears in E4. In the recent tomographic model (Nakajima, 2022), an anomalously high Vp/Vs ratio was observed in the southwestern area of the Noto Peninsula. A plausible explanation for this stopping phase without higher-frequency emission could be the fluid-rich conditions in this region (Noda & Lapusta, 2013; Madden et al., 2022).

Meanwhile, from E2 to E4, the frequency components of radiated P-waves evolve continuously. E4 can also be triggered by E2, after which the frequency range of emitted P-waves gradually shifts to lower frequencies (0.05–0.5 Hz) (Figures 6.4 and 6.6), possibly reflecting the evolution process of fault rupture propagation. After around 36 s, an opposite transition occurs, with the main frequency range smoothly shifting from low to high frequencies (Figures 6.4 and 6.6).

A plausible reason for the frequency transition observed toward the end of E4 can be the fault geometry. As suggested by the JSPJ model (MEXT, 2013), aftershock distribution (JMA, 2024a), and the results by Okuwaki et al. (2024), the source region comprises a complex, multi-segmented fault system. Differences in the strike angles are evident between the southwestern inland and northeastern offshore areas. Comparing the two frequency bands (0.05–0.5 Hz and 0.1–1.0 Hz) visualized in Figure 6.4 (b, c), we observe that, despite the limited resolution of teleseismic P-wave data, the higher- and lower-frequency P-waves at 40–45 s are radiated from the locations near NT3 and NT4, respectively (Figure 6.4 (b,c)). NT3 and NT4 have apparently different dipping directions (Figure 6.1 and MEXT (2013)). This significant frequency transition toward the end of E4 may result from such complex multi-segmented fault geometry.

Thus, the intriguing frequency-dependent P-wave radiation sequence of the Mw 7.5

Noto Peninsula earthquake likely results from the effects of the complex fault network under fluid-rich conditions. The presence of crustal fluid may play a key role in triggering the initial stage of this earthquake (E1) and the main bilateral rupture process (E3, and E4). The complex fault geometry beneath this area likely contributes to the observed variations in frequency-dependent behavior between E3 and E4, indicating the influence of the fault geometry on the slip and rupture processes during this earthquake.

6.5 Conclusions

In this study, we performed multi-frequency P-wave back-projection to image the frequency-dependent source radiation process for the Mw 7.5 Noto Peninsula earthquake on January 1st, 2024 (or the doublet earthquake of M_{jma} 5.9 and M_{jma} 7.6). Our main findings on the complex radiation process are summarized in the following points:

1. The main source radiation process of the Mw 7.5 Noto Peninsula earthquake lasted approximately 44 s, which can be divided into four episodes (E1–E4).

2. *Episode 1 (E1, 0–15 s):* The P-wave radiation initiates from the hypocenter, with the intense high-frequency energy preceding the lower-frequency radiation, concentrated mainly in the hypocentral region.

3. *Episode 2 (E2, 15–30 s):* This stage bridges E1 and the subsequent episodes, radiating the most intensive high-frequency P-waves from the hypocentral area. This stage likely represents the initial growth for the larger event in the doublet earthquake sequence.

4. *Episodes 3 and 4 (E3 and E4):* These stages encompass the main rupture process, propagating bilaterally from the hypocentral region towards the southwestern inland and northeastern offshore areas. The rupture during E4 appears to terminate abruptly at the northeastern fault patch, marked by the high-frequency emission at the end of E4.

5. During E3, the low-frequency signals dominate the P-wave radiation, suggesting a relatively longer rise time for the main rupture propagating towards the southwestern inland region.

6. In the initial half of E4, the frequency range of the P-wave radiation transitions smoothly from low to high frequencies, then reverses to a high-to-low frequency transition in the latter half of E4, likely influenced by the complex fault geometry in the northeastern offshore region.

Chapter 7

Summary and prospects for future research

7.1 Summary of this thesis

In this thesis, we explored the upper mantle discontinuities beneath the Australian continent and several seismic wave sources, demonstrating new approaches using teleseismic P-waves:

1. A series of station-based body wave analyses to investigate the upper mantle structure, including the mapping of multiple seismic discontinuities through the application to the Australian continent (Part I).

2. New applications of the back-projection method of teleseismic P waves to image the complex multiple wave sources with applications to the massive volcanic eruption in Tonga and the disastrous earthquake in Japan (Part II).

In Chapter 2, we applied the complex polarization analysis (Vidale, 1986) to almost all broadband seismic stations in Australia to estimate the misorientations of horizontal components using long-period teleseismic P-waves. Using a large number of arrival-angle measurements of P-waves, we compiled a comprehensive catalog of horizontal-component orientations for both permanent and temporary stations in Australia. The waveform analyses in the subsequent two chapters are based on this station-orientation catalog.

In Chapter 3, we incorporated azimuth-dependent P-wave receiver functions (P-RFs) into a joint Bayesian inversion with multimode surface waves (Taira & Yoshizawa, 2020), applying this approach to five permanent broadband stations in Australia. The resulting models showed a clear dependence on the direction of seismic events. By

identifying P-to-S conversion depths from the inverted models, we constructed a localized map of conversion points. We successfully demonstrated the effectiveness of azimuth-dependent P-RFs in detecting localized changes in the upper mantle discontinuities and their associated elastic properties, providing new insights into the complex layering of the upper mantle.

In Chapter 4, we extensively applied the joint inversion method to a large number of permanent and temporary seismic stations across Australia to map the upper mantle discontinuities. The mapped lithosphere-asthenosphere boundary (LAB) is shallow (70–100 km) in Phanerozoic eastern Australia and deepens toward western cratonic regions (120–200 km). Beneath central Australia, we observed a thick lithosphere (170–200 km) with significant radial anisotropy but minimal S-velocity reductions. For the mid-lithospheric discontinuity (MLD) and X-discontinuity (X-D), statistical cluster analysis of locally detected discontinuities revealed multiple depths. In cratonic regions, MLDs were identified at three distinct depths (from 60 to 130 km), exhibiting either negative or positive S-velocity changes depending on the tectonic setting. X-Ds, characterized by velocity increases beneath the LAB, were detected at multiple depths (∼170 km, 220–280 km, and ∼310 km) and were commonly associated with a weakening of radial anisotropy below the X-Ds. This study provided a comprehensive view of the upper mantle discontinuities beneath Australia and offered new insights into the tectonic evolution of the Australian continent.

In Chapter 5, we demonstrated that teleseismic P-wave back-projection (BP) analysis is a powerful tool for unraveling the sequence of multiple explosive eruptions. The BP results successfully detected the locations and timings of individual explosions, even when the P-waves from each eruption overlapped and were masked by other seismic signals and noises. Besides, our results suggested that the eruption cycle may be synchronized with the eigenperiod of the atmosphere-lithosphere coupled mode, a phenomenon related to the Earth's free oscillations (e.g., Kanamori & Mori, 1992; Watada & Kanamori, 2010).

We investigated the frequency-dependent seismic radiation process of the 2024 Noto earthquake using the multi-frequency teleseismic P-wave BP in Chapter 6. We incorporated the ray-coordinate system (Vinnik, 1977) to enhance the P-wave signals

during the stacking process. The resulting source process revealed complex frequency-dependent behavior, with ruptures propagating bilaterally from the hypocentral area toward the southwestern inland and northeastern offshore regions. The fluid-rich condition near the hypocenter likely played a significant role in controlling fault rupture, contributing to the observed complex rupture processes. In addition, the intricate fault geometry in the source region may have influenced the characteristic frequency-dependent P-wave radiation observed during this earthquake.

In summary, Part I demonstrated that our new approach for utilizing P-RF is effective for both localized and large-scale investigations of upper mantle discontinuities and their elastic natures. Part II introduced new applications of the BP method, enabling the tracking of intermittent and continuous multiple sources and resolving frequency-dependent radiation processes linked to complex rupture dynamics. In essence, observed teleseismic body waveforms retain plentiful information about seismic structures and wave sources, making them invaluable for investigating seismic phenomena. Through the application of new approaches, teleseismic data-oriented studies enable us to deepen our understanding of the Earth's dynamics processes.

7.2 Future prospects

To conclude this thesis, we discuss potential future directions for advancing the use of teleseismic body waves in structural and source studies.

7.2.1 Extending station-orientation catalog

In Chapter 2, we constructed a comprehensive station-orientation catalog for the Australian broadband seismic stations and demonstrated its importance for accurate waveform analysis, especially when using the horizontal components of seismograms. This issue has long been recognized in seismology, as highlighted by earlier studies (Laske, 1995; Laske & Masters, 1996; Yoshizawa et al., 1999), which emphasized the influence of sensor misorientation on surface wave analyses. It remains a challenge in both inland and ocean bottom observations (e.g., Deng et al., 2024; Ai et al., 2024). This work represents a fundamental step in seismic waveform analyses and provides a basic framework for future studies. Extending such catalog to other permanent and tempo-

rary seismic networks will enhance the accuracy and reliability of waveform analysis in a variety of future seismological research.

7.2.2 Additional constraints on the localized seismic discontinuity image

Azimuth-dependent radial P-RFs provide valuable information on localized shapes of seismic discontinuities. In Chapters 3 and 4, we incorporated these into a joint inversion approach with surface wave dispersions (SWDs). However, synthetic waveform modeling in complex media and their comparisons with observed data will offer a more sophisticated approach for investigating such features (e.g., Frederiksen & Bostock, 2000). Also, the harmonic decomposition approach (e.g., Park & Levin, 2016) can be a useful tool for determining the dipping angle of seismic interfaces.

Besides, we observed back-azimuthal variations in P-wave polarization anomaly data, which can be highly sensitive to lateral heterogeneities and anisotropic properties (e.g., Crampin et al., 1982; Bokelmann, 1995; Frederiksen & Bostock, 2000). Further investigations of these variations will enable us to estimate horizontal velocity gradients at discontinuity depths, providing potentially beneficial information for understanding seismic interfaces (e.g., Fontaine et al., 2009).

In the future, integrating these seismological approaches and additional datasets derived from teleseismic P-waves could offer new constraints on the trends and physical properties of the seismic discontinuities identified in this study.

7.2.3 Azimuthal anisotropy

Seismic azimuthal anisotropy reflects past deformation and/or present mantle dynamics, providing valuable information to understand the dynamics processes in the Earth (e.g., Vinnik et al., 1992). As described in Chapters 3 and 4, the mid-lithospheric discontinuity, which can be a potential key to unraveling tectonic history, may be related to a complex anisotropic layering system.

Earlier works have estimated the anisotropic structure beneath the Australian continent using surface-wave tomography and PKS/SKS (XKS) splitting analyses, discussing the tectonic history and mantle dynamics. However, these remain subjects of ongoing debate (e.g., Debayle et al., 2005; Fishwick et al., 2008; Eakin et al., 2021,

2023; Ba et al., 2023; de Laat et al., 2023). In addition, Chen et al. (2021b) and Birkey & Ford (2023) used azimuth-dependent P-RFs to demonstrate that MLD depths are indicative of a complex anisotropic layering. Beyond Australia, studies of the Superior and Wyoming cratons in North America have also suggested the role of azimuthal anisotropy in lithospheric depths (e.g., Yuan & Romanowicz, 2010; Bodin et al., 2016; Ford et al., 2016; Chen et al., 2021b). In this thesis (Chapters 3 and 4), however, we resolved radial anisotropy by jointly analyzing multimode Rayleigh and Love wave dispersion data but did not include the effects of azimuthal anisotropy. Incorporating azimuthal anisotropic structures in future studies of the Australian continent could significantly enhance our current knowledge of upper mantle discontinuities.

Azimuth-dependent P-RFs, as used in Chapters 3 and 4, are among the most effective tools for investigating anisotropic layered structures and lateral variations in seismic interfaces (e.g., Levin & Park, 1997; Nagaya et al., 2008; Park & Levin, 2016). Previous studies have developed and applied advanced methods to retrieve complex anisotropic characteristics from azimuth-dependent radial and transverse P-RFs, including the harmonic decomposition (e.g., Shiomi & Park, 2008; Bianchi et al., 2010; Park & Levin, 2016), splitting analysis of P-to-SH conversion phases (e.g., Nagaya et al., 2011; Tonegawa et al., 2024), and receiver function inversions (Frederiksen et al., 2003). Moreover, Bodin et al. (2016) developed a trans-dimensional hybrid Bayesian approach that combines azimuth-dependent radial RFs, SKS phases, and surface wave dispersion data to simultaneously constrain both layered seismic wave speeds and vertical variations in the fast-axis direction.

In addition to azimuth-dependent RFs, P-wave polarization anomaly data can be used to constrain azimuthal anisotropy, as they are sensitive to anisotropic structures (Crampin et al., 1982). Schulte-Pelkum et al. (2001) pioneered the use of P-wave polarization anomaly data to estimate the azimuthal anisotropy in the upper mantle, which was further applied by Fontaine et al. (2009) and Cristiano et al. (2016). The polarization data obtained in Chapter 2 clearly exhibited dependencies on the incoming directions of teleseismic P-waves, likely reflecting the complex lateral heterogeneity and anisotropic structure beneath the Australian continent. Further analyses of this polarization data set may provide independent insights, complementing those from the

XKS splitting and surface wave studies.

7.2.4 Applications to other regions: Global perspectives on seismic discontinuities

This thesis applied the proposed approach of azimuth-dependent P-RFs in Chapters 3 and 4 to investigate the spatial distribution, elastic properties, and the origin of upper mantle discontinuities beneath the Australian continent. Specifically, the characteristics of MLDs were found to depend on the tectonic setting of Australia, potentially reflecting the ancient history of the Earth (Chapter 4). Recent observations have also identified MLDs in oceanic plates (e.g., Ohira et al., 2017; Chen et al., 2024), implying that MLDs are not confined to cratonic regions. Applying our approach to other continental and oceanic regions will provide further geophysical insights into the nature of MLDs, enabling a deeper understanding of these enigmatic features through global comparisons across cratonic and oceanic regions (e.g., Chen et al., 2021b; Krueger et al., 2021). Additionally, such investigations may provide us with more detailed images of X-Ds, which have been sporadically detected in global studies (e.g., Deuss & Woodhouse, 2002; Pugh et al., 2021), enhancing our understanding of their properties and origins.

7.2.5 Capturing multiple earthquakes or non-earthquake sources

Seismic events involving multiple sources often challenge our ability to interpret and detect them accurately, which can obstruct automatic detection systems and lead to greater risks during destructive disasters. For example, the 2021 South Sandwich Island Mw 8.2 Earthquake likely involved multiple sources generating tsunamis, making it difficult for automatic systems to detect individual sources of the event (e.g., Metz et al., 2022; Jia et al., 2022). Also, non-earthquake events, such as volcanic eruptions, also generate complex seismic waveforms. These volcanic events are often characterized by multiple explosions (Matoza et al., 2022; Mizutani & Melgar, 2023; Sandanbata et al., 2024) and/or exhibit frequency-dependent wave radiation (Fontaine et al., 2019; Poli & Shapiro, 2022; Svennevig et al., 2024). The back-projection (BP) method is a powerful tool for resolving such overlapping waveforms from multiple events and analyzing frequency-dependent radiation processes (Chapters 5 and 6). Since teleseismic P-waves

are the fastest-arriving seismic phase compared to surface waves or other phases, P-wave BP has great potential for the early detection and localization of enigmatic seismic wave sources, whether from multiple earthquake sources or non-earthquake events.

Appendix A

Supplementary information for Chapter 2

In this Appendix, we provide supplemental information for Chapter 2.

A.1 Station-orientation table

This section includes supporting tables referenced in Chapters 2–4. Table A.1 presents the station orientation catalog for permanent stations except for the S1 network. The details of the tabulated parameters are summarized in the caption in Table A.1. Tables A.2 and A.3 are the same as Table A.1 but for the S1 network and temporary stations, respectively.

Table A.1: Station orientation catalog for permanent stations except for the S1 network. The first column includes the network code and station name. The second and third columns represent the period (start and end time) used for calculating two statistical values: the median station orientation (fourth column) and its standard errors (fifth column). The last column indicates the number of earthquakes used to estimate the misorientation during the designated period.

Network.Station	Start Time	End Time	Median [deg]	Std. err [deg]	Nev
AU.ARMA	2004-11-09T21:48:34.105000Z	2019-12-31T23:59:59.000000Z	2.28	0.22	588
AU.ARPS	2019-06-25T00:00:00.000000Z	2019-12-31T23:59:59.000000Z	-9.37	4.36	6
AU.AS31	2006-06-07T05:38:00.000000Z	2019-12-31T23:59:59.000000Z	-4.35	0.42	561
AU.BBOO	2004-11-09T21:48:37.220000Z	2008-11-24T00:00:00.000000Z	-2	0.43	159
AU.BBOO	2008-11-24T00:00:00.000000Z	2019-12-31T23:59:59.000000Z	3.62	0.14	652
AU.BLDU	2004-11-09T21:48:33.800000Z	2008-05-12T00:00:00.000000Z	-11.88	0.24	142
AU.BLDU	2008-05-12T00:00:00.000000Z	2019-12-31T23:59:59.000000Z	12.72	0.16	657
AU.CMSA	2008-01-23T00:00:00.000000Z	2019-12-31T23:59:59.000000Z	5.16	0.42	508
AU.CNB	2007-08-10T02:32:30.594500Z	2019-12-31T23:59:59.000000Z	-3.55	0.18	645
AU.COEN	2003-06-14T00:00:00.000000Z	2005-08-15T00:00:00.000000Z	-17.24	1.23	20
AU.COEN	2005-08-15T00:00:00.000000Z	2013-10-01T00:00:00.000000Z	2.62	0.29	333
AU.COEN	2013-10-01T00:00:00.000000Z	2017-12-01T00:00:00.000000Z	19.97	0.78	104
AU.COEN	2017-12-01T00:00:00.000000Z	2019-12-31T23:59:59.000000Z	-1.41	0.47	81
AU.CTA	2005-01-31T00:00:00.000000Z	2019-12-31T23:59:59.000000Z	0.81	0.19	538
AU.EIDS	2003-06-23T00:00:00.019500Z	2007-08-03T00:00:00.000000Z	-7.39	0.74	130
AU.EIDS	2007-08-03T00:00:00.000000Z	2019-12-31T23:59:59.000000Z	5.09	0.29	534
AU.FITZ	2004-12-15T00:00:00.000000Z	2019-12-31T23:59:59.000000Z	-2.27	0.25	427

Table A.1: Station orientation catalog for permanent stations except for the S1 network. The first column includes the network code and station name. The second and third columns represent the period (start and end time) used for calculating two statistical values: the median station orientation (fourth column) and its standard errors (fifth column). The last column indicates the number of earthquakes used to estimate the misorientation during the designated period.

Network.Station	Start Time	End Time	Median [deg]	Std. err [deg]	Nev
AU.FORT	2003-06-19T00:00:00.000000Z	2011-01-23T00:00:00.000000Z	4.36	0.38	69
AU.FORT	2011-01-23T00:00:00.000000Z	2019-12-31T23:59:59.000000Z	1.37	0.18	404
AU.GIRL	2009-06-22T00:00:00.000000Z	2019-12-31T23:59:59.000000Z	-1.38	0.18	373
AU.HTT	2010-03-15T00:00:00.000000Z	2019-12-31T23:59:59.000000Z	-6.29	0.23	399
AU.INKA	2013-07-17T00:00:00.000000Z	2019-12-31T23:59:59.000000Z	0.27	0.63	37
AU.KDU	2012-05-23T00:00:00.000000Z	2019-12-31T23:59:59.000000Z	-2.57	0.24	311
AU.KELC	2019-01-01T00:00:00.000000Z	2019-12-31T23:59:59.000000Z	-9.05	1.26	19
AU.KMBL	2004-11-09T21:48:40.360000Z	2009-09-17T00:00:00.000000Z	6.62	0.28	202
AU.KMBL	2009-09-17T00:00:00.000000Z	2016-11-09T00:00:00.000000Z	7.81	0.29	203
AU.KMBL	2016-11-09T00:00:00.000000Z	2019-12-31T23:59:59.000000Z	1.28	0.41	93
AU.KNRA	2008-08-21T00:00:00.000000Z	2019-12-31T23:59:59.000000Z	1.5	0.37	356
AU.LCRK	2013-06-16T00:00:00.000000Z	2019-12-31T23:59:59.000000Z	-1.57	0.24	252
AU.LHI	2007-09-03T04:36:09.594500Z	2008-04-15T00:00:00.000000Z	31.47	0.81	16
AU.LHI	2008-04-15T00:00:00.000000Z	2019-12-31T23:59:59.000000Z	4.3	0.39	117
AU.MANU	2009-05-26T00:00:00.000000Z	2018-07-18T00:00:00.000000Z	1.62	0.89	107
AU.MANU	2018-07-18T00:00:00.000000Z	2019-12-31T23:59:59.000000Z	-27.05	3.47	18
AU.MAW	2003-01-31T00:00:00.000000Z	2019-12-31T23:59:59.000000Z	2.89	0.16	666
AU.MCQ	2004-06-28T00:00:00.000000Z	2019-12-31T23:59:59.000000Z	3.42	0.64	44
AU.MEEK	2008-05-12T00:00:00.000000Z	2019-12-31T23:59:59.000000Z	2.08	0.17	574
AU.MGBR	2019-06-24T00:11:23.600000Z	2019-12-31T23:59:59.000000Z	4.37	1.83	30
AU.MILA	2012-11-27T00:00:00.000000Z	2014-12-31T00:00:00.000000Z	1.68	0.55	44
AU.MILA	2014-12-31T00:00:00.000000Z	2016-06-22T00:00:00.000000Z	-2.51	1.63	22
AU.MILA	2016-06-22T00:00:00.000000Z	2018-10-12T00:00:00.000000Z	82.67	0.92	18
AU.MILA	2018-10-12T00:00:00.000000Z	2019-08-21T23:59:59.000000Z	16.74	1.11	17
AU.MILA	2019-08-21T23:59:59.000000Z	2019-12-31T23:59:59.000000Z	6.45	1.02	12
AU.MOO	2005-05-20T01:36:40.000000Z	2007-01-25T00:00:00.000000Z	-13.84	1.58	21
AU.MOO	2007-01-25T00:00:00.000000Z	2019-12-31T23:59:59.000000Z	1.09	0.16	530
AU.MORW	2008-06-03T00:05:17.594500Z	2019-12-31T23:59:59.000000Z	-0.08	0.17	665
AU.MTN	2006-08-11T00:00:00.000000Z	2019-12-31T23:59:59.000000Z	-1.09	0.16	650
AU.MULG	2013-05-28T00:00:00.000000Z	2019-12-31T23:59:59.000000Z	4.99	0.36	219
AU.MUN	2001-05-30T00:00:00.000000Z	2010-11-18T00:00:00.000000Z	-2.47	0.68	110
AU.MUN	2010-11-18T00:00:00.000000Z	2019-12-31T23:59:59.000000Z	-3.41	0.28	424
AU.NFK	2008-05-20T00:00:00.000000Z	2019-03-26T05:26:20.000000Z	0.81	0.5	150
AU.NFK	2019-03-26T05:26:20.000000Z	2019-12-31T23:59:59.000000Z	40.39	1.58	9
AU.NIUE	2007-06-21T00:00:00.000000Z	2019-12-31T23:59:59.000000Z	4.02	0.6	123
AU.NRFK	2006-09-26T00:00:00.000000Z	2008-4-23T00:00:00.000000Z	6.92	3.08	15
AU.NWAO	2005-01-31T13:00:00.000000Z	2019-12-31T23:59:59.000000Z	-0.07	0.35	171
AU.OOD	2013-07-17T00:00:00.000000Z	2019-12-31T23:59:59.000000Z	0.99	0.4	251
AU.PSA00	2011-01-01T00:00:00.000000Z	2019-12-31T23:59:59.000000Z	2.6	0.28	234
AU.PSAB2	2011-01-01T00:00:00.000000Z	2019-12-31T23:59:59.000000Z	0.8	0.49	71
AU.PSAC1	2011-01-01T00:00:00.000000Z	2019-12-31T23:59:59.000000Z	-2.29	0.65	75
AU.PSAC2	2011-01-01T00:00:00.000000Z	2019-12-31T23:59:59.000000Z	-0.69	0.72	45
AU.PSAD1	2011-01-01T00:00:00.000000Z	2019-12-31T23:59:59.000000Z	-3.35	0.16	279
AU.QIS	2009-10-01T00:00:00.000000Z	2019-12-31T23:59:59.000000Z	-3.41	0.18	447
AU.QLP	2009-07-10T00:00:00.000000Z	2013-06-26T00:00:00.000000Z	-0.99	0.81	62
AU.QLP	2013-06-26T00:00:00.000000Z	2019-12-31T23:59:59.000000Z	-5.36	0.79	40
AU.RABL	2009-04-26T00:00:00.000000Z	2019-12-31T23:59:59.000000Z	-5.78	0.38	271
AU.RIV	2012-11-28T00:00:00.000000Z	2019-12-31T23:59:59.000000Z	0.34	0.49	76
AU.RKGY	2019-02-19T00:00:00.000000Z	2019-07-15T00:00:00.000000Z	-25.1	1.6	9
AU.RKGY	2019-07-15T00:00:00.000000Z	2019-12-31T23:59:59.000000Z	-1.44	1.25	16
AU.SDAN	2018-06-10T00:00:00.000000Z	2019-12-31T23:59:59.000000Z	-1.49	0.65	48
AU.STKA	2003-05-20T16:41:00.000000Z	2003-11-11T23:59:59.000000Z	-0.14	0.64	23
AU.STKA	2003-11-11T23:59:59.000000Z	2019-12-31T23:59:59.000000Z	30.98	0.15	899
AU.TOO	2003-06-25T00:00:00.000000Z	2019-12-31T23:59:59.000000Z	-1.2	0.15	658
AU.WRKA	2009-04-26T00:00:00.000000Z	2019-12-31T23:59:59.000000Z	-3.23	0.19	542

Table A.1: Station orientation catalog for permanent stations except for the S1 network. The first column includes the network code and station name. The second and third columns represent the period (start and end time) used for calculating two statistical values: the median station orientation (fourth column) and its standard errors (fifth column). The last column indicates the number of earthquakes used to estimate the misorientation during the designated period.

Network.Station	Start Time	End Time	Median [deg]	Std. err [deg]	Nev
AU.XMIS	2005-08-16T00:00:00.000000Z	2019-12-31T23:59:59.000000Z	-3.36	0.45	166
AU.YAPP	2018-06-27T23:00:32.875000Z	2019-12-31T23:59:59.000000Z	-13	0.45	55
AU.YNG	2004-04-16T00:00:00.000000Z	2017-02-23T02:00:00.000000Z	8.73	0.31	429
AU.YNG	2017-02-23T02:00:00.000000Z	2019-12-31T23:59:59.000000Z	56	1.21	42
G.CAN	1987-11-27T00:00:00.000000Z	2019-12-31T23:59:59.000000Z	0.58	0.12	1450
II.TAU	1994-01-17T00:00:00.000000Z	2019-12-31T23:59:59.000000Z	-0.5	0.11	1004
II.WRAB	1994-03-27T00:00:00.000000Z	2019-12-31T23:59:59.000000Z	-1.98	0.19	954
IU.CTAO	1991-06-17T00:00:00.000000Z	2019-12-31T23:59:59.000000Z	-1.07	0.14	1477
IU.HNR	2004-10-01T00:00:00.000000Z	2019-12-31T23:59:59.000000Z	11.24	0.84	248
IU.MBWA	2001-08-25T00:00:00.000000Z	2019-12-31T23:59:59.000000Z	0.62	0.14	1051
IU.NWAO	1991-11-25T00:00:00.000000Z	2001-09-13T04:50:00.000000Z	5.82	0.19	365
IU.NWAO	2001-09-13T04:50:00.000000Z	2019-12-31T23:59:59.000000Z	-0.59	0.14	820
IU.PMG	1993-09-10T00:00:00.000000Z	2019-12-31T23:59:59.000000Z	0.09	1.15	31

Table A.2: Same as Table A.1, but for the S1 network stations.

Network.Station	Start Time	End Time	Median [deg]	Std. err [deg]	Nev
S1.AUALB	2013-09-26T00:00:00.000000Z	2019-12-31T23:59:59.000000Z	-1.78	1.61	18
S1.AUALC	2015-08-19T00:00:00.000000Z	2019-12-31T23:59:59.000000Z	-6.37	3.53	8
S1.AUAYR	2013-08-26T00:00:00.000000Z	2019-12-31T23:59:59.000000Z	-4.21	1.4	8
S1.AUCAS	2013-08-26T00:00:00.000000Z	2019-12-31T23:59:59.000000Z	-0.9	6.81	18
S1.AUDCS	2013-05-30T00:00:00.000000Z	2019-12-31T23:59:59.000000Z	0.27	0.87	11
S1.AUDHS	2013-08-26T00:00:00.000000Z	2019-12-31T23:59:59.000000Z	1.61	1.81	20
S1.AUHAR	2014-09-18T00:00:00.000000Z	2019-12-31T23:59:59.000000Z	-3.63	1.2	6
S1.AUHPC	2013-05-24T00:00:00.000000Z	2019-12-31T23:59:59.000000Z	-0.31	3.09	19
S1.AUKAL	2013-09-26T00:00:00.000000Z	2019-12-31T23:59:59.000000Z	4.07	12.16	16
S1.AUKAR	2013-09-15T00:00:00.000000Z	2019-12-31T23:59:59.000000Z	3.77	3.74	5
S1.AUKSC	2013-05-24T00:00:00.000000Z	2019-12-31T23:59:59.000000Z	13.83	3.44	10
S1.AULHS	2013-10-31T00:00:00.000000Z	2019-12-31T23:59:59.000000Z	-2.56	2.39	10
S1.AUMTS	2011-09-01T02:22:00.000000Z	2019-12-31T23:59:59.000000Z	-2.3	0.56	26

Table A.3: Same as Table A.1, but for temporary stations.

Network.Station	Start Time	End Time	Median [deg]	Std. err [deg]	Nev
1E.SQA01	2013-11-17T00:58:59.000000Z	2014-11-10T15:22:20.620000Z	3.5	2.37	7
1E.SQA06	2013-11-13T03:48:59.000000Z	2014-10-14T05:20:27.020000Z	1.12	1.93	6
1E.SQA09	2013-11-14T04:42:59.000000Z	2014-11-02T17:29:06.360000Z	15.64	1.36	7
1E.SQA11	2013-11-14T00:26:59.000000Z	2014-11-06T09:31:39.640000Z	9.19	1.34	7
1K.FA10	2013-11-06T08:51:59.000000Z	2015-09-05T10:26:37.380000Z	0.05	0.68	38
1K.FA15	2013-11-16T23:06:59.000000Z	2015-09-05T16:55:18.660000Z	-13	0.54	18
1K.FA22	2013-11-08T06:57:59.000000Z	2014-09-03T11:07:39.340000Z	-2.02	1.18	15
1K.FA27	2013-11-15T07:08:59.000000Z	2015-09-08T01:45:32.060000Z	-3.62	0.71	30
1K.FA30	2013-11-07T07:40:59.000000Z	2014-09-25T00:36:32.020000Z	-9.47	1.09	9
1K.FA36	2013-11-16T03:26:59.000000Z	2014-10-09T00:40:00.140000Z	-11.31	0.79	13
1K.FB01	2013-11-12T04:16:59.000000Z	2015-09-09T12:11:27.900000Z	-13.05	0.87	24
1K.FB02	2014-02-23T03:35:59.000000Z	2015-08-13T00:23:36.400000Z	-7.5	0.59	20
1K.FB03	2013-11-13T08:30:59.000000Z	2015-09-05T03:15:22.140000Z	-8.29	0.78	24
1K.FB04	2013-11-10T07:59:59.020000Z	2015-09-10T07:36:17.140000Z	-2.18	0.73	24
1K.FB05	2013-11-12T06:46:59.000000Z	2015-04-23T15:33:44.620000Z	-4.86	1.6	11
1K.FB07	2014-02-23T08:05:59.000000Z	2015-09-13T13:42:50.660000Z	-11.54	0.67	33
1K.FB08	2014-02-23T02:39:59.000000Z	2015-08-31T00:54:58.720000Z	-9.11	0.6	34
1K.FC42	2014-10-14T05:09:59.000000Z	2015-08-15T15:13:01.200000Z	-0.74	0.87	11
1K.FD54	2014-10-16T04:53:59.000000Z	2015-08-22T10:36:17.020000Z	4.95	1.28	8
1K.FD56	2014-10-15T07:15:59.000000Z	2015-09-01T15:59:05.800000Z	-4.34	0.92	13
1P.BA05	2011-06-02T21:40:59.000000Z	2012-05-13T05:08:45.140000Z	21.05	0.67	11
1P.BA06	2011-07-08T02:21:59.000000Z	2012-07-11T05:12:47.060000Z	-2.78	0.88	6
1P.BA08	2011-06-09T03:44:59.000000Z	2012-09-04T01:17:49.460000Z	-3.55	1.03	13
1P.BA09	2011-06-11T04:59:59.000000Z	2012-09-01T05:27:54.260000Z	-4.34	1.73	8
1P.BA10	2011-06-17T23:40:57.000000Z	2012-08-06T05:56:48.020000Z	-0.24	0.7	14
1P.BA11	2012-01-18T03:38:59.000000Z	2012-08-06T03:00:41.300000Z	3.22	1.13	10
1P.BA12	2011-06-15T06:30:43.000000Z	2013-04-22T03:44:00.980000Z	-36.34	0.88	9
1P.BA13	2011-06-16T01:44:59.000000Z	2013-04-22T23:04:00.980000Z	-1.8	0.81	26
1P.BA14	2011-06-16T05:42:59.000000Z	2013-04-23T01:38:00.980000Z	-0.72	0.59	23
1P.BA19	2011-06-18T02:15:19.000000Z	2013-04-24T23:08:00.980000Z	-2.68	0.75	16
1P.BA20	2011-06-20T02:37:59.000000Z	2013-04-26T02:12:00.980000Z	4.62	0.43	21
1P.BA22	2011-06-21T01:46:59.000000Z	2013-04-28T01:21:00.980000Z	-1.63	0.68	16
6F.BL01	2008-09-14T00:20:59.000000Z	2010-12-20T11:28:00.980000Z	4.35	0.82	17
6F.BL02	2008-09-13T06:13:59.000000Z	2011-02-20T00:00:00.980000Z	3.2	0.74	13
6F.BL03	2008-09-13T01:15:10.000000Z	2011-02-15T07:55:00.960000Z	3.88	0.35	62
6F.BL04	2008-09-12T05:21:59.000000Z	2010-02-28T10:56:00.980000Z	5.86	0.73	22
6F.BL05	2008-09-12T00:51:59.000000Z	2009-09-12T23:36:00.980000Z	0.95	0.4	38
6F.BL06	2008-09-11T01:38:17.000000Z	2011-03-22T02:06:00.980000Z	-1.36	0.43	91
6F.BL07	2008-09-11T07:01:02.000000Z	2011-05-16T02:17:00.980000Z	0.64	0.66	43
6F.BL08	2008-09-10T05:26:59.000000Z	2011-02-15T12:15:00.980000Z	5.86	0.61	49
6F.BL09	2008-09-10T00:49:26.000000Z	2011-05-16T04:41:00.980000Z	-1.36	0.29	88
6F.BL10	2008-09-09T07:10:59.000000Z	2011-05-16T02:07:00.980000Z	1.08	0.34	82
6F.BL11	2008-09-09T01:26:15.000000Z	2011-05-17T00:51:00.980000Z	0.4	0.36	125
6F.BL12	2008-09-08T07:58:15.000000Z	2011-05-17T04:40:00.980000Z	2.92	0.51	59

Table A.3: Same as Table A.1, but for temporary stations.

Network.Station	Start Time	End Time	Median [deg]	Std. err [deg]	Nev
6F.BL13	2008-09-08T01:33:20.000000Z	2011-05-19T04:35:54.980000Z	1.9	0.6	76
6F.BL14	2008-09-03T01:11:59.000000Z	2011-05-18T02:45:00.980000Z	-0.69	0.67	46
6F.BL15	2008-09-02T09:23:59.000000Z	2011-05-18T07:40:00.980000Z	3.05	0.8	24
6F.BL16	2008-09-02T01:04:59.000000Z	2011-03-31T04:13:00.980000Z	-1.27	0.75	26
6F.BL17	2008-09-01T03:51:59.000000Z	2011-05-21T01:03:00.980000Z	1.26	0.4	62
6F.BL18	2008-08-31T08:40:54.000000Z	2010-11-11T02:04:00.980000Z	-0.26	0.48	63
6F.BL19	2008-09-01T00:16:59.000000Z	2011-05-22T00:57:00.980000Z	2.12	0.64	44
6F.BL20	2008-08-31T01:19:59.000000Z	2010-07-12T03:40:00.980000Z	0.7	0.52	67
6F.BL23	2008-08-28T23:59:59.000000Z	2010-10-12T00:10:01.980000Z	1.5	0.27	32
6F.BL24	2008-08-28T02:18:13.000000Z	2011-05-24T00:35:00.980000Z	1.27	0.45	75
6F.BL25	2008-08-27T03:27:11.000000Z	2011-05-09T03:00:00.980000Z	1.99	0.77	14
7B.SA03	1993-05-13T01:16:11.857000Z	1993-10-05T03:22:29.526000Z	1.96	1.22	13
7B.SA04	1993-05-14T06:26:50.846000Z	1993-10-03T22:00:59.799000Z	3.83	0.8	21
7B.SA06	1993-05-05T00:44:49.846000Z	1993-09-01T00:54:49.800000Z	-0.27	0.68	10
7B.SA08	1993-05-03T03:00:57.846000Z	1993-10-10T01:30:52.798000Z	1.67	0.77	6
7B.SC01	1994-05-26T05:45:36.846000Z	1994-10-05T20:48:47.574000Z	1.52	1.1	18
7B.SC03	1994-08-05T09:40:54.846000Z	1994-10-15T19:20:56.806000Z	-5.74	1.63	8
7B.SC05	1994-05-23T05:59:16.381000Z	1994-09-14T06:04:33.250000Z	-1.72	1.97	10
7B.SC06	1994-06-01T00:14:07.846000Z	1994-10-17T03:27:48.800000Z	-3.74	1.56	10
7B.SC10	1994-08-09T03:59:03.846000Z	1994-10-19T13:59:05.639000Z	2.32	1.95	6
7B.SD02	1995-03-20T06:17:29.846000Z	1995-05-07T06:37:31.806000Z	3.04	0.96	10
7B.SD03	1995-03-23T06:11:46.846000Z	1995-08-07T03:08:31.516000Z	2.86	0.68	14
7B.SD05	1995-03-19T04:34:22.846000Z	1995-08-04T14:27:15.963000Z	1.24	1.13	8
7B.SD06	1995-03-18T02:38:46.846000Z	1995-05-24T02:28:48.098000Z	5.14	0.92	12
7B.SD07	1995-03-26T07:49:26.846000Z	1995-07-08T00:00:00.976000Z	-2.88	2.5	6
7B.SD08	1995-03-27T09:03:21.842000Z	1995-08-10T01:25:17.015000Z	-0.31	1.34	12
7B.SD10	1995-03-31T07:38:35.846000Z	1995-06-03T06:48:39.346000Z	0.34	0.92	8
7D.KA02	1997-07-21T03:17:09.846000Z	1997-10-07T08:47:12.016000Z	3.33	1.32	8
7D.KA09	1997-07-27T04:26:09.846000Z	1997-10-13T02:07:21.806000Z	7.98	1.83	10
7F.QA01	1999-03-04T01:17:40.720000Z	1999-06-29T03:28:32.920000Z	8.7	2.32	5
7F.QR01	1999-05-14T13:54:18.760000Z	1999-11-04T05:19:10.800000Z	4.85	0.5	10
7F.QR07	1999-03-24T07:38:11.840000Z	1999-10-28T05:37:15.600000Z	-8.69	1.27	7
7F.QR08	1999-03-22T04:06:11.840000Z	1999-10-04T05:06:19.480000Z	-13.36	1.53	8
7F.QR09	1999-03-22T23:54:37.840000Z	1999-06-12T03:26:16.040000Z	-13.19	0.76	6
7F.QR10	1999-03-24T00:54:45.400000Z	1999-10-27T10:25:02.520000Z	-17.63	1.46	8
7G.WR02	2000-07-15T04:17:48.720000Z	2001-01-29T07:33:21.815300Z	2.24	0.9	12
7G.WR04	2000-07-20T04:04:12.712300Z	2001-01-28T03:34:21.465200Z	2.49	1.36	14
7G.WR05	2000-07-19T02:25:43.720000Z	2001-07-13T02:32:14.820100Z	-3.36	0.74	27
7G.WR06	2000-07-11T04:19:57.720000Z	2001-01-31T07:49:11.102700Z	-8.36	0.67	30
7G.WR07	2000-07-21T06:29:08.720000Z	2000-10-13T02:01:40.299400Z	-2.23	1.33	10
7G.WR08	2000-10-21T06:32:29.719900Z	2001-07-05T03:07:43.343900Z	-1.6	0.81	21
7G.WR09	2000-10-12T02:53:58.720000Z	2001-07-06T04:57:10.175800Z	6.39	1.17	24
7H.TA01	2001-10-04T03:19:27.840000Z	2002-07-18T21:22:44.200000Z	6.49	0.43	6
7H.TA04	2001-10-05T01:46:50.720000Z	2002-07-03T00:37:34.720000Z	-1.45	0.85	10
7H.TA06	2001-10-06T01:14:39.720000Z	2002-08-07T01:04:29.440000Z	-1.29	0.61	7
7H.TA10	2001-10-11T00:36:33.720000Z	2002-08-16T00:54:24.520000Z	-3.13	0.64	11
7H.TA11	2001-10-08T04:35:41.720000Z	2002-08-15T01:58:40.040000Z	4.13	0.38	10
7H.TA12	2001-10-07T23:30:51.720000Z	2002-08-15T00:18:47.280000Z	0.31	1.51	8
7H.TB03	2001-12-13T00:03:48.840000Z	2002-05-15T08:12:10.560000Z	-3.27	1.02	8
7I.GA06	2004-06-05T01:25:40.520000Z	2004-12-31T23:57:33.800000Z	-6.3	0.94	9
7I.GA07	2004-06-05T06:09:39.840000Z	2005-04-14T00:48:40.800000Z	-0.91	1.64	8
7I.GA08	2004-11-19T02:02:38.880000Z	2005-04-14T23:33:46.440000Z	-3.41	0.87	10
7I.TL01	2003-05-28T04:37:01.680000Z	2005-05-23T11:37:32.240000Z	-0.19	0.57	29
7I.TL02	2003-05-29T03:00:28.680000Z	2005-06-02T03:48:31.640000Z	-1.33	0.51	31
7I.TL03	2003-05-26T05:31:03.680000Z	2004-09-27T04:30:17.800000Z	-4.14	0.85	13
7I.TL04	2003-05-27T03:51:59.000000Z	2004-01-01T00:00:00.960000Z	1.44	0.96	15
7I.TL05	2003-05-30T02:28:59.000000Z	2005-06-04T01:28:54.720000Z	-3.84	1.09	6
7I.TL06	2003-05-25T07:28:59.000000Z	2004-11-13T03:44:22.080000Z	-0.67	0.38	57
7I.TL07	2003-05-25T02:21:59.000000Z	2005-03-14T08:00:00.960000Z	1.26	0.52	41
7I.TL08	2003-06-01T02:59:59.000000Z	2005-06-04T02:09:25.440000Z	0.47	0.78	16
7I.TL09	2003-05-23T03:19:59.000000Z	2005-05-27T03:25:33.120000Z	-0.95	1.42	8
7I.TL10	2003-06-02T01:09:34.720000Z	2005-06-05T00:00:39.080000Z	-6.1	0.76	19

Table A.3: Same as Table A.1, but for temporary stations.

Network.Station	Start Time	End Time	Median [deg]	Std. err [deg]	Nev
7I.TL12	2003-05-22T07:16:59.000000Z	2005-11-17T05:02:42.240000Z	-2.25	1.42	23
7I.TL14	2003-05-02T02:59:59.000000Z	2005-08-18T00:00:00.960000Z	-4.37	0.72	38
7I.TL15	2003-05-21T00:27:59.000000Z	2005-08-18T00:00:00.960000Z	-3.83	0.59	26
7I.TL16	2003-05-01T00:29:59.000000Z	2005-04-19T03:09:25.440000Z	2.4	0.94	18
7I.TL17	2003-05-03T03:27:59.000000Z	2005-08-18T00:00:00.960000Z	-1.42	0.4	30
7I.TL18	2003-05-04T01:25:00.840000Z	2005-08-17T23:00:00.960000Z	-7.62	0.75	43
7I.TL19	2003-12-02T03:45:59.000000Z	2004-11-16T03:02:42.240000Z	1.68	2.43	7
7J.CP01	2006-06-18T08:23:52.000000Z	2007-05-25T00:00:00.960000Z	1.28	0.51	40
7J.CP02	2006-06-18T04:36:59.000000Z	2007-04-05T02:00:00.960000Z	3.91	0.42	21
7J.CP03	2006-06-21T07:49:29.000000Z	2007-05-28T00:00:00.960000Z	1.84	0.77	17
7J.CP04	2006-06-22T01:38:46.000000Z	2006-11-24T06:57:00.960000Z	4.85	1.06	20
7J.CP05	2006-06-22T06:26:59.000000Z	2007-05-29T00:00:00.960000Z	8.3	0.56	30
7J.CP06	2006-06-23T07:14:28.000000Z	2007-05-29T00:00:00.960000Z	-2.26	1.07	22
7J.CP08	2006-11-14T23:59:59.000000Z	2007-05-30T06:27:00.960000Z	-1.18	0.63	20
7J.CP09	2006-06-25T07:01:59.000000Z	2007-05-31T00:00:00.960000Z	1	0.96	15
7J.CP10	2006-06-25T02:51:59.000000Z	2007-05-31T00:00:00.960000Z	-1.13	0.71	25
7J.CP11	2006-06-26T03:59:59.000000Z	2007-01-06T00:00:00.960000Z	1.21	0.77	20
7J.CP12	2006-06-26T06:36:20.000000Z	2007-01-06T00:00:00.960000Z	-4.93	0.74	19
7J.CP13	2006-11-17T23:59:59.000000Z	2007-02-06T00:00:00.960000Z	-2.02	1.11	11
7J.CP14	2006-06-27T07:33:59.000000Z	2007-02-06T00:00:00.960000Z	1.24	0.52	34
7J.LP02	2005-10-20T02:44:30.846000Z	2007-01-11T12:21:47.844000Z	-2.88	0.99	12
7J.LP05	2006-02-04T07:22:13.846000Z	2007-02-05T00:00:00.966000Z	4.17	1.53	14
7J.RP01	2006-02-04T03:12:14.846000Z	2007-01-05T00:00:00.966000Z	-6.84	0.78	13
7J.RP03	2006-06-19T03:26:17.000000Z	2007-05-27T00:00:00.960000Z	0.91	0.71	15
7J.RP04	2006-06-21T01:28:59.000000Z	2007-05-27T00:00:00.960000Z	1.64	0.69	18
7J.RP06	2006-06-20T07:46:59.000000Z	2007-05-26T00:00:00.960000Z	2.38	1.73	10
7K.MUR03	2007-02-19T01:06:05.718100Z	2008-04-29T18:05:59.998500Z	-8.29	1.6	7
7K.MUR04	2007-02-20T00:40:11.718000Z	2008-03-07T00:00:01.935400Z	-3.91	0.92	9
7K.MUR05	2007-02-21T06:35:16.718000Z	2008-02-06T00:00:01.669100Z	2.4	0.75	10
7K.SOC03	2007-07-25T06:57:39.720000Z	2008-06-16T23:18:17.921200Z	2.71	1.26	6
7K.SOC04	2008-01-21T22:48:59.000000Z	2008-06-16T00:00:00.960000Z	4.9	1.25	13
7K.SOC05	2007-09-07T23:59:59.000000Z	2008-06-18T23:55:47.520000Z	1.92	1.15	7
7K.SOC06	2007-08-06T03:05:59.000000Z	2008-06-19T05:22:51.840000Z	-2.57	0.85	28
7K.SOC07	2007-10-24T02:08:59.000000Z	2008-08-14T03:53:46.560000Z	0.15	0.5	19
7K.SOC08	2007-10-25T03:27:59.000000Z	2008-08-13T00:00:00.960000Z	1.97	0.46	33
7K.SOC09	2007-10-27T03:02:59.000000Z	2008-08-12T01:22:51.840000Z	-0.08	1.32	12
7K.SOC11	2007-10-28T23:59:59.000000Z	2008-08-10T00:50:24.960000Z	-2.53	1.54	9
7K.SOC12	2007-10-29T02:46:59.000000Z	2008-08-09T02:02:42.240000Z	3.85	0.9	15
7K.SOC13	2007-10-30T03:37:53.000000Z	2008-08-08T00:00:00.960000Z	0.96	0.65	29
7K.SOC14	2007-10-31T02:28:59.000000Z	2008-07-09T00:00:00.960000Z	0.74	1.58	8
7K.SOC15	2007-11-01T23:59:59.000000Z	2008-06-09T00:00:00.960000Z	-1.54	0.7	36
7K.SOC16	2007-11-01T08:01:59.000000Z	2008-06-08T00:00:00.960000Z	2.62	0.92	22
YS.ALRB	2014-11-11T07:26:54.380000Z	2018-12-31T23:59:59.000000Z	-2.35	0.53	41
YS.BAOP	2014-11-01T00:00:00.000000Z	2016-10-10T07:26:09.200000Z	-14.02	0.53	42
YS.BKOR	2014-10-28T04:59:59.200000Z	2016-11-05T02:13:03.180001Z	-1.66	0.53	55
YS.ENDE	2014-11-03T05:33:32.200000Z	2018-12-31T23:59:59.000000Z	-6.36	0.52	42
YS.HADA	2014-11-01T04:13:50.200000Z	2016-10-11T00:05:59.180001Z	-3.8	0.4	105
YS.LMBR	2014-11-06T07:41:25.200000Z	2016-11-08T02:36:46.180001Z	-3.37	0.83	10
YS.SINA	2014-10-29T07:03:10.200000Z	2016-11-05T06:47:01.180001Z	3.18	1.01	39

A.2 Supplementary figures

In this section, we show the supplemental figures for Chapter 2. The contents are briefly summarized below.

- Figures A.1–A.5: Bar graphs illustrating station orientations.
- Figure A.6: Comparison of teleseismic P-wave traces between station-orientation uncorrected and corrected data.
- Figure A.5: Summary of measured station orientations in the S1 network stations.
- Figure A.8 and A.9: Comparisons of teleseismic receiver functions between uncorrected and corrected teleseismic P-waves.

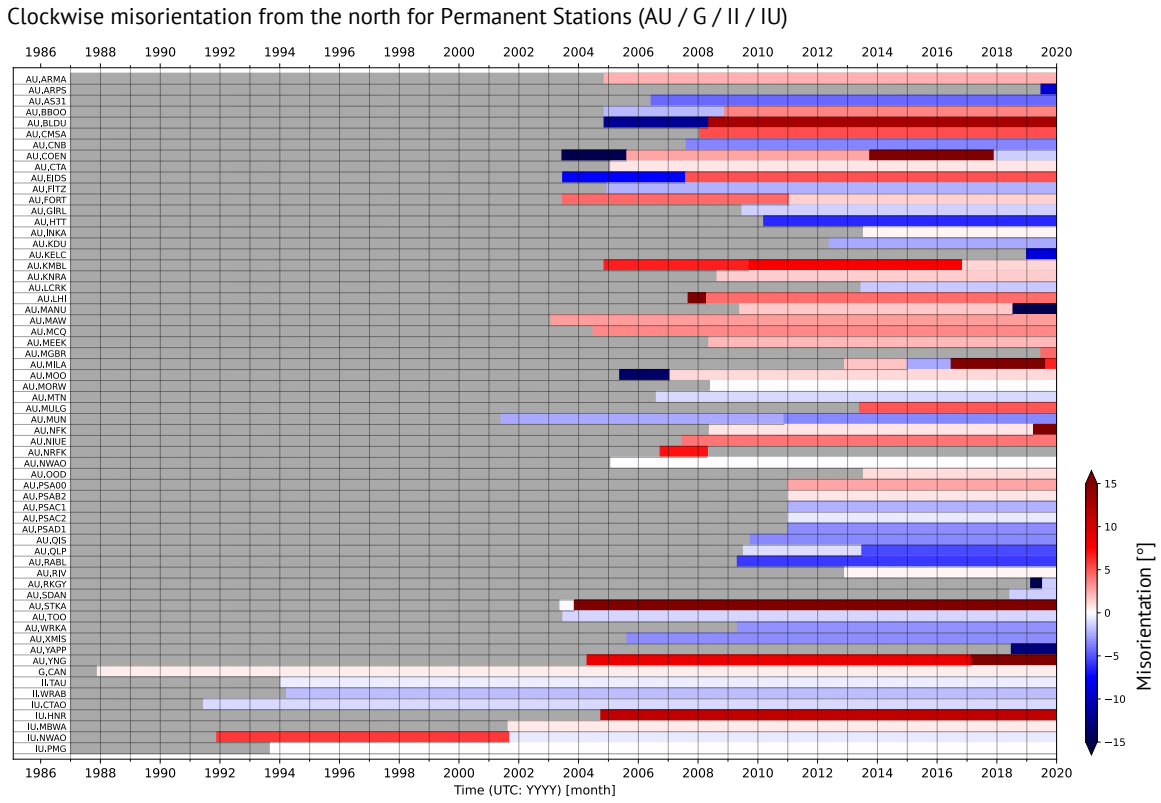

Figure A.1: Summary of clockwise misorientation from the geographic north for permanent stations (except for the S1 network). A positive misorientation value represents the eastward rotation of horizontal sensors from the north. The gray-shaded region represents periods when the seismic station was not operational. Note the operation periods for some stations (AU.ARPS, AU.KELC, AU.MGBR, AU.RKGY, and AU.SDAN) are too short to reliably estimate misorientation using our polarization analysis; see Table A.1 for details.

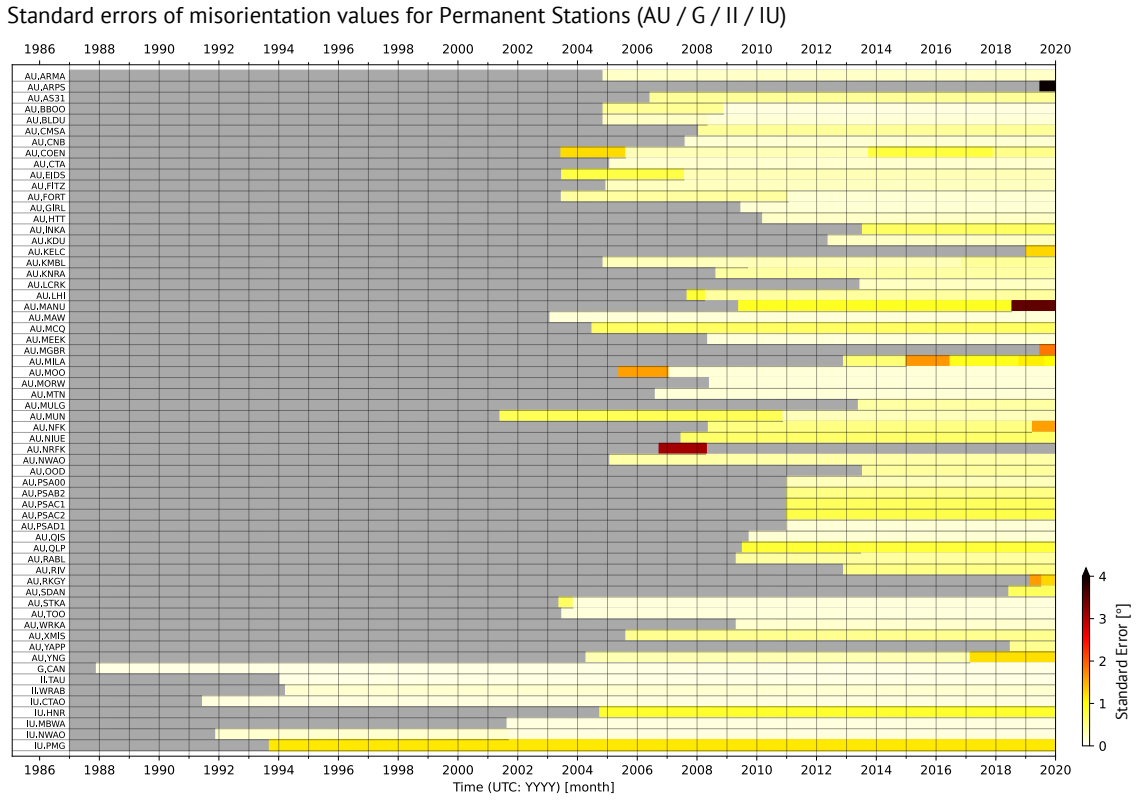

Figure A.2: Same as Figure A.1, but the summary of standard errors for the estimated misorientation values.

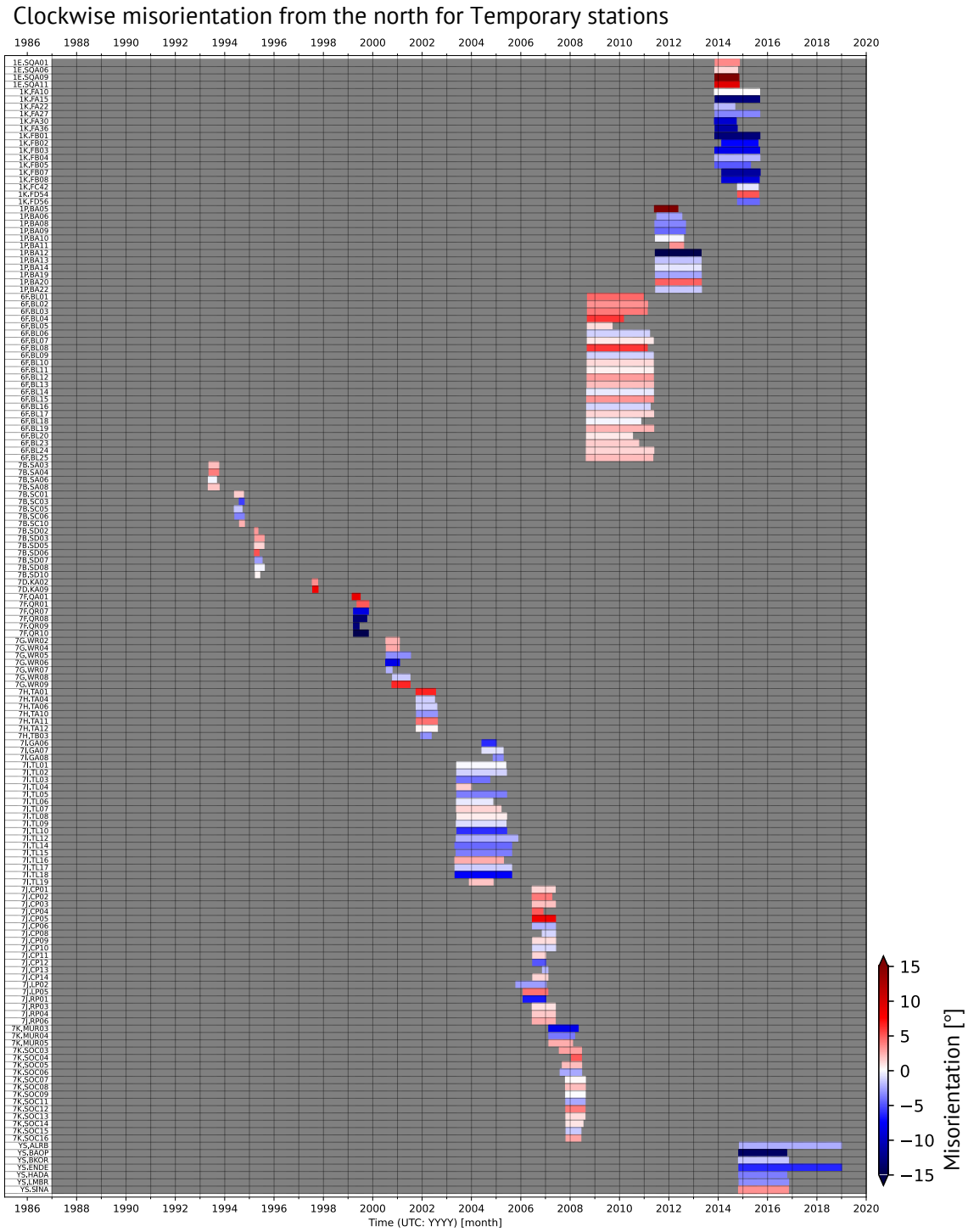

Figure A.3: Same as Figure A.1, but for the temporary stations.

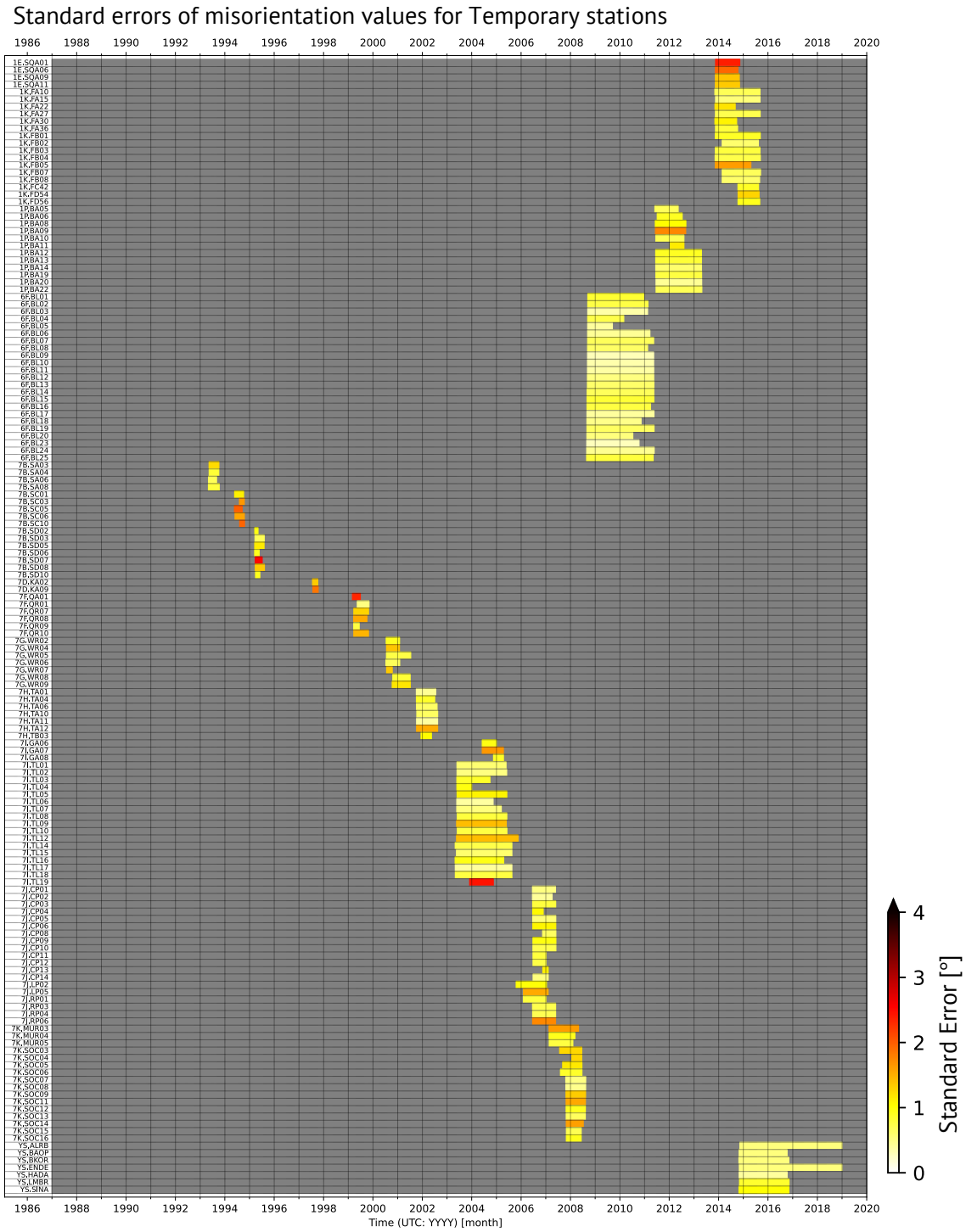

Figure A.4: Same as Figure A.2, but for the temporary stations.

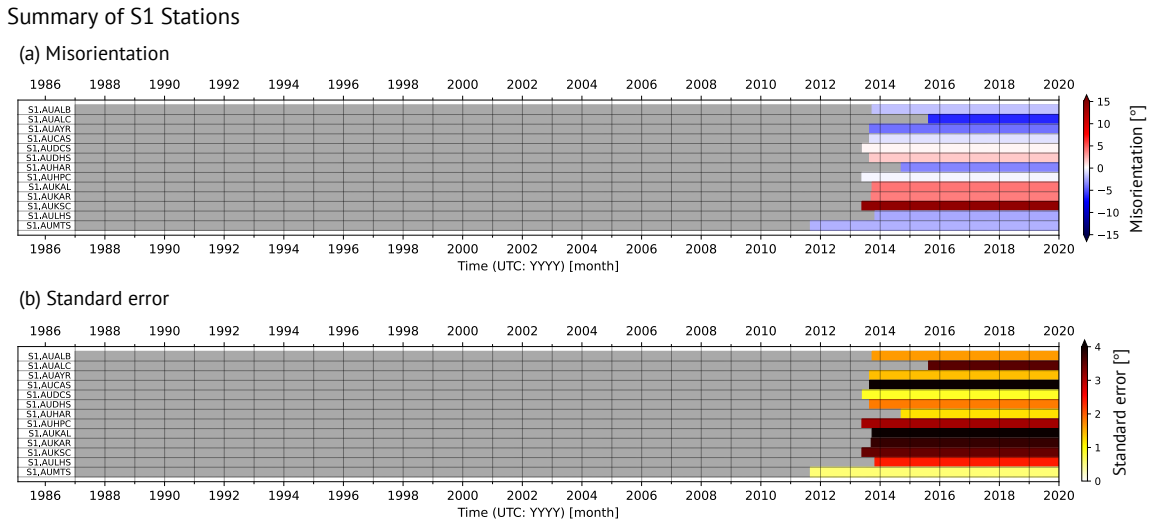

Figure A.5: Summary of the S1 network stations. (a) and (b) are the same as Figures A.1 and A.2, respectively, but for the S1 network.

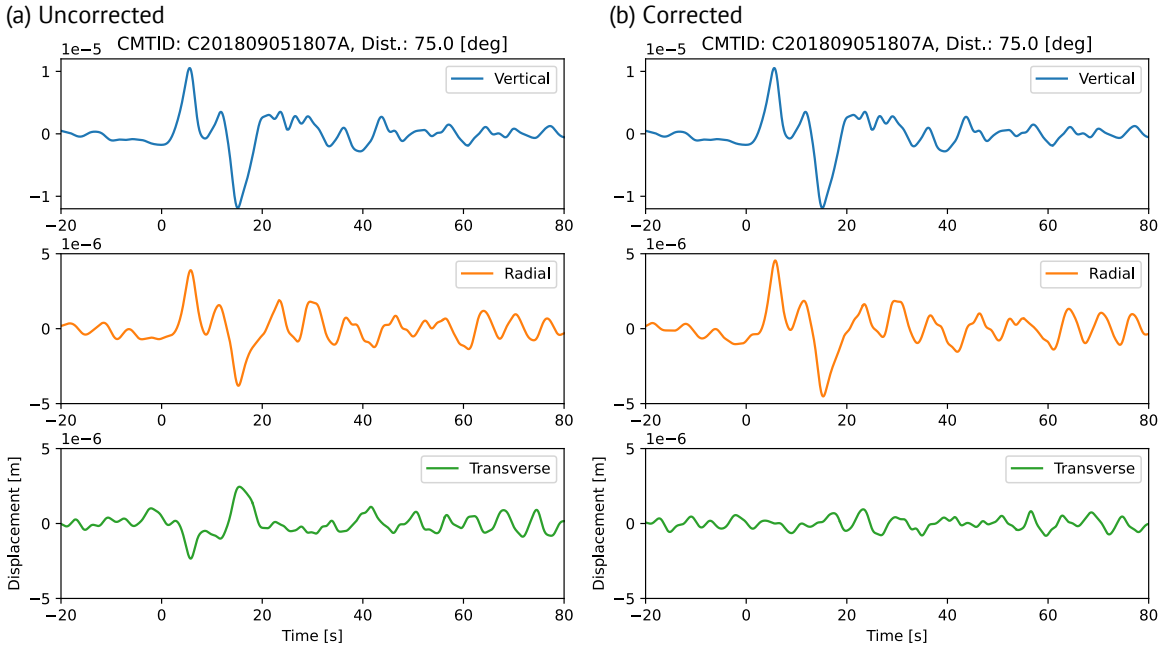

Figure A.6: An example of teleseismic P-wave at AU.STKA for a seismic event (Mw 6.6) in Hokkaido, Japan, on September 5, 2018 (UTC). Three-component seismograms (a) before the correction of the station misorientation, and (b) after the correction. Blue, orange, and green lines indicate the vertical, radial, and transverse components. For the uncorrected waveforms in (a), we used the horizontal orientation reported by IRIS/AusPass, while for (b), we employed our new catalog of misorientation. Note that the amplitude scale in the top panel (vertical) is different from the other two horizontal components.

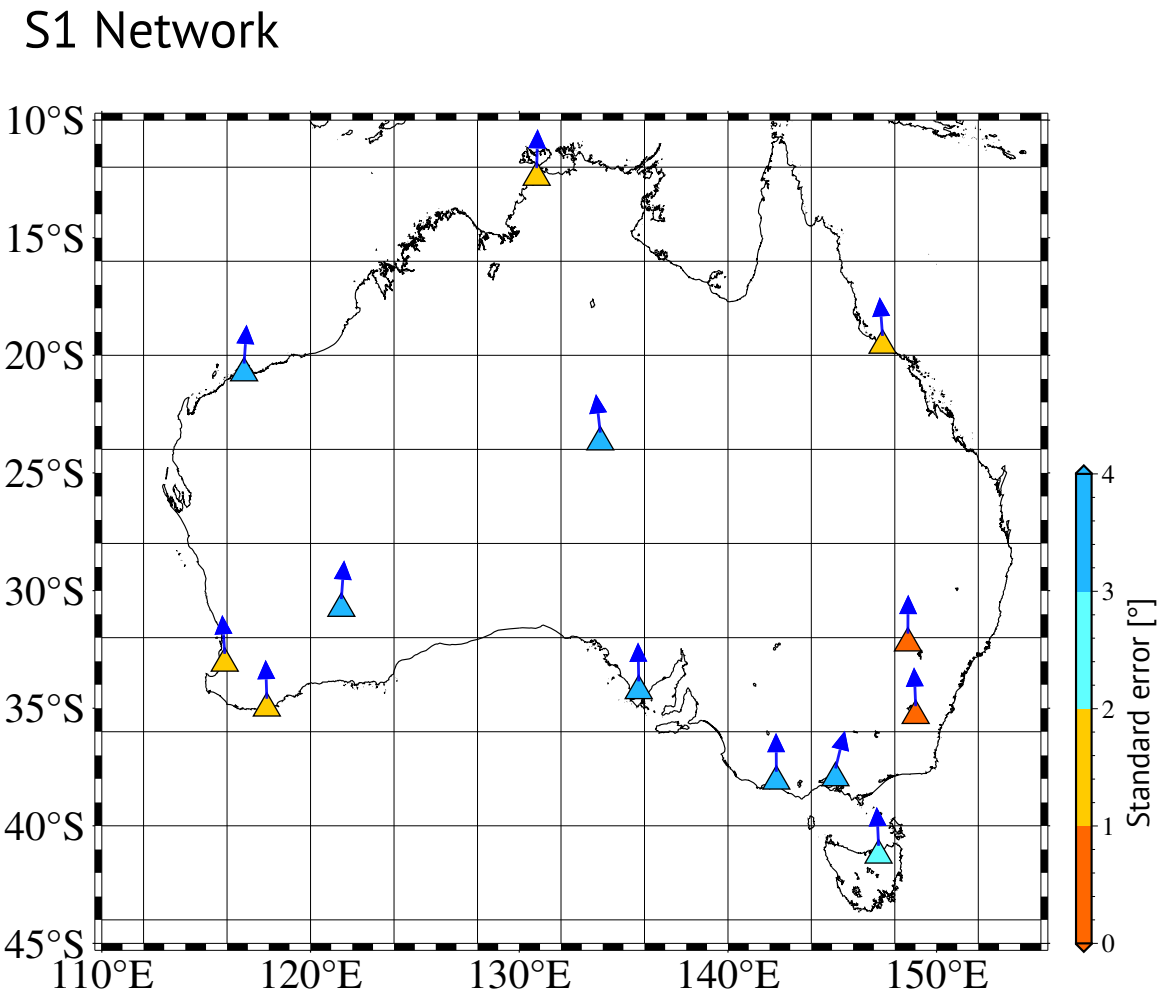

Figure A.7: Same as Figures 2.4 (a-e) and 2.5, but for the S1 network.

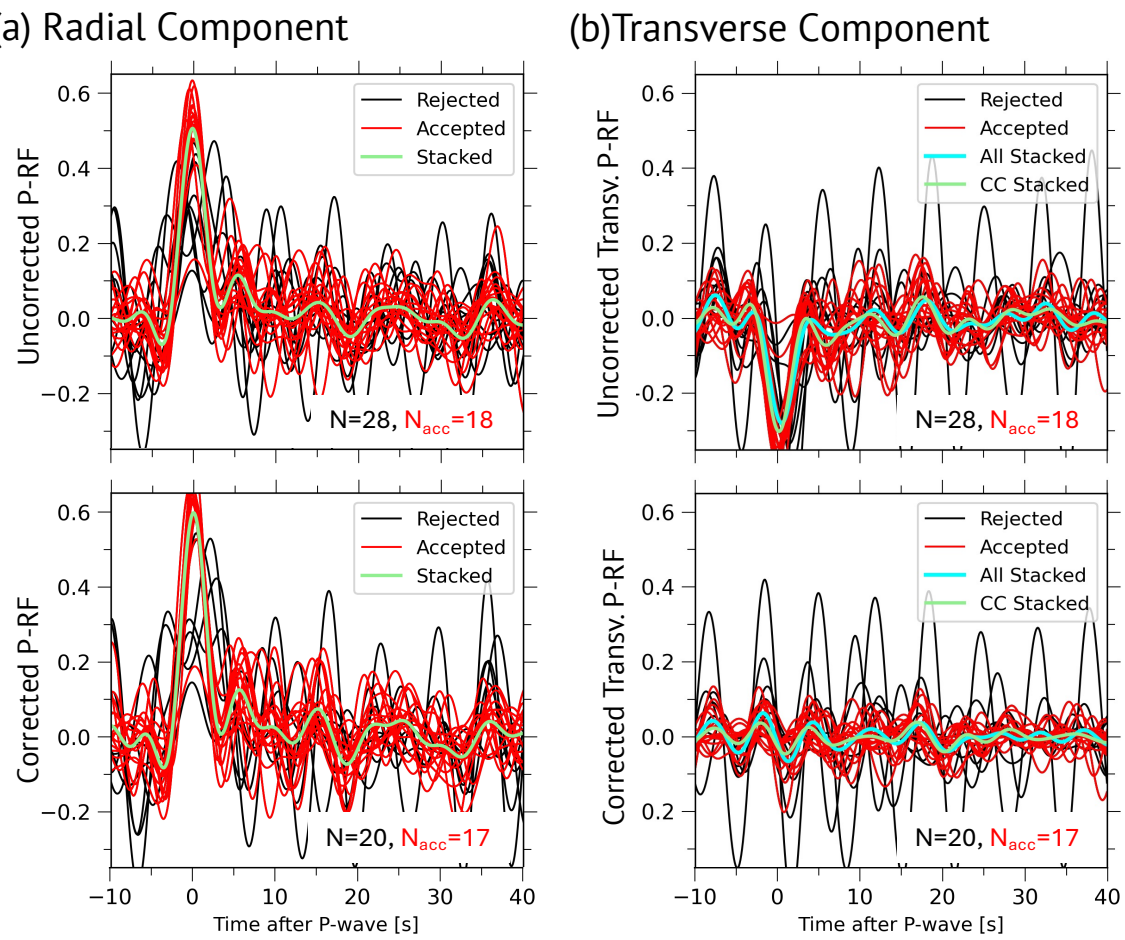

Figure A.8: Examples of individual and stacked traces of P-wave receiver functions from the eastern event groups at AU.STKA shown in Figure 2.6. (a) P-RFs in radial component and (b) transverse component; (top) without and (bottom) with a correction for the station misorientation. Black and red lines are the rejected and accepted traces, respectively, through the cross-correlation-based selection step explained in the main text. Green traces represent the stacked traces, shown as the blue or orange line in Figure 2.6 (b).

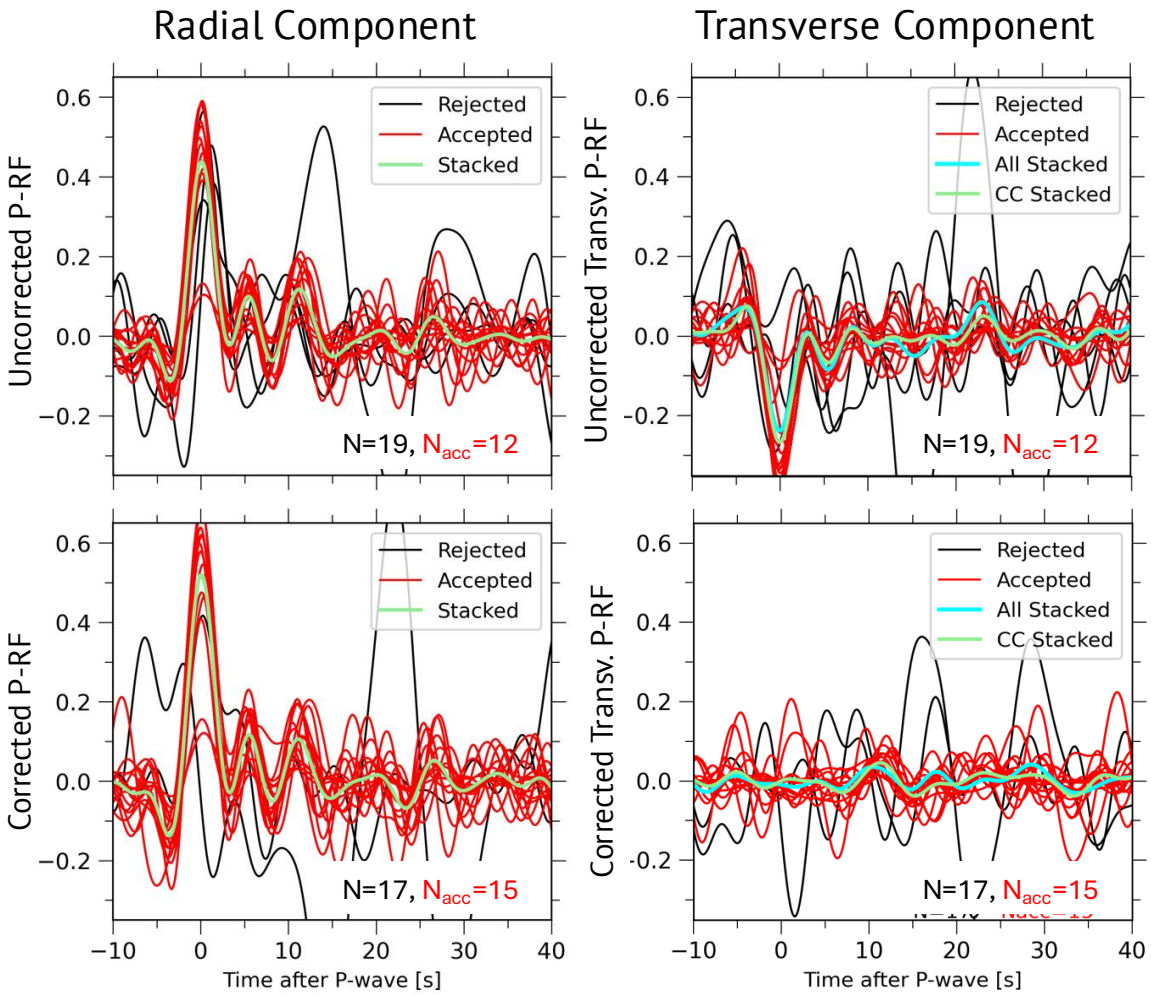

Figure A.9: Same as Figure A.8, but the P-wave receiver functions from the western event groups.

Appendix B

Supplementary information for Chapter 3

B.1 Theoretical background of Receiver Functions

Receiver Function (RF) analysis is a popular technique for isolating seismic converted phases from direct phases, which has been used for seismic imaging of the crust and upper mantle, particularly for investigating internal boundaries. The method for RFs analysis has been developed and applied in numerous earlier studies since the 1970s (Langston, 1979). In this section, we briefly review the fundamental theory of the RF analysis.

The observed seismograms $U(t)$ are generally expressed as follows,

$$U(t) = S(t) * G(t) * I(t), \tag{B.1}$$

where $S(t)$, $G(t)$, and $I(t)$ are the seismic source term, structural response, and instrumental response, respectively, and the asterisk denotes the convolution operator. The structural response term contains information about the seismic structure, which can be extracted from coda waves and precursors of the main phases.

While coda waves are generally too complicated to extract the structural information from their visual inspections, RFs allow us to isolate converted phases in observed seismograms. RFs can be computed by deconvolving one component of incident phases from another component of converted phases, effectively removing the source term and instrumental response as follows,

$$RF(t) = \frac{S(t) * G_1(t) * I(t)}{S(t) * G_2(t) * I(t)}, \tag{B.2}$$

where the division indicates spectral division (deconvolution).

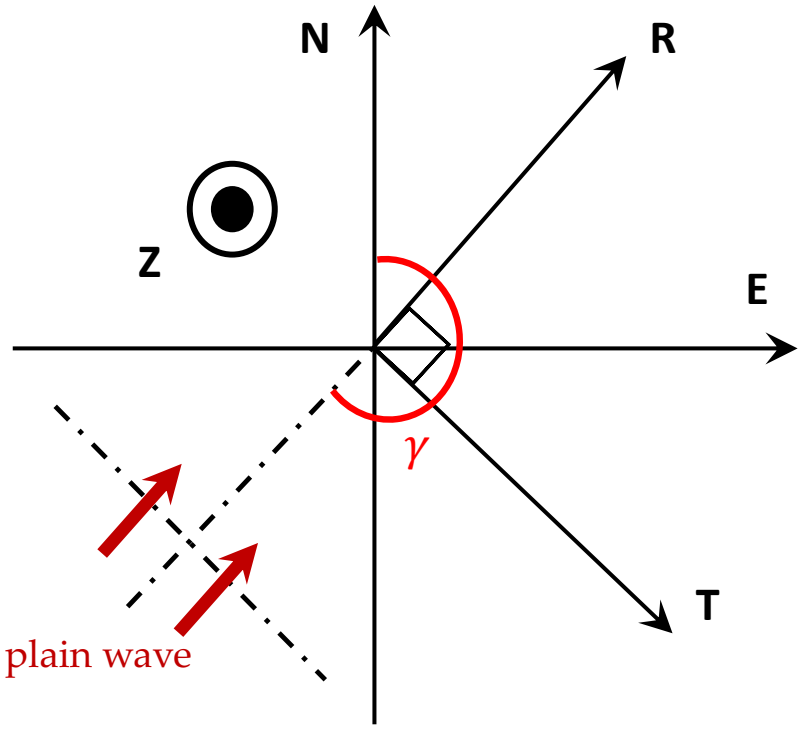

Figure B.1: Radial-Transverse-Vertical (RTZ) coordinate system viewed from above. γ is the back-azimuth toward the seismic source.

In conventional RF analyses, observed seismograms are firstly rotated the coordinate system from North-East-Vertical (NEZ) to Radial-Transverse-Vertical (RTZ) using the back-azimuth. This process is illustrated in Figure B.1.

Figure B.2 illustrates examples of teleseismic body waves and the corresponding receiver functions. In the RTZ coordinate system, the incident P-wave (parent component) mainly dominates the vertical component, while the converted phases (daughter component) are typically observed in the radial component. Therefore, the P-wave receiver function (P-RF) can be produced by the deconvolution of the vertical component from the radial component. In the case of the S-wave receiver function (S-RF) using an incident S-wave, the parent and daughter components are swapped so that the deconvolution procedure is reversed.

In Figure B.2, converted phases at major interfaces, such as the Moho, are clearly seen in the RFs. The P-RF exhibits many peaks, including main converted signals and multiple reverberations at internal interfaces (e.g., a positive signal at about 8 s). The latter tends to contaminate the P-RFs. On the other hand, the S-RF generally

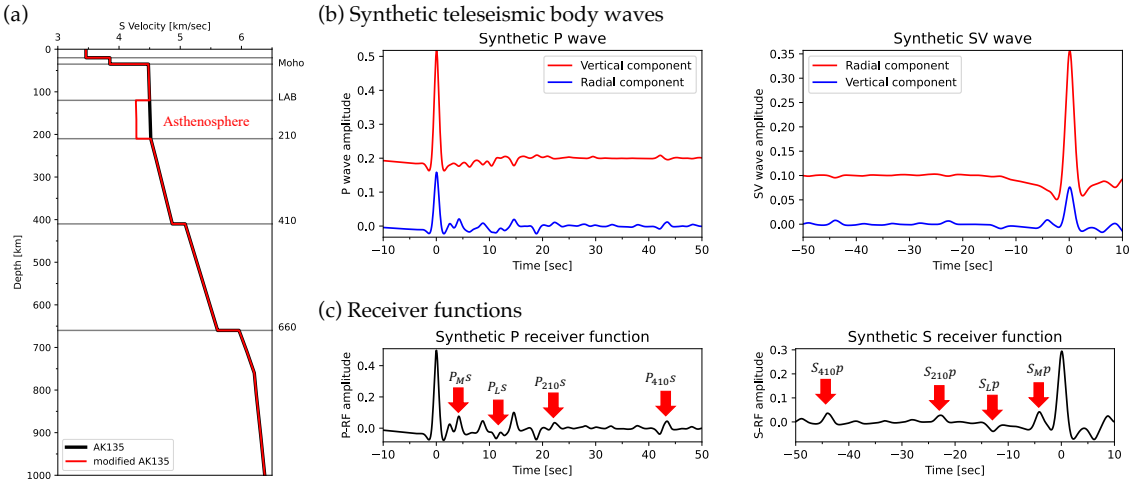

Figure B.2: Examples of teleseismic body waves and receiver functions. (a) Reference seismic velocity models, AK135 (black) and modified AK135 (red). (b) Synthetic teleseismic body waves in the vertical and radial components. The left panels show a case of incident P-wave, and the right ones S-waves. In each panel, red and blue lines indicate the parent component and daughter component (see legends). (c) Receiver functions from the synthetic seismograms in (a). Red arrows indicate arrival times of converted phases (e.g., $P_M s$, $S_L p$).

looks simpler because the converted Sp phases arrive before the direct S-wave, while multiple reflection phases at internal interfaces arrive after the direct phase. Thus, the converted phases in the S-RF are not contaminated by the multiple reflections, making S-RFs useful for seismic imaging of discontinuities in the upper mantle.

B.2 Supplementary figures for Chapter 3

This section contains supporting figures for Chapter 3, which are briefly explained below.

- Figure B.3: Sensitivity kernels for seismic surface waves.
- Figure B.4: Dispersion curves of Rayleigh and Love wave phase speed used in Chapter 3.
- Figure B.5: Event distributions for each station
- Figure B.6: Frequency-dependent P-wave receiver functions at CTAO
- Figure B.7: Short-period (0.03-0.5 Hz) receiver function datasets at four stations (CAN, MBWA, NWAO, and WRAB)
- Figure B.8: Examples of the reference model in the trans-dimensional Bayesian inversion
- Figure B.9–B.11: Posterior distributions of hyperparameters and marginal distributions of data misfit for Figure 3.5.

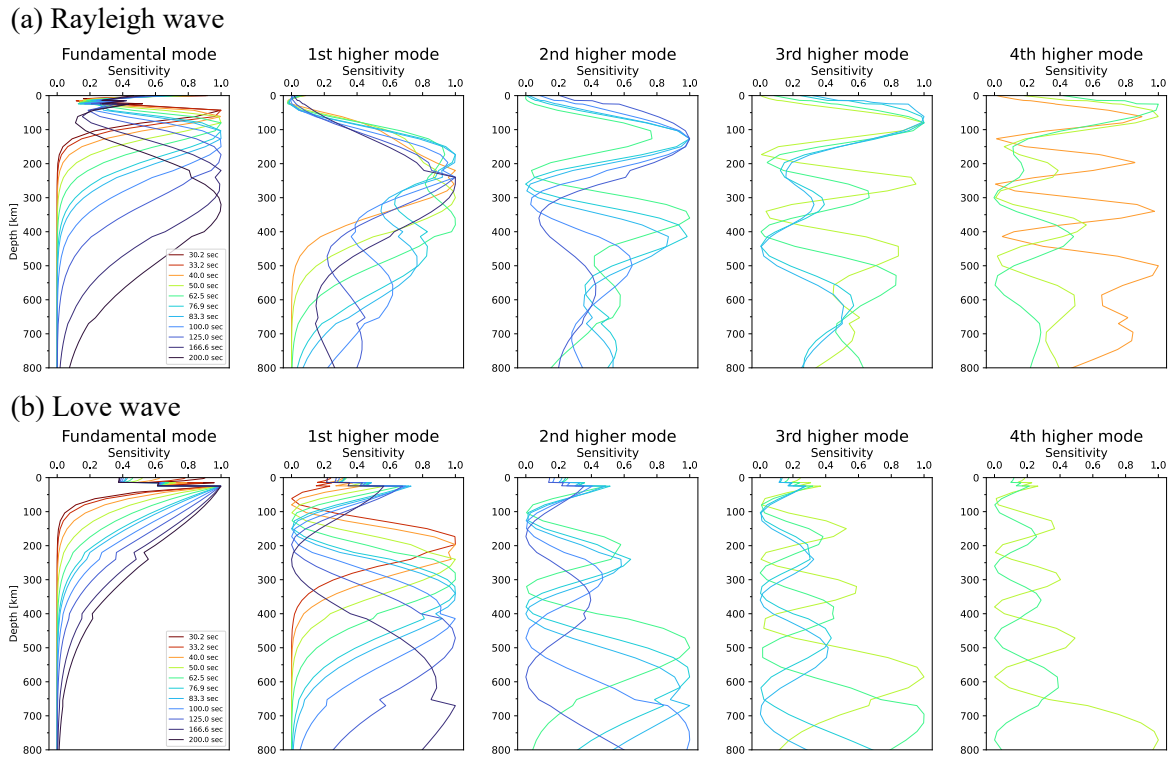

Figure B.3: Normalized sensitivity kernels of surface waves for anisotropic PREM (Dziewonski & Anderson, 1981) from the fundamental to the 4th higher mode of (a) Rayleigh waves and (b) Love waves. Line colors indicate the period of surface waves.

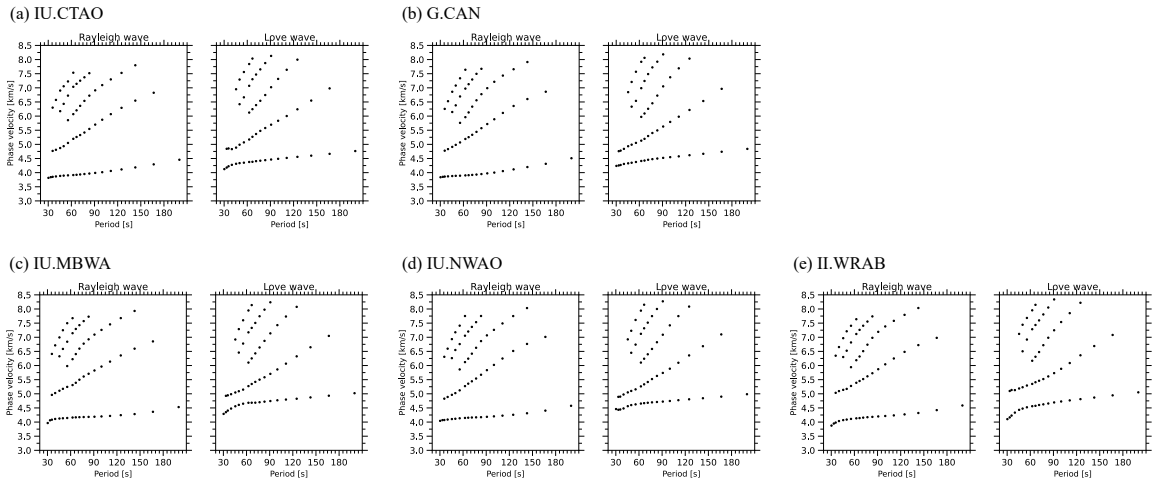

Figure B.4: Phase speed dispersion data of multimode Rayleigh and Love waves for five stations used in Chapter 3 (a: IU.CTAO; b: G.CAN; c: IU.MBWA; d: IU.NWAO; e: II.WRAB). These dispersion data are extracted from multimode phase velocity maps by Yoshizawa (2014).

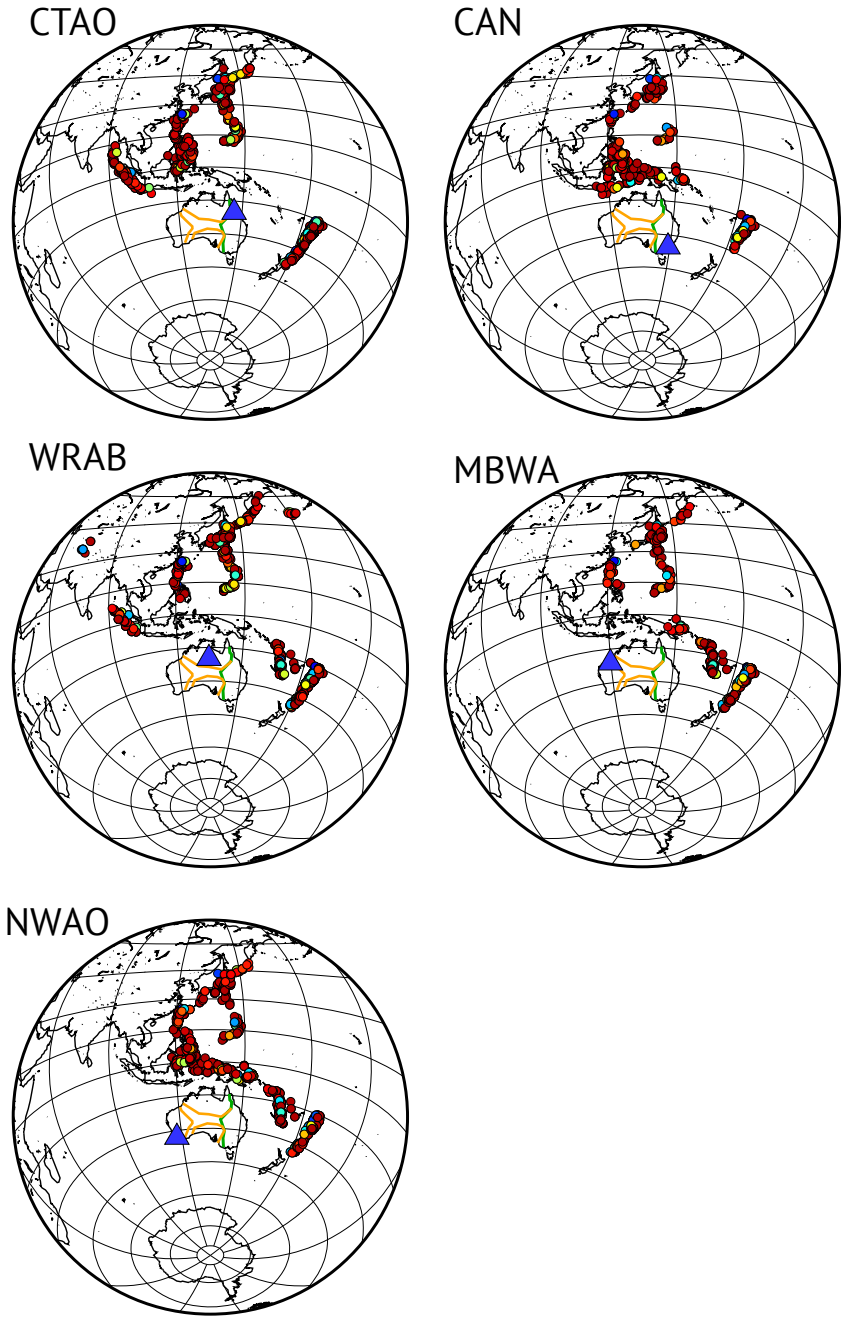

Figure B.5: Event distributions for each station used in this study. Notations are the same as Figure 3.4 (e).

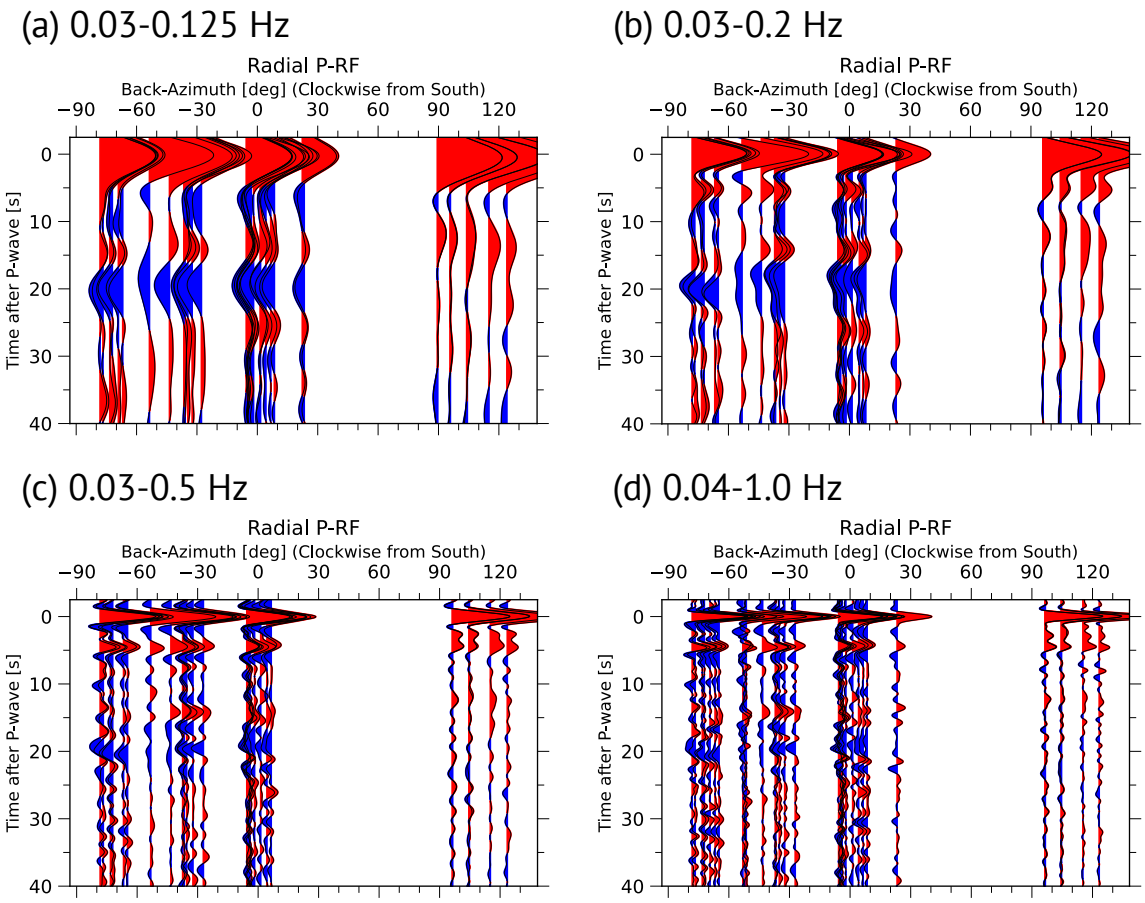

Figure B.6: Frequency-dependent P-wave receiver functions (P-RFs) at IU.CTAO for four frequency ranges: (a) 0.03-0.125 Hz, (b) 0.03-0.2 Hz, (c) 0.03-0.5 Hz, and (d) 0.04-1.0 Hz. Red and blue colors represent the positive and negative phases in receiver functions.

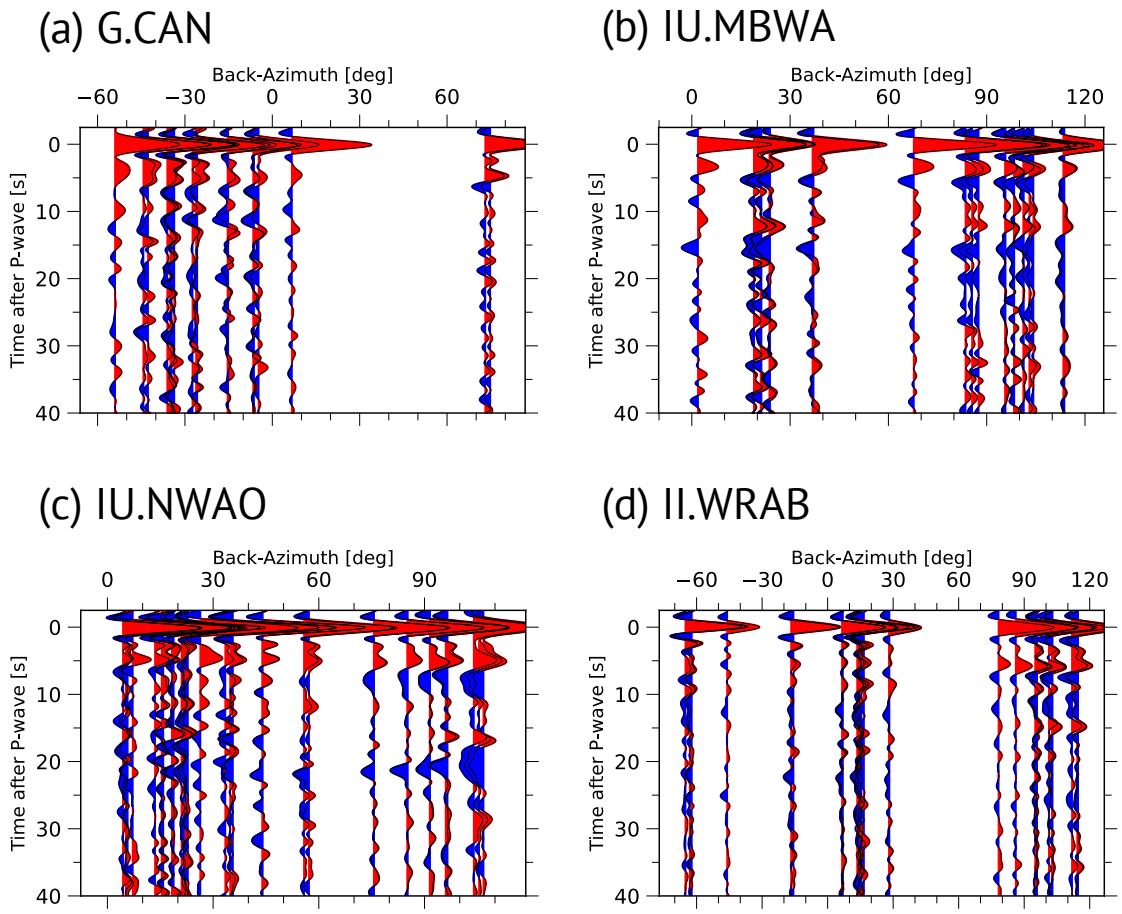

Figure B.7: Same as Figure 3.4 in the main text, but for 0.03-0.5 Hz.

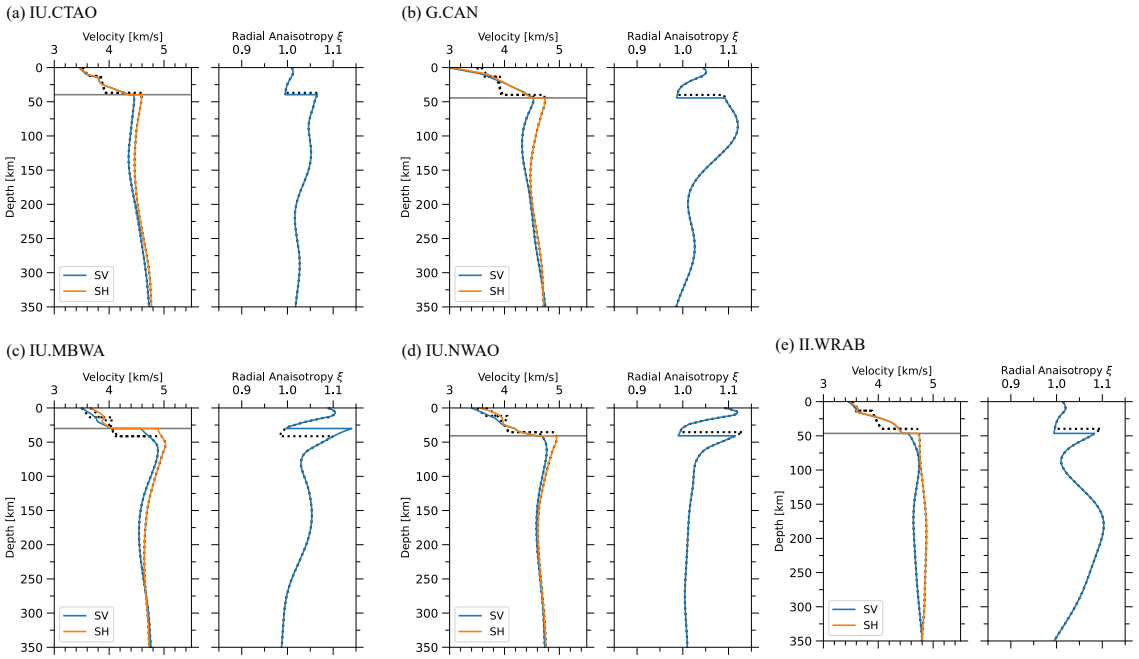

Figure B.8: Local reference structural models (SV and SH velocities and radial anisotropy) for each station. Solid colored lines represent the reference SV and SH wave models used in this study taken from the 3-D radially anisotropic tomographic model (Yoshizawa, 2014), replacing the crust with AuSREM (Kennett et al., 2013; Salmon et al., 2013) and AusMoho (Kennett et al., 2023).

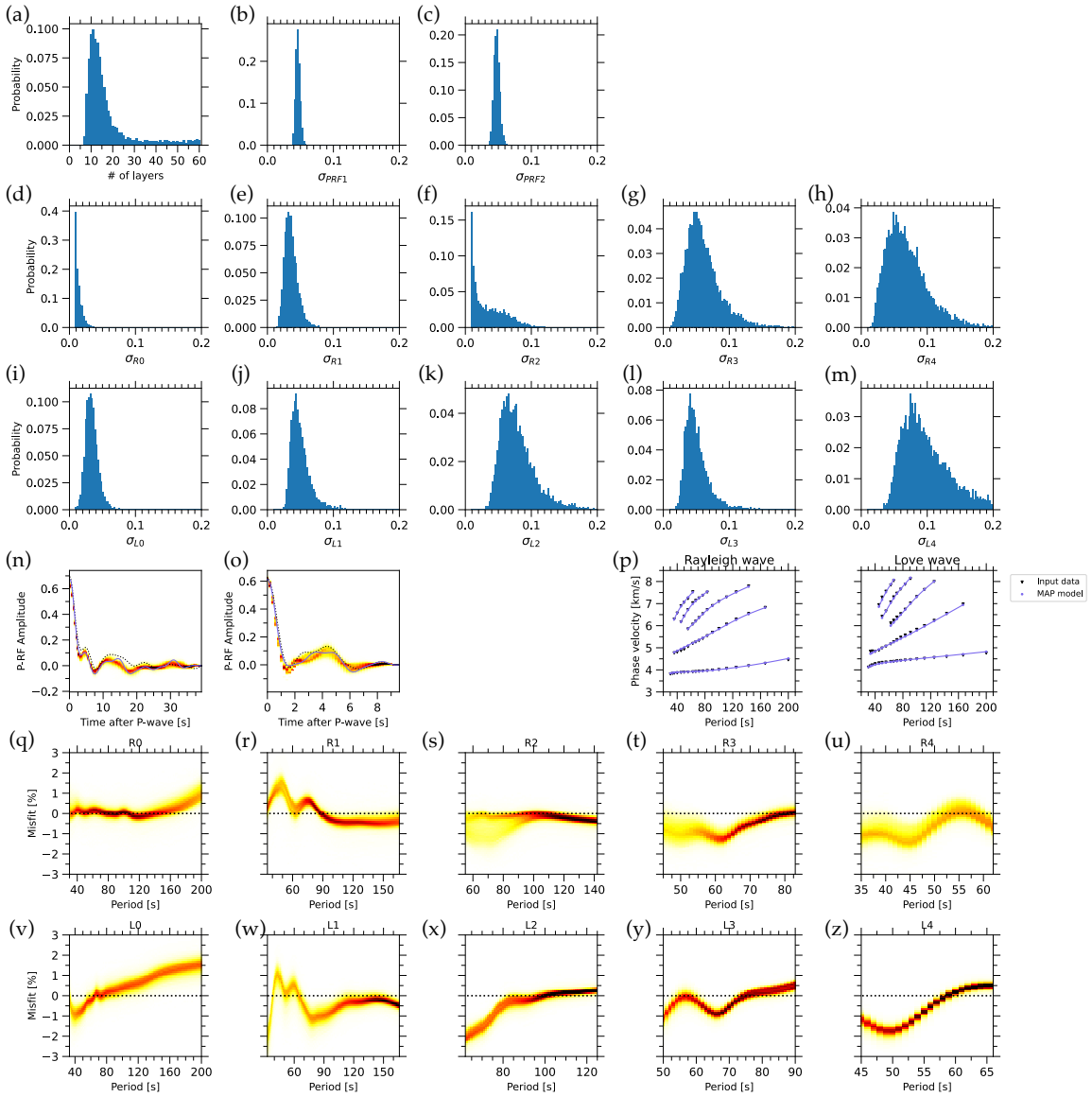

Figure B.9: Posterior distributions of hyperparameters and marginal distributions of data misfit for IU.CTAO results using the eastern event group (Figure 3.5 (b)). (a) The number of layers. (b, c) Data noises for the low-frequency P-RF () and the high-frequency P-RF (). Data noises for each mode of (d-h) Rayleigh waves (d-h) and (i-m) Love wave. R0 and L0 indicate the fundamental-mode Rayleigh and Love waves, and Rx and Lx (1x4) represent their overtones. (n, o) Marginal posteriors of misfit distribution of (n) low- and (o) high-frequency P-RFs. Black dotted lines and purple solid lines indicate the objective data to be fitted in the inversion process and best-fitted P-RF traces. (p) The best-fitted dispersion curves for Rayleigh and Love waves. Purple lines and dots represent the best-fit synthetic data. Black inverse triangles show the dispersion data from phase speed maps (Yoshizawa, 2014). Marginal misfit distributions between the objective and predicted dispersion curves for (q-u) Rayleigh and (v-z) Love waves. The misfit values are shown in the form of fractional perturbation, $100 \times \frac{c_{pre}-c_{obs}}{c_{pre}}$, following (Taira & Yoshizawa, 2020). Notations of Rx and Lx are the same as (d-m). Black dotted lines represent the zero-misfit.

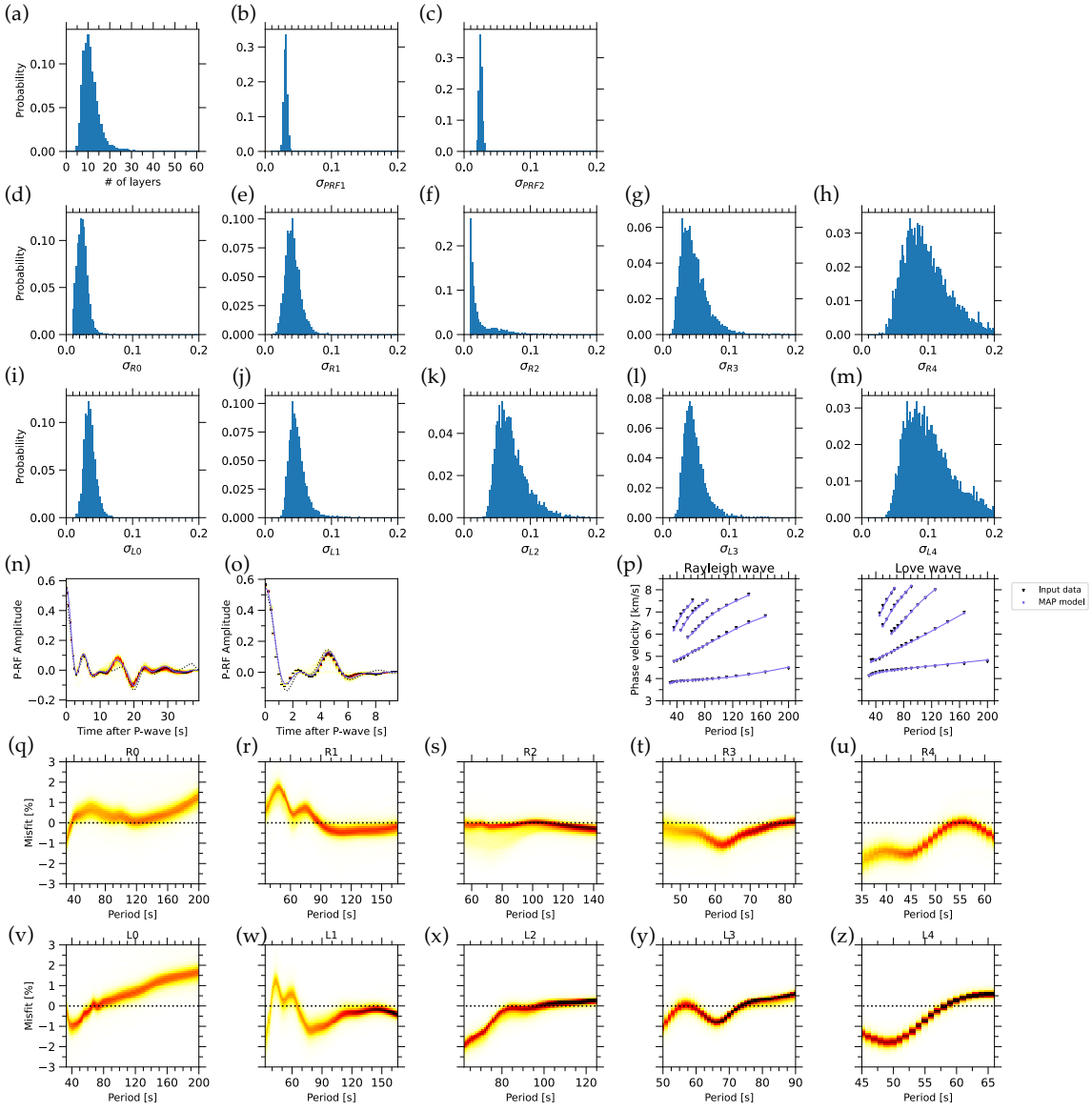

Figure B.10: Same as Figure B.9, but for the western event group (Figure 3.5 (c) in Chapter 3).

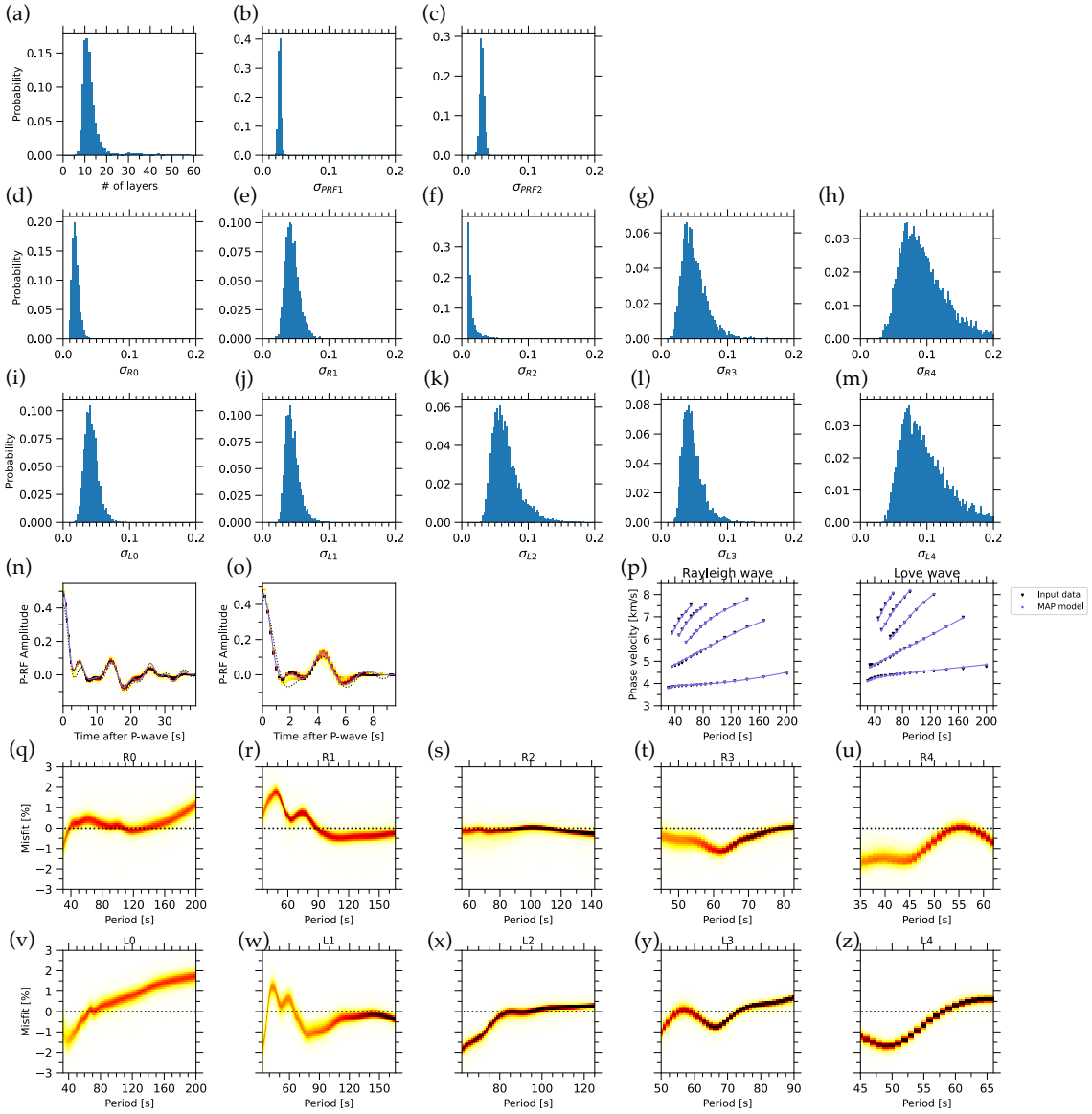

Figure B.11: Same as Figure B.9, but for the northern event group (Figure 3.5 (d) in Chapter 3)

Appendix C

Supplementary information for Chapter 4

This appendix provides supplemental content for Chapter 4. The descriptions for each figure are as follows:

- Figure C.1: Phase speed maps of multimode surface waves (Yoshizawa, 2014).
- Figure C.2: Station distribution with their names.
- Figure C.3: All event distributions used for P-RF analyses for permanent stations employed in this study.
- Figure C.4: Examples of the short-period (0.03–0.5 Hz) P-RF datasets at six AU network stations.
- Figure C.5: Examples of stacking processes for P-RFs at temporary stations.
- Figures C.6 and C.7: Azimuthally averaged 1-D radially anisotropic S-wave velocity models.
- Figure C.8: Uncertainties of X-Ds for $N_c = 3$.
- Figures C.9, C.10, and C.11: Clustering and mapping results for X-discontinuity using $N_c = 4$.
- Figure C.12: Uncertainties of picked depths for multiple MLDs.

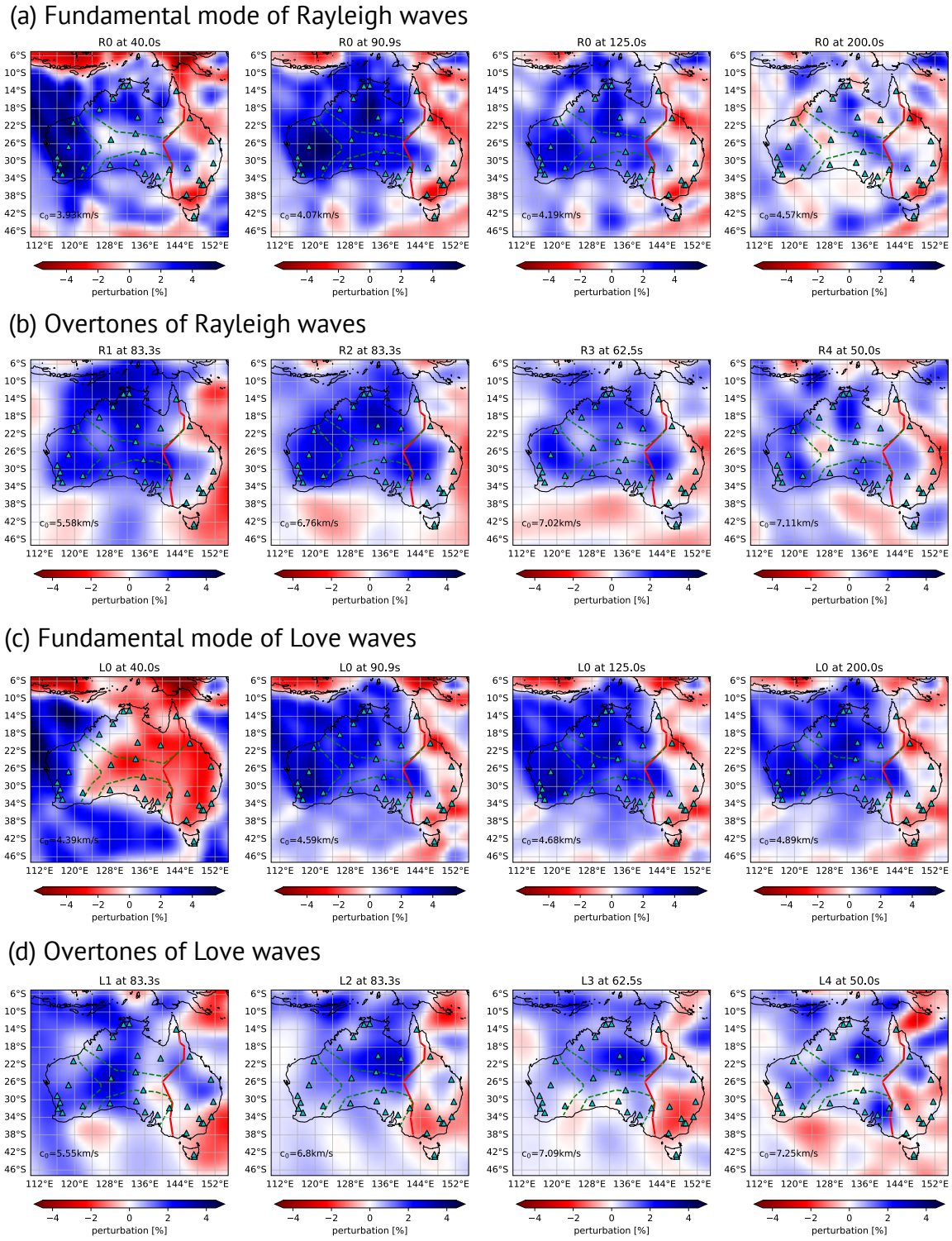

Figure C.1: Selected-period phase speed maps estimated by (Yoshizawa, 2014). R0 and L0 mean the fundamental modes of Rayleigh and Love waves. Other notations such as R2 and L4 indicate the overtones of Rayleigh and Love waves. These phase speed maps are represented as the perturbation from the reference velocity which is drawn at the bottom of each map. Cyan triangles in each figure denote the seismic stations used in this study. For the multimode phase velocity dispersion data, we constructed the localized dispersion curves from these multimode phase speed maps.

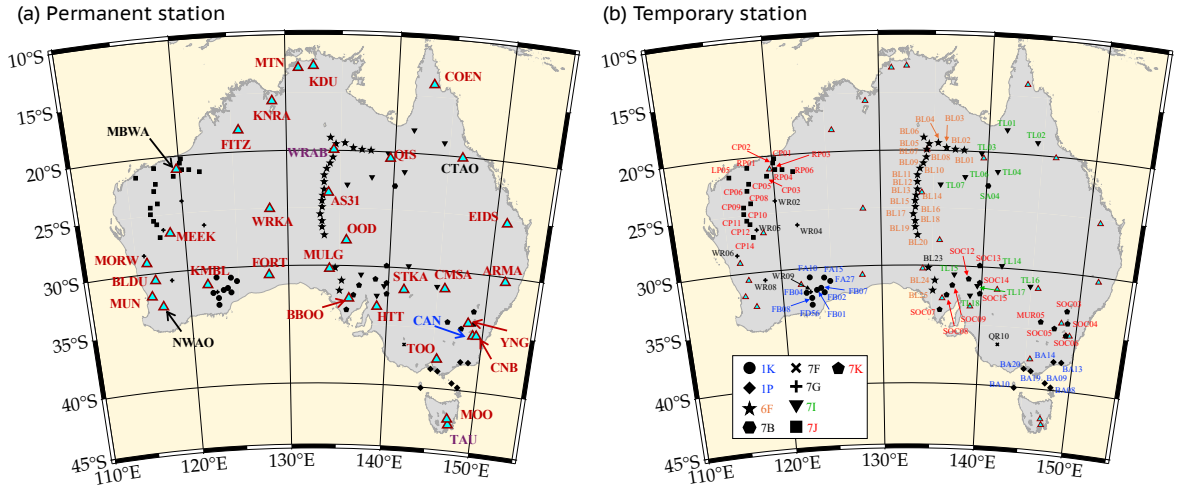

Figure C.2: Employed station distributions labeled with station names. (a) Permanent stations (triangles with the corresponding station name). Colors indicate the station network (IU: black; II: purple; G: blue; AU: red). Black symbols are the temporary stations. (b) Temporary stations.

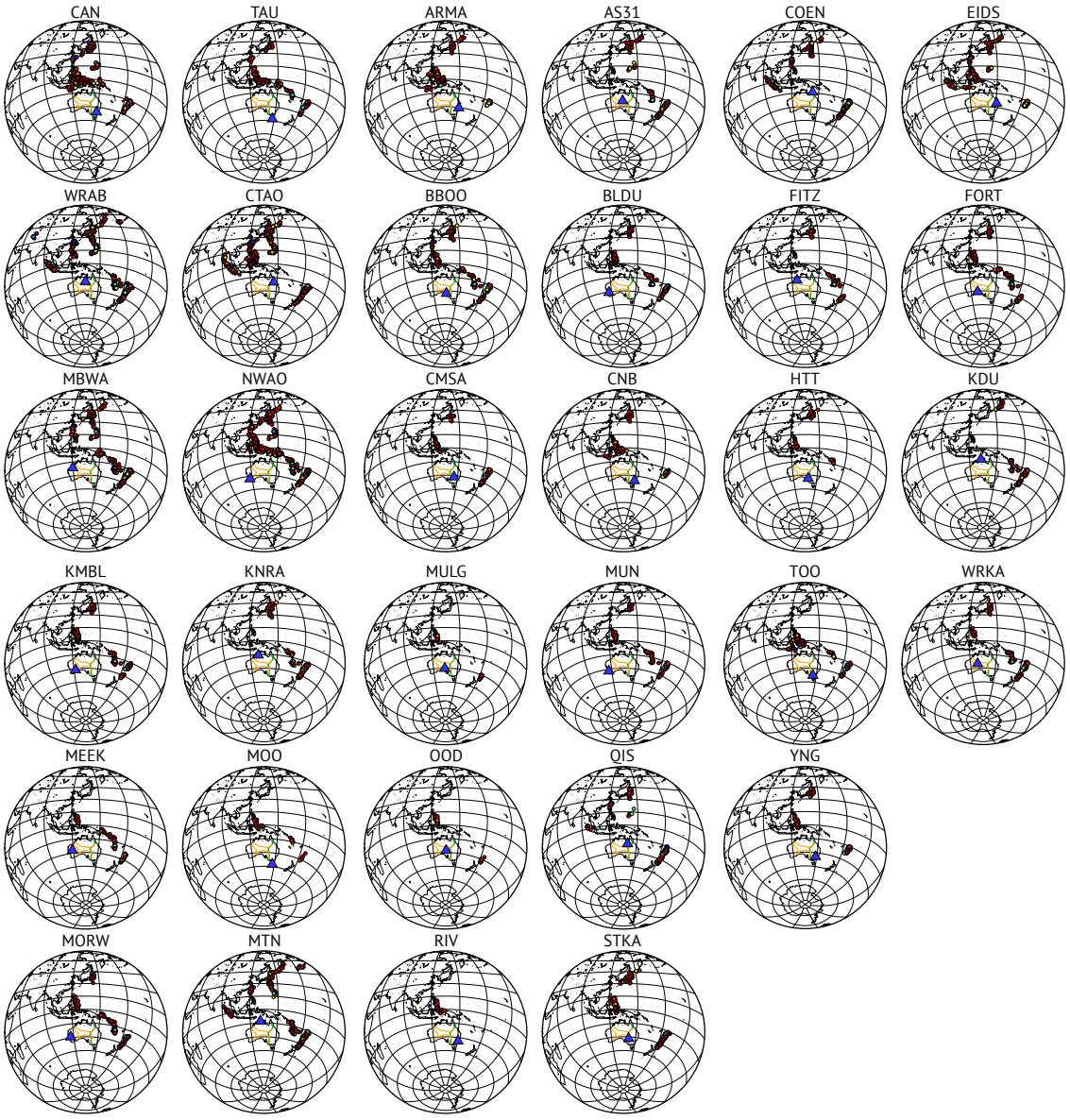

Figure C.3: Event distributions for each permanent station used in this study. Notations are the same as Figure 4.2 (b).

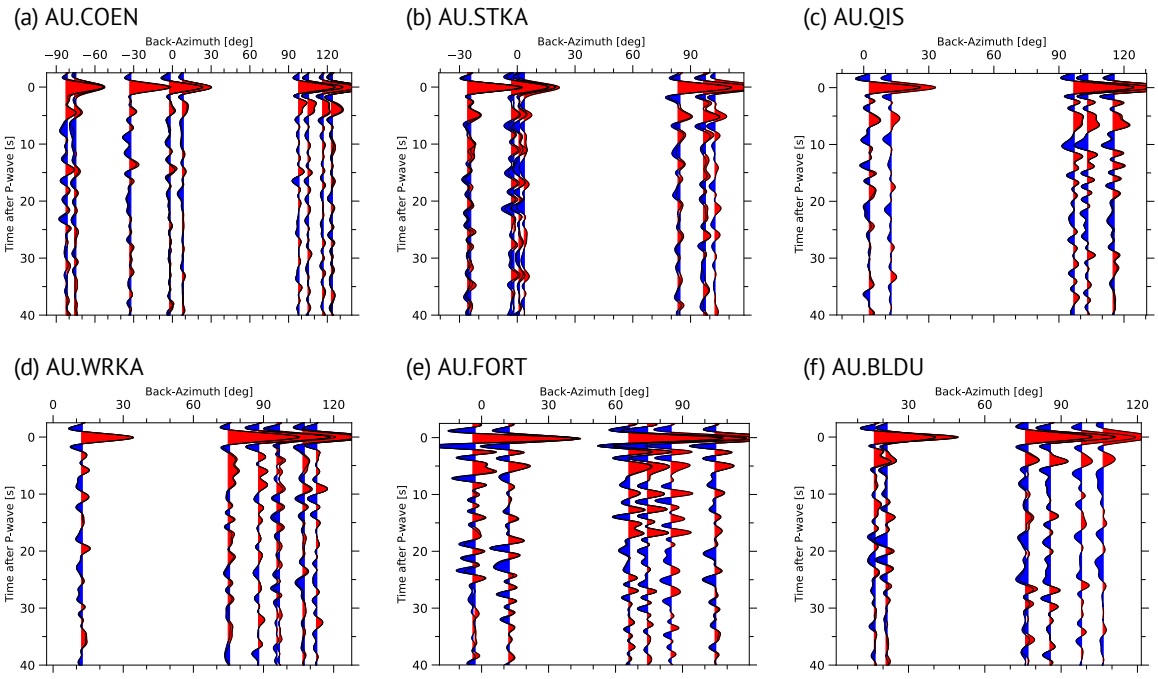

Figure C.4: Same as Figure 4.3, but for 0.03–0.5 Hz.

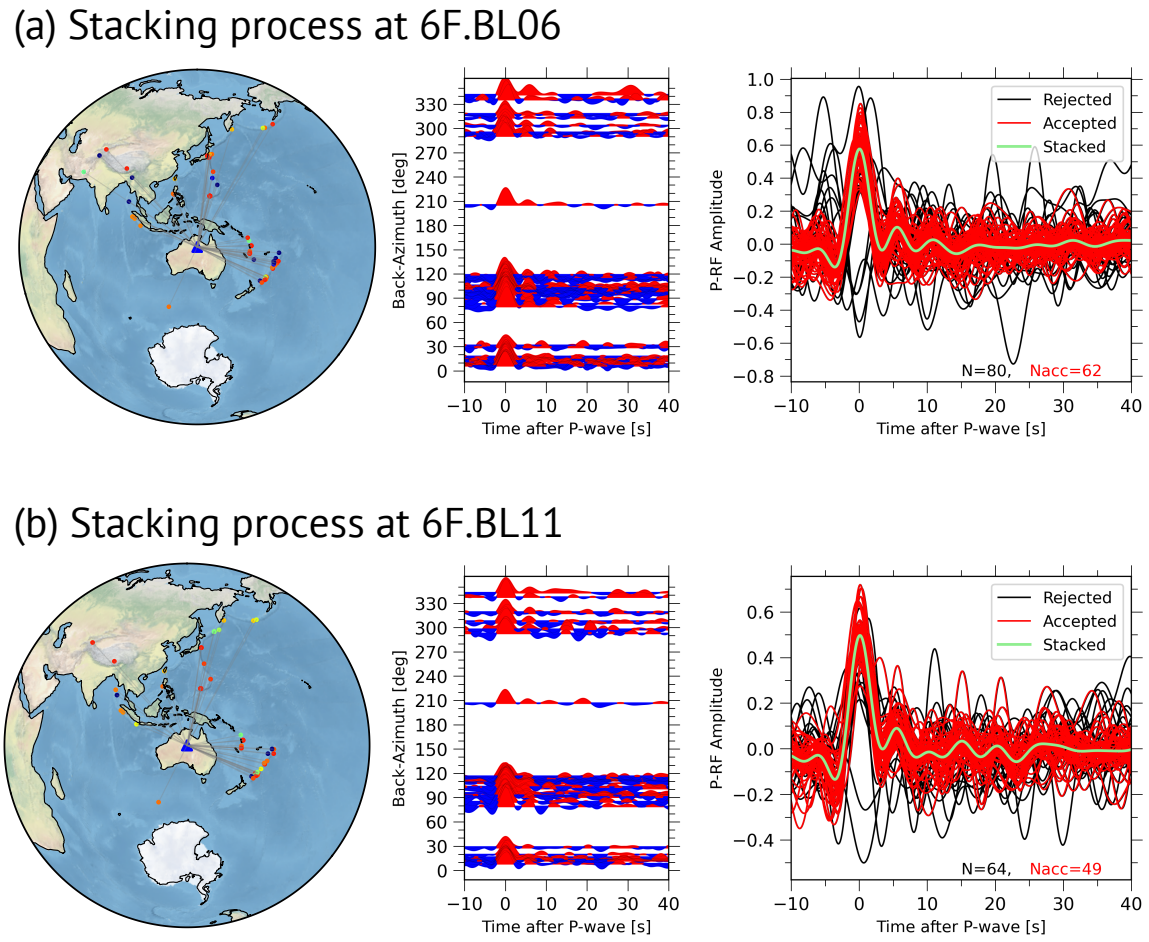

Figure C.5: Examples of stacking processes of the P-wave receiver functions (P-RFs) for two selected temporary stations: (a) 6F.BL06 and (b) 6F.BL11. (a) Stacking procedure for 6F.BL0. The leftmost panel corresponds to the event distribution. The second panel shows back-azimuth-ordered individual traces, where the positive and negative amplitudes in P-RFs are represented as red and blue, respectively. The rightmost panel displays the processing of the stacking process for P-RF. Black and red lines denote rejected and accepted traces through the cross-correlation selection process (Tkalčić et al., 2011). A light green indicates the resulting stacking trance used in our inversion analysis. T(b) Same as (a), but for 6F.BL11.

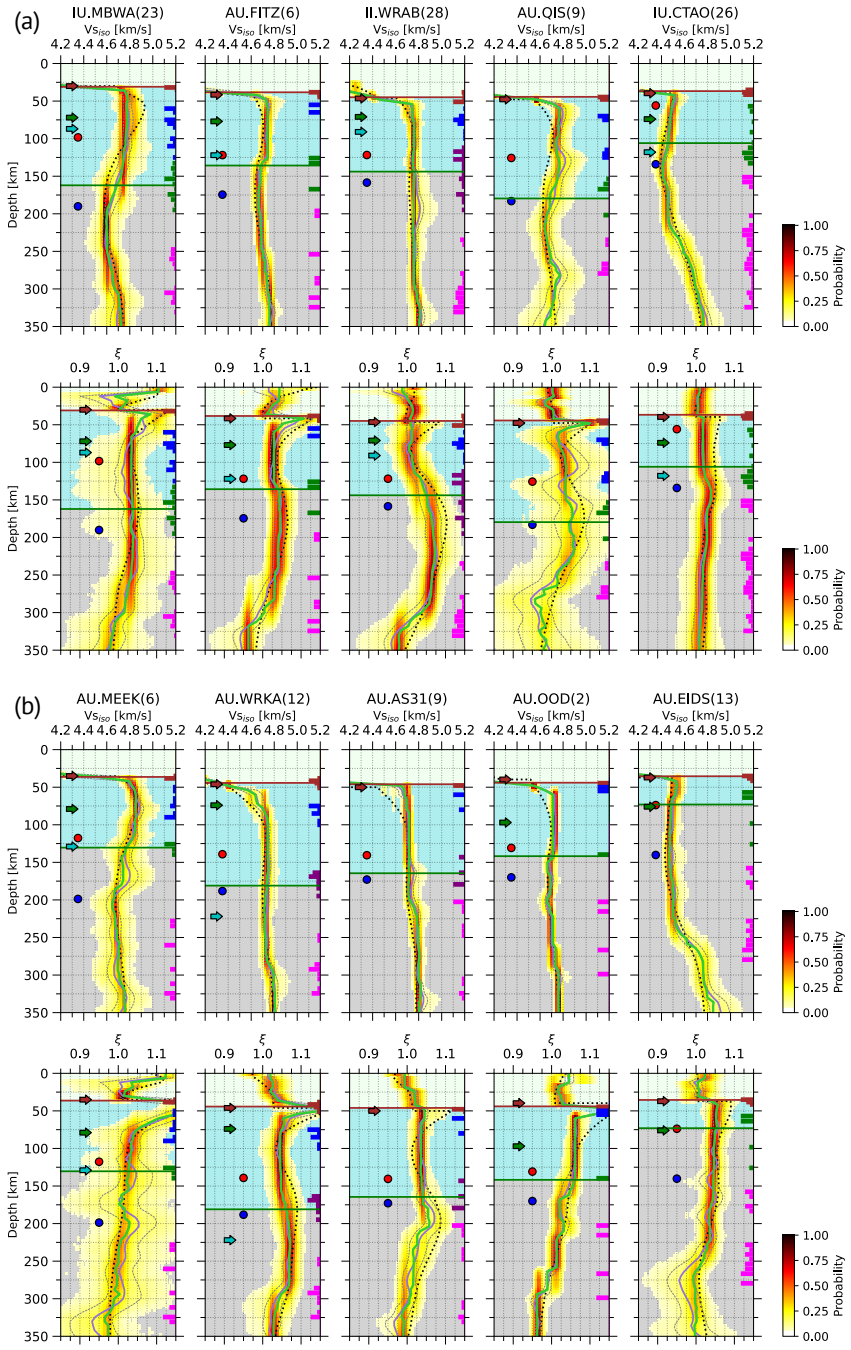

Figure C.6: Same as Figures 4.6 and 4.7, but for along (a) S20° and (b) S26°.

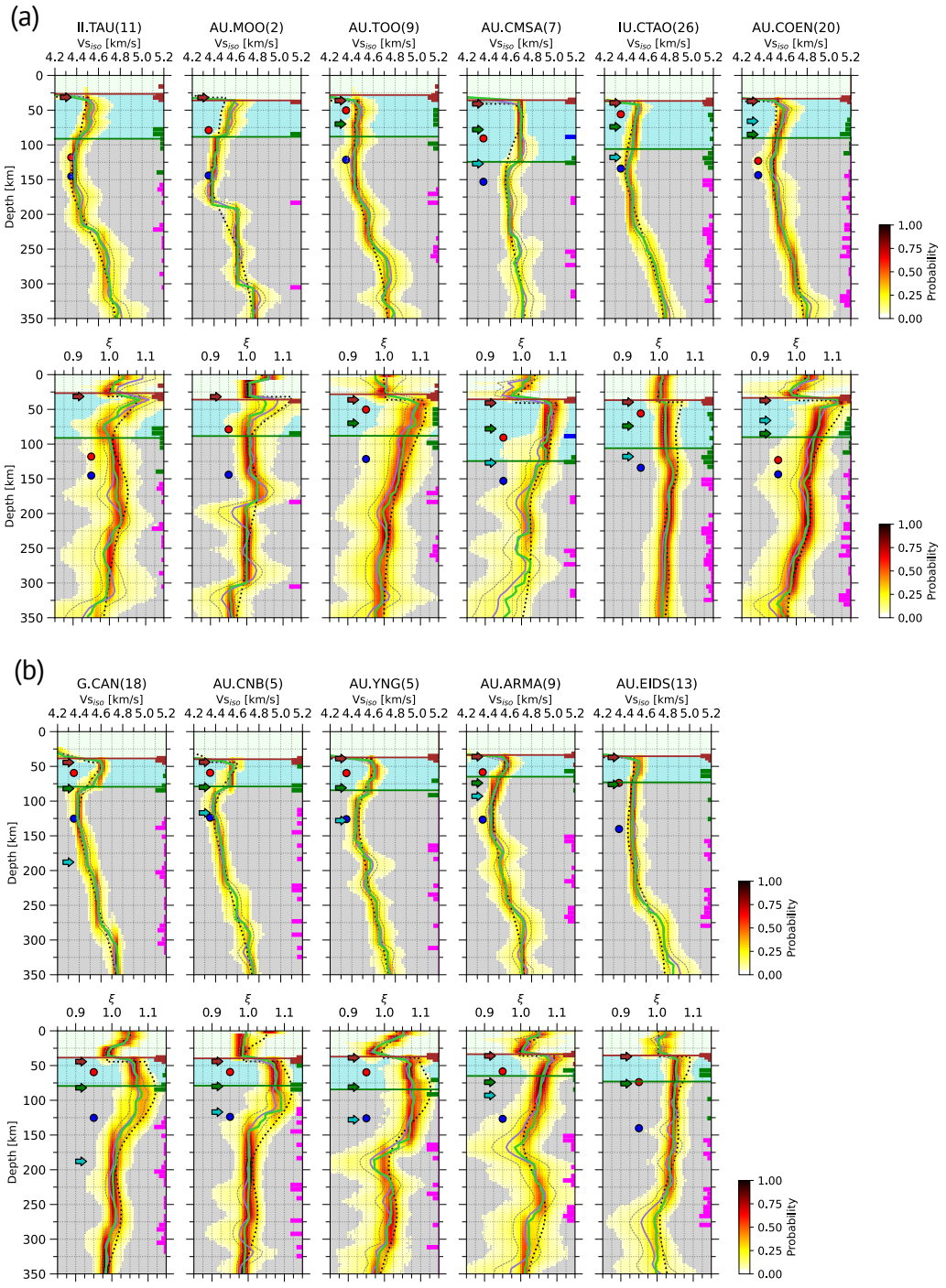

Figure C.7: ame as Figures 4.6 and 4.7, but for along (a) E145° and (b) S150°

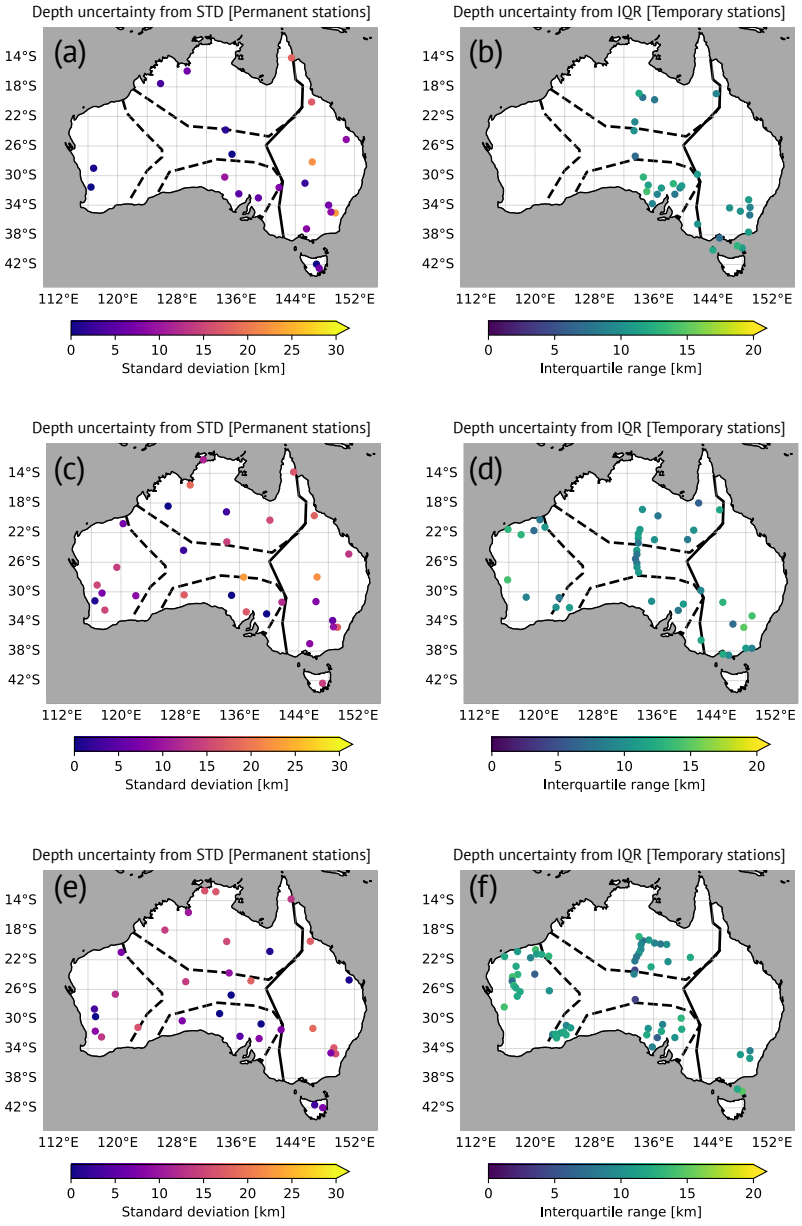

Figure C.8: Uncertainties of the three clustered X-Ds (a,b: 170km-D, c,d: 260km-D, e,f: 310km-D). (a, c, e) The standard deviations for each X-D depth under the permanent stations based on the azimuth-dependent conversion points. (b, d, f) The interquartile ranges for each X-D under the temporary stations.

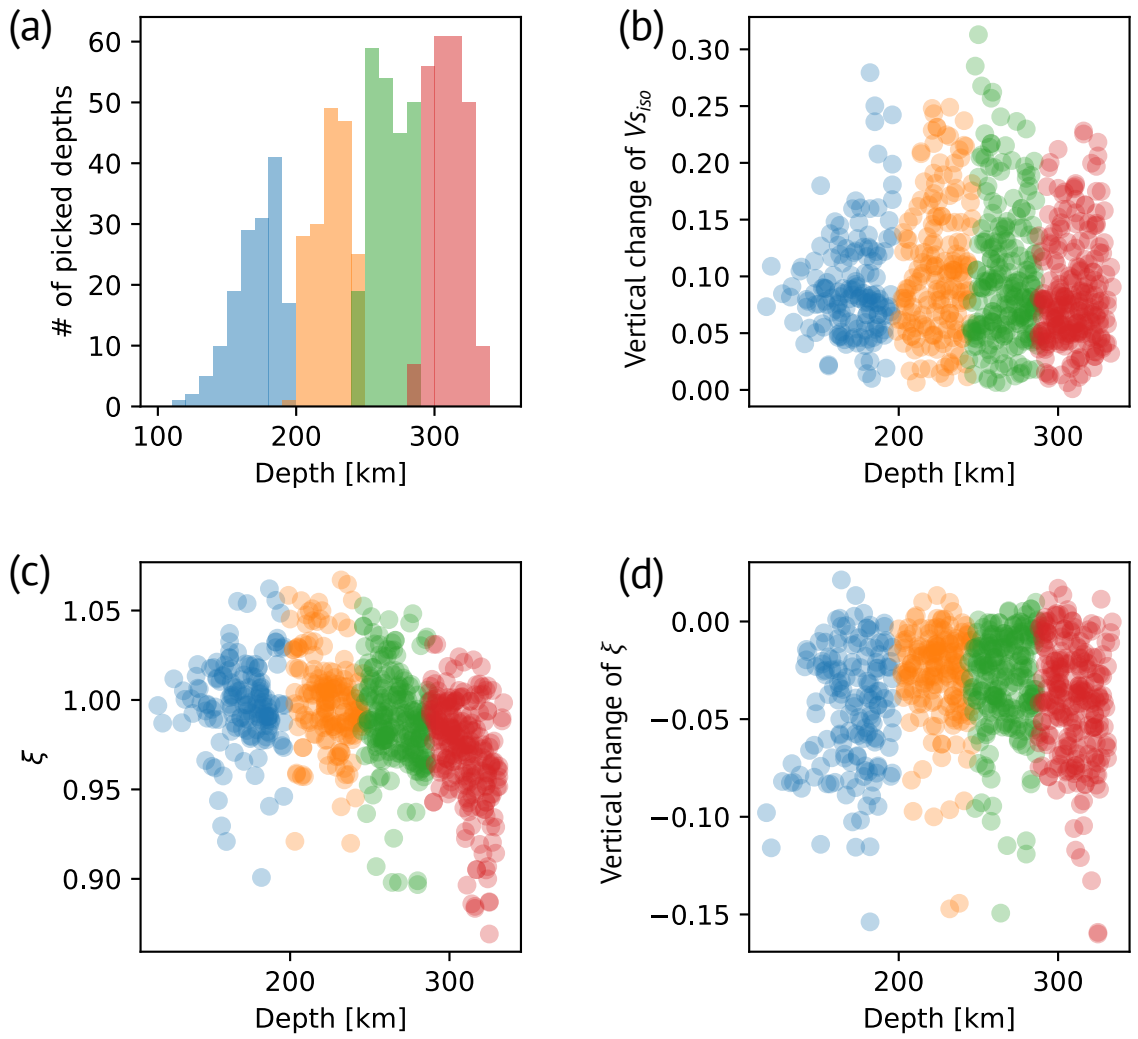

Figure C.9: Same as Figure 4.10, but for $N_c = 4$ case. Notations of colors are also the same as in Figure 10, but cluster 4 is represented by red dots. Here, we identify the X-Ds at four distinctive depths: around 170 km, 220 km, 270 km, 310 km

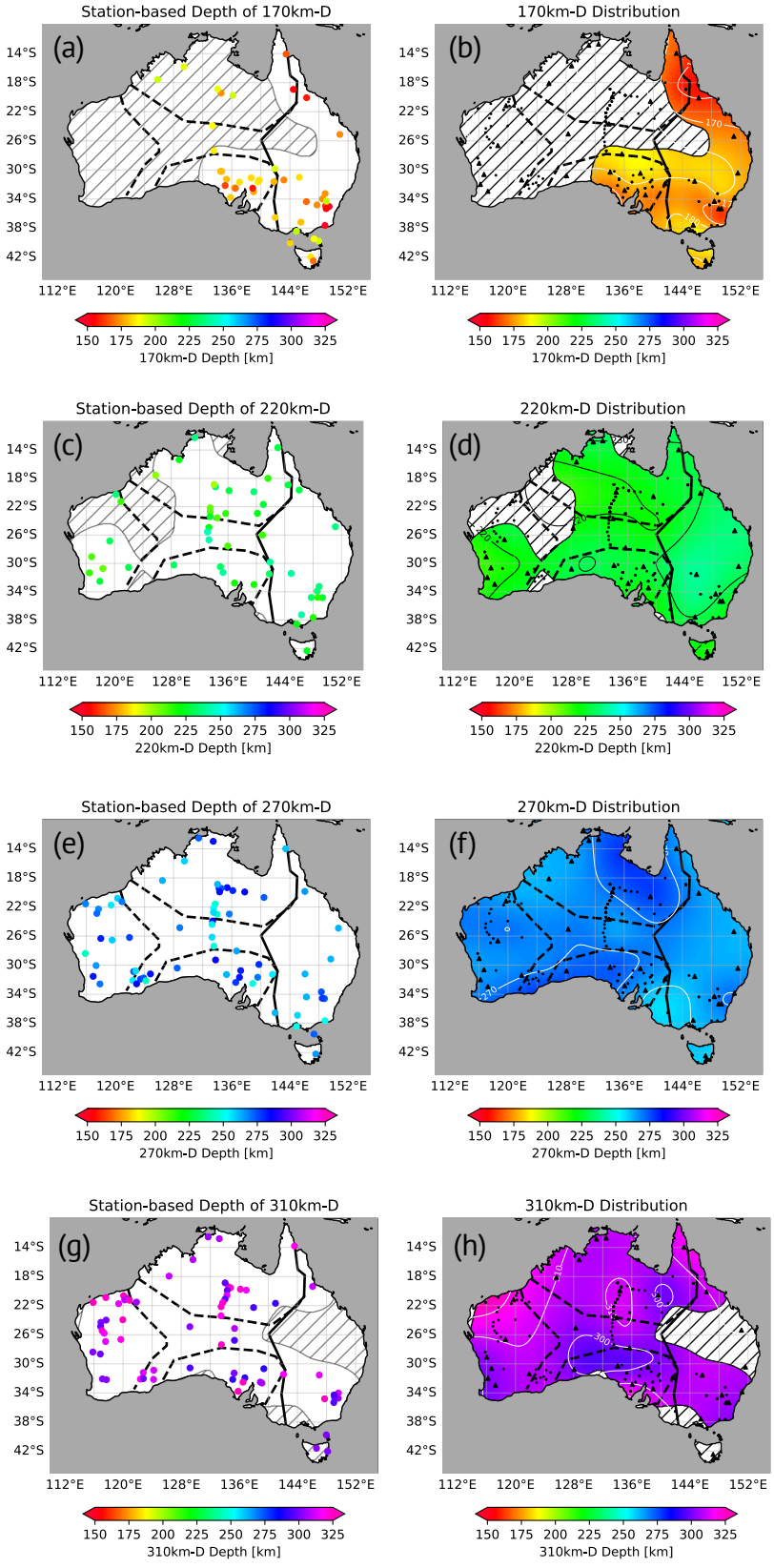

Figure C.10: Same as Figure 4.11, but for $N_c = 4$ case.

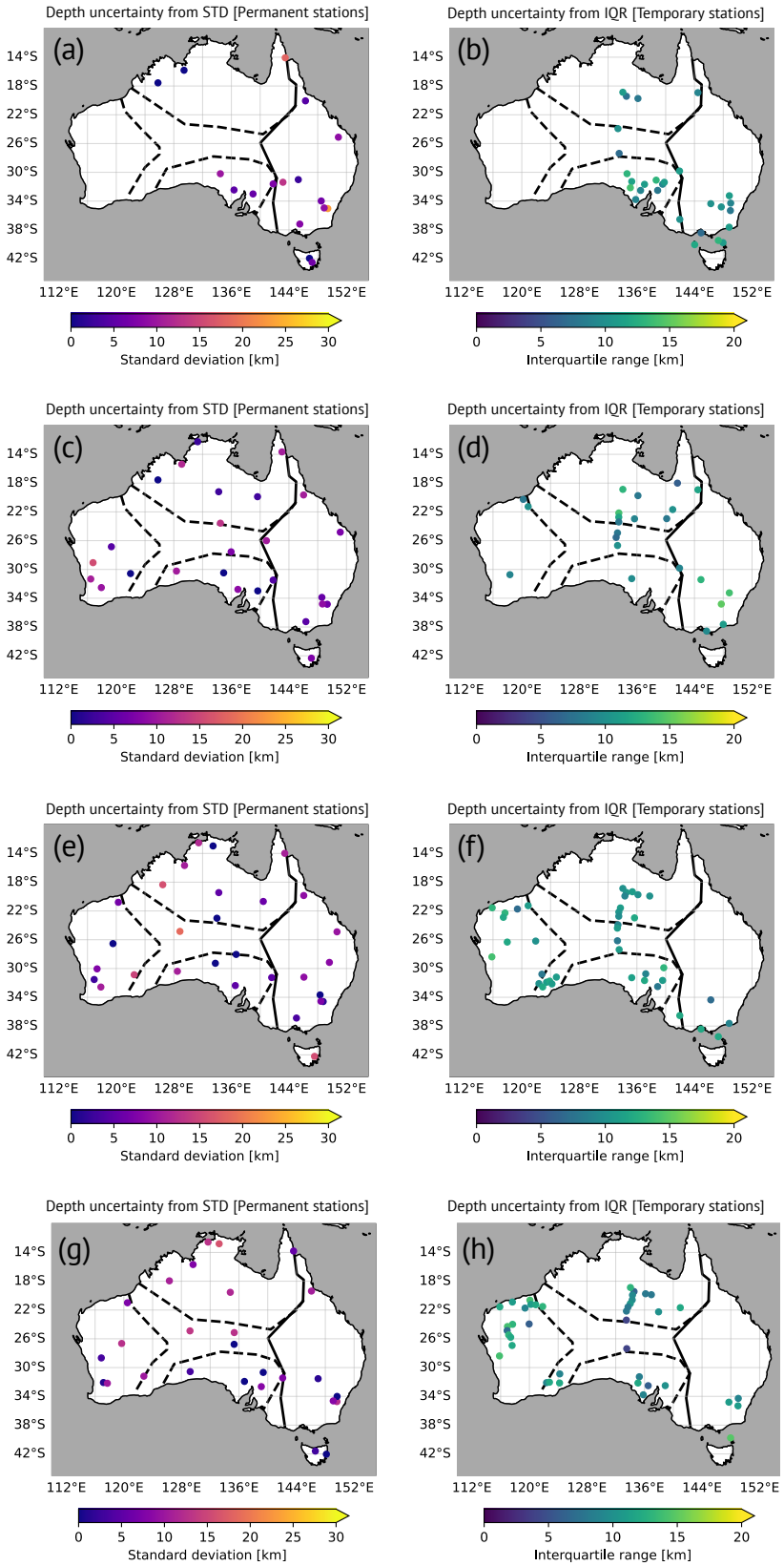

Figure C.11: Same as Figure C.8, but for $N_c = 4$ case.

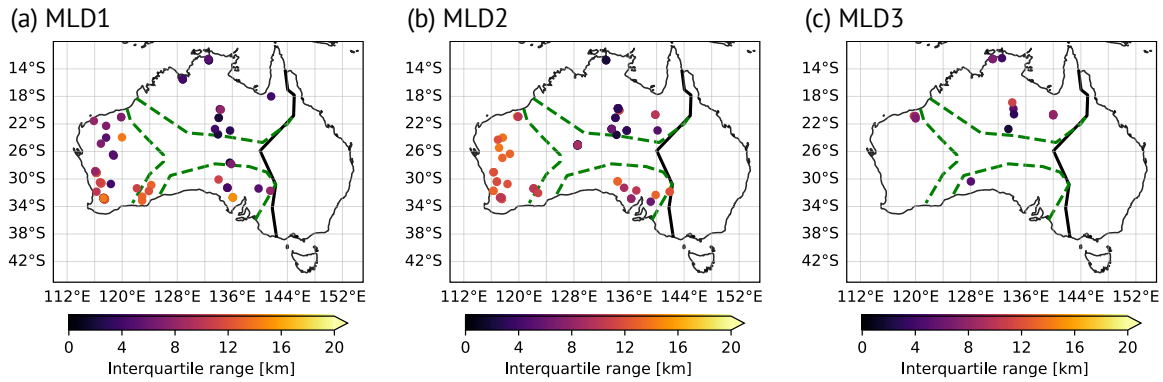

Figure C.12: Interquartile range of MLDs: (a) MLD1, (b) MLD2, (c) MLD3.

Appendix D

Supplementary information for Chapter 5

This appendix includes the supplementary information for Chapter 5.

D.1 Air-Earth coupled seismic normal mode: the 1991 Pinatubo and the 2022 Tonga

The Earth's free oscillations are of great importance to understanding seismic wave propagation at lower frequency, the Earth's internal structure, and seismic source properties, which have been utilized in seismology (e.g., Gilbert & Dziewonski, 1975; Jordan, 1978; Dziewonski & Anderson, 1981; Widmer et al., 1991; Ishii & Tromp, 1999; Nishida, 2013). In addition to large earthquakes, massive volcanic eruptions, such as the 1991 Pinatubo eruption, have also been known to generate Earth's normal modes (Kanamori & Mori, 1992).

However, the seismic energy radiated by even significant volcanic eruptions is generally much weaker than that produced by great earthquakes, often making it difficult to observe Earth's normal modes. Nevertheless, these eruptions can excite atmospheric vibrations (or the atmospheric normal modes), which can couple with the normal modes of the solid Earth; i.e., the air-Earth coupled mode. Oscillation modes with the specific eigenperiods can resonate with the solid Earth, resulting in intense atmosphere-lithosphere resonant oscillations (Lognonné et al., 1998; Watada & Kanamori, 2010). These eigenperiods typically occur around 270 s (3.7 mHz) and 235 s (4.4 mHz) (Lognonné et al., 1998; Watada & Kanamori, 2010; Nakashima et al., 2016). In this appendix, we provide additional information on the comparison of the air-Earth coupled normal modes generated by the 1991 Pinatubo and the 2022 Tonga

eruption.

Figure D.1 displays the low-frequency amplitude spectra generated by these two large eruptions, observed at multiple stations other than those shown in Figure 5.8. For most stations, the Pinatubo eruption exhibits stronger amplitude around 4.4 mHz compared to 3.7 mHz, while the 2022 Tonga eruption shows pronounced signals at 3.7 mHz. These global characteristics of the amplitude spectra provide valuable insights into the excitation process of the air-Earth coupled normal modes triggered by large volcanic events.

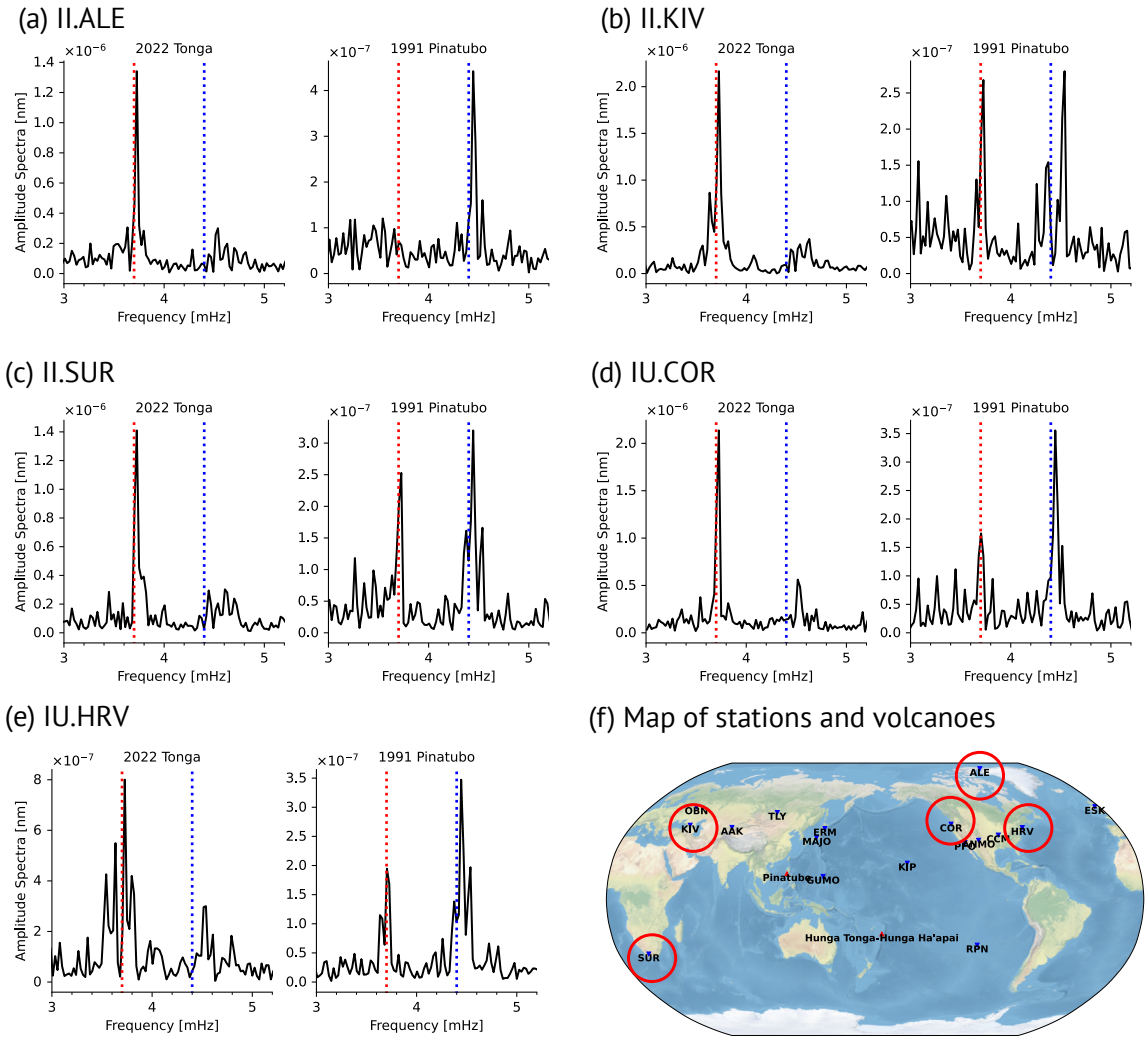

Figure D.1: Comparison of amplitude spectra generated by the two large eruptions. (a-e) Same as Figure 5.8, but for additional global stations. (f) Map showing the locations of stations and two volcanoes. Red circles indicate the stations displayed in (a-e).

D.2 Event catalog detected by BP

Tables D.1 and D.2 summarize information on detected events by P-wave back-projection (BP), including the origin time, locations (longitude, latitude), great circle distances from Hunga Tonga-Hunga Ha'apai, normalized BP amplitude, and estimated event type. We identified the origin time from the peak amplitude of each event, and the event locations (longitude and latitude) were estimated similarly. The criteria for classifying event types (volcanic eruptions or other sources, such as earthquakes) are explained in Chapter 5.

Table D.1: Detected events in the first sequence. "BP time" represents the difference between the origin time for detected events and a reference time at 04:14:45 UTC. BP amp. is the peak amplitude in the BP time series. The event type "V" represents events identified as volcanic eruptions, and "S" other events including seismic sources.

BP time	Time (UTC)	Lon. [deg]	Lat. [deg]	Dist. [deg]	BP amp.	Event type	Event ID
-760	04:02:05	-175.4	-20.4	0.1	0.012	V	A
-440	04:07:25	-175.5	-20.6	0.14	0.011	V	B
-310	04:09:35	-175.6	-20.7	0.27	0.087	V	C
-140	04:12:25	-174.7	-20.3	0.69	0.011	S	
-90	04:13:15	-173.2	-21.8	2.43	0.018	S	
-80	04:13:25	-175.7	-20.6	0.3	0.025	V	D
-70	04:13:35	-173.7	-21.0	1.67	0.022	S	
-50	04:13:55	-175.6	-21.0	0.53	0.035	S	
-30	04:14:15	-177.4	-20.5	1.87	0.025	S	
-10	04:14:35	-175.2	-20.6	0.21	0.126	V	E
10	04:14:55	-175.6	-20.7	0.27	0.922	V	F
60	04:15:45	-174.8	-20.6	0.57	0.54	V	
80	04:16:05	-175.6	-20.6	0.21	0.45	S	G
110	04:16:35	-173.5	-21.4	1.99	0.369	S	
140	04:17:05	-173.6	-21.4	1.91	0.264	S	
200	04:18:05	-175.7	-20.1	0.49	0.25	S	
230	04:18:35	-175.4	-20.5	0.0	0.756	V	H
290	04:19:35	-175.5	-20.5	0.09	1.0	V	I
340	04:20:25	-175.6	-20.7	0.27	0.334	V	J
360	04:20:45	-173.6	-21.2	1.82	0.326	S	
400	04:21:25	-175.9	-20.4	0.48	0.117	S	
430	04:21:55	-175.4	-20.7	0.2	0.012	V	K
490	04:22:55	-175.2	-21.3	0.82	0.021	S	
520	04:23:25	-175.4	-21.1	0.6	0.028	S	
540	04:23:45	-175.2	-20.4	0.21	0.123	V	L
570	04:24:15	-175.0	-20.5	0.37	0.151	V	M
610	04:24:55	-175.6	-21.0	0.53	0.059	S	
830	04:28:35	-175.4	-20.2	0.3	0.09	V	N
940	04:30:25	-174.9	-20.5	0.47	0.027	S	
1250	04:35:00	-175.4	-21.4	0.9	0.011	S	

Table D.2: Same as D.1, but for detected events in the second sequence.

BP time	Time (UTC)	Lon.[deg]	Lat. [deg]	Dist.[deg]	BP amp.	Event type	Event ID
15000	08:24:45	-175.7	-20.8	0.41	0.005	S	
15060	08:25:45	-175.4	-20.5	0.0	0.005	V	O
15250	08:28:55	-175.4	-20.5	0.0	0.083	V	P
15280	08:29:25	-175.4	-20.1	0.1	0.024	V	Q
15380	08:31:05	-175.3	-20.3	0.22	0.22	V	R
15440	08:32:05	-175.1	-20.3	0.34	0.006	V	S

D.3 Supplementary Figures

In this appendix, we display the supplementary figures for Chapter 5:

- Figure D.2: Non-volcanic events detected by the P-wave back-projection.
- Figures D.3 and D.4: Back-projection results by using other assumptions such as for the 1-D structural model.

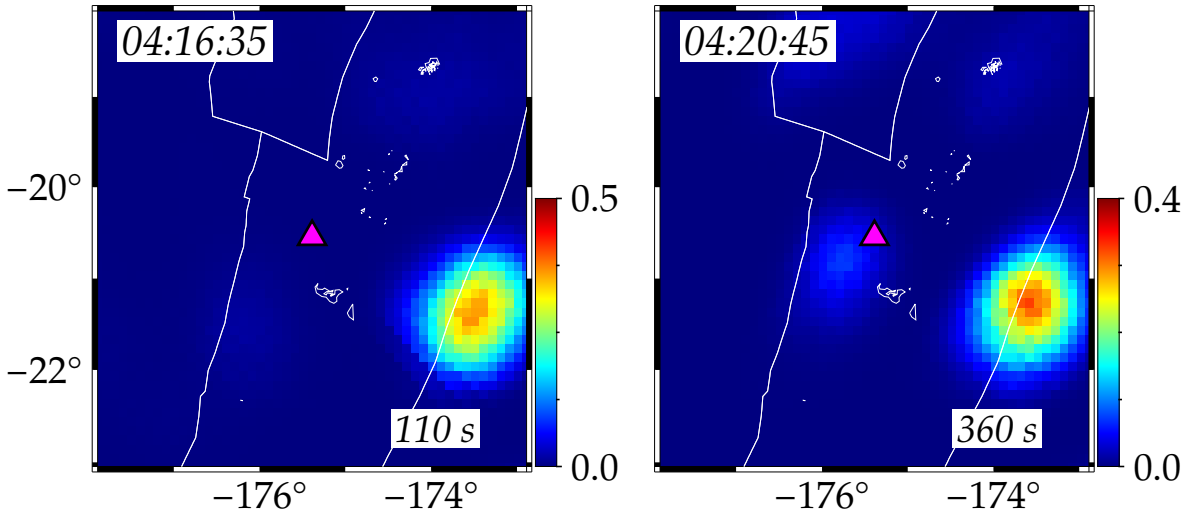

Figure D.2: Examples of detected non-volcanic events (possibly shallow earthquakes near the Tonga trench).

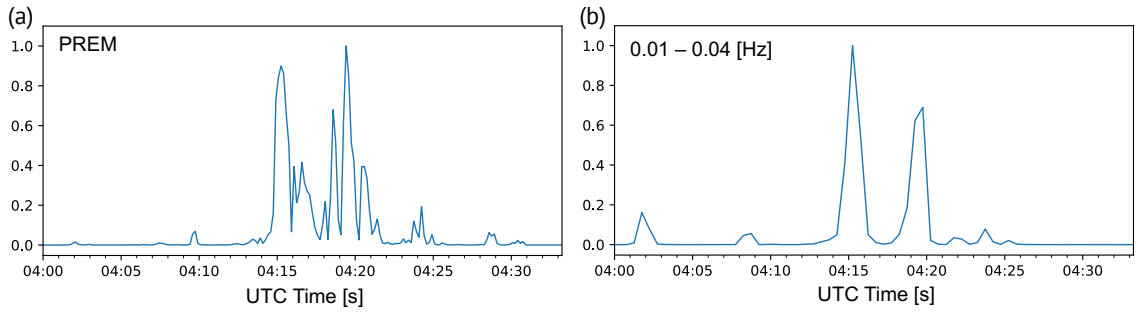

Figure D.3: BP results (time series of BP amplitude) for a different reference model (a: PREM (Dziewonski & Anderson, 1981)) and a different frequency range (b: 0.01–0.04 Hz). (a) The employed frequency range is 0.03-0.08 Hz. (b) Note that the time window for the integration in Chapter 5.3 of the main text is different; i.e., $\delta = 5$ s for the higher frequency range (0.03-0.08 Hz) and $\delta = 15$ s for the lower frequency range (0.01-0.04 Hz).

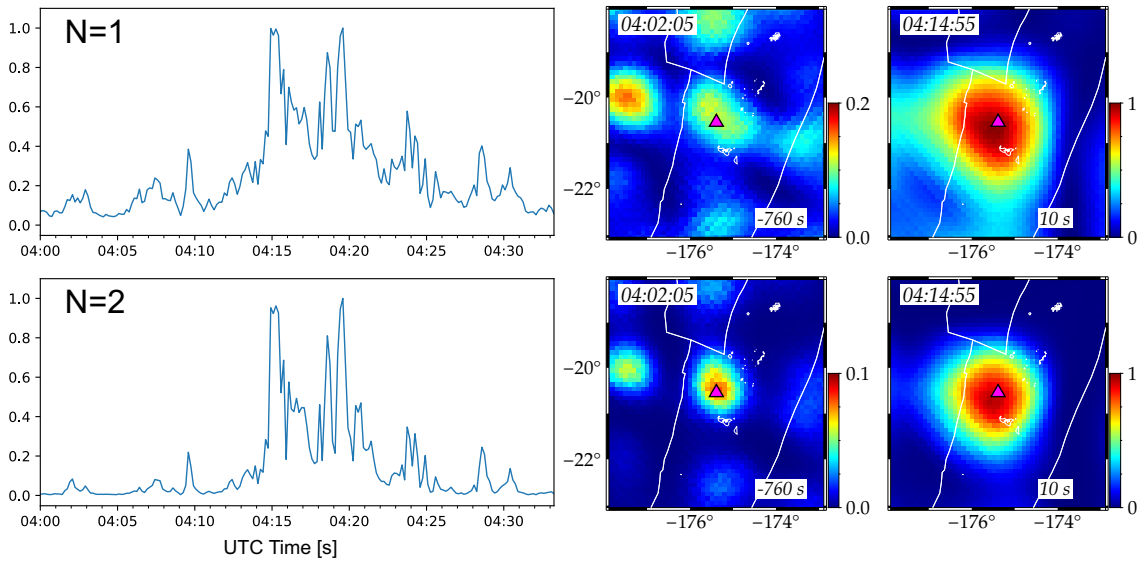

Figure D.4: Comparison of (left) time series of BP amplitude and (right) BP images derived from various N-th root stacks. (top) N=1, (middle) N=2.

Appendix E

Supplementary information for Chapter 6

This appendix includes the supplementary figures for Chapter 6, briefly described as follows:

- Figures E.1–E.3: Galleries of dataset for various frequency range.
- Figure E.4: Potential source grids used to generate the time evolution of P-wave radiation, as visualized in Figure 6.6.
- Figure E.5: Summary of back-projection results using only vertical components.

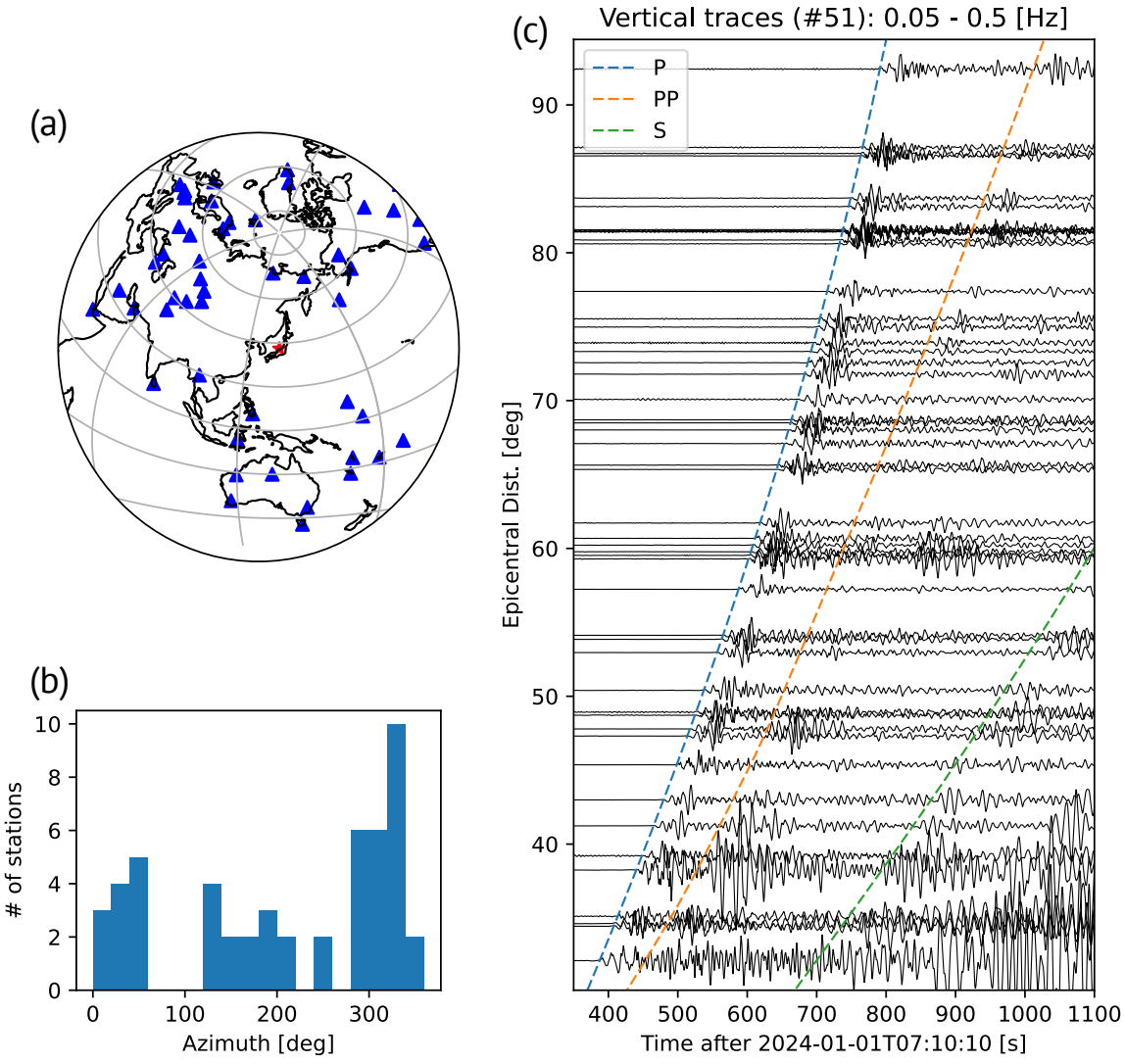

Figure E.1: Teleseismic dataset for the frequency range 0.05-0.5 Hz. The figure configuration follows that of Figure 6.2.

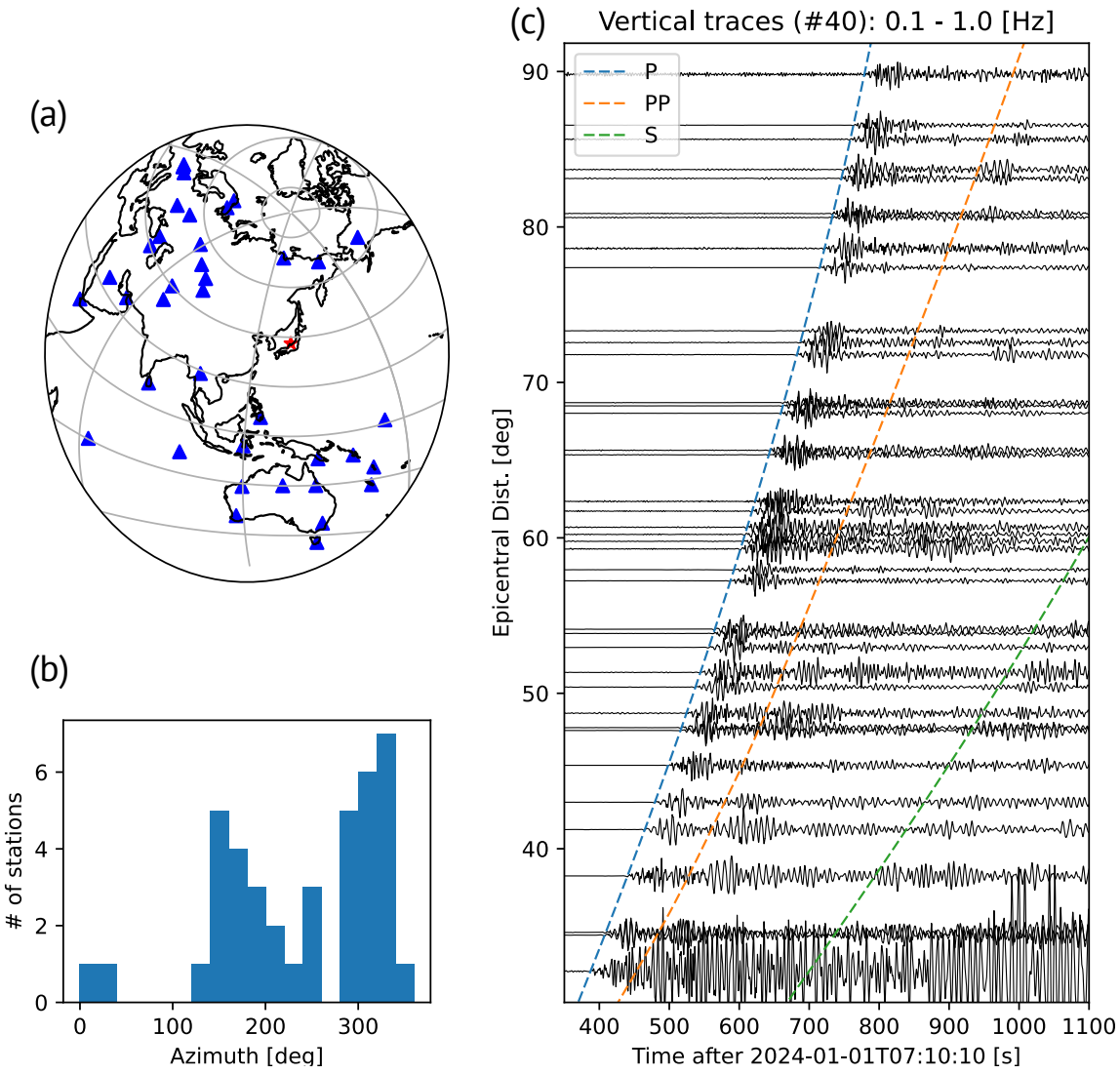

Figure E.2: Same as Figure E.1, but for 0.1-1.0 Hz.

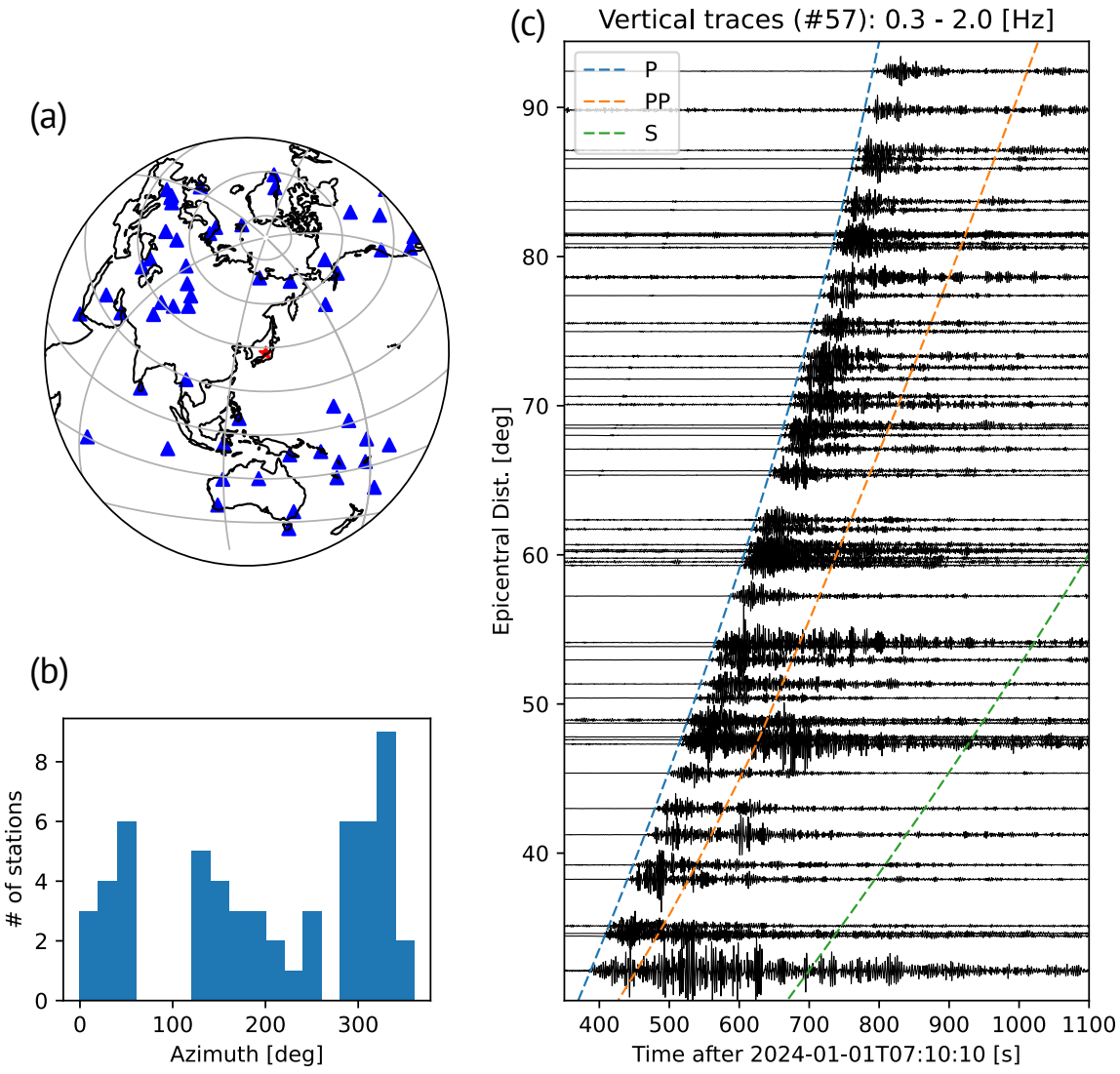

Figure E.3: Same as Figure E.1, but for 0.3-2.0 Hz.

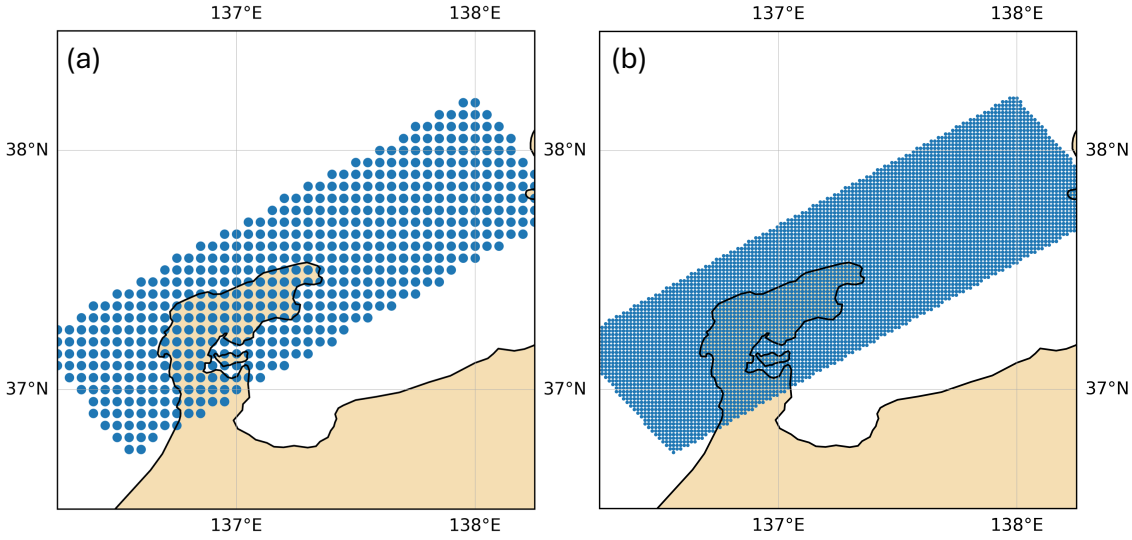

Figure E.4: Map view of projected potential source grid points used to generate Figures 6.6 and E.5. (a) 0.05 deg girds used for 0.03-0.3, 0.05-0.5, and 0.1-1.0 Hz, (b) 0.015 deg used for 0.3-2.0Hz

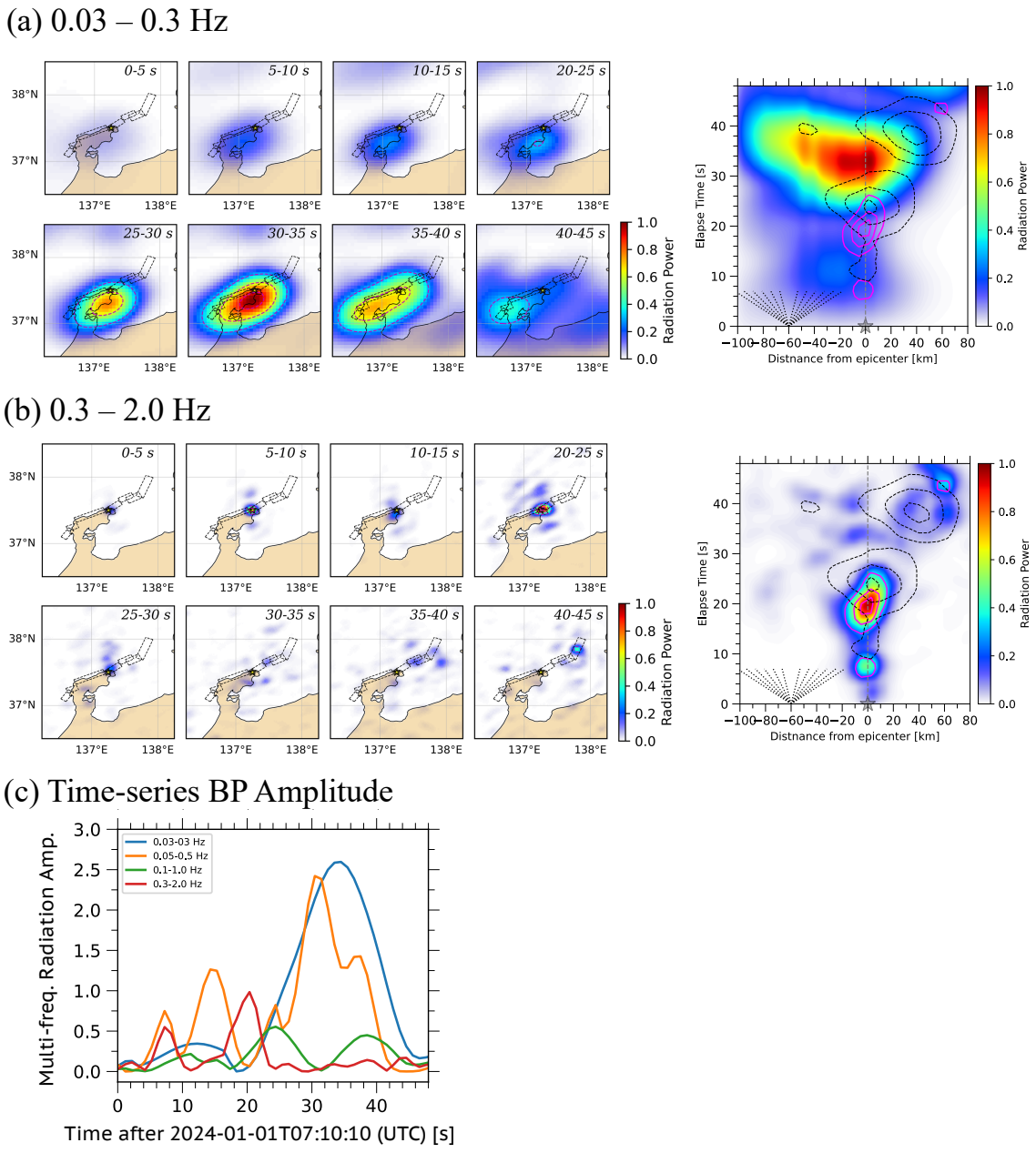

Figure E.5: Examples of selected multi-frequency back-projection results using the vertical components without the LQT conversion, following the conventional method. (a, b) Snapshots of BP (left panels) and time-dependent P-wave radiation from the source (right panels), projected along N60E^{o}, as in Figures 6.4 and 6.6 but using the conventional BP approach. (c) Same as Figure 6.5, but for the conventional BP method.

Bibliography

Abt, D. L., Fischer, K. M., French, S. W., Ford, H. A., Yuan, H., & Romanowicz, B., 2010. North American lithospheric discontinuity structure imaged by Ps and Sp receiver functions, *Journal of Geophysical Research: Solid Earth (1978–2012)*, **115**(B9).

Adda-Bedia, M. & Madariaga, R., 2008. Seismic Radiation from a Kink on an Antiplane FaultSeismic Radiation from a Kink on an Antiplane Fault, *Bulletin of the Seismological Society of America*, **98**(5), 2291–2302.

Afonso, J. C., Salajegheh, F., Szwillus, W., Ebbing, J., & Gaina, C., 2019. A global reference model of the lithosphere and upper mantle from joint inversion and analysis of multiple data sets, *Geophysical Journal International*, **217**(3), 1602–1628.

Ai, S., Akuhara, T., Morishige, M., Yoshizawa, K., Shinohara, M., & Nakahigashi, K., 2023. Layered Evolution of the Oceanic Lithosphere Beneath the Japan Basin, the Sea of Japan, *Journal of Geophysical Research: Solid Earth*, **128**(2).

Ai, S., Akuhara, T., He, L., Xiong, C., Yan, Z., & Zheng, Y., 2024. Seafloor Rayleigh ellipticity, measured from unoriented data, and its significance for passive seismic imaging in the ocean, *Geophysical Journal International*, **239**(1), 37–48.

Aitken, A. R. A. & Betts, P. G., 2009. Constraints on the Proterozoic supercontinent cycle from the structural evolution of the south-central Musgrave Province, central Australia, *Precambrian Research*, **168**(3-4), 284–300.

Aitken, A. R. A., Betts, P. G., Weinberg, R. F., & Gray, D., 2009. Constrained potential field modeling of the crustal architecture of the Musgrave Province in central

Australia: Evidence for lithospheric strengthening due to crust-mantle boundary uplift, *Journal of Geophysical Research: Solid Earth*, **114**(B12).

Akaogi, M., Yusa, H., Shiraishi, K., & Suzuki, T., 1995. Thermodynamic properties of α-quartz, coesite, and stishovite and equilibrium phase relations at high pressures and high temperatures, *Journal of Geophysical Research: Solid Earth*, **100**(B11), 22337–22347.

Akashi, A., Nishihara, Y., Takahashi, E., Nakajima, Y., Tange, Y., & Funakoshi, K., 2009. Orthoenstatite/clinoenstatite phase transformation in MgSiO3 at high-pressure and high-temperature determined by in situ X-ray diffraction: Implications for nature of the X discontinuity, *Journal of Geophysical Research: Solid Earth*, **114**(B4).

Akuhara, T., Nakahigashi, K., Shinohara, M., Yamada, T., Shiobara, H., Yamashita, Y., Mochizuki, K., & Uehira, K., 2021. Lithosphere–asthenosphere boundary beneath the Sea of Japan from transdimensional inversion of S-receiver functions, *Earth, Planets and Space*, **73**(1), 171.

Akuhara, T., Yamashita, Y., Ohyanagi, S., Sawaki, Y., Yamada, T., & Shinohara, M., 2023. Shallow Low-Velocity Layer in the Hyuga-Nada Accretionary Prism and Its Hydrological Implications: Insights From a Passive Seismic Array, *Journal of Geophysical Research: Solid Earth*, **128**(4).

Amezawa, Y., Hiramatsu, Y., Miyakawa, A., Imanishi, K., & Otsubo, M., 2023. Long-Living Earthquake Swarm and Intermittent Seismicity in the Northeastern Tip of the Noto Peninsula, Japan, *Geophysical Research Letters*, **50**(8).

Argus, D. F., Gordon, R. G., & DeMets, C., 2011. Geologically current motion of 56 plates relative to the no-net-rotation reference frame, *Geochemistry, Geophysics, Geosystems*, **12**(11).

Astafyeva, E., Maletckii, B., Mikesell, T. D., Munaibari, E., Ravanelli, M., Coisson, P., Manta, F., & Rolland, L., 2022. The 15 January 2022 Hunga Tonga Eruption

History as Inferred From Ionospheric Observations, *Geophysical Research Letters*, **49**(10).

Ba, K., Gao, S. S., Song, J., & Liu, K. H., 2023. Seismic Azimuthal Anisotropy Beneath a Fast Moving Ancient Continent: Constraints From Shear Wave Splitting Analysis in Australia, *Journal of Geophysical Research: Solid Earth*, **128**(2).

Balfour, N. J., Salmon, M., & Sambridge, M., 2014. The Australian Seismometers in Schools Network: Education, Outreach, Research, and Monitoring, *Seismological Research Letters*, **85**(5), 1063–1068.

Beresnev, I. A., 2017. Factors controlling high-frequency radiation from extended ruptures, *Journal of Seismology*, **21**(5), 1277–1284.

Bernard, P. & Madariaga, R., 1984. High-frequency seismic radiation from a buried circular fault, *Geophysical Journal of the Royal Astronomical Society*, **78**(1), 1–17.

Beyreuther, M., Barsch, R., Krischer, L., Megies, T., Behr, Y., & Wassermann, J., 2010. ObsPy: A Python Toolbox for Seismology, *Seismological Research Letters*, **81**(3), 530–533.

Bianchi, I., Park, J., Agostinetti, N. P., & Levin, V., 2010. Mapping seismic anisotropy using harmonic decomposition of receiver functions: An application to Northern Apennines, Italy, *Journal of Geophysical Research: Solid Earth*, **115**(B12).

Bird, P., 2003. An updated digital model of plate boundaries, *Geochemistry, Geophysics, Geosystems*, **4**(3).

Birkey, A. & Ford, H. A., 2023. Anisotropic structure of the Australian continent, *Frontiers in Earth Science*, **10**, 1055480.

Birkey, A., Ford, H. A., Dabney, P., & Goldhagen, G., 2021. The Lithospheric Architecture of Australia From Seismic Receiver Functions, *Journal of Geophysical Research: Solid Earth*, **126**(4).

Bodin, T., Sambridge, M., Tkalčić, H., Arroucau, P., Gallagher, K., & Rawlinson, N., 2012. Transdimensional inversion of receiver functions and surface wave dispersion, *Journal of Geophysical Research: Solid Earth (1978–2012)*, **117**(B2).

Bodin, T., Yuan, H., & Romanowicz, B., 2014. Inversion of receiver functions without deconvolution—application to the Indian craton, *Geophysical Journal International*, **196**(2), 1025–1033.

Bodin, T., Leiva, J., Romanowicz, B., Maupin, V., & Yuan, H., 2016. Imaging anisotropic layering with Bayesian inversion of multiple data types, *Geophysical Journal International*, **206**(1), 605–629.

Bokelmann, G. H. R., 1995. P-wave array polarization analysis and effective anisotropy of the brittle crust, *Geophysical Journal International*, **120**(1), 145–162.

Bostock, M. G. & Rondenay, S., 1999. Migration of scattered teleseismic body waves, *Geophysical Journal International*, **137**(3), 732–746.

Bouchon, M., 1976. Teleseismic body wave radiation from a seismic source in a layered medium, *Geophysical Journal International*, **47**(3), 515–530.

Boyce, A., Bodin, T., Durand, S., Soergel, D., & Debayle, E., 2024. Seismic Evidence for Craton Formation by Underplating and Development of the MLD, *Geophysical Research Letters*, **51**(4).

Bruhat, L., Fang, Z., & Dunham, E. M., 2016. Rupture complexity and the supershear transition on rough faults, *Journal of Geophysical Research: Solid Earth*, **121**(1), 210–224.

Byrnes, J., Gaherty, J., & Hopper, E., 2023. Seismic Architecture of the Lithosphere-Asthenosphere System in the Western United States from a Joint Inversion of Body- and Surface-wave Observations: Distribution of Partial Melt in the Upper Mantle, *Seismica*, **2**(2).

Calò, M., Bodin, T., & Romanowicz, B., 2016. Layered structure in the upper mantle across North America from joint inversion of long and short period seismic data, *Earth and Planetary Science Letters*, **449**, 164–175.

Chaudhury, J., Mitra, S., & Sarkar, T., 2021. Hales Discontinuity in the Southern Indian Continental Lithosphere: Seismological and Petrological Models, *Journal of Geophysical Research: Solid Earth*, **126**(2).

Chen, C., Gilbert, H., Fischer, K. M., Andronicos, C. L., Pavlis, G. L., Hamburger, M. W., Marshak, S., Larson, T., & Yang, X., 2018. Lithospheric discontinuities beneath the U.S. Midcontinent – signatures of Proterozoic terrane accretion and failed rifting, *Earth and Planetary Science Letters*, **481**, 223–235.

Chen, K., Forsyth, D. W., & Fischer, K. M., 2024. A Mid-Lithospheric Discontinuity Detected Beneath 155 Ma Western Pacific Seafloor Using Sp Receiver Functions, *Geophysical Research Letters*, **51**(5).

Chen, X., Levin, V., & Yuan, H., 2021a. Small Shear Wave Splitting Delays Suggest Weak Anisotropy in Cratonic Mantle Lithosphere, *Geophysical Research Letters*, **48**(16).

Chen, X., Levin, V., Yuan, H., Klaser, M., & Li, Y., 2021b. Seismic Anisotropic Layering in the Yilgarn and Superior Cratonic Lithosphere, *Journal of Geophysical Research: Solid Earth*, **126**(8).

Cheng, C., Bodin, T., Tauzin, B., & Allen, R. M., 2017. Cascadia subduction slab heterogeneity revealed by three-dimensional receiver function Kirchhoff migration, *Geophysical Research Letters*, **44**(2), 694–701.

Clark, D., Hensen, B., & Kinny, P., 2000. Geochronological constraints for a two-stage history of the Albany–Fraser Orogen, Western Australia, *Precambrian Research*, **102**(3-4), 155–183.

Crampin, S., 1975. Distinctive Particle Motion of Surface Waves as a Diagnostic of Anisotropic Layering, *Geophysical Journal of the Royal Astronomical Society*, **40**(2), 177 – 186.

Crampin, S., Stephen, R. A., & McGonigle, R., 1982. The polarization of P-waves in anisotropic media, *Geophysical Journal of the Royal Astronomical Society*, **68**(2), 477–485.

Cristiano, L., Meier, T., Krüger, F., Keers, H., & Weidle, C., 2016. Teleseismic P -wave polarization analysis at the Gräfenberg array, *Geophysical Journal International*, **207**(3), 1456–1471.

Dai, M. & Sun, D., 2023. Martian Crustal Model From a Joint Inversion of Receiver Functions and Apparent Shear Wave Velocity, *Journal of Geophysical Research: Planets*, **128**(11).

Dalton, C. A., Ekström, G., & Dziewoński, A. M., 2008. The global attenuation structure of the upper mantle, *Journal of Geophysical Research: Solid Earth (1978–2012)*, **113**(B9).

Davies, D. R., Rawlinson, N., Iaffaldano, G., & Campbell, I. H., 2015. Lithospheric controls on magma composition along Earth's longest continental hotspot track, *Nature*, **525**(7570), 511–514.

Debayle, E. & Kennett, B. L. N., 2000. The Australian continental upper mantle: Structure and deformation inferred from surface waves, *Journal of Geophysical Research: Solid Earth*, **105**(B11), 25423–25450.

Debayle, E., Kennett, B., & Priestley, K., 2005. Global azimuthal seismic anisotropy and the unique plate-motion deformation of Australia, *Nature*, **433**(7025), 509–512.

de Laat, J. I., Lebedev, S., Celli, N. L., Bonadio, R., Chagas de Melo, B., & Rawlinson, N., 2023. Structure and evolution of the Australian plate and underlying upper mantle from waveform tomography with massive data sets, *Geophysical Journal International*, **234**(1), 153–189.

Deng, W., Han, G., Li, J., & Sun, L., 2024. Seismometer Orientation Measurements of Broadband Seismic Stations in the China Digital Seismograph Network, *Bulletin of the Seismological Society of America*.

Deuss, A. & Woodhouse, J. H., 2002. A systematic search for mantle discontinuities using SS-precursors, *Geophysical Research Letters*, **29**(8), 90–1–90–4.

Deuss, A. & Woodhouse, J. H., 2004. The nature of the Lehmann discontinuity from its seismological Clapeyron slopes, *Earth and Planetary Science Letters*, **225**(3-4), 295–304.

Drummond, B. J., Muirhead, K. J., & Hales, A. L., 1982. Evidence for a seismic discontinuity near 200km depth under a continental margin, *Geophysical Journal International*, **70**(1), 67–77.

Dziewonski, A. & Hales, A., 1972. Numerical Analysis of Dispersed Seismic Waves, *Methods in Computational Physics: Advances in Research and Applications*, **11**, 39–85.

Dziewonski, A. M. & Anderson, D. L., 1981. Preliminary reference Earth model, *Physics of the Earth and Planetary Interiors*, **25**(4), 297–356.

Dziewonski, A. M., Chou, T., & Woodhouse, J. H., 1981. Determination of earthquake source parameters from waveform data for studies of global and regional seismicity, *Journal of Geophysical Research: Solid Earth*, **86**(B4), 2825–2852.

Eakin, C. M., Flashman, C., & Agrawal, S., 2021. Seismic anisotropy beneath Central Australia: A record of ancient lithospheric deformation, *Tectonophysics*, **820**, 229123.

Eakin, C. M., Davies, D. R., Ghelichkhan, S., O'Donnell, J. P., & Agrawal, S., 2023. The Influence of Lithospheric Thickness Variations Beneath Australia on Seismic Anisotropy and Mantle Flow, *Geochemistry, Geophysics, Geosystems*, **24**(9).

Eaton, D. W., Darbyshire, F., Evans, R. L., Grütter, H., Jones, A. G., & Yuan, X., 2009. The elusive lithosphere–asthenosphere boundary (LAB) beneath cratons, *Lithos*, **109**(1-2), 1–22.

Ekström, G., 2006. Global Detection and Location of Seismic Sources by Using Surface Waves, *Bulletin of the Seismological Society of America*, **96**(4A), 1201–1212.

Ekström, G., 2008. Polarization anomalies at various stations.

Ekström, G. & Busby, R. W., 2008. Measurements of Seismometer Orientation at US-Array Transportable Array and Backbone Stations, *Seismological Research Letters*, **79**(4), 554–561.

Ekström, G., Dalton, C. A., & Nettles, M., 2006. Observations of Time-dependent Errors in Long-period Instrument Gain at Global Seismic Stations, *Seismological Research Letters*, **77**(1), 12–22.

Ekström, G., Nettles, M., & Dziewoński, A., 2012. The global CMT project 2004–2010: Centroid-moment tensors for 13,017 earthquakes, *Physics of the Earth and Planetary Interiors*, **200**, 1–9.

FDMA, 2024. Information on Noto Peninsula Earthquake.

Fichtner, A., Kennett, B. L. N., & Trampert, J., 2013. Separating intrinsic and apparent anisotropy, *Physics of the Earth and Planetary Interiors*, **219**, 11–20.

Fischer, K. M., Ford, H. A., Abt, D. L., & Rychert, C. A., 2010. The Lithosphere-Asthenosphere Boundary, *Annual Review of Earth and Planetary Sciences*, **38**(1), 551–575.

Fischer, K. M., Rychert, C. A., Dalton, C. A., Miller, M. S., Beghein, C., & Schutt, D. L., 2020. A comparison of oceanic and continental mantle lithosphere, *Physics of the Earth and Planetary Interiors*, **309**, 106600.

Fishwick, S., Heintz, M., Kennett, B. L. N., Reading, A. M., & Yoshizawa, K., 2008. Steps in lithospheric thickness within eastern Australia, evidence from surface wave tomography, *Tectonics*, **27**(4).

Fontaine, F. & Kennet, B., 2007. SOC - Southern Craton.

Fontaine, F. R., Barruol, G., Kennett, B. L. N., Bokelmann, G. H. R., & Reymond, D., 2009. Upper mantle anisotropy beneath Australia and Tahiti from P wave polarization: Implications for real-time earthquake location, *Journal of Geophysical Research: Solid Earth*, **114**(B3).

Fontaine, F. R., Roult, G., Hejrani, B., Michon, L., Ferrazzini, V., Barruol, G., Tkalčić, H., Muro, A. D., Peltier, A., Reymond, D., Staudacher, T., & Massin, F., 2019. Very- and ultra-long-period seismic signals prior to and during caldera formation on La Réunion Island, *Scientific Reports*, **9**(1), 8068.

Ford, H. A., Fischer, K. M., Abt, D. L., Rychert, C. A., & Elkins-Tanton, L. T., 2010. The lithosphere–asthenosphere boundary and cratonic lithospheric layering beneath Australia from Sp wave imaging, *Earth and Planetary Science Letters*, **300**(3-4), 299–310.

Ford, H. A., Long, M. D., & Wirth, E. A., 2016. Midlithospheric discontinuities and complex anisotropic layering in the mantle lithosphere beneath the Wyoming and Superior Provinces, *Journal of Geophysical Research: Solid Earth*, **121**(9), 6675–6697.

Frederiksen, A. W. & Bostock, M. G., 2000. Modelling teleseismic waves in dipping anisotropic structures, *Geophysical Journal International*, **141**(2), 401–412.

Frederiksen, A. W., Folsom, H., & Zandt, G., 2003. Neighbourhood inversion of teleseismic Ps conversions for anisotropy and layer dip, *Geophysical Journal International*, **155**(1), 200–212.

Fu, H., Li, Z., & Chen, L., 2022. Continental Mid-Lithosphere Discontinuity: A Water Collector During Craton Evolution, *Geophysical Research Letters*, **49**(23).

Fujii, Y. & Satake, K., 2024. Slip distribution of the 2024 Noto Peninsula earthquake (MJMA 7.6) estimated from tsunami waveforms and GNSS data, *Earth, Planets and Space*, **76**(1), 44.

Fukahata, Y., Yagi, Y., & Rivera, L., 2014. Theoretical relationship between back-projection imaging and classical linear inverse solutions, *Geophysical Journal International*, **196**(1), 552–559.

Gabriel, A., Ampuero, J., Dalguer, L. A., & Mai, P. M., 2012. The transition of dynamic rupture styles in elastic media under velocity-weakening friction, *Journal of Geophysical Research: Solid Earth*, **117**(B9).

Gaherty, J. B. & Jordan, T. H., 1995. Lehmann Discontinuity as the Base of an Anisotropic Layer Beneath Continents, *Science*, **268**(5216), 1468–1471.

Gama, I., Fischer, K. M., Eilon, Z., Krueger, H. E., Dalton, C. A., & Flesch, L. M., 2021. Shear-wave velocity structure beneath Alaska from a Bayesian joint inversion of Sp receiver functions and Rayleigh wave phase velocities, *Earth and Planetary Science Letters*, **560**, 116785.

Ghosh, A., Holt, W. E., & Wen, L., 2013. Predicting the lithospheric stress field and plate motions by joint modeling of lithosphere and mantle dynamics, *Journal of Geophysical Research: Solid Earth*, **118**(1), 346 – 368.

Gilbert, F. & Dziewonski, A. M., 1975. An application of normal mode theory to the retrieval of structural parameters and source mechanisms from seismic spectra, *Philosophical Transactions of the Royal Society of London. Series A, Mathematical and Physical Sciences*, **278**(1280), 187–269.

Gilbert, H., Beck, S., & Zandt, G., 2006. Lithospheric and upper mantle structure of central Chile and Argentina, *Geophysical Journal International*, **165**(1), 383–398.

Global Volcanism Program, 2013. Hunga Tonga-Hunga Ha'apai (243040) in Volcanoes of the World.

Goes, S., Simons, F. J., & Yoshizawa, K., 2005. Seismic constraints on temperature of the Australian uppermost mantle, *Earth and Planetary Science Letters*, **236**(1-2), 227–237.

Green, P. J., 1995. Reversible jump Markov chain Monte Carlo computation and Bayesian model determination, *Biometrika*, **82**(4), 711–732.

Hales, A., 1969. A seismic discontinuity in the lithosphere, *Earth and Planetary Science Letters*, **7**(1), 44–46.

Hales, A., Muirhead, K., & Rynn, J., 1980. A compressional velocity distribution for the upper mantle, *Tectonophysics*, **63**(1-4), 309–348.

Hao, J., Ji, C., & Yao, Z., 2017. Slip history of the 2016 Mw 7.0 Kumamoto earthquake: Intraplate rupture in complex tectonic environment, *Geophysical Research Letters*, **44**(2), 743–750.

Hartzell, S., Mendoza, C., Ramirez-Guzman, L., Zeng, Y., & Mooney, W., 2013. Rupture History of the 2008 Mw 7.9 Wenchuan, China, Earthquake: Evaluation of Separate and Joint Inversions of Geodetic, Teleseismic, and Strong-Motion DataRupture History of 2008 Mw 7.9 Wenchuan, China, Earthquake, *Bulletin of the Seismological Society of America*, **103**(1), 353–370.

Hartzell, S. H. & Heaton, T. H., 1983. Inversion of strong ground motion and teleseismic waveform data for the fault rupture history of the 1979 Imperial Valley, California, earthquake, *Bulletin of the Seismological Society of America*, **73**(6A), 1553–1583.

Haskell, N. A., 1962. Crustal reflection of plane P and SV waves, *Journal of Geophysical Research*, **67**(12), 4751–4768.

Hasterok, D., Halpin, J. A., Collins, A. S., Hand, M., Kreemer, C., Gard, M. G., & Glorie, S., 2022. New Maps of Global Geological Provinces and Tectonic Plates, *Earth-Science Reviews*, **231**, 104069.

Hastings, W. K., 1970. Monte Carlo sampling methods using Markov chains and their applications, *Biometrika*, **57**(1), 97–109.

Hejrani, B. & Tkalčić, H., 2020. Resolvability of the Centroid-Moment-Tensors for Shallow Seismic Sources and Improvements From Modeling High-Frequency Waveforms, *Journal of Geophysical Research: Solid Earth*, **125**(7).

Honda, R. & Aoi, S., 2009. Array Back-Projection Imaging of the 2007 Niigataken Chuetsu-oki Earthquake Striking the World's Largest Nuclear Power Plant, *Bulletin of the Seismological Society of America*, **99**(1), 141–147.

Honda, R., Yukutake, Y., Ito, H., Harada, M., Aketagawa, T., Yoshida, A., Sakai, S., Nakagawa, S., Hirata, N., Obara, K., & Kimura, H., 2011. A complex rupture image of the 2011 off the Pacific coast of Tohoku Earthquake revealed by the MeSO-net, *Earth, Planets and Space*, **63**(7), 583–588.

Honda, R., Yukutake, Y., Ito, H., Harada, M., Aketagawa, T., Yoshida, A., Sakai, S., Nakagawa, S., Hirata, N., Obara, K., Matsubara, M., & Kimura, H., 2013. Rupture process of the largest aftershock of the M 9 Tohoku-oki earthquake obtained from a back-projection approach using the MeSO-net data, *Earth, Planets and Space*, **65**(8), 917–921.

Hua, J., Fischer, K. M., Becker, T. W., Gazel, E., & Hirth, G., 2023. Asthenospheric low-velocity zone consistent with globally prevalent partial melting, *Nature Geoscience*, **16**(2), 175–181.

Hunter, J. D., 2007. Matplotlib: A 2D Graphics Environment, *Computing in Science & Engineering*, **9**(3), 90–95.

Imanishi, K. & Takeo, M., 1998. Estimates of fault dimensions for small earthquakes using stopping phases, *Geophysical Research Letters*, **25**(15), 2897–2900.

Imanishi, K. & Takeo, M., 2002. An inversion method to analyze rupture processes of small earthquakes using stopping phases, *Journal of Geophysical Research: Solid Earth*, **107**(B3), ESE 2–1–ESE 2–16.

Ishii, M., 2011. High-frequency rupture properties of the Mw 9.0 off the Pacific coast of Tohoku Earthquake, *Earth, Planets and Space*, **63**(7), 18.

Ishii, M. & Tromp, J., 1999. Normal-Mode and Free-Air Gravity Constraints on Lateral Variations in Velocity and Density of Earth9s Mantle, *Science*, **285**(5431), 1231–1236.

Ishii, M., Shearer, P. M., Houston, H., & Vidale, J. E., 2005. Extent, duration and speed of the 2004 Sumatra–Andaman earthquake imaged by the Hi-Net array, *Nature*, **435**(7044), 933–936.

Ishii, M., Shearer, P. M., Houston, H., & Vidale, J. E., 2007. Teleseismic P wave imaging of the 26 December 2004 Sumatra-Andaman and 28 March 2005 Sumatra earthquake ruptures using the Hi-net array, *Journal of Geophysical Research: Solid Earth (1978–2012)*, **112**(B11).

Isse, T., Kawakatsu, H., Yoshizawa, K., Takeo, A., Shiobara, H., Sugioka, H., Ito, A., Suetsugu, D., & Reymond, D., 2019. Surface wave tomography for the Pacific Ocean incorporating seafloor seismic observations and plate thermal evolution, *Earth and Planetary Science Letters*, **510**, 116–130.

Jacobsen, S. D., Liu, Z., Ballaran, T. B., Littlefield, E. F., Ehm, L., & Hemley, R. J., 2010. Effect of H2O on upper mantle phase transitions in MgSiO3: Is the depth of the seismic X-discontinuity an indicator of mantle water content?, *Physics of the Earth and Planetary Interiors*, **183**(1-2), 234–244.

Ji, C., Archuleta, R. J., & Twardzik, C., 2015. Rupture history of 2014 Mw 6.0 South Napa earthquake inferred from near-fault strong motion data and its impact to the practice of ground strong motion prediction, *Geophysical Research Letters*, **42**(7), 2149–2156.

Jia, Z., Zhan, Z., & Kanamori, H., 2022. The 2021 South Sandwich Island Mw 8.2 Earthquake: A Slow Event Sandwiched Between Regular Ruptures, *Geophysical Research Letters*, **49**(3).

JMA, 2024a. JMA Earthquake Catalog.

JMA, 2024b. The Seismological Bulletin of Japan.

Jordan, T. H., 1975. The continental tectosphere, *Reviews of Geophysics*, **13**(3), 1–12.

Jordan, T. H., 1978. A procedure for estimating lateral variations from low-frequency eigenspectra data, *Geophysical Journal of the Royal Astronomical Society*, **52**(3), 441–455.

Jordan, T. H., 1988. Structure and Formation of the Continental Tectosphere, *Journal of Petrology*, **Special_Volume**(1), 11–37.

Joshi, R., Knapmeyer-Endrun, B., Mosegaard, K., Wieczorek, M. A., Igel, H., Christensen, U. R., & Lognonné, P., 2023. Joint Inversion of Receiver Functions and Apparent Incidence Angles to Determine the Crustal Structure of Mars, *Geophysical Research Letters*, **50**(3).

Julià, J., Ammon, C. J., Herrmann, R. B., & Correig, A. M., 2000. Joint inversion of receiver function and surface wave dispersion observations, *Geophysical Journal International*, **143**(1), 99–112.

Kanamori, H. & Given, J. W., 1982. Analysis of long-period seismic waves excited by the May 18, 1980, eruption of Mount St. Helens—A terrestrial monopole?, *Journal of Geophysical Research: Solid Earth*, **87**(B7), 5422–5432.

Kanamori, H. & Mori, J., 1992. Harmonic excitation of mantle Rayleigh waves by the 1991 eruption of Mount Pinatubo, Philippines, *Geophysical Research Letters*, **19**(7), 721–724.

Kanamori, H., Given, J. W., & Lay, T., 1984. Analysis of seismic body waves excited by the Mount St. Helens eruption of May 18, 1980, *Journal of Geophysical Research: Solid Earth*, **89**(B3), 1856–1866.

Karato, S., 1992. On the Lehmann discontinuity, *Geophysical Research Letters*, **19**(22), 2255–2258.

Karato, S.-i., Olugboji, T., & Park, J., 2015. Mechanisms and geologic significance of the mid-lithosphere discontinuity in the continents, *Nature Geoscience*, **8**(7), 509–514.

Kawakatsu, H., Kumar, P., Takei, Y., Shinohara, M., Kanazawa, T., Araki, E., & Suyehiro, K., 2009. Seismic Evidence for Sharp Lithosphere-Asthenosphere Boundaries of Oceanic Plates, *Science*, **324**(5926), 499–502.

Kehoe, H. L., Kiser, E. D., & Okubo, P. G., 2019. The Rupture Process of the 2018 Mw 6.9 Hawaii Earthquake as Imaged by a Genetic Algorithm-Based Back-Projection Technique, *Geophysical Research Letters*, **46**(5), 2467–2474.

Kemp, M., Jenkins, J., Maclennan, J., & Cottaar, S., 2019. X-discontinuity and transition zone structure beneath Hawaii suggests a heterogeneous plume, *Earth and Planetary Science Letters*, **527**, 115781.

Kennet, B., 2000. West Australian Cratons.

Kennett, B., 1997. KIMBA97.

Kennett, B., 1998. KIMBA98.

Kennett, B., 2003. TASMAL.

Kennett, B. & Iaffaldano, G., 2013. Role of lithosphere in intra-continental deformation: Central Australia, *Gondwana Research*, **24**(3-4), 958–968.

Kennett, B. & Saygin, E., 2015. The nature of the Moho in Australia from reflection profiling: A review, *GeoResJ*, **5**, 74–91.

Kennett, B., Debayle, E., & Gorbatov, A., 1999. QUOLL.

Kennett, B., Yoshizawa, K., & Furumura, T., 2017. Interactions of multi-scale heterogeneity in the lithosphere: Australia, *Tectonophysics*, **717**, 193–213.

Kennett, B. L. N., 2015. Lithosphere–asthenosphere P-wave reflectivity across Australia, *Earth and Planetary Science Letters*, **431**, 225–235.

Kennett, B. L. N. & Furumura, T., 2008. Stochastic waveguide in the lithosphere: Indonesian subduction zone to Australian craton, *Geophysical Journal International*, **172**(1), 363 – 382.

Kennett, B. L. N. & Sippl, C., 2018. Lithospheric discontinuities in Central Australia, *Tectonophysics*, **744**, 10–22.

Kennett, B. L. N., Engdahl, E. R., & Buland, R., 1995. Constraints on seismic velocities in the Earth from traveltimes, *Geophysical Journal International*, **122**(1), 108–124.

Kennett, B. L. N., Salmon, M., Saygin, E., & Group, A. W., 2011. AusMoho: the variation of Moho depth in Australia, *Geophysical Journal International*, **187**(2), 946–958.

Kennett, B. L. N., Fichtner, A., Fishwick, S., & Yoshizawa, K., 2013. Australian Seismological Reference Model (AuSREM): mantle component, *Geophysical Journal International*, **192**(2), 871–887.

Kennett, B. L. N., Gorbatov, A., Yuan, H., Agrawal, S., Murdie, R., Doublier, M. P., Eakin, C. M., Miller, M. S., Zhao, L., Czarnota, K., O'Donnell, J. P., Dentith, M., & Gessner, K., 2023. Refining the Moho across the Australian continent, *Geophysical Journal International*, **233**(3), 1863–1877.

Kikuchi, M. & Kanamori, H., 1982. Inversion of complex body waves, *Bulletin of the Seismological Society of America*, **72**(2), 491.

Kikuchi, M. & Kanamori, H., 1991. Inversion of complex body waves—III, *Bulletin of the Seismological Society of America*, **81**(6), 2335–2350.

Kim, H., Kawakatsu, H., Akuhara, T., Shinohara, M., Shiobara, H., Sugioka, H., & Takagi, R., 2021. Receiver Function Imaging of the Amphibious NE Japan Subduction Zone—Effects of Low-Velocity Sediment Layer, *Journal of Geophysical Research: Solid Earth*, **126**(9).

Kim, S., Dettmer, J., Rhie, J., & Tkalčić, H., 2016. Highly efficient Bayesian joint inversion for receiver-based data and its application to lithospheric structure beneath the southern Korean Peninsula, *Geophysical Journal International*, **206**(1), 328–344.

Kind, R. & Yuan, X., 2011. Seismic, Receiver Function Technique, pp. 1258–1269, ed. Gupta"], H. K., Springer Netherlands, Dordrecht.

Kind, R., Yuan, X., & Kumar, P., 2012. Seismic receiver functions and the lithosphere–asthenosphere boundary, *Tectonophysics*, **536**, 25–43.

Kind, R., Mooney, W. D., & Yuan, X., 2020. New insights into the structural elements of the upper mantle beneath the contiguous United States from S-to-P converted seismic waves, *Geophysical Journal International*.

Kiser, E. & Ishii, M., 2013a. Hidden aftershocks of the 2011 Mw 9.0 Tohoku, Japan earthquake imaged with the backprojection method, *Journal of Geophysical Research: Solid Earth*, **118**(10), 5564–5576.

Kiser, E. & Ishii, M., 2013b. The 2010 Maule, Chile, Coseismic Gap and Its Relationship to the 25 March 2012 Mw 7.1 Earthquake, *Bulletin of the Seismological Society of America*, **103**(2A), 1148–1153.

Kiser, E. & Ishii, M., 2017. Back-Projection Imaging of Earthquakes, *Annual Review of Earth and Planetary Sciences*, **45**(1), 271 – 299.

Kiser, E., Kehoe, H., Chen, M., & Hughes, A., 2021. Lower Mantle Seismicity Following the 2015 Mw 7.9 Bonin Islands Deep-Focus Earthquake, *Geophysical Research Letters*, **48**(13).

Knapmeyer-Endrun, B., Panning, M. P., Bissig, F., Joshi, R., Khan, A., Kim, D., Lekić, V., Tauzin, B., Tharimena, S., Plasman, M., Compaire, N., Garcia, R. F., Margerin, L., Schimmel, M., Stutzmann, c., Schmerr, N., Bozdağ, E., Plesa, A.-C., Wieczorek, M. A., Broquet, A., Antonangeli, D., McLennan, S. M., Samuel, H., Michaut, C., Pan, L., Smrekar, S. E., Johnson, C. L., Brinkman, N., Mittelholz, A., Rivoldini, A., Davis, P. M., Lognonné, P., Pinot, B., Scholz, J.-R., Stähler, S., Knapmeyer, M., Driel, M. v., Giardini, D., & Banerdt, W. B., 2021. Thickness and structure of the martian crust from InSight seismic data, *Science*, **373**(6553), 438–443.

Kobayashi, H., Koketsu, K., & Miyake, H., 2017. Rupture processes of the 2016 Kumamoto earthquake sequence: Causes for extreme ground motions, *Geophysical Research Letters*, **44**(12), 6002–6010.

Koper, K. D., Hutko, A. R., Lay, T., Ammon, C. J., & Kanamori, H., 2011. Frequency-dependent rupture process of the 2011 Mw 9.0 Tohoku Earthquake: Comparison of short-period P wave backprojection images and broadband seismic rupture models, *Earth, Planets and Space*, **63**(7), 16.

Koper, K. D., Hutko, A. R., Lay, T., & Sufri, O., 2012. Imaging short-period seismic radiation from the 27 February 2010 Chile (M W 8.8) earthquake by back-projection of P , PP , and PKIKP waves: RUPTURE IMAGING OF 2010 CHILE EARTHQUAKE, *Journal of Geophysical Research: Solid Earth*, **117**(B2).

Krueger, H. E., Gama, I., & Fischer, K. M., 2021. Global Patterns in Cratonic Mid-Lithospheric Discontinuities From Sp Receiver Functions, *Geochemistry, Geophysics, Geosystems*, **22**(6).

Kubota, T., Saito, T., & Nishida, K., 2022. Global fast-traveling tsunamis driven by atmospheric Lamb waves on the 2022 Tonga eruption, *Science*, p. eabo4364.

Kumar, P. & Kawakatsu, H., 2011. Imaging the seismic lithosphere-asthenosphere boundary of the oceanic plate, *Geochemistry, Geophysics, Geosystems*, **12**(1).

Kumar, P., Kawakatsu, H., Shinohara, M., Kanazawa, T., Araki, E., & Suyehiro, K., 2011. P and S receiver function analysis of seafloor borehole broadband seismic data, *Journal of Geophysical Research: Solid Earth*, **116**(B12).

Kumar, P., Kind, R., Yuan, X., & Mechie, J., 2012. USArray Receiver Function Images of the Lithosphere-Asthenosphere Boundary, *Seismological Research Letters*, **83**(3), 486–491.

Kutschera, F., Jia, Z., Oryan, B., Wong, J. W. C., Fan, W., & Gabriel, A., 2024. The Multi-Segment Complexity of the 2024 MW ${M}_{W}$ 7.5 Noto Peninsula Earthquake Governs Tsunami Generation, *Geophysical Research Letters*, **51**(21).

Langston, C. A., 1979. Structure under Mount Rainier, Washington, inferred from teleseismic body waves, *Journal of Geophysical Research: Solid Earth*, **84**(B9), 4749–4762.

Larson, E. W. F. & Ekström, G., 2002. Determining surface wave arrival angle anomalies, *Journal of Geophysical Research*, **107**(B6).

Laske, G., 1995. Global observation of off-great-circle propagation of Long-Period surface waves, *Geophysical Journal International*, **123**(1), 245 – 259.

Laske, G. & Masters, G., 1996. Constraints on global phase velocity maps from long-period polarization data, *Journal of Geophysical Research: Solid Earth*, **101**(B7), 16059–16075.

Lehmann, I., 1961. S and the Structure of the Upper Mantle, *Geophysical Journal International*, **4**(s0), 124–138.

Leven, J., 1985. The application of synthetic seismograms to the interpretation of the upper mantle P-wave velocity structure in northern Australia, *Physics of the Earth and Planetary Interiors*, **38**(1), 9–27.

Levin, V. & Park, J., 1997. P-SH conversions in a flat-layered medium with anisotropy of arbitrary orientation, *Geophysical Journal International*, **131**(2), 253–266.

Li, B., Wu, B., Bao, H., Oglesby, D. D., Ghosh, A., Gabriel, A., Meng, L., & Chu, R., 2022. Rupture Heterogeneity and Directivity Effects in Back-Projection Analysis, *Journal of Geophysical Research: Solid Earth*, **127**(3).

Liu, L., Tong, S., Li, S., & Qaysi, S., 2020. Sp Receiver-Function Images of African and Arabian Lithosphere: Survey of Newly Available Broadband Data, *Seismological Research Letters*, **91**(3), 1813–1819.

Liu, T., Chin, E. J., & Shearer, P., 2023. Strong Physical Contrasts Across Two Mid-Lithosphere Discontinuities Beneath the Northwestern United States: Evidence for Cratonic Mantle Metasomatism, *AGU Advances*, **4**(6).

Lognonné, P., Clévédé, E., & Kanamori, H., 1998. Computation of seismograms and atmospheric oscillations by normal-mode summation for a spherical earth model with realistic atmosphere, *Geophysical Journal International*, **135**(2), 388–406.

Ma, Z., Zeng, H., Luo, H., Liu, Z., Jiang, Y., Aoki, Y., Wang, W., Itoh, Y., Lyu, M., Cui, Y., Yun, S.-H., Hill, E. M., & Wei, S., 2024. Slow rupture in a fluid-rich fault zone initiated the 2024 Mw 7.5 Noto earthquake, *Science*, p. eado5143.

Madariaga, R., 1977. High-frequency radiation from crack (stress drop) models of earthquake faulting, *Geophysical Journal of the Royal Astronomical Society*, **51**(3), 625–651.

Madariaga, R., 1983. High frequency radiation from dynamic earthquake fault models, *Annales de Geophysique*, **1**(1), 17–23.

Madariaga, R., 2003. Radiation from a Finite Reverse Fault in a Half Space, *pure and applied geophysics*, **160**(3), 555–577.

Madden, E. H., Ulrich, T., & Gabriel, A., 2022. The State of Pore Fluid Pressure and 3-D Megathrust Earthquake Dynamics, *Journal of Geophysical Research: Solid Earth*, **127**(4).

Magrini, F., Kästle, E., Pilia, S., Rawlinson, N., & Siena, L., 2023. A New Shear-Velocity Model of Continental Australia Based on Multi-Scale Surface-Wave Tomography, *Journal of Geophysical Research: Solid Earth*, **128**(7).

Mai, P. M., Aspiotis, T., Aquib, T. A., Cano, E. V., Castro-Cruz, D., Espindola-Carmona, A., Li, B., Li, X., Liu, J., Matrau, R., Nobile, A., Palgunadi, K. H., Ribot, M., Parisi, L., Suhendi, C., Tang, Y., Yalcin, B., Avşar, U., Klinger, Y., & Jónsson, S., 2023. The Destructive Earthquake Doublet of 6 February 2023 in South-Central Türkiye and Northwestern Syria: Initial Observations and Analyses, *The Seismic Record*, **3**(2), 105–115.

Marty, S., Passelègue, F. X., Aubry, J., Bhat, H. S., Schubnel, A., & Madariaga, R., 2019. Origin of High-Frequency Radiation During Laboratory Earthquakes, *Geophysical Research Letters*, **46**(7), 3755–3763.

Masters, T. G., Johnson, S., Laske, G., & Bolton, H., 1996. A shear - velocity model of the mantle, *Philosophical Transactions of the Royal Society of London. Series A: Mathematical, Physical and Engineering Sciences*, **354**(1711), 1385–1411.

Matoza, R. S., Fee, D., Assink, J. D., Iezzi, A. M., Green, D. N., Kim, K., Toney, L., Lecocq, T., Krishnamoorthy, S., Lalande, J.-M., Nishida, K., Gee, K. L., Haney, M. M., Ortiz, H. D., Brissaud, Q., Martire, L., Rolland, L., Vergados, P., Nippress, A., Park, J., Shani-Kadmiel, S., Witsil, A., Arrowsmith, S., Caudron, C., Watada, S., Perttu, A. B., Taisne, B., Mialle, P., Pichon, A. L., Vergoz, J., Hupe, P., Blom, P. S., Waxler, R., Angelis, S. D., Snively, J. B., Ringler, A. T., Anthony, R. E., Jolly, A. D., Kilgour, G., Averbuch, G., Ripepe, M., Ichihara, M., Arciniega-Ceballos, A., Astafyeva, E., Ceranna, L., Cevuard, S., Che, I.-Y., Negri, R. D., Ebeling, C. W., Evers, L. G., Franco-Marin, L. E., Gabrielson, T. B., Hafner, K., Harrison, R. G., Komjathy, A., Lacanna, G., Lyons, J., Macpherson, K. A., Marchetti, E., McKee, K. F., Mellors, R. J., Mendo-Pérez, G., Mikesell, T. D., Munaibari, E., Oyola-

Merced, M., Park, I., Pilger, C., Ramos, C., Ruiz, M. C., Sabatini, R., Schwaiger, H. F., Tailpied, D., Talmadge, C., Vidot, J., Webster, J., & Wilson, D. C., 2022. Atmospheric waves and global seismoacoustic observations of the January 2022 Hunga eruption, Tonga, *Science (New York, N.Y.)*, p. eeeeeeeeeee.

McLaren, S., Sandiford, M., Hand, M., Neumann, N., Wyborn, L., & Bastrakova, I., 2003. Evolution and Dynamics of the Australian Plate.

Metropolis, N., Rosenbluth, A. W., Rosenbluth, M. N., Teller, A. H., & Teller, E., 1953. Equation of State Calculations by Fast Computing Machines, *The Journal of Chemical Physics*, **21**(6), 1087–1092.

Metz, M., Vera, F., Ponce, A. C., Cesca, S., Babeyko, A., Dahm, T., Saul, J., & Tilmann, F., 2022. Seismic and Tsunamigenic Characteristics of a Multimodal Rupture of Rapid and Slow Stages: The Example of the Complex 12 August 2021 South Sandwich Earthquake, *Journal of Geophysical Research: Solid Earth*, **127**(11).

MEXT, 2013. Integrated Research Project on Seismic and Tsunami Hazards Around the Sea of Japan.

Miller, M. S., 2014. Transitions in the Banda Arc-Australia continental collision.

Mizutani, A. & Melgar, D., 2023. Potential Volcanic Origin of the 2023 Short-period Tsunami in the Izu Islands, Japan, *Seismica*, **2**(2).

Mizutani, A. & Yomogida, K., 2022. Back-projection imaging of a tsunami excitation area with ocean-bottom pressure gauge array data, *Journal of Geophysical Research: Oceans*.

Mizutani, A., Adriano, B., Mas, E., & Koshimura, S., 2024. Fault Model of the 2024 Noto Peninsula Earthquake Based on Aftershock, Tsunami, and GNSS Data.

Myers, J. S., Shaw, R. D., & Tyler, I. M., 1996. Tectonic evolution of Proterozoic Australia, *Tectonics*, **15**(6), 1431–1446.

Nagaya, M., Oda, H., Akazawa, H., & Ishise, M., 2008. Receiver Functions of Seismic Waves in Layered Anisotropic Media: Application to the Estimate of Seismic

AnisotropyReceiver Functions of Seismic Waves in Layered Anisotropic Media, *Bulletin of the Seismological Society of America*, **98**(6), 2990–3006.

Nagaya, M., Oda, H., & Kamimoto, T., 2011. Regional variation in shear-wave polarization anisotropy of the crust in southwest Japan as estimated by splitting analysis of Ps-converted waves on receiver functions, *Physics of the Earth and Planetary Interiors*, **187**(1-2), 56–65.

Nakajima, J., 2022. Crustal structure beneath earthquake swarm in the Noto peninsula, Japan, *Earth, Planets and Space*, **74**(1), 160.

Nakanishi, I. & Anderson, D. L., 1983. Measurement of mantle wave velocities and inversion for lateral heterogeneity and anisotropy: 1. Analysis of Great Circle Phase Velocities, *Journal of Geophysical Research: Solid Earth*, **88**(B12), 10267–10283.

Nakashima, Y., Heki, K., Takeo, A., Cahyadi, M. N., Aditiya, A., & Yoshizawa, K., 2016. Atmospheric resonant oscillations by the 2014 eruption of the Kelud volcano, Indonesia, observed with the ionospheric total electron contents and seismic signals, *Earth and Planetary Science Letters*, **434**, 112–116.

NASA, 2022. Tonga volcano plume reached the mesosphere (2022).

Nataf, H., Nakanishi, I., & Anderson, D. L., 1986. Measurements of mantle wave velocities and inversion for lateral heterogeneities and anisotropy: 3. Inversion, *Journal of Geophysical Research: Solid Earth*, **91**(B7), 7261–7307.

Nataf, H.-C. & Ricard, Y., 1996. 3SMAC: an a priori tomographic model of the upper mantle based on geophysical modeling, *Physics of the Earth and Planetary Interiors*, **95**(1-2), 101–122.

Nishida, K., 2013. Earth's Background Free Oscillations, *Annual Review of Earth and Planetary Sciences*, **41**(1), 719–740.

Nishimura, T., Hiramatsu, Y., & Ohta, Y., 2023. Episodic transient deformation revealed by the analysis of multiple GNSS networks in the Noto Peninsula, central Japan, *Scientific Reports*, **13**(1), 8381.

Noda, H. & Lapusta, N., 2013. Stable creeping fault segments can become destructive as a result of dynamic weakening, *Nature*, **493**(7433), 518–521.

Office, M., 2010. *Cartopy: a cartographic python library with a Matplotlib interface*.

Ohira, A., Kodaira, S., Nakamura, Y., Fujie, G., Arai, R., & Miura, S., 2017. Evidence for frozen melts in the mid-lithosphere detected from active-source seismic data, *Scientific Reports*, **7**(1), 15770.

Okuwaki, R. & Yagi, Y., 2017. Role of geometric barriers in irregular-rupture evolution during the 2008 Wenchuan earthquake, *Geophysical Journal International*, **212**(3), 1657–1664.

Okuwaki, R., Yagi, Y., & Hirano, S., 2014. Relationship between High-frequency Radiation and Asperity Ruptures, Revealed by Hybrid Back-projection with a Non-planar Fault Model, *Scientific Reports*, **4**(1), 7120.

Okuwaki, R., Kasahara, A., Yagi, Y., Hirano, S., & Fukahata, Y., 2018. Backprojection to image slip, *Geophysical Journal International*, **216**(3), 1529–1537.

Okuwaki, R., Yagi, Y., Taymaz, T., & Hicks, S. P., 2023. Multi-Scale Rupture Growth With Alternating Directions in a Complex Fault Network During the 2023 South-Eastern Türkiye and Syria Earthquake Doublet, *Geophysical Research Letters*, **50**(12).

Okuwaki, R., Yagi, Y., Murakami, A., & Fukahata, Y., 2024. A Multiplex Rupture Sequence Under Complex Fault Network Due To Preceding Earthquake Swarms During the 2024 Mw 7.5 Noto Peninsula, Japan, Earthquake, *Geophysical Research Letters*, **51**(11).

Ono, S., Kikegawa, T., Higo, Y., & Tange, Y., 2017. Precise determination of the phase boundary between coesite and stishovite in SiO2, *Physics of the Earth and Planetary Interiors*, **264**, 1–6.

Oshima, M. & Takenaka, H., 2020. A P- and S-Wave Picking Technique Based on the Probabilistic Density Function of Seismic-Waveform Amplitude, *Bulletin of the Seismological Society of America*, **110**(2), 763–782.

Palo, M., Tilmann, F., Krüger, F., Ehlert, L., & Lange, D., 2014. High-frequency seismic radiation from Maule earthquake (Mw 8.8, 2010 February 27) inferred from high-resolution backprojection analysis, *Geophysical Journal International*, **199**(2), 1058–1077.

Pampillón, P., Santillán, D., Mosquera, J. C., & Cueto-Felgueroso, L., 2023. The role of pore fluids in supershear earthquake ruptures, *Scientific Reports*, **13**(1), 398.

Panning, M. P., Lekić, V., & Romanowicz, B. A., 2010. Importance of crustal corrections in the development of a new global model of radial anisotropy, *Journal of Geophysical Research: Solid Earth*, **115**(B12).

Park, J. & Levin, V., 2016. Anisotropic shear zones revealed by backazimuthal harmonics of teleseismic receiver functions, *Geophysical Journal International*, **207**(2), 1216–1243.

Plomerová, J., Kouba, D., & Babuška, V., 2002. Mapping the lithosphere–asthenosphere boundary through changes in surface-wave anisotropy, *Tectonophysics*, **358**(1-4), 175–185.

Poli, P. & Shapiro, N. M., 2022. Rapid Characterization of Large Volcanic Eruptions: Measuring the Impulse of the Hunga Tonga Ha'apai Explosion From Teleseismic Waves, *Geophysical Research Letters*, **49**(8).

Pugh, S., Jenkins, J., Boyce, A., & Cottaar, S., 2021. Global receiver function observations of the X-discontinuity reveal recycled basalt beneath hotspots, *Earth and Planetary Science Letters*, **561**, 116813.

Pugh, S., Boyce, A., Bastow, I. D., Ebinger, C. J., & Cottaar, S., 2023. Multigenetic Origin of the X-Discontinuity Below Continents: Insights From African Receiver Functions, *Geochemistry, Geophysics, Geosystems*, **24**(3).

Rawlinson, N. & Kennett, B., 2001. TIGGER BB.

Rawlinson, N., Pilia, S., Young, M., Salmon, M., & Yang, Y., 2016. Crust and upper mantle structure beneath southeast Australia from ambient noise and teleseismic tomography, *Tectonophysics*, **689**, 143–156.

Rawlinson, S. & Kennet, B., 2008. BILBY.

Reading, A. & Kennett, B., 2005. CAPRA - Linkage.

Reading, A. & Rawlinson, N., 2011. Bass Strait.

Rein, T., Hannemann, K., Thomas, C., & Korn, M., 2020. Location and characteristics of the X-discontinuity beneath SW Morocco and the adjacent shelf area using P-wave receiver functions, *Geophysical Journal International*, **223**(3), 1780–1793.

Revenaugh, J. & Jordan, T. H., 1991. Mantle layering from ScS reverberations: 3. The upper mantle, *Journal of Geophysical Research: Solid Earth*, **96**(B12), 19781–19810.

Rondenay, S., 2009. Upper Mantle Imaging with Array Recordings of Converted and Scattered Teleseismic Waves, *Surveys in Geophysics*, **30**(4-5), 377–405.

Rost, S. & Thomas, C., 2002. ARRAY SEISMOLOGY: METHODS AND APPLICATIONS: ARRAY SEISMOLOGY, *Reviews of Geophysics*, **40**(3), 2–1–2–27.

Roten, D., Miyake, H., & Koketsu, K., 2012. A Rayleigh wave back-projection method applied to the 2011 Tohoku earthquake, *Geophysical Research Letters*, **39**(2).

Rychert, C. A. & Shearer, P. M., 2009. A Global View of the Lithosphere-Asthenosphere Boundary, *Science*, **324**(5926), 495–498.

Rychert, C. A., Fischer, K. M., & Rondenay, S., 2005. A sharp lithosphere–asthenosphere boundary imaged beneath eastern North America, *Nature*, **436**(7050), 542–545.

Rychert, C. A., Rondenay, S., & Fischer, K. M., 2007. P-to-S and S-to-P imaging of a sharp lithosphere-asthenosphere boundary beneath eastern North America, *Journal of Geophysical Research: Solid Earth (1978–2012)*, **112**(B8).

Rychert, C. A., Harmon, N., & Schmerr, N., 2014. Synthetic waveform modelling of SS precursors from anisotropic upper-mantle discontinuities, *Geophysical Journal International*, **196**(3), 1694–1705.

Saito, M., 1988. DISPER80 : A subroutine package for the calculation of seismic normal mode solutions, Seismological Algorithms, p. 293–319, eds Doornbos, D., & Elsevier.

Salmon, M., Balfour, N., & Sambridge, M., 2011. Australian Seismometers in Schools.

Salmon, M., Kennett, B. L. N., & Saygin, E., 2013. Australian Seismological Reference Model (AuSREM): crustal component, *Geophysical Journal International*, **192**(1), 190–206.

Sambridge, M., 2014. A Parallel Tempering algorithm for probabilistic sampling and multimodal optimization, *Geophysical Journal International*, **196**(1), 357–374.

Sandanbata, O., Satake, K., Takemura, S., Watada, S., Maeda, T., & Kubota, T., 2024. Enigmatic Tsunami Waves Amplified by Repetitive Source Events Near Sofugan Volcano, Japan, *Geophysical Research Letters*, **51**(2).

Sandiford, M., Hand, M., & McLaren, S., 2001. Tectonic feedback, intraplate orogeny and the geochemical structure of the crust: a central Australian perspective, *Geological Society, London, Special Publications*, **184**(1), 195–218.

Savage, J. C., 1965. The stopping phase on seismograms, *Bulletin of the Seismological Society of America*, **55**(1), 47–58.

Schmerr, N. & Garnero, E., 2006. Investigation of upper mantle discontinuity structure beneath the central Pacific using SS precursors, *Journal of Geophysical Research: Solid Earth*, **111**(B8).

Schulte-Pelkum, V., Masters, G., & Shearer, P. M., 2001. Upper mantle anisotropy from long-period P polarization, *Journal of Geophysical Research: Solid Earth*, **106**(B10), 21917–21934.

Scibiorski, E., Tohver, E., & Jourdan, F., 2015. Rapid cooling and exhumation in the western part of the Mesoproterozoic Albany-Fraser Orogen, Western Australia, *Precambrian Research*, **265**, 232–248.

Scibiorski, E., Tohver, E., Jourdan, F., Kirkland, C. L., & Spaggiari, C., 2016. Cooling and exhumation along the curved Albany-Fraser orogen, Western Australia, *Lithosphere*, **8**(5), 551–563.

Selway, K., Ford, H., & Kelemen, P., 2015. The seismic mid-lithosphere discontinuity, *Earth and Planetary Science Letters*, **414**, 45–57.

Shearer, P. M., 1993. Global mapping of upper mantle reflectors from long-period SS precursors, *Geophysical Journal International*, **115**(3), 878–904.

Shi, D., Wu, Z., Klemperer, S. L., Zhao, W., Xue, G., & Su, H., 2015. Receiver function imaging of crustal suture, steep subduction, and mantle wedge in the eastern India–Tibet continental collision zone, *Earth and Planetary Science Letters*, **414**, 6–15.

Shi, J., Plasman, M., Knapmeyer-Endrun, B., Xu, Z., Kawamura, T., Lognonné, P., McLennan, S. M., Sainton, G., Banerdt, W. B., Panning, M. P., & Wang, T., 2023. High-Frequency Receiver Functions With Event S1222a Reveal a Discontinuity in the Martian Shallow Crust, *Geophysical Research Letters*, **50**(5).

Shi, Q. & Wei, S., 2020. Highly Heterogeneous Pore Fluid Pressure Enabled Rupture of Orthogonal Faults During the 2019 Ridgecrest Mw7.0 Earthquake, *Geophysical Research Letters*, **47**(20).

Shi, Q., Wei, S., & Chen, M., 2018. An MCMC multiple point sources inversion scheme and its application to the 2016 Kumamoto Mw 6.2 earthquake, *Geophysical Journal International*, **215**(2), 737–752.

Shibutani, T., Ueno, T., & Hirahara, K., 2008. Improvement in the Extended-Time Multitaper Receiver Function Estimation TechniqueShort Note, *Bulletin of the Seismological Society of America*, **98**(2), 812–816.

Shimizu, K., Yagi, Y., Okuwaki, R., & Fukahata, Y., 2019. Development of an inversion method to extract information on fault geometry from teleseismic data, *Geophysical Journal International*, **220**(2), 1055–1065.

Shiomi, K., 2017. Dissimilar receiver functions observed at very close stations in the Kii Peninsula, central Japan: features and causes, *Earth, Planets and Space*, **69**(1), 48.

Shiomi, K. & Park, J., 2008. Structural features of the subducting slab beneath the Kii Peninsula, central Japan: Seismic evidence of slab segmentation, dehydration, and anisotropy, *Journal of Geophysical Research: Solid Earth*, **113**(B10).

Simons, F. J., van der Hilst, R. D., Montagner, J., & Zielhuis, A., 2002. Multimode Rayleigh wave inversion for heterogeneity and azimuthal anisotropy of the Australian upper mantle, *Geophysical Journal International*, **151**(3), 738–754.

Sippl, C., 2016. Moho geometry along a north–south passive seismic transect through Central Australia, *Tectonophysics*, **676**, 56–69.

Sippl, C., Brisbout, L., Spaggiari, C., Gessner, K., Tkalčić, H., Kennett, B., & Murdie, R., 2017. Crustal structure of a Proterozoic craton boundary: East Albany-Fraser Orogen, Western Australia, imaged with passive seismic and gravity anomaly data, *Precambrian Research*, **296**, 78–92.

Smithies, R., Kirkland, C., Korhonen, F., Aitken, A., Howard, H., Maier, W., Wingate, M., Gromard, R. Q. d., & Gessner, K., 2015. The Mesoproterozoic thermal evolution of the Musgrave Province in central Australia — Plume vs. the geological record, *Gondwana Research*, **27**(4), 1419–1429.

Smithies, R. H., Howard, H. M., Evins, P. M., Kirkland, C. L., Kelsey, D. E., Hand, M., Wingate, M. T. D., Collins, A. S., & Belousova, E., 2011. High-Temperature Granite Magmatism, Crust–Mantle Interaction and the Mesoproterozoic Intracontinental Evolution of the Musgrave Province, Central Australia, *Journal of Petrology*, **52**(5), 931–958.

Sodoudi, F., Yuan, X., Kind, R., Heit, B., & Sadidkhouy, A., 2009. Evidence for a missing crustal root and a thin lithosphere beneath the Central Alborz by receiver function studies, *Geophysical Journal International*, **177**(2), 733–742.

Sodoudi, F., Yuan, X., Kind, R., Lebedev, S., Adam, J. M., Kästle, E., & Tilmann, F., 2013. Seismic evidence for stratification in composition and anisotropic fabric within the thick lithosphere of Kalahari Craton, *Geochemistry, Geophysics, Geosystems*, **14**(12), 5393–5412.

Spaggiari, C., Kirkland, C., Smithies, R., Wingate, M., & Belousova, E., 2015. Transformation of an Archean craton margin during Proterozoic basin formation and magmatism: The Albany–Fraser Orogen, Western Australia, *Precambrian Research*, **266**, 440–466.

Spudich, P. & Frazer, L. N., 1984. Use of ray theory to calculate high-frequency radiation from earthquake sources having spatially variable rupture velocity and stress drop, *Bulletin of the Seismological Society of America*, **74**(6), 2061–2082.

Srinu, U., Kumar, P., Haldar, C., Kumar, M. R., Srinagesh, D., & Illa, B., 2021. X-Discontinuity Beneath the Indian Shield—Evidence for Remnant Tethyan Oceanic Lithosphere in the Mantle, *Journal of Geophysical Research: Solid Earth*, **126**(8).

Sudholz, Z. J., Zhang, P., Eakin, C. M., Yaxley, G. M., Jaques, A. L., Frigo, C., & Czarnota, K., 2024. Ancient Craton-Wide Mid-Lithosphere Discontinuity Controlled by Pargasite Channels, *Geophysical Research Letters*, **51**(9).

Sun, W., Fu, L., Saygin, E., & Zhao, L., 2018. Insights Into Layering in the Cratonic Lithosphere Beneath Western Australia, *Journal of Geophysical Research: Solid Earth*, **123**(2), 1405–1418.

Svennevig, K., Hicks, S. P., Forbriger, T., Lecocq, T., Widmer-Schnidrig, R., Mangeney, A., Hibert, C., Korsgaard, N. J., Lucas, A., Satriano, C., Anthony, R. E., Mordret, A., Schippkus, S., Rysgaard, S., Boone, W., Gibbons, S. J., Cook, K. L., Glimsdal, S., Løvholt, F., Noten, K. V., Assink, J. D., Marboeuf, A., Lomax, A., Vanneste, K., Taira, T., Spagnolo, M., Plaen, R. D., Koelemeijer, P., Ebeling, C., Cannata, A., Harcourt, W. D., Cornwell, D. G., Caudron, C., Poli, P., Bernard, P., Larose, E., Stutzmann, E., Voss, P. H., Lund, B., Cannavo, F., Castro-Díaz, M. J., Chaves, E., Dahl-Jensen, T., Dias, N. D. P., Déprez, A., Develter, R., Dreger, D., Evers, L. G., Fernández-Nieto, E. D., Ferreira, A. M. G., Funning, G., Gabriel, A.-A.,

Hendrickx, M., Kafka, A. L., Keiding, M., Kerby, J., Khan, S. A., Dideriksen, A. K., Lamb, O. D., Larsen, T. B., Lipovsky, B., Magdalena, I., Malet, J.-P., Myrup, M., Rivera, L., Ruiz-Castillo, E., Wetter, S., & Wirtz, B., 2024. A rockslide-generated tsunami in a Greenland fjord rang Earth for 9 days, *Science*, **385**(6714), 1196–1205.

Taira, T. & Yoshizawa, K., 2020. Upper-mantle discontinuities beneath Australia from transdimensional Bayesian inversions using multimode surface waves and receiver functions, *Geophysical Journal International*, **223**(3), 2085–2100.

Takagi, R. & Nishida, K., 2022. Multimode dispersion measurement of surface waves extracted by multicomponent ambient noise cross-correlation functions, *Geophysical Journal International*, **231**(2), 1196–1220.

Takeuchi, H. & Saito, M., 1972. Seismic Surface Waves, *Methods in Computational Physics: Advances in Research and Applications*, **11**, 217–295.

Tan, F., Ge, Z., Kao, H., & Nissen, E., 2019. Validation of the 3-D phase-weighted relative back projection technique and its application to the 2016 M w 7.8 Kaikōura earthquake, *Geophysical Journal International*, **217**(1), 375–388.

Tarumi, K., 2022. Upper mantle discontinuities from Bayesian inversion using receiver functions and surface waves, *Master of Philosophy of The Hokkaido University*.

Tarumi, K. & Yoshizawa, K., 2023. Eruption sequence of the 2022 Hunga Tonga-Hunga Ha'apai explosion from back-projection of teleseismic P waves, *Earth and Planetary Science Letters*, **602**, 117966.

Tarumi, K. & Yoshizawa, K., 2024. Numerical Sheet for "Station-orientation catalog for Australian broadband seismic stations".

Tesauro, M., Kaban, M. K., & Aitken, A. R. A., 2020. Thermal and Compositional Anomalies of the Australian Upper Mantle From Seismic and Gravity Data, *Geochemistry, Geophysics, Geosystems*, **21**(11).

Thiel, S., Goleby, B. R., Pawley, M. J., & Heinson, G., 2020. AusLAMP 3D MT imaging of an intracontinental deformation zone, Musgrave Province, Central Australia, *Earth, Planets and Space*, **72**(1), 98.

Thomson, W. T., 1950. Transmission of Elastic Waves through a Stratified Solid Medium, *Journal of Applied Physics*, **21**(2), 89–93.

Thybo, H., 2006. The heterogeneous upper mantle low velocity zone, *Tectonophysics*, **416**(1-4), 53–79.

Thybo, H. & Perchuć, E., 1997. The Seismic 8° Discontinuity and Partial Melting in Continental Mantle, *Science*, **275**(5306), 1626–1629.

Tkalčić, H., Pasyanos, M. E., Rodgers, A. J., Gök, R., Walter, W. R., & Al-Amri, A., 2006. A multistep approach for joint modeling of surface wave dispersion and teleseismic receiver functions: Implications for lithospheric structure of the Arabian Peninsula: MULTISTEP MODELING OF ARABIAN LITHOSPHERE, *Journal of Geophysical Research: Solid Earth*, **111**(B11).

Tkalčić, H., Chen, Y., Liu, R., Zhibin, H., Sun, L., & Chan, W., 2011. Multistep modelling of teleseismic receiver functions combined with constraints from seismic tomography: crustal structure beneath southeast China, *Geophysical Journal International*, **187**(1), 303–326.

Tkalčić, H., Kennett, B., Sippl, C., Spaggiari, C., & Gessner, K., 2013a. Albany-Fraser Experiment.

Tkalčić, H., Kennett, B., Tanaka, S., & Stipčević, J., 2013b. Australia.

Tonegawa, T., Hirahara, K., & Shibutani, T., 2005. Detailed structure of the upper mantle discontinuities around the Japan subduction zone imaged by receiver function analyses, *Earth, Planets and Space*, **57**(1), 5–14.

Tonegawa, T., Shiomi, K., & Takagi, R., 2024. Anisotropic structure at shallow depths across the Japan Trench, *Earth, Planets and Space*, **76**(1), 113.

Uchide, T., Yao, H., & Shearer, P. M., 2013. Spatio-temporal distribution of fault slip and high-frequency radiation of the 2010 El Mayor-Cucapah, Mexico earthquake, *Journal of Geophysical Research: Solid Earth*, **118**(4), 1546–1555.

Uieda, L., Tian, D., Leong, W. J., Jones, M., Schlitzer, W., Toney, L., Grund, M., Yao, J., Magen, Y., Materna, K., Newton, T., Anant, A., Ziebarth, M., Wessel, P., & Quinn, J., 2021. PyGMT: A Python interface for the Generic Mapping Tools, The development of PyGMT has been supported by NSF grants OCE-1558403 and EAR-1948603.

USGS, 2022. M 5.8 Volcanic Eruption -68 km NNW of Nuku'alofa,Tonga (2022).

USGS, 2024. M 7.5 - 2024 Noto Peninsula, Japan Earthquake.

van der Hilst, R., Kennett, B., Christie, D., & Grant, J., 1994. Project Skippy explores lithosphere and mantle beneath Australia, *Eos, Transactions American Geophysical Union*, **75**(15), 177–181.

van der Hilst, R. & Kennett, B., 1993. SKIPPY.

Vergoz, J., Hupe, P., Listowski, C., Pichon, A. L., Garcés, M., Marchetti, E., Labazuy, P., Ceranna, L., Pilger, C., Gaebler, P., Näsholm, S., Brissaud, Q., Poli, P., Shapiro, N., Negri, R. D., & Mialle, P., 2022. IMS observations of infrasound and acoustic-gravity waves produced by the January 2022 volcanic eruption of Hunga, Tonga: A global analysis, *Earth and Planetary Science Letters*, **591**, 117639.

Vidale, J. E., 1986. Complex polarization analysis of particle motion, *Bulletin of the Seismological Society of America*, **76**(5), 1393–1405.

Vinnik, L., 1977. Detection of waves converted from P to SV in the mantle, *Physics of the Earth and Planetary Interiors*, **15**(1), 39–45.

Vinnik, L., Kurnik, E., & Farra, V., 2005. Lehmann discontinuity beneath North America: No role for seismic anisotropy, *Geophysical Research Letters*, **32**(9).

Vinnik, L. P., Makeyeva, L. I., Milev, A., & Usenko, A. Y., 1992. Global patterns of azimuthal anisotropy and deformations in the continental mantle, *Geophysical Journal International*, **111**(3), 433–447.

Vinnik, L. P., Erduran, M., Oreshin, S. I., Kosarev, G. L., Kutlu, Y. A., Çakir, c., & Kiselev, S. G., 2014. Joint inversion of P- and S-receiver functions and dispersion

curves of Rayleigh waves: The results for the Central Anatolian Plateau, *Izvestiya, Physics of the Solid Earth*, **50**(5), 622–631.

Walker, K. T., Ishii, M., & Shearer, P. M., 2005. Rupture details of the 28 March 2005 Sumatra Mw 8.6 earthquake imaged with teleseismic P waves, *Geophysical Research Letters*, **32**(24).

Wang, D. & Mori, J., 2011. Rupture process of the 2011 off the Pacific coast of Tohoku Earthquake (Mw 9.0) as imaged with back-projection of teleseismic P-waves, *Earth, Planets and Space*, **63**(7), 17.

Watada, S. & Kanamori, H., 2010. Acoustic resonant oscillations between the atmosphere and the solid earth during the 1991 Mt. Pinatubo eruption, *Journal of Geophysical Research: Solid Earth*, **115**(B12).

Wessel, P., Luis, J. F., Uieda, L., Scharroo, R., Wobbe, F., Smith, W. H. F., & Tian, D., 2019. The Generic Mapping Tools Version 6, *Geochemistry, Geophysics, Geosystems*, **20**(11), 5556–5564.

Widmer, R., Masters, G., & Gilbert, F., 1991. Spherically symmetric attenuation within the Earth from normal mode data, *Geophysical Journal International*, **104**(3), 541–553.

Williams, Q. & Revenaugh, J., 2005. Ancient subduction, mantle eclogite, and the 300 km seismic discontinuity, *Geology*, **33**(1), 1.

Williams, S. E., Whittaker, J. M., Halpin, J. A., & Müller, R. D., 2019. Australian-Antarctic breakup and seafloor spreading: Balancing geological and geophysical constraints, *Earth-Science Reviews*, **188**, 41–58.

Wirth, E. A. & Long, M. D., 2014. A contrast in anisotropy across mid-lithospheric discontinuities beneath the central United States—A relic of craton formation, *Geology*, **42**(10), 851–854.

Xu, H. & Beghein, C., 2019. Measuring higher mode surface wave dispersion using a transdimensional Bayesian approach, *Geophysical Journal International*, **218**(1), 333–353.

Xu, H., Beghein, C., Panning, M. P., Drilleau, M., Lognonné, P., Driel, M. v., Ceylan, S., Böse, M., Brinkman, N., Clinton, J., Euchner, F., Giardini, D., Horleston, A., Kawamura, T., Kenda, B., Murdoch, N., & Stähler, S., 2021. Measuring Fundamental and Higher Mode Surface Wave Dispersion on Mars From Seismic Waveforms, *Earth and Space Science*, **8**(2).

Xu, L., Ji, C., Meng, L., Ampuero, J.-P., Yunjun, Z., Mohanna, S., & Aoki, Y., 2024. Dual-initiation ruptures in the 2024 Noto earthquake encircling a fault asperity at a swarm edge, *Science*, **385**(6711), 871–876.

Xu, Y., Koper, K. D., Sufri, O., Zhu, L., & Hutko, A. R., 2009. Rupture imaging of the Mw 7.9 12 May 2008 Wenchuan earthquake from back projection of teleseismic P waves, *Geochemistry, Geophysics, Geosystems*, **10**(4).

Yagi, Y., 2004. Source rupture process of the 2003 Tokachi-oki earthquake determined by joint inversion of teleseismic body wave and strong ground motion data, *Earth, Planets and Space*, **56**(3), 311–316.

Yagi, Y., Nakao, A., & Kasahara, A., 2012. Smooth and rapid slip near the Japan Trench during the 2011 Tohoku-oki earthquake revealed by a hybrid back-projection method, *Earth and Planetary Science Letters*, **355**, 94–101.

Yamashita, S., Yagi, Y., Okuwaki, R., Shimizu, K., Agata, R., & Fukahata, Y., 2022. Potency density tensor inversion of complex body waveforms with time-adaptive smoothing constraint, *Geophysical Journal International*, **231**(1), 91–107.

Ye, L., Lay, T., Kanamori, H., & Koper, K. D., 2013. Energy Release of the 2013 Mw 8.3 Sea of Okhotsk Earthquake and Deep Slab Stress Heterogeneity, *Science*, **341**(6152), 1380–1384.

Ye, L., Lay, T., Zhan, Z., Kanamori, H., & Hao, J.-L., 2016. The isolated ∼680 km deep 30 May 2015 Mw 7.9 Ogasawara (Bonin) Islands earthquake, *Earth and Planetary Science Letters*, **433**, 169–179.

Yin, J. & Yao, H., 2016. Rupture and frequency-dependent seismic radiation of the 2012

Mw 8.6 Sumatra strike-slip earthquake, *Geophysical Journal International*, **205**(3), 1682–1693.

Yoshida, K., Uchida, N., Matsumoto, Y., Orimo, M., Okada, T., Hirahara, S., Kimura, S., & Hino, R., 2023a. Updip Fluid Flow in the Crust of the Northeastern Noto Peninsula, Japan, Triggered the 2023 Mw 6.2 Suzu Earthquake During Swarm Activity, *Geophysical Research Letters*, **50**(21).

Yoshida, K., Uchida, N., Matsumoto, Y., Orimo, M., Okada, T., Hirahara, S., Kimura, S., & Hino, R., 2023b. Earthquake Data for the 2023 Mw6.2 Suzu Earthquake in the Northeastern Noto Peninsula, Japan.

Yoshida, K., Takagi, R., Fukushima, Y., Ando, R., Ohta, Y., & Hiramatsu, Y., 2024. Role of a Hidden Fault in the Early Process of the 2024 Mw7.5 Noto Peninsula Earthquake, *Geophysical Research Letters*, **51**(16).

Yoshida, M., 2012. Dynamic role of the rheological contrast between cratonic and oceanic lithospheres in the longevity of cratonic lithosphere: A three-dimensional numerical study, *Tectonophysics*, **532**, 156–166.

Yoshida, M. & Yoshizawa, K., 2020. Continental Drift with Deep Cratonic Roots, *Annual Review of Earth and Planetary Sciences*, **49**(1), 1–23.

Yoshimoto, M. & Yamanaka, Y., 2014. Teleseismic inversion of the 2004 Sumatra-Andaman earthquake rupture process using complete Green's functions, *Earth, Planets and Space*, **66**(1), 152.

Yoshizawa, K., 2014. Radially anisotropic 3-D shear wave structure of the Australian lithosphere and asthenosphere from multi-mode surface waves, *Physics of the Earth and Planetary Interiors*, **235**, 33–48.

Yoshizawa, K. & Ekström, G., 2010. Automated multimode phase speed measurements for high-resolution regional-scale tomography: application to North America, *Geophysical Journal International*, **183**(3), 1538–1558.

Yoshizawa, K. & Kennett, B. L. N., 2002a. Determination of the influence zone for surface wave paths, *Geophysical Journal International*, **149**(2), 440–453.

Yoshizawa, K. & Kennett, B. L. N., 2002b. Non-linear waveform inversion for surface waves with a neighbourhood algorithm—application to multimode dispersion measurements, *Geophysical Journal International*, **149**(1), 118–133.

Yoshizawa, K. & Kennett, B. L. N., 2004. Multimode surface wave tomography for the Australian region using a three-stage approach incorporating finite frequency effects: THREE-STAGE SURFACE WAVE TOMOGRAPHY, *Journal of Geophysical Research: Solid Earth*, **109**(B2).

Yoshizawa, K. & Kennett, B. L. N., 2015. The lithosphere-asthenosphere transition and radial anisotropy beneath the Australian continent, *Geophysical Research Letters*, **42**(10), 3839–3846.

Yoshizawa, K., Yomogida, K., & Tsuboi, S., 1999. Resolving power of surface wave polarization data for higher-order heterogeneities, *Geophysical Journal International*, **138**(1), 205–220.

Yuan, H. & Romanowicz, B., 2010. Lithospheric layering in the North American craton, *Nature*, **466**(7310), 1063–1068.

Yuan, H., Romanowicz, B., Fischer, K. M., & Abt, D., 2011. 3-D shear wave radially and azimuthally anisotropic velocity model of the North American upper mantle, *Geophysical Journal International*, **184**(3), 1237–1260.

Zhao, W., Sun, C., & Guo, Z., 2022. Reawaking of Tonga volcano, *The Innovation*, **3**(2), 100218.

Zheng, Z. & Romanowicz, B., 2012. Do double 'SS precursors' mean double discontinuities?, *Geophysical Journal International*, **191**(3), 1361–1373.